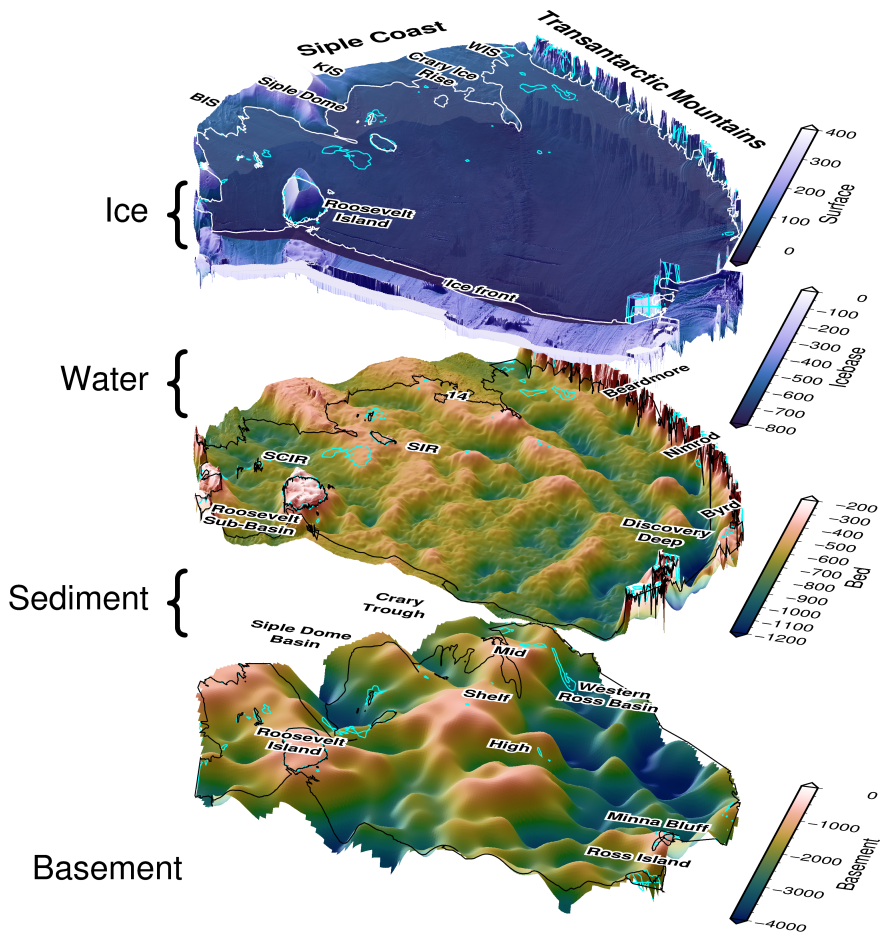


UPDATE TITLE



A thesis presented for the degree of
Doctor of Philosophy in Geophysics

Matthew Tankersley



Antarctic Research Centre
Victoria University of Wellington
New Zealand
June 28, 2023

¹¹ Abstract

¹² The Ross Ice Shelf controls the flow of ice into the ocean from catchments consisting
¹³ of both the East and West Antarctic Ice Sheets. These catchments hold a volume of
¹⁴ ice equivalent to \sim 12 m of global sea level rise. To adequately understand how this
¹⁵ ice will respond to a warming world requires knowledge of the solid-earth boundary
¹⁶ conditions which influence how the ice sheet behaves. These boundary conditions
¹⁷ include fundamental knowledge of the Earth, such as the shape of the bed beneath
¹⁸ the ice, the seafloor, and the geologic structures of the upper crust. Knowledge of
¹⁹ the physiography and sub-surface geology is severely lacking for the Ross Ice Shelf
²⁰ region. Here, we use airborne geophysical data from an extensive survey over the
²¹ Ross Ice Shelf to better understand these boundary conditions. From the analysis
²² of airborne magnetics data, we model the thickness of sediment, the shape of the
²³ crystalline basement, and the likely locations of faults throughout the crust under the
²⁴ Ross Ice Shelf. We find a continuous drape of sediment over the seafloor, including
²⁵ deep and narrow fault-bound sedimentary basins beneath the Siple Coast. Using
²⁶ airborne gravity data, and distributed seismic constraints over the ice shelf, we
²⁷ develop and implement a gravity inversion to recover a higher-resolution bathymetry
²⁸ model beneath the ice shelf. This bathymetry model and our quantification of spatial
²⁹ uncertainty highlight locations likely important for sub-ice shelf ocean circulation
³⁰ and possible recent pinning points. In the process of these geophysical investigations,
³¹ we reveal a wide range of insights relating to how the solid-earth plays a critical role
³² in the past, present, and future dynamics of the ice sheet, and how this region has
³³ developed over its tectonic history.

³⁴ Plain language summary

³⁵ Acknowledgements

³⁶ Contents

37 1 Introduction	15
38 1.1 Motivation	15
39 1.2 Solid-earth influence	15
40 1.2.1 Bedrock topography	15
41 1.2.2 Geologic structures	18
42 1.2.3 Basal roughness	19
43 1.3 Ross Ice Shelf	20
44 1.3.1 Past investigations	20
45 1.4 Research questions	21
46 1.5 Outline	22
47 1.6 Data and Code	23
48 2 Airborne magnetic analysis: Basement depths and sediment thickness	25
50 2.1 Introduction	26
51 2.2 Data and Methods	28
52 2.3 Results	29
53 2.4 Discussion	31
54 2.4.1 West Antarctic Rift System extensional basins	31
55 2.4.2 Consequences for ice sheet dynamics	33
56 2.4.3 Mid-Shelf High - Central High	33
57 2.4.4 Thermal subsidence and sedimentation	34
58 2.5 Conclusions	34
59 2.6 Open Research	35
60 2.7 Acknowledgements	35
61 3 Gravity inversion: a tool for bathymetry modelling	37
62 3.1 Introduction	38
63 3.2 Methods	39
64 3.2.1 Geophysical inversion	40
65 3.2.1.1 Non-Linear inversions	42
66 3.2.1.2 Geometric inversions	42
67 3.2.2 Forward modelling	42
68 3.2.2.1 Discretization	42
69 3.2.2.2 Gravity edge effects	43
70 3.2.3 Isolating anomalies	44
71 3.2.4 Regional vs. Residual gravity	44
72 3.2.5 Running the inversion	46
73 3.2.5.1 Jacobian matrix	46

74	3.2.5.2 Least-squares solver	48
75	3.2.5.3 Regularization	48
76	3.2.6 Stopping Criteria	50
77	3.2.7 Software implementation	50
78	3.3 Synthetic models	51
79	3.3.1 Simple model	51
80	3.3.1.1 Model setup	51
81	3.3.1.2 Cross validation	52
82	3.3.1.3 Comparing vertical derivative methods	54
83	3.3.1.4 Added noise	54
84	3.3.1.5 Down-sampled data	55
85	3.3.2 Ensemble of Noise and Sampling values	58
86	3.4 Adding a regional component	59
87	3.4.1 Regional separation methods	60
88	3.4.2 Constraint point minimization	62
89	3.4.2.1 Tensioned minimum curvature	62
90	3.4.2.2 Bi-harmonic splines	63
91	3.4.2.3 Gridding comparison	63
92	3.4.3 Inversion results	64
93	3.4.4 Ensemble of Noise and Sampling values	65
94	3.4.5 Simple model comparison	66
95	3.5 Ross Sea model	67
96	3.5.1 Observed gravity	67
97	3.5.2 Starting bathymetry	68
98	3.5.3 Gravity misfit	70
99	3.5.4 Inversion	70
100	3.5.5 Uncertainty analysis	71
101	3.5.6 Effects of constraint spacing	74
102	3.5.7 Effects of gravity data	75
103	3.6 Discussion	76
104	3.6.1 Simple synthetic model	76
105	3.6.1.1 Inversion results	76
106	3.6.1.2 Ensemble results	77
107	3.6.2 Regional component	78
108	3.6.2.1 Regional separation methods	78
109	3.6.2.2 Constraint point minimization	79
110	3.6.2.3 Inversion results	79
111	3.6.2.4 Ensemble results	80
112	3.6.3 Ross Sea model	81
113	3.6.3.1 Effects of the gravity data	81
114	3.6.3.2 Effects of the constraints	82
115	3.6.3.3 Uncertainties	83
116	3.7 Future work	84
117	3.8 Conclusion	85
118	4 Ross Ice Shelf bathymetry inversion	87
119	4.1 Introduction	87
120	4.2 Methods	90
121	4.2.1 Gravity reduction	90

122	4.2.1.1	Attraction of normal Earth	91
123	4.2.1.2	Topographic mass effects	92
124	4.2.1.3	Regional separation	95
125	4.2.2	Bathymetry inversion	97
126	4.2.3	Starting bathymetry	98
127	4.2.4	Uncertainty quantification	98
128	4.3	Past inversions	100
129	4.3.1	Gravity reduction comparison	101
130	4.3.1.1	Regional separation	102
131	4.3.2	Inversion comparison	103
132	4.3.3	Uncertainty comparison	104
133	4.4	Results	105
134	4.4.1	Starting bathymetry	105
135	4.4.2	Gravity processing results	108
136	4.4.3	Gravity reduction results	110
137	4.4.4	Inversion results	111
138	4.4.5	Uncertainty	113
139	4.4.5.1	Partitioning uncertainty	116
140	4.5	Discussion	117
141	4.5.1	Uncertainties and parameter importance	118
142	4.5.1.1	Gravity component	118
143	4.5.1.2	Constraints component	118
144	4.5.1.3	Density component	119
145	4.5.1.4	Interpolation component	119
146	4.5.1.5	Reducing uncertainties	120
147	4.5.1.6	Past estimations of uncertainty	120
148	4.5.2	Past bathymetry models	121
149	4.5.2.1	Starting model comparison	121
150	4.5.2.2	Inversion result comparisons	122
151	4.5.2.3	Ocean cavity comparison	127
152	4.5.3	Implications	127
153	4.5.3.1	New pinning points	127
154	4.5.3.2	Basal melting	129
155	4.5.3.3	Geologic and tectonic significance	130
156	4.6	Conclusion	131
157	5	Synthesis	133
158	5.1	Geologic structures	134
159	5.2	Inversion	134
160	5.3	Ross Ice Shelf bathymetry	136
161	5.4	Geologic controls	137
162	5.4.1	Present controls	137
163	5.4.1.1	Basal melt	137
164	5.4.1.2	Modern pinning points	138
165	5.4.1.3	Sediment distribution	140
166	5.4.1.4	Geothermal heat flux at Siple Coast	140
167	5.4.2	Past and future implications	141
168	5.4.2.1	Retreat dynamics	142
169	5.4.2.2	Glacial initialization	143

170	5.5 Future work	144
171	5.6 Concluding remark	146
172	Appendix A	147
173	A.1 Introduction	147
174	A.2 Depth to basement assumptions	147
175	A.3 Magnetic data collection, processing, and Werner deconvolution	148
176	A.4 Tying magnetic basement to seismic basement	149
177	A.5 Tying Ross Sea magnetic basement to Ross Ice Shelf magnetic basement	150
178	A.6 Gridding, merging, and filtering	150
179	A.7 Sediment thickness and β -factor calculations	151
180	A.8 Uncertainties	152
181	Appendix B	159
182	B.1 Synthetic inversion with a regional field	159
183	B.2 Ross Sea synthetic model	160
184	Appendix C	165
185	C.1 Gravity disturbance vs anomaly	165
186	Appendix D Antarctic-Plots	167
187	D.1 Fetch	167
188	D.2 Map	168
189	D.3 Profile	168
190	D.4 Regions	168

¹⁹¹ List of Figures

192	1.1	Past observations and future predictions of sea level rise	16
193	1.2	Summary of existing geologic and geophysical data for Antarctica . .	17
194	2.1	Bathymetry, magnetics, and acoustic basement	27
195	2.2	Ross Sea magnetic and seismic basement comparison	29
196	2.3	Basement elevation and sediment thickness	30
197	2.4	Tectonic interpretation of the sub-Ross Ice Shelf	32
198	3.1	Ice shelves of Antarctica	38
199	3.2	Equivalent methods of discretizing a density contrast	43
200	3.3	Annulus approximation of a vertical prism	46
201	3.4	Training and testing set configuration	49
202	3.5	Weighting grid for the simple synthetic inversion	50
203	3.6	Simple synthetic model bathymetry	52
204	3.7	Simple synthetic gravity anomalies	53
205	3.8	Annulus approximation inversion results	53
206	3.9	Annulus approximation inversion cross-validation and profile	54
207	3.10	Finite differences inversion results	55
208	3.11	Finite differences and annulus approximation convergence curves . .	55
209	3.12	Synthetic inversion with noise	56
210	3.13	Synthetic inversion with noise, CV and profile	56
211	3.14	Creating a low-resolution observed gravity survey	57
212	3.15	Synthetic inversion with sampled gravity	58
213	3.16	Synthetic inversion with sampled gravity, CV and profile	58
214	3.17	Gravity data ensemble for synthetic model	59
215	3.18	Gravity anomalies with a regional field	60
216	3.19	Regional separation methods	61
217	3.20	Constraint point minimization gridding techniques	64
218	3.21	Synthetic inversion with regional component, CV and profile	65
219	3.22	Synthetic inversion with regional component results	65
220	3.23	Gravity data ensemble with regional component	66
221	3.24	Ross Sea semi-synthetic model	68
222	3.25	Ross Sea synthetic airborne survey	69
223	3.26	Ross Sea starting bathymetry	70
224	3.27	Ross Sea synthetic gravity anomalies	71
225	3.28	Ross Sea inversion, CV and convergence	71
226	3.29	Ross Sea inversion results	72
227	3.30	Ross Sea Monte Carlo simulation	73
228	3.31	Constraint spacing effects	74
229	3.32	Ross Sea ensemble of noise levels and gravity spacing	76

230	3.33 Grouped synthetic inversion ensemble	78
231	3.34 Synthetic inversion error and regional error	80
232	3.35 Grouped synthetic inversion with regional ensemble	81
233	3.36 Ross Sea inversion error and regional error	82
234	3.37 Grouped Ross Sea inversion with regional ensemble	83
235	4.1 Ross Ice Shelf inversion inputs	88
236	4.2 Schematic inversion workflow diagram	90
237	4.3 Observed gravity data reduction for Antarctica	93
238	4.4 Components of the topographic mass effect	94
239	4.5 Discretizing the topographic mass effect	95
240	4.6 Topographic mass effect for Antarctica	96
241	4.7 Schematic Monte Carlo workflow diagram	100
242	4.8 Random vs Latin hypercube sampling	101
243	4.9 Ross Ice Shelf starting bathymetry	107
244	4.10 Ross Ice Shelf weighting grid	108
245	4.11 Re-levelling of the ROSETTA-Ice gravity data	109
246	4.12 Gravity reduction results for the Ross Ice Shelf	111
247	4.13 Ross Ice Shelf singular bathymetry inversion results	112
248	4.14 Latin hypercube sampling distributions and correlations	114
249	4.15 Ross Ice Shelf inverted bathymetry and uncertainty	115
250	4.16 Monte Carlo results	116
251	4.17 Inverted bathymetry comparisons	123
252	4.18 Ross Ice Shelf assorted cross-sections	125
253	4.19 Water column thickness comparisons	128
254	4.20 Basal melt	129
255	5.1 Ross Embayment geophysical and geologic information	135
256	5.2 Uncertainty bounds for Ross Ice Shelf bathymetry and ocean cavity .	138
257	5.3 3D perspective view of Ross Ice Shelf	142
258	A.1 Various Ross Ice Shelf grids	153
259	A.2 OIB 403.3 magnetic and seismic basement comparison	154
260	A.3 Werner deconvolution solutions for ROSETTA-Ice lines	155
261	A.4 Unfiltered magnetic basement and point solutions	156
262	A.5 Uncertainty limits of basement and sediment thickness	157
263	A.6 Misfit distributions between magnetic and seismic basement	158
264	B.1 Comparison of four methods of regional separation	159
265	B.2 Constraint point minimization gridding comparison profiles	160
266	B.3 Synthetic inversion with regional and noise, CV and profile	161
267	B.4 Synthetic inversion with regional and noise, results	161
268	B.5 Inversion and regional error for model with regional and noise	161
269	B.6 Synthetic inversion with regional and re-sampling, CV and profile	162
270	B.7 Synthetic inversion with regional and re-sampling, results	162
271	B.8 Inversion and regional error for model with regional and low-res gravity	162
272	B.9 Inversion and regional error for Ross Sea constraint ensemble	163
273	C.1 Gravity disturbance vs. anomaly	165

²⁷⁴ List of Tables

²⁷⁵	4.1 Bathymetry uncertainties comparison	117
²⁷⁶	A.1 Previous Ross Ice Shelf seismic sediment thickness measurements . .	152

₂₇₇ **Chapter 1**

₂₇₈ **Introduction**

₂₇₉ **1.1 Motivation**

₂₈₀ Improving projections of the rate of global sea level rise in response to a warming
₂₈₁ world is vital for effectively mitigating future environment and socio-economic im-
₂₈₂ pacts (Durand et al., 2022). A large portion of the uncertainties in modern and
₂₈₃ projected sea level rise is related to the contribution from the Antarctic Ice Sheet
₂₈₄ (Figure 1.1b, Bamber et al., 2022; Edwards et al., 2021; Otosaka et al., 2023; Slater
₂₈₅ & Shepherd, 2018). The Antarctic Ice Sheet contains a total volume of ice equivalent
₂₈₆ to 57.2 m of sea level rise (Fretwell et al., 2013). Satellite observations show that
₂₈₇ Antarctica contributed \sim 7.4 mm to mean sea level since 1992 (Otosaka et al., 2023),
₂₈₈ and of the various components of sea level rise, the contribution from Antarctica is
₂₈₉ accelerating the fastest (Figure 1.1a, Nerem et al., 2018). Since the early 1990s, the
₂₉₀ sea level contribution from Antarctica has increased by 25% (Otosaka et al., 2023).
₂₉₁ By the end of the century, Antarctica is projected to contribute between 0.03 and
₂₉₂ 0.28 m to mean sea level (RCP 8.5, Intergovernmental Panel on Climate Change
₂₉₃ (IPCC), 2022). Optimal strategies for preparing coastal communities to best miti-
₂₉₄ gate the impacts of rising sea level depends on where in this range of uncertainties
₂₉₅ the true sea level rise will be. Some of the uncertainty in how the Antarctic Ice
₂₉₆ Sheet will respond to a warming world stems from a lack of understanding of the
₂₉₇ complex interactions between the ice and the underlying earth (e.g. Schlegel et al.,
₂₉₈ 2018; Zhao et al., 2018).

₂₉₉ **1.2 Solid-earth influences on ice dynamics**

₃₀₀ The solid-earth influences ice sheets through several mechanisms, which we group as
₃₀₁ those resulting from bedrock topography, geologic structures, and bedrock physical
₃₀₂ properties. Here we describe each of these categories of solid-earth influence on the
₃₀₃ Antarctic Ice Sheet, followed by introducing our specific study area, the Ross Ice
₃₀₄ Shelf.

₃₀₅ **1.2.1 Bedrock topography**

₃₀₆ Offshore bathymetry and onshore bed topography exert several fundamental controls
₃₀₇ on how the Antarctic Ice Sheet behaves. Offshore, where the ice is floating, the influ-
₃₀₈ ence of the bathymetry is limited to the guiding of ocean circulations. Bathymetric

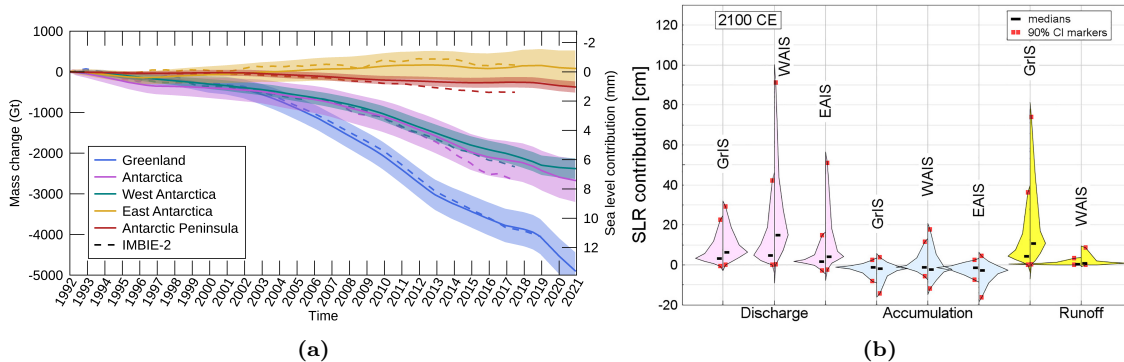


Figure 1.1: Past observations and future predictions of sea level rise. **a)** Observed cumulative mass change and sea level contributions from the various ice sheets. Data comes from satellite-altimetry estimates of volume changes, gravimetric estimates of mass changes, and quantification of input-output fluxes. Figure from Otosaka et al. (2023). **b)** Probability distributions for projected global sea level rise contributions for the year 2100 from the Greenland Ice Sheet (GrIS), West Antarctic Ice Sheet (WAIS), and East Antarctic Ice Sheet (EAIS), separated into three processes; discharge, accumulation, and runoff. Left and right sides of each distribution show the +2°C and +5°C global temperature trajectories, respectively. Figure from Bamber et al. (2022).

ridges have been shown to block, or re-direct, the inflow of melt-inducing waters to the ocean cavity beneath floating ice shelves (De Rydt et al., 2014; Goldberg et al., 2020; Zhao et al., 2019). Approximately 75% of Antarctica's coastline is composed of these floating ice shelves, and 83% of total ice discharged into the Southern Ocean from Antarctica is through these shelves, highlighting their significance to Antarctica's ice budget (Rignot et al., 2013). Of the 83% of total ice loss from Antarctica through ice shelves, basal melt is responsible for 55% (Rignot et al., 2013). Some of this melt occurs from surface waters, where bathymetry has little effect, but for many of the largest ice shelves, the majority of basal melt occurs along the deep grounding zone (Adusumilli et al., 2020). Here, the melt-inducing water bodies are dense and flow into the ice shelf cavities along the seafloor (Holland, 2008; Tinto et al., 2015). Therefore, bathymetric features act to guide or block these circulations from reaching the grounding zone where they can melt the ice base. In addition to steering ocean currents, bed topography, in regions of grounded ice, acts to steer the ice flow.

As revealed by extensive seismic and swath bathymetry data in Antarctica's Ross Sea (Figure 1.2a), the dynamics of an advancing or retreating ice sheet are predominantly controlled by the physiography of the bed (Anderson et al., 2019; Halberstadt et al., 2016). If large troughs and banks exist, advancing ice is initially confined by these features, while the banks remain ice-free (Anderson et al., 2014). Eventually, after the ice has covered the entire region, the retreat is initially confined to these narrow troughs, while the banks retain grounded ice for much longer (Anderson et al., 2019; Halberstadt et al., 2016). As the ice thins or retreats into regions of deeper bed topography, these banks remain grounded, while the rest of the ice sheet decouples from the bed, begins floating and forms an ice shelf (Shipp et al., 1999). This remaining grounded ice on bathymetric highs forms pinning points.

Pinning points are regions of locally grounded ice within a floating ice shelf (Matsuoka et al., 2015). The friction between the bed and ice base at these points impart a critical resisting force to the discharge of upstream ice; an effect known as buttressing (Dupont & Alley, 2005; Thomas, 1979). Since the base of ice shelves

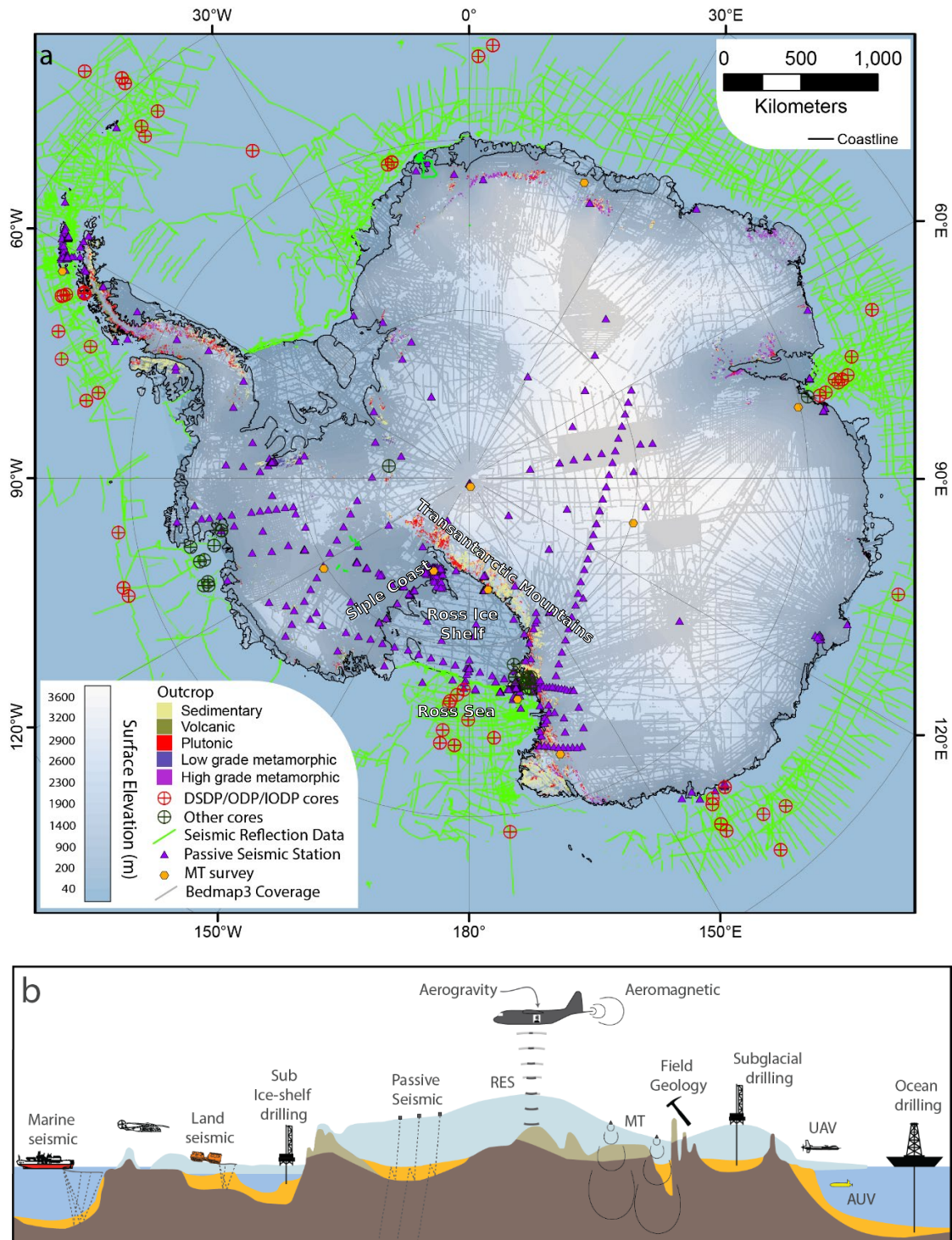


Figure 1.2: Summary of existing geologic and geophysical data for Antarctica. **a)** Map of data coverage in Antarctica indicating outcropping regions, drill core sites, seismic and magnetotelluric surveys, and bed elevation data points of Bedmap3, mostly from airborne radio-echo sounding (Frémand et al., 2022). **b)** Various methods of acquiring information sub-surface geology. Figure adapted from Aitken et al. (2023b).

is flat relative to the underlying bathymetry, the morphology of the seafloor is the dominant controls the location and geometry of these pinning points. The bedrock topography has been thought to be relatively constant over a millennial timescale, meaning that pinning points geometries vary mostly by temporal changes in the ice thickness. However, recent studies of glacial isostatic adjustment, the vertical re-

345 bound of the Earth following deglaciation, throughout West Antarctica have demon-
346 strated high spatial variability and short (multi-centennial-to-millennial) timescales
347 for these vertical land movements (Barletta et al., 2018; Coulon et al., 2021; Kachuck
348 et al., 2020). As the bedrock beneath portions of West Antarctica continues to re-
349 bounds, the number and extent of these pinning points will likely increase, possibly
350 providing a stabilizing effect to the ice sheet.

351

352 All of these above controls on ice dynamics imparted by the physiography of the
353 bed rely on accurate knowledge of bed topography and bathymetry. Due to the
354 inherently challenging nature of Antarctic fieldwork, and the logistical challenge of
355 measuring bed elevations beneath thick ice, 50% of the Antarctic Ice Sheet is more
356 than 5 km from the nearest measurement of bed elevation (Figure 1.2a, Morlighem
357 et al., 2020). This value increases greatly if the floating ice shelves are included. For
358 grounded ice, the dominant techniques for direct measurements of bed elevation data
359 are airborne radio-echo sounding, over-snow radar, and seismic surveying (Figure
360 1.2b, Fretwell et al., 2013). In the open ocean, bathymetry data is typically collected
361 with ship-borne multibeam echo sounding, seismic surveying (Figure 1.2b), or from
362 satellite-altimetry. Acquiring bathymetry data beneath floating ice shelves presents
363 a particular challenge. The efficient shipborne methods are unavailable since the ice
364 shelves are persistent year-round, unlike the sea ice in the open ocean. Radio-echo
365 sounding, either ground-based or airborne, cannot image through the water column.
366 Direct observations through drilling are possible and exist, but typically require
367 drilling through 100's to 1000's of meters of ice (Figure 1.2, Clough & Hansen, 1979;
368 Patterson et al., 2022). Autonomous underwater vehicles (Figure 1.2b) present
369 another option, but are expensive and have limited range (Dowdeswell et al., 2008;
370 Nicholls et al., 2006). The only feasible method of direct observations of sub-ice shelf
371 bathymetry is over-snow seismic surveying (Figure 1.2b). However, for the vast area
372 of many ice shelves, even sparse coverage (~ 50 km spacing) of seismic points across
373 the ice shelf takes several field seasons of data acquisition (Bentley, 1984).

374 1.2.2 Geologic structures

375 Additional solid-earth influences on the overriding ice include the delivery of geother-
376 mal heat and subglacial water to the ice base and the vertical deformation of the
377 bedrock in response to changing ice loads. Geothermal heat influences ice dynamics
378 through several mechanisms; 1) increasing the temperature of the ice which lowers
379 its viscosity, leading to enhanced flow via internal deformation (Llubes et al., 2006),
380 2) meltwater lubrication of the bed reduces friction, enhancing flow (Pollard et al.,
381 2005), and 3) increasing the ability of the bed to deform via increased pore-fluid
382 pressure, which increases ice flow (Tulaczyk et al., 2000). The latter two effects,
383 while enhanced by geothermal heat through the melting of ice, also occur with sim-
384 plely the presence of liquid water at the ice-bed interface. As briefly mentioned in
385 the above section, glacial isostatic adjustments of the bedrock following changes in
386 ice load can influence the ice by altering the geometry and locations of grounded ice.

387

388 Each of these effects; geothermal heat flow, subglacial water availability, and
389 glacial isostatic adjustment, are in turn influenced by geologic structures within the
390 upper crust. A portion of subglacial water comes from either transport along the
391 ice-bed interface, or from the melting of the ice base. However, an often overlooked

component of the subglacial hydrologic system is groundwater stored in deep sedimentary aquifers. For example, hydrologic modelling of the ice streams of the Siple Coast (Figure 1.2a) estimated the components of the hydrologic budget to be 8% from local basal melting, 47% from inflow from the ice sheet interior, and 45% from groundwater reservoirs (Christoffersen et al., 2014). These modelling observations of extensive groundwater have been recently verified beneath the Whillans Ice Stream by a magnetotelluric survey. This survey imaged an extensive groundwater aquifer within a sedimentary basin, containing at least an order of magnitude more water than the shallow hydrologic system (Gustafson et al., 2022). The vertical flow of this basinal groundwater is controlled by the pressure of the overriding ice sheet. As this overburden pressure decreases with thinning ice, groundwater is discharged to the ice base (Gooch et al., 2016; Li et al., 2022). This discharge is likely concentrated along pre-existing weaknesses or impermeable surfaces, such as fault damage zones, or the margins of crystalline basement (Jolie et al., 2021). During this ice-induced hydraulic unloading, regional geothermal heat is advected along the fluid pathways, leading to potentially highly elevated heat flow delivered to the ice base (Li et al., 2022; Ravier & Buoncristiani, 2018). In addition to concentrating both subglacial water and geothermal heat, these faults, or more generically, regions of the crust which have experienced recent faulting, will respond differently to stresses induced by glacial isostatic adjustment. To a first order, the isostatic response of the solid-earth to changing ice load is controlled by the rheology of the mantle (Whitehouse et al., 2019). However, on a more local scale, pre-existing faults are shown to accommodate glacial isostatic rebound-induced stresses (Peltier et al., 2022; Steffen et al., 2021).

To be able to understand the above influence of the solid-earth on the ice, we must have some fundamental knowledge of the geologic structures beneath the ice. This includes knowing where sedimentary basins, and possible aquifers within, are located, where faults likely intersect the ice base, and the geometry of the crystalline basement. Each of these components is difficult to image directly. Drilling, seismic surveys, or geologic analysis of rock outcrops all provide valuable information but are not feasible to cover wide regions (Figure 1.2). Indirect methods are therefore needed. These include techniques such as gravity, magnetic, or electromagnetic methods. Each of these techniques records measurements of the spatial variation of a potential field, such as the Earth's gravity, magnetic, or electromagnetic fields. These fields are all partially dependant on a physical Earth property, such as rock density, magnetic susceptibility, or resistivity. From these relationships, sub-surface geologic information can be learned.

1.2.3 Basal roughness

The last major influence on the ice from the solid-earth we present is the roughness of the bed which the ice sheet flows over. This bed roughness is important on both a micro and macro scale. At a micro-scale, roughness is determined by the material which the bed is composed of. A bed of erosion-resistance crystalline basement, for example, can greatly hinder the flow of ice. This material results in high friction with the ice base, slowing the sliding of ice (Bell et al., 1998). Conversely, beds composed of fine-grained tills allow fast ice flow. This fast flow is predominantly due to deformation within the till as the ice flows (Alley et al., 1986). In between

the end members of crystalline basement and fine grain till are lithified sedimentary rocks, for example. This type of bed may initially lead to high friction with the ice, but due to their high erodability, sedimentary rock will quickly generate till (Anandakrishnan et al., 1998). A macro-scale view of basal roughness is also important for ice dynamics. As observed at the Siple Coast (Figure 1.2a) ice streams, there is a strong inverse relation between bed roughness, from scales of 5 km to >40km, and ice stream velocities (Siegert et al., 2004). The composition of the bed also plays an important role in the total effective resistance imparted on ice flow from pinning points (Still et al., 2019).

To best quantify the effect of basal roughness on ice dynamics, information on the material properties of the bed is needed. While sediment samples beneath the ice yield valuable information, they may only represent the bed at the specific location where they were sampled. The most fundamental information needed is the generic rock type of the bed, namely, is the bed loose, unconsolidated sediment, lithified sedimentary rock, or crystalline rock? Aitken et al. (2023b) provide a detailed review of Antarctica's sedimentary basins, and the methods employed to determine both the presence of sediment and the sediment thickness. These methods, as well as the methods described in the above sections, are shown in Figure 1.2, as reproduced from Aitken et al. (2023b).

With the dominant solid-earth influences on ice dynamics laid out, we will now introduce the study area of this thesis, Antarctica's Ross Ice Shelf.

1.3 Ross Ice Shelf

The Ross Ice Shelf is Antarctica's largest ice shelf ($\sim 480,000 \text{ km}^2$), Figure 1.2). It is situated between the Transantarctic Mountains and Marie Byrd Land. It buttresses a catchment of ice that flows from both the East and West Antarctic Ice Sheets. This catchment contains 11.6 m of global sea level equivalent (Fretwell et al., 2013; Rignot et al., 2011; Tinto et al., 2019). Compared to many other ice shelves, the Ross Ice Shelf is currently relatively stable (Moholdt et al., 2014; Rignot et al., 2013). However, geologic evidence from throughout the Ross Sea and the Siple Coast shows that in the past $\sim 7,000$ years the shelf has experienced rapid destabilization, disintegration, and large-scale grounding line retreat (e.g., Naish et al., 2009; Venturelli et al., 2020). This major Holocene retreat is thought to have been primarily caused by ocean forcings (Lowry et al., 2019), as bathymetric troughs guided in the inflow of melt-inducing ocean circulations (Tinto et al., 2019). Once destabilized, the grounding line retreat from the outer continental shelf to the present-day location was controlled primarily by the physiography and geology of the bed (Anderson et al., 2019; Halberstadt et al., 2016). This shows the importance of the solid-earth's influence on the dynamics of the Ross Ice Shelf.

1.3.1 Past investigations

By examining solid-earth influence on ice dynamics, we identified some key data needed to understand these influences. This data included onshore bed topography, offshore bathymetry, the distribution of sediment, and upper crustal structures such as faults and the topography of the basement. Here, we summarize the history of

483 data collection in the Ross Ice Shelf region specific to these geologic and physio-
484 graphic features. Geological and geophysical exploration has occurred in the Ross
485 Embayment for over a century. The earliest of these include the 1901-1904 *Discovery*
486 expedition, the 1907-1909 *Nimrod* expedition, and the 1910-1913 *Terra Nova*
487 expedition. These expeditions laid the groundwork of interest in the Ross Embay-
488 ment from a scientific perspective. The first major survey of the Ross Ice Shelf was
489 part of the 1957-1959 International Geophysics Year traverses. The three over-snow
490 traverses all included a portion of the ice shelf and collected radar, gravity, and
491 seismic data to determine ice thickness, surface elevation, and bed elevation (Crary,
492 1959). These surveys produced early evidence of the extensive below-sea-level bed,
493 thin crust, and distinct geologic provinces throughout West Antarctica (Bentley et
494 al., 1960). In the 1970s the Ross Ice Shelf Geophysical and Glaciological Survey
495 (RIGGS, Bentley, 1984) consisted of a systematic grid of seismic surveys over the
496 entire ice shelf with an average spacing between survey points of 55 km. After the
497 RIGGS survey, there were a total of ~ 223 point-source seismic surveys across the
498 ice shelf, all yielding single-point sub-ice shelf bathymetry depths. Of these, eight
499 reported sediment thicknesses beneath. Several faults were hypothesized, based on
500 2D gravity profiles conducted at many of the stations (Greischar et al., 1992). Since
501 the 1970s, there have been many additional local surveys on the ice shelf, but these
502 have been focused along the grounding zones (e.g., Horgan et al., 2017; Muto et al.,
503 2013b; Patterson et al., 2022; Stern et al., 1994; ten Brink et al., 1993; Wannamaker
504 et al., 2017). The next, and most recent major data-collection campaign on the Ross
505 Ice Shelf was the ROSETTA-ice project.

506

507 The Ross Ocean and ice Shelf Environment, and Tectonic setting Through Aero-
508 geophysical surveys and modelling project (ROSETTA-ice, Tinto et al., 2019), was
509 a 3-season (2015-2017) airborne geophysical survey of the Ross Ice Shelf. It flew
510 a regular grid of flight lines, with nominal N-S and E-W line spacings of 10 and
511 55 km, respectively. During each flight, various geophysical data was collected, in-
512 cluding ice-penetrating radar, gravity, magnetics and laser altimetry. So far, these
513 ROSETTA-ice data have been used to begin characterizing the geologic nature of
514 the crust (Tinto et al., 2019), to model the depths to the sea floor (Tinto et al.,
515 2019), and to quantify basal melt (Das et al., 2020).

516

517 Following 60 years of surveying and exploration of the Ross Ice Shelf, our fun-
518 damental understanding of the subglacial geology and physiography is still lacking.
519 For an area almost twice the size of New Zealand, we have approximately 8 locations
520 of reported sediment thickness, several hypothesized locations of faults, gaps of over
521 100 km without bathymetric depths, and limited understanding of our uncertainty
522 in the bathymetry where it has been modelled/interpolated. We propose several
523 research questions which we aim to answer in this thesis.

524 1.4 Research questions

525 The aim of this thesis is to improve our knowledge of boundary conditions beneath
526 the Ross Ice Shelf in order to better understand the past, present, and future
527 interactions between the ice, ocean, and solid-earth. We aim to accomplish this by
528 answering the following questions:

- 529 1. What is the geologic structure of the upper crust beneath the Ross Ice Shelf?
530 If there are sediments, what is their thickness and distribution? Where are
531 the major faults likely located?
- 532 2. How can bathymetry beneath an ice shelf best be modelled? Are there further
533 improvements that can be made to the currently employed gravity-inversion
534 process? What are the predominant sources of uncertainty, and how can these
535 be limited?
- 536 3. How deep is the bathymetry beneath the Ross Ice Shelf and where are we most
537 and least certain about it?
- 538 4. What are the geologic controls on the Ross Ice Shelf's stability?

539

1.5 Outline

540 This thesis is comprised of five chapters.

541

542 This chapter, Chapter 1, establishes the context behind the research, introduces
543 the study region, proposes a series of research questions, and contains an outline of
544 this thesis.

545

546 Chapter 2 is adapted from a journal article published in Geophysical Research
547 Letters (Tankersley et al., 2022), reformatted to be included in this thesis. It presents
548 a model of the basement topography, and overlying sediment distribution, beneath
549 the Ross Ice Shelf. We use airborne magnetic data from the ROSETTA-ice project,
550 and a depth-to-magnetic source technique to model the sediment-basement contact.
551 This reveals large-scale, fault-controlled extensional basins throughout the sub-Ross
552 Ice Shelf crust. From this, we are able to draw a wide range of inferences on the
553 likely influence of this basement topography on the past, present, and future ice
554 sheet, as well as some tectonic implications. These results provide the first holistic
555 view of the upper crust beneath the Ross Ice Shelf.

556

557 Chapter 3 details our development of a method to model the depth to the sea floor
558 beneath a floating ice shelf. This method is a gravity inversion, where observations
559 of Earth's gravitational field are used to model bathymetry beneath an ice shelf. We
560 develop open-source Python code with the aim for other researchers to utilize the
561 inversion. We test the inversion against a suite of synthetic and semi-realistic data.
562 This confirms the feasibility of using gravity data to attain bathymetry depths in an
563 Antarctic setting. Additionally, these synthetic tests reveal the relative importance
564 of various aspects of a gravity inversion. These include the importance of *a priori*
565 constraints on the bathymetry, the large errors which can be introduced during the
566 removal of the regional component of gravity, and several suggestions for optimal
567 survey design to minimize error in the resulting bathymetry model. Our use of
568 Monte Carlo simulation provides both a spatially variable estimation of uncertainty
569 in the resulting bathymetry and an estimate of the various sources of this uncertainty.

570

571 Chapter 4 uses the inversion algorithm developed in Chapter 3 to create a new
572 bathymetry model and associated uncertainties beneath the Ross Ice Shelf. Our

model shows some major differences with past bathymetry models, highlighting areas of the ice shelf that should be carefully considered in future surveys. These include a deeper bathymetric trench along the Transantarctic Mountains, a thicker ocean cavity along a portion of the ice front which may allow the incursion of warm ocean waters and a thicker ocean cavity proximal to the Siple Coast grounding line. Our uncertainty analysis shows the region of highest uncertainties is along the Transantarctic Mountain Front. Within this chapter, we perform a comprehensive review of past bathymetry-gravity inversions, for all Antarctic studies, and several Greenland studies. This highlighted some key differences, which we believe we have improved on.

583

Chapter 5 presents a synthesis of the 3 research chapters, and provides a discussion of the research questions. Various future works are suggested and the main conclusions of this thesis are presented. The research chapters in this thesis were written with the intent to publish, including Chapter 2 which is already published. Therefore, I have chosen to keep the style of writing consistent throughout the thesis, with the use of plural possessive pronouns ("we") instead of singular ("I").

590 1.6 Data and Code Availability Statement

In an effort to adhere to the principles of FAIR scientific investigations, Findability, Accessibility, Interoperability, and Reusability (Wilkinson et al., 2016), we have used only open-access data and published all code¹ used in this thesis. Here we describe where this code and data can be found. All data used from other studies has been cited within each chapter and can be accessed through their respective DOIs. However, most of these datasets were downloaded using the Python package Antarctic-Plots (Tankersley, 2023). I have developed this package during this PhD to help with several aspects of conducting research related to Antarctica. See Appendix D for a quick overview of the capabilities of Antarctic-Plots. Analysis in this study was executed on a computer with an x86_64 processor with a maximum clock frequency of 2600 MHz with 56 physical cores, 112 logical cores, and 1TB of RAM, using the Operating System Linux-Ubuntu.

603 Chapter 2

All of the Python code used to perform the analysis and create the figures of Chapter 2 is available from the following GitHub repository; https://github.com/mdtanker/RIS_basement_sediment, and the version of the repository used in the published paper is archived at <https://doi.org/10.5281/zenodo.6499863> (Tankersley, 2022).

608 Chapters 3 & 4

The gravity inversion python code, the workflow conducted within Jupyter Notebooks, and the creation of all the figures is available from the following GitHub repository; https://github.com/mdtanker/RIS_gravity_inversion and the version of the repository used in this thesis is archived at <https://doi.org/10.5281/zenodo.8084469> (Tankersley et al., 2023).

The code for creating the figures in the remainder of this thesis, and the latex files of the thesis itself are available at the following GitHub repository; <https://>

¹This excludes one component of Chapter 1 which was performed with proprietary software.

- ⁶¹⁶ github.com/mdtanker/phdthesis and is citable with the following DOI; 10.5281/zen-
⁶¹⁷ odo.8084606.

618 Chapter 2

619 Airborne magnetic analysis: 620 Basement depths and sediment 621 thickness

622 Abstract

623 New geophysical data from Antarctica's Ross Embayment reveal the structure and
624 subglacial geology of extended continental crust beneath the Ross Ice Shelf. We use
625 airborne magnetic data from the ROSETTA-Ice Project to locate the contact be-
626 tween magnetic basement and overlying sediments. We delineate a broad, segmented
627 basement high with thin (0-500 m) non-magnetic sedimentary cover which trends
628 northward into the Ross Sea's Central High. Before subsiding in the Oligocene, this
629 feature likely facilitated early glaciation in the region and subsequently acted as a
630 pinning point and ice flow divide. Flanking the high are wide sedimentary basins,
631 up to 3700 m deep, which parallel the Ross Sea basins and likely formed during
632 Cretaceous-Neogene intracontinental extension. NW-SE basins beneath the Siple
633 Coast grounding zone, by contrast, are narrow, deep, and elongate. They suggest
634 tectonic divergence upon active faults that may localize geothermal heat and/or
635 groundwater flow, both important components of the subglacial system.

636 Plain Language Summary

637 The bedrock geology of Antarctica's southern Ross Embayment is concealed by
638 100s-1000s of meters of sedimentary deposits, seawater, and the floating Ross Ice
639 Shelf (RIS). Our research strips away those layers to discover the shape of the
640 consolidated bedrock below, which we refer to as the basement. To do this, we use
641 the contrast between non-magnetic sediments and magnetic basement rocks to map
642 out the depth of the basement surface under the RIS. Our primary data source is
643 airborne measurements of the variation in Earth's magnetic field across the ice shelf,
644 from flight lines spaced 10-km apart. We use the resulting basement topography to
645 highlight sites of possible influence upon the Antarctic Ice Sheet and to further
646 understand the tectonic history of the region. We discover contrasting basement
647 characteristics on either side of the ice shelf, separated by a N-S trending basement
648 high. The West Antarctic side displays evidence of active faults, which may localize
649 geothermal heat, accommodate movements of the solid earth caused by changes in

the size of the Antarctic Ice Sheet, and control the flow of groundwater between the ice base and aquifers. This work addresses critical interactions between ice and the solid earth.

Key Points:

1. Aeromagnetic analysis reveals basement surface and evidence of fault-controlled extensional basins beneath Antarctica's Ross Ice Shelf (RIS)
2. Active faults at Siple Coast likely influence ice streams through control of geothermal heat, groundwater, and glacioisostatic adjustments
3. A basement high beneath RIS spatially coincides with a lithospheric boundary, with contrasting sedimentary basins on either side

2.1 Introduction

The southern sector of Antarctica's Ross Embayment beneath the Ross Ice Shelf (RIS; area $\sim 480,000 \text{ km}^2$) is poorly resolved because the region is not accessible to conventional seismic or geophysical surveying. Rock exposures on land suggest that Ross Ice Shelf (RIS) crust consists of early Paleozoic post-orogenic sediments, intruded in places by mid-Paleozoic and Cretaceous granitoids (Goodge, 2020; Luyendyk et al., 2003). Following the onset of extension in the mid-Cretaceous, grabens formed and filled with terrestrial and marine deposits, continuing into the Cenozoic (e.g. Coenen et al., 2019; Sorlien et al., 2007), as the Ross Embayment underwent thermal subsidence (Karner et al., 2005; Wilson & Luyendyk, 2009). The physiography of this region then responded to the onset of glaciation in the Oligocene (Paxman et al., 2019), coinciding with localized extension in the western Ross Sea until 11 Ma (Granot & Dyment, 2018). The Oligocene-early-Miocene paleo-landscape of the Ross Sea sector was revealed by marine seismic data (e.g. Brancolini et al., 1995; Pérez et al., 2021) and offshore drilling that penetrated crystalline basement (DSDP Site 270; Ford & Barrett, 1975) (Figure 2.1). Recognition of the role of elevated topography in Oligocene formation of the Antarctic Ice Sheet (DeConto & Pollard, 2003; Wilson et al., 2013) and the likely influence of subglacial topography upon ice sheet processes during some climate states (Austermann et al., 2015; Colleoni et al., 2018) motivated our effort to determine basement topography beneath the Ross Ice Shelf.

Ice sheet dynamics are of high interest in the RIS region because its grounding zone (GZ) and pinning points (Still et al., 2019) buttress Antarctica's second-largest drainage basin (Tinto et al., 2019). Our work in this sensitive region seeks to delimit the extent and geometry of competent basement because the margins of basement highs are sites of strong contrasts in permeability that influence the circulation of subglacial waters. A spectacular example of the confinement of subglacial water between the ice sheet and basement exists in ice radar profiles for the continental interior (Bell et al., 2011), but little is known about the subglacial hydrology of deep groundwater reservoirs within sediment-filled marine basins that receive terrestrial freshwater influx (Gustafson et al., 2022; Siegert et al., 2018). These basins may contain up to 50% of total subglacial freshwater (Christoffersen et al., 2014), where the discharge and recharge along fault-damage zones (Jolie et al., 2021) is controlled by pressure from the overriding ice sheet (Gooch et al., 2016). Possible

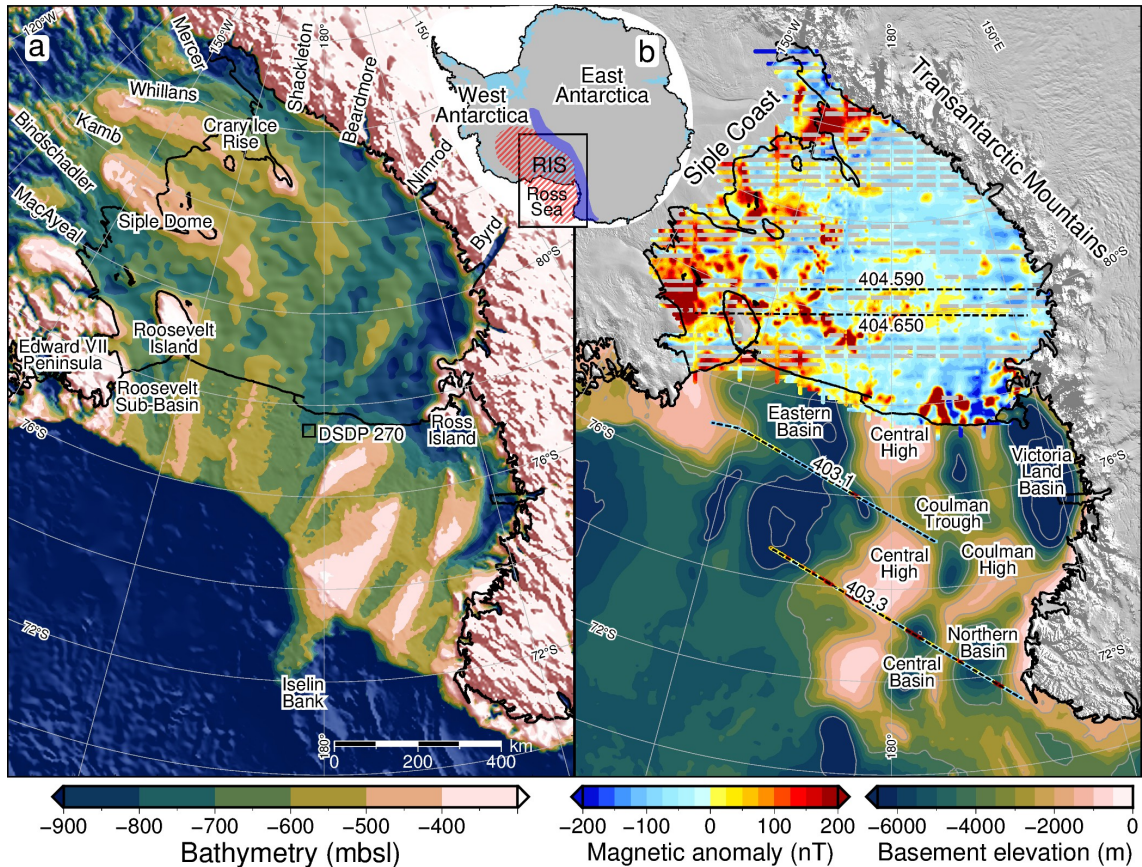


Figure 2.1: (a) Bathymetry and sub-ice bed elevations (Morlighem et al., 2020) including ROSETTA-Ice gravity-derived bathymetry (Tinto et al., 2019) beneath the Ross Ice Shelf (RIS). Labels include ice streams and outlet glaciers. (b) Basement elevation from Antarctic Offshore Stratigraphy project marine seismic compilation in the Ross Sea Brancolini et al. (1995) and air-borne magnetic data from ROSETTA-Ice (over RIS) and Operation IceBridge (black dashed lines). Inset map shows figure location, West Antarctic Rift System (hatched red), Transantarctic Mountains (dark blue), and ice shelves (light blue). Shelf edge, grounding line, and coastlines in black (Rignot et al., 2013). MODIS imagery from Scambos et al. (2007).

evidence that RIS basement margins localize basinal waters, causing the advection of geothermal heat, comes from elevated values and significant spatial variability of measured geothermal heat flux (GHF) at points around the Ross Embayment (Begeaman et al., 2017). Here we present the first map of magnetic basement topography and thickness of overlying non-magnetic sediments for the southern Ross Embayment, developed using ROSETTA-Ice (2015-2019) airborne magnetic data (Figure 2.1b, Tinto et al., 2019). Our work reveals three major sedimentary basins and a broad basement ridge that separates crust of contrasting basement characteristics.

2.2 Data and Methods

We use ROSETTA-Ice aeromagnetic data to image the shallowest magnetic signals in the crust. Assuming that the overlying sediments and sedimentary rocks produce smaller magnetic anomalies than the crystalline basement, we treat the resulting solutions as the depth to the magnetic basement (Section A.2). To do this, we implemented Werner deconvolution (Werner, 1953) on 2D moving and expanding windows of line data, isolating anomalies and solving for their source parameters (Section A.3, location, depth, susceptibility, body type). The resulting solutions are non-unique; each observed magnetic anomaly can be solved by bodies at multiple locations and depths by varying the source's magnetic susceptibility and width. The result is a depth scatter of solutions (Figures 2.2 & A.2), which tend to vertically cluster beneath the true source. This magnetic basement approach has been used to map sedimentary basins throughout Antarctica (i.e. Bell et al., 2006; Frederick et al., 2016; Karner et al., 2005; Studinger et al., 2004a) where typically, the tops of solution clusters are manually selected to represent the basement depth. Our approach expands on this method by utilizing a reliable, automated method of draping a surface over these depth-scattered solutions to produce a continuous basement surface (Section A.4 & A.5).

We implemented a 2-step tuning process that ties our RIS magnetic basement to well-constrained seismic basement in the Ross Sea, from the Antarctic Offshore Stratigraphy project (ANTOSTRAT) (Figure 2.1b, Brancolini et al., 1995). This involved using Operation IceBridge (OIB) airborne magnetic data (Cochran et al., 2014a) collected over the RIS and Ross Sea. Minimizing misfits between OIB magnetic basement and ANTOSTRAT basement, as well as between OIB and ROSETTA-Ice magnetic basements, enabled tuning of our method to optimal basement depths (Figures 2.2, A.2, A.3e&f, Section A.4 & A.5).

Our RIS results (Figure A.4) were merged with offshore ANTOSTRAT data (Brancolini et al., 1995) and smoothed with an 80 km Gaussian filter to match the characteristic wavelengths of the Ross Sea basement (Section A.6). The combined grid (Figure 2.3a) was then subtracted from BedMachine bathymetry (Figure 2.1a, Section A.7, Morlighem et al., 2020), to obtain the sediment thickness distribution for the Ross Embayment (Figure 2.3b).

These sub-RIS results together with free-air gravity data allowed us to infer the locations of regional scale faults beneath the RIS. Criteria used to locate faults include 1) high relief on the magnetic basement surface, 2) linear trends that cross zones of shallow basement, 3) high gradient gravity anomalies (Figure A.1a, ROSETTA-Ice) and 4) large contrasts in sediment thickness. Narrow, deep, linear basins are likely to be controlled by active faults (e.g. Drenth et al., 2019; Finn, 2002). We display the inferred faults upon a base map of crustal stretching factors (β -factor;

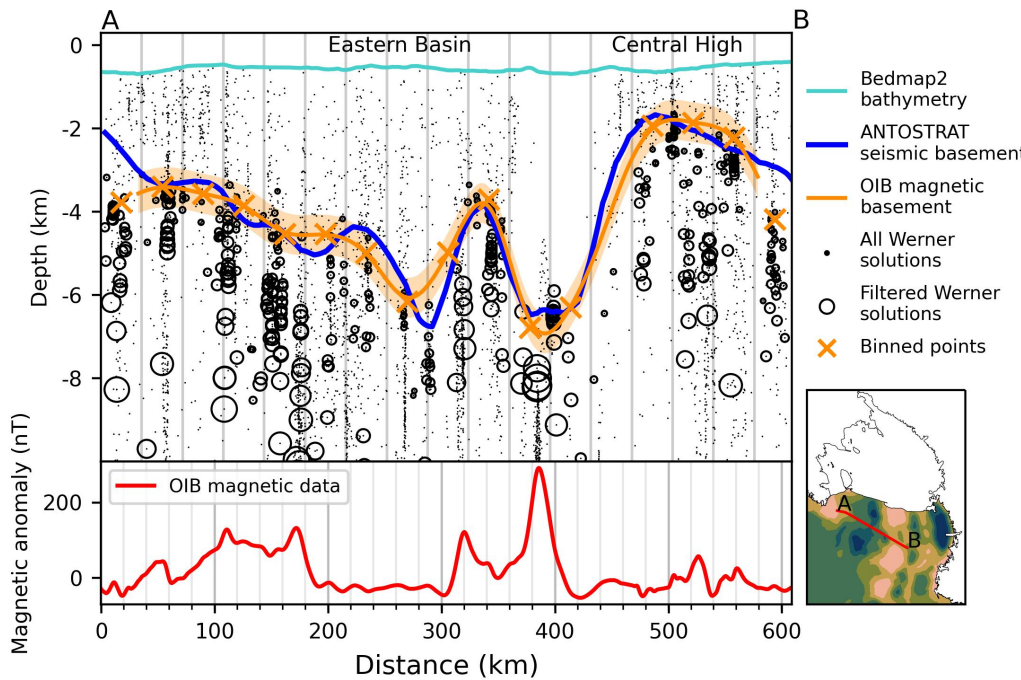


Figure 2.2: Ross Sea magnetic and seismic basement comparison. Operation IceBridge airborne magnetic data (lower panel) from segment 403.1 used in Werner deconvolution to produce magnetic anomaly source solutions (black dots). Filtering removed shallow solutions, and remaining solutions (circles scaled to magnetic susceptibility) were binned and interpolated to produce the magnetic basement (orange line with uncertainty band).

the ratio of crustal thickness before and after extension, Figure 2.4a), using an initial crustal thickness of 38 km (Müller et al., 2007), a continent-wide Moho model (An et al., 2015), and our basement surface as the top of the crust (Section A.7).

2.3 Results

We find that an almost continuous drape of sediment covers the RIS region (Figure 2.3b), with only \sim 3% of the area having $<$ 200 m of sedimentary cover. Prominent beneath the midline of the RIS is a broad NNW-SSE trending basement ridge (Figure 2.3a, Mid-Shelf High; MSH), which comprises most of the shallowest ($<$ 700 meters below sea level (mbsl)) sub-RIS basement, with several regions with as little as 100 m of sedimentary cover. Basement is deeper on the East Antarctic side of the MSH, where it averages \sim 2400 mbsl, compared to an average depth of \sim 1900 mbsl on the West Antarctic side (Figure 2.3a histogram). Sedimentary fill is \sim 400 m greater and more uniformly distributed on the East Antarctic side than the West Antarctic side (Figure 2.3b histogram).

To estimate our uncertainty (Section A.8), we examined the misfit between OIB and ANTOSTRAT basement (Figures 2.2 & A.2) and between our basement and OIB basement (Figures A.3e&f). There is a median misfit of 480 m (22% of average RIS depth) for basement (Figures A.5 & A.6). A similar 470 m median basement misfit is estimated by comparing our results to eight active source seismic surveys (Figure 2.3b, Table A.1). Incorporating the \sim 70 m uncertainty in the bathymetry model (Tinto et al., 2019), our representative sediment thickness uncertainty is 550

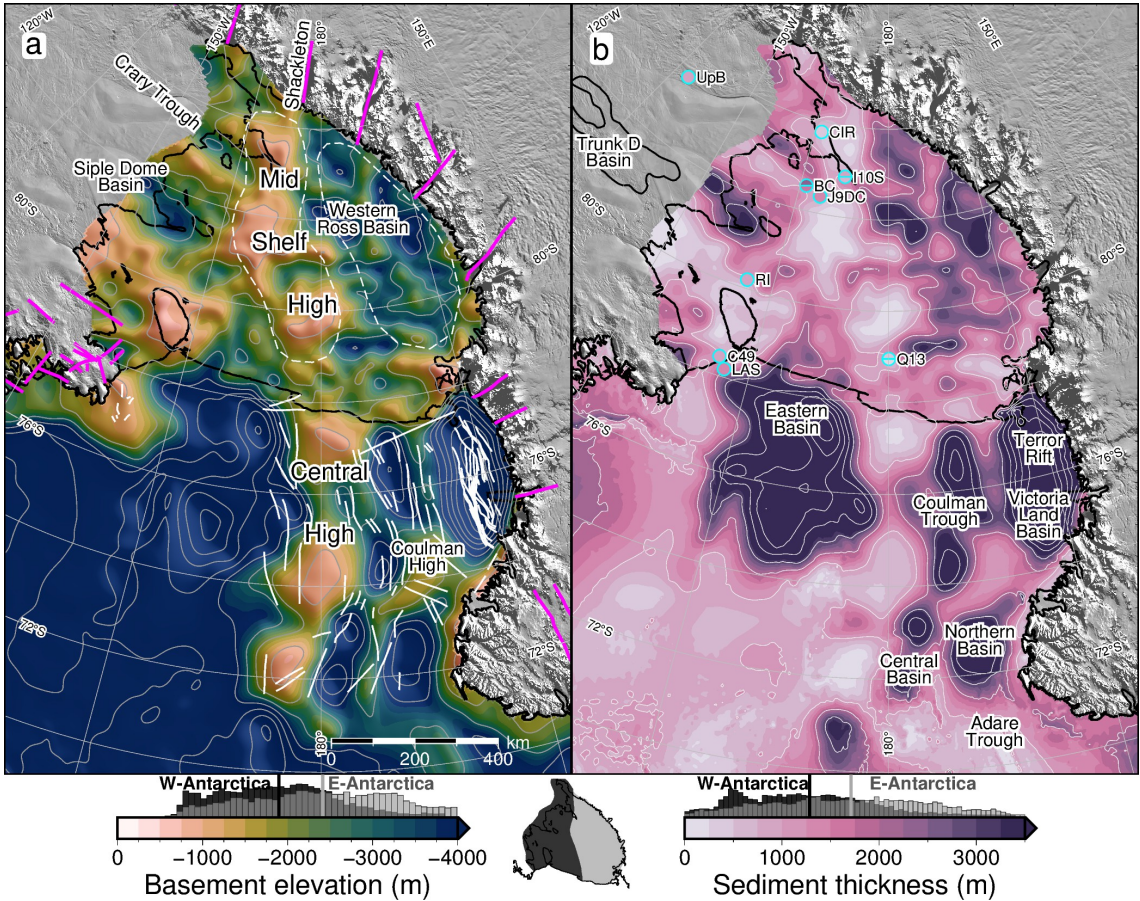


Figure 2.3: (a) Basement elevation (magnetic for Ross Ice Shelf (RIS), seismic elsewhere) contoured at 1 km intervals. Pink lines are onshore mapped and inferred faults (Ferraccioli et al., 2002; Goodge, 2020; Siddoway, 2008). White lines are offshore faults (Chiappini et al., 2002; Luyendyk et al., 2001; Salvini et al., 1997; Sauli et al., 2021). Dashed white lines show Mid Shelf High and Western Ross Basin extents. (b) Sediment thickness contoured at 1km intervals. Previous basement-imaging RIS seismic surveys (cyan circles, Table A.1) are plotted on same color scale, with upper and lower uncertainty ranges as circle halves, where reported. Trunk D Basin outlined in West Antarctica (Bell et al., 2006). Color scales for both a) and b) are set to sub-RIS data range. Colorbar histograms show data distribution for East vs West Antarctic sides of the sub-RIS, separated by the Mid-Shelf High. Inset map shows East vs West divide. Vertical lines on histograms denote average values of each side.

762 m (37% of average RIS thickness, Figure A.5).

763 A single broad and deep basin (300 x 600 km) separates the MSH and the
 764 Transantarctic Mountains (TAM) (Figure 2.3a, Western Ross Basin). The West-
 765 ern Ross Basin parallels the TAM and has the deepest-observed sub-RIS basement
 766 depths of 4500 mbsl, accommodating sediments up to 3800 m thick (Figure 2.3b).
 767 It contains a long, narrow NW-SE trending ridge with ~1500 m structural relief
 768 above the basement sub-basins on either side. Bordering the MSH on the east, an
 769 elongate NW-SE trending basin runs from the RIS calving front to the Siple Coast
 770 GZ (Figure 2.3a), where beneath Siple Dome we discover a 100 x 200 km depocenter
 771 reaching basement depths up to 4000 mbsl, with sediments up to 370 0m thick. We
 772 refer to this depocenter as Siple Dome Basin, a feature bounded on the east by a
 773 basement high that trends southward from Roosevelt Island. This high rises to its
 774 shallowest point at the GZ, where its sedimentary cover is less than 100 m. A second
 775 deep, narrow basin (50 x 200 km in dimension) is found along the north margin of
 776 Cray Ice Rise, separated from the Siple Dome Basin by a NW-SE ridge underlying

777 Kamb Ice Stream. The basin, labelled Crary Trough in Figure 2.3a, reaches base-
 778 ment depths of 3200 mbsl, with sediments 1800-2700 m thick. The southernmost
 779 RIS has an additional depocenter with up to 2000 m of fill beneath Whillans Ice
 780 Stream (location in Figure 2.1a).

781 Inferred active sub-RIS faults (Figures 2.4a & A.1) correspond to narrow, lin-
 782 ear basement basins with high-gradient gravity anomalies, prevalent on the West
 783 Antarctic side (Figure A.1a). Inactive normal and strike-slip faults are inferred
 784 along lineaments that segment the shallow MSH into blocks and are oriented par-
 785 allel to TAM outlet glacier faults. β -factors are indicative of thinned crust and are
 786 different on either side of the MSH. The TAM side shows higher β -factors (aver-
 787 age 1.99) with low variability. The West Antarctic side has lower β -factors overall
 788 (average 1.82), but with some higher values up to 2.1 (Figure 2.4a).

789 2.4 Discussion

790 Sub-RIS sedimentary basins align with and show lateral continuity with the Ross
 791 Sea's Roosevelt Sub-Basin, Eastern Basin, Coulman Trough, and Victoria Land
 792 Basin (Figure 2.3, e.g. Cooper et al., 1995). The MSH passes northward into the Ross
 793 Sea's prominent Central High (CH). At the southern RIS margin, the narrow Siple
 794 Dome Basin has continuity with the previously identified Trunk D Basin (Figure
 795 2.3a, Bell et al., 2006). The throughgoing trends imply regional continuity of crustal
 796 structure and a common tectonic development of the Ross Sea and RIS regions. Our
 797 sediment thicknesses are compatible with those determined by a) eight active-source
 798 seismic surveys (Figure 2.3b), for which the median misfit is 470 m (Table A.1), and
 799 b) surface wave dispersion indicating 2-4 km of sediment under the RIS, similar to
 800 our range, with the maximum beneath Crary Ice Rise (Zhou et al., 2022). Three
 801 additional western RIS seismic profiles report up to several kilometers of sediment,
 802 in general accordance with our results (Beaudoin et al., 1992; Stern et al., 1991; ten
 803 Brink et al., 1993). Additionally, machine learning applied to geophysical datasets
 804 predicts a high likelihood of sedimentary basins at the locations of Siple Dome Basin
 805 and Crary Trough (Li et al., 2021).

806 2.4.1 West Antarctic Rift System extensional basins

807 The Western Ross Basin has a configuration similar to the western Ross Sea rift
 808 basins (e.g. Salvini et al., 1997) with a broad and deep basin, separated into dis-
 809 tinct depocenters by a linear, low relief ridge. The deeper of the depocenters, on
 810 the TAM side of the ridge, coincides with alternating high and low free-air grav-
 811 ity anomalies (Figure A.1a). These similarities suggest the sub-RIS continuations
 812 of Coulman Trough and Victoria Land Basin (Figure 2.3b) likely share a common
 813 tectonic origin as fault-controlled basins (Figures 2.3a & 2.4a) formed through Cre-
 814 taceous distributed continental extension across the WARS (Jordan et al., 2020a).
 815 These sub-RIS basins terminate against the southern segment of the MSH (Figure
 816 2.3a).

817 The linear ridge within the Western Ross Basin (Figure 2.3a) may be an ex-
 818 pression of normal or oblique faults linked to the southward-narrowing Terror Rift
 819 (Sauli et al., 2021), formed due to Cenozoic oceanic spreading in the Adare Trough
 820 (Figure 2.3b, Granot & Dyment, 2018). The Western Ross Basin, with up to 3800
 821 m of fill, terminates along the prominent edge of the MSH that lines up with the

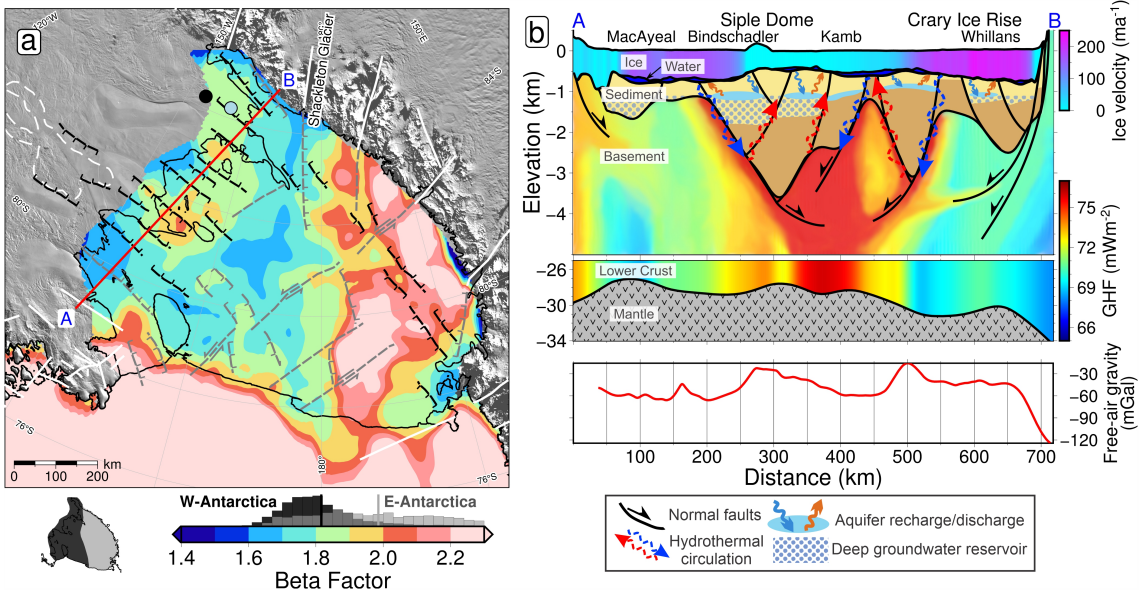


Figure 2.4: Tectonic interpretation of the sub-Ross Ice Shelf (RIS). (a) β stretching factors (Section A.7). Colorbar histogram shows data distribution of West vs. East Antarctic sides, same as Figure 2.3. Black and grey lines indicate inferred active and inactive faults, respectively, with kinematics shown with half-arrows (strike or oblique-slip) and hachures (normal-sense). White lines show previously reported faults, same as Figure 2.3a. Dashed-white outline is Trunk D Basin (Bell et al., 2006). Black and blue dots show Subglacial Lake Whillans and sedimentary basin from Gustafson et al. (2022), respectively. Cross-section A-B in red. (b) Siple Coast cross-section from A-B, showing basin sediments bounded by faults, with geothermal heat flux (GHF) through the crust (lower panel from Burton-Johnson et al. (2020), upper panel interpreted). Ice surface, ice base, and bathymetry from Morlighem et al. (2020). Ice streams colored by velocity (Mouginot et al., 2019; Venturelli et al., 2020). Moho is from Shen et al. (2018a). Lower panel shows ROSETTA-Ice gravity. Named features are labeled on top.

fault-controlled trough and crustal boundary that passes southward beneath Shackleton Glacier (Borg et al., 1990). We interpret the basement lineament (Figure 2.4a) as a transfer fault separating sectors of crust extended to different degrees.

The southeastern RIS margin is distinguished by linear ridges and narrow, deep basins. The prominent NW-SE basement trends coincide with high-gradient gravity anomalies (Figure A.1a, Tinto et al., 2019) and thick sediments, suggesting normal fault control and active divergent tectonics beneath the GZ. Our Siple Coast cross-section (Figure 2.4b) displays dramatic basement relief, exceeding 2 km, in the Siple Dome Basin and Crary Trough, which we attribute to displacement upon high angle faults. Portions of basin-bounding faults were previously detected by ground-based gravity surveys upon the Whillans Ice Stream flank (Figure 2.4a, Muto et al., 2013b) and site J9DC (Figure 2.3b), where large variations in sediment thickness indicate up to 600 m of fault throw (Grieschar et al., 1992). The continuity between the narrow Siple Dome Basin (this study) and the Trunk D Basin (Figure 2.3a, Bell et al., 2006) suggests that the active tectonic domain continues southward past the GZ. The fault-controlled tectonic basins may reflect a crustal response to the lithospheric foundering hypothesized beneath the South Pole region (Shen et al., 2018b) or be a broader regional expression of Neogene extension that formed the Bentley Subglacial Trench (Lloyd et al., 2015).

2.4.2 Consequences for ice sheet dynamics

Our basement topography and suggested crustal faults likely exert a strong influence on the overriding ice, especially along the Siple Coast. Here, we show deep and thick sedimentary basins which likely contain voluminous basinal aquifers (Figure 2.4b; cf. Gustafson et al., 2022). Where these aquifers discharge along fault-damage zones, they can enhance GHF and promote basal melting (Gooch et al., 2016), as depicted in Figure 2.4a. The elevated GHF seen at Subglacial Lake Whillans (285 mW/m^2 , Fisher et al., 2015) may arise from fault localization (Figure 2.4a). Confinement of the aquifers between the ice bed and low-permeability basement may promote fluid overpressure, enabling ice streaming (e.g. Ravier & Buoncristiani, 2018). Additionally, the Siple Coast faults likely accommodate the solid Earth's response to fluctuating ice volume. A matter receiving considerable debate (Lowry et al., 2019; Neuhaus et al., 2021; Venturelli et al., 2020), is Kingslake et al.'s 2018 finding of rapid re-advance of the Siple Coast GZ following Holocene deglaciation. The re-advance was in part due to swift glacioisostatic rebound (cf. Coulon et al., 2021; Lowry et al., 2020), a process aided by the region's low-viscosity mantle (Whitehouse et al., 2019) and likely to be accommodated upon pre-existing crustal faults, as observed in the Lambert Graben (Phillips & Läufer, 2009). Our proposed graben-bounding faults would provide a tectonic control on the glacioisostatic adjustment of the Siple Coast region.

2.4.3 Mid-Shelf High - Central High

The 650-km-long Mid-Shelf High features three shallow, blocky segments $>150 \text{ km}$ in breadth, which have only thin sediment cover ($<200 \text{ m}$). At their shallowest points, the top of basement lies within $\sim 30 \text{ m}$ of the ice shelf base, at a depth comparable to the basement high at Roosevelt Island. Roosevelt Island is a modern pinning point (Still et al., 2019) owing to the thicker sediment, there (Figure 2.3b). We introduce the MSH as a prominent pinning point at times of advance and greater extent of the Antarctic Ice Sheet, in keeping with evidence from subglacial sediment records that indicate a major ice flow divide between East and West Antarctic ice during and since Last Glacial Maximum (Coenen et al., 2019; Li et al., 2020; Licht et al., 2014).

The prominence of the MSH is due in part to the contrasting geologic properties of the East versus West Antarctic type crust and their respective responses to WARS extension. We distinguished β -factors on the TAM-side that are high and uniform, indicating distributed crustal extension. The West Antarctic side displays lower β -factors overall, but with localized extreme thinning beneath Siple Coast (Figure 2.4a). The greater amount of extension on the East Antarctic side coincides with the deeper bathymetry (Figure 2.1a), deeper basement, and thicker sediments (Figure 2.3). The contrasting properties are also evident in ROSETTA-Ice magnetic and gravity anomalies, used by Tinto et al. (2019) to identify a north-south trending tectonic boundary along the midline of Ross Embayment. The MSH in the magnetic basement coincides with and spans this boundary, which has been further substantiated by passive-seismic studies that show a lithospheric-scale boundary (Cheng et al., 2021; White-Gaynor et al., 2019). To the north, the features continue into the Ross Sea's Central High. Southward, the MSH basement feature trends into the TAM, where its western edge aligns with Shackleton Glacier, occupying a major fault separating the distinct geologic domains of the central and southern TAM

(Borg et al., 1990; Paulsen et al., 2004), which also parallels a prominent magnetic lineament at the South Pole (Studinger et al., 2006). The structure may be an expression of the East Antarctic craton margin or a major intracontinental transform (Figure 2.4a, Studinger et al., 2006).

At the time of Oligocene initiation of the Antarctic Ice sheet, paleotopographic reconstructions of the proto-Ross Embayment depict a long, broad range, emergent above sea level (Paxman et al., 2019; Wilson et al., 2012), that we equate to the MSH-CH that divides the Embayment. The CH hosted small ice caps with alpine glaciers formed during the initial glacial stage in the region (De Santis et al., 1995), and continental ice expanded to the outer Ross Sea continental shelf from those centers (Bart & De Santis, 2012). Between the late Oligocene and mid-Miocene, the CH subsided by up to 500 m (Kulhanek et al., 2019; Leckie, 1983), receiving 100's of meters of sediment cover (\sim 400 m at DSDP 270; De Santis et al., 1995). The geophysical similarities and continuity between the Ross Sea's CH and the RIS's MSH imply a similar glaciation and subsidence history for the MSH. A terrestrial/alpine stage for the MSH helps to explain the region's potential to hold the late Oligocene's larger-than-modern ice volumes (Pekar et al., 2006; Wilson et al., 2013), with the MSH-CH having a central role in Oligocene ice sheet development and the subsequent evolution of the ice sheet and ice shelf, as is documented in the Ross Sea (Halberstadt et al., 2016).

2.4.4 Thermal subsidence and sedimentation

Incorporating the updated basement basin extents and geometries into post-rift thermal subsidence modeling will enable better constrained paleotopographic reconstructions. For the sub-RIS, these reconstructions (Paxman et al., 2019; Wilson et al., 2012) use a post-Eocene subsidence model based on gravity-derived basin geometries and uniform β -factors (Wilson & Luyendyk, 2009). This model predicts uniform stretching of the eastern sub-RIS from the ice front to the Siple Coast, while our β -factors show increasing stretching from the ice front to the Siple Coast. This observed additional thinning likely has resulted in more subsidence for Siple Dome and the north flank of Crary Ice Rise, which can now be accounted for in reconstructions. Our sediment thickness comparison with past models (Section A.7, Wilson & Luyendyk, 2009) shows the majority of the sub-RIS, especially the Siple Coast, contains more total sediment than previously estimated (Figure A.1f). Depending on the age of this sediment, reconstructions may need to account for the additional sediment deposition and loading.

2.5 Conclusions

Here we present a depth to magnetic basement map for the Ross Ice Shelf (RIS) from Werner deconvolution of airborne magnetic data. The RIS magnetic basement is tied to Ross Sea seismic basement, providing the first synthetic view of Ross Embayment crustal structure. Using a bathymetry model, we obtain the sediment thickness distribution and calculate crustal extension factors for the sub-RIS. The extensional features we image, resulting from West Antarctic Rift System extension, have continuity with Ross Sea basement structures to the north, and the prominent Mid-Shelf High trends northward into the Ross Sea's Central High. This combined high separates East and West Antarctic type crust, affected by different degrees of

933 continental extension. The Mid-Shelf High was likely subaerial in the Oligocene,
934 able to support alpine ice caps in early Antarctic glaciation. Subsequently it formed
935 a prominent pinning point and ice flow divide between the East and West Antarctic
936 Ice Sheets.

937 Newly identified narrow, linear, deep sedimentary basins provide evidence of
938 active faults beneath the Siple Coast grounding zone, where thinned crust overlying
939 anomalous mantle (Shen et al., 2018a) likely experiences elevated geothermal heat
940 flow promoting the formation of subglacial water. Faults that control basement
941 margins may accommodate motion caused by the glacioisostatic response to ice sheet
942 volume changes. Subglacial sedimentary basins in this setting likely contain confined
943 aquifers within permeable basin fill. Here, ice overburden pressure would control
944 flow both between and within the subglacial and groundwater systems, possibly
945 localizing geothermal heat. Updated sediment thickness and basin extents should be
946 incorporated into new paleotopographic reconstructions of time intervals of interest
947 for paleo-ice sheet modeling. Our work contributes critical information about Ross
948 Embayment basement topography and subglacial boundary conditions that arise
949 from an interplay of geology, tectonics, and glaciation.

950 2.6 Open Research

951 ROSETTA-Ice and Operation IceBridge magnetics data are available through <https://www.usap-dc.org/view/project/p0010035> and <https://nsidc.org/data/IMCS31b>,
952 respectively. Results from this study are available to download from <https://doi.pangaea.de/10.1594/PANGAEA.941238> and a Jupyter notebook documenting our
953 workflow and figure creation is available at <https://zenodo.org/badge/latestdoi/470814953>.
954

955 2.7 Acknowledgements

956 Chapter 2, in full, is a reprint of material as it appears in Geophysical Research
957 Letters: Tankersley, M. D., Horgan, H. J., Siddoway, C. S., Caratori Tontini, F.,
958 & Tinto, K. J. (2022). Basement topography and sediment thickness beneath
959 Antarctica's Ross Ice Shelf. *Geophysical Research Letters*, 49, e2021GL097371.
960 <https://doi.org/10.1029/2021GL097371>. The paper was reviewed by Katharina
961 Hochmuth and Guy Paxman.

962 Funding support from the New Zealand Ministry of Business and Innovation
963 and Employment through the Antarctic Science Platform contract (ANTA1801)
964 Antarctic Ice Dynamics Project (ASP-021-01) and the National Science Foundation
965 (1443497 and 1443534), and Antarctica New Zealand. We are grateful to Robin Bell,
966 Isabel Cordero, Alec Lockett, Joel Wilner, Zoe Krauss, and the entire ROSETTA-
967 Ice team for undertaking the ambitious data acquisition and processing effort. We
968 thank Katharina Hochmuth and Guy Paxman for thoughtful reviews which greatly
969 improved the manuscript, as well as Chris Sorlien, Tim Stern, Simon Lamb, Lara
970 Pérez, Ryan Venturelli, Wei Ji Leong, and Dan Lowry for valuable input. Figures
971 used GMT6/PyGMT (Uieda et al., 2021; Wessel et al., 2019), with a script adapted
972 from Venturelli et al. (2020). Geosoft Oasis Montaj™ was used for magnetics pro-
973 cessing and Werner deconvolution. Open access publishing facilitated by Victoria
974 University of Wellington.

- ⁹⁷⁶ University of Wellington, as part of the Wiley - Victoria University of Wellington
⁹⁷⁷ agreement via the Council of Australian University Librarians.

978 **Chapter 3**

979 **Gravity inversion: a tool for
980 bathymetry modelling**



981 **Abstract**

982 Sub ice-shelf bathymetry exerts a primary control on the stability of many Antarctic
983 ice shelves through the geometry of pinning points and the guiding of melt-inducing
984 water masses. Collecting sub-ice shelf bathymetry data using typical polar sur-
985 veying methods (e.g. seismic surveying or direct observations) can be inefficient,
986 expensive or unfeasible. Gravity inversions provide a more practical alternative,
987 in which observed variations in Earth's gravitational field are used to predict the
988 bathymetry. This chapter describes a gravity inversion algorithm developed specifi-
989 cally for modelling bathymetry. The inversion is tested on a suite of models, created
990 with a combination of synthetic and real bathymetric data. These tests provide the
991 ability to 1) determine the best practices for conducting bathymetric inversions, 2)
992 recognize the limitations of the inversions, and 3) identify where community efforts
993 should be focused for the future of modelling Antarctica's sub ice shelf bathymetry.
994 We find that the estimation and removal of the regional component of gravity prior
995 to the inversion is the largest source of error in the resulting bathymetry model. To
996 address this, we propose procedures to limit this error and provide recommendations
997 on the minimum spatial density of bathymetry constraint points. Additionally, for
998 common airborne gravity survey designs, we find minimizing noise in the data is
999 more important than collecting closer-spaced data.

1000 **Key Points:**

- 1001 1. We present a new constrained geometric gravity inversion algorithm for recov-
1002 ering density contrasts
- 1003 2. Synthetic models show the regional-residual separation of the gravity data
1004 prior to inversion is the dominant source of error
- 1005 3. Quality over quantity for gravity data; efforts should be focused on reducing
1006 noise not increasing coverage

3.1 Introduction

In the last two decades, the Antarctic Ice Sheet has experienced significant ice mass loss, averaging 118 billion tons per year, contributing 5.2mm to sea-level rise (Smith et al., 2020a). This mass loss has been concentrated along the coast, where ocean currents are able to bring warm waters in contact with the ice (Rignot et al., 2019). Much of Antarctica is fringed with floating extensions of the ice sheet, known as ice shelves (Figure 3.1). These ice shelves provide a critical buttressing effect on the upstream ice, slowing the flow of ice from the continent into the oceans (Dupont & Alley, 2005). This buttressing results from lateral drag along the margins of the ice shelf and friction between the ice and the bed at pinning points. Thinning of the ice shelves lowers these resistive forces. Due to the cold climate and lack of surface melt, the majority of Antarctic ice shelves' thinning occurs as basal melt. This basal melt (Figure 3.1b) occurs from contact with relatively warm ocean waters, such as circumpolar deep water and high-salinity shelf water (CDW and HSSW) (Jenkins et al., 2010; Rignot et al., 2019).

These deep-lying warm masses of water originate offshore from the ice shelves and thus can only induce basal melting if they circulate under the shelves. A large enough ocean draft, the distance between the ice base and the bathymetry (Figure 3.1a), is required for this circulation to be possible. This connection between ocean draft and basal melting is shown by generally low ice shelf basal melt rates for shelves, or sections of shelves, with shallow ocean drafts (e.g. Pritchard et al., 2012; Tinto et al., 2019). Additionally, deep bathymetric troughs in regions of otherwise thin drafts, or conversely, bathymetry ridges in regions of thick drafts, can control the incursion of these water masses (St-Laurent et al., 2013; Yang et al., 2021).

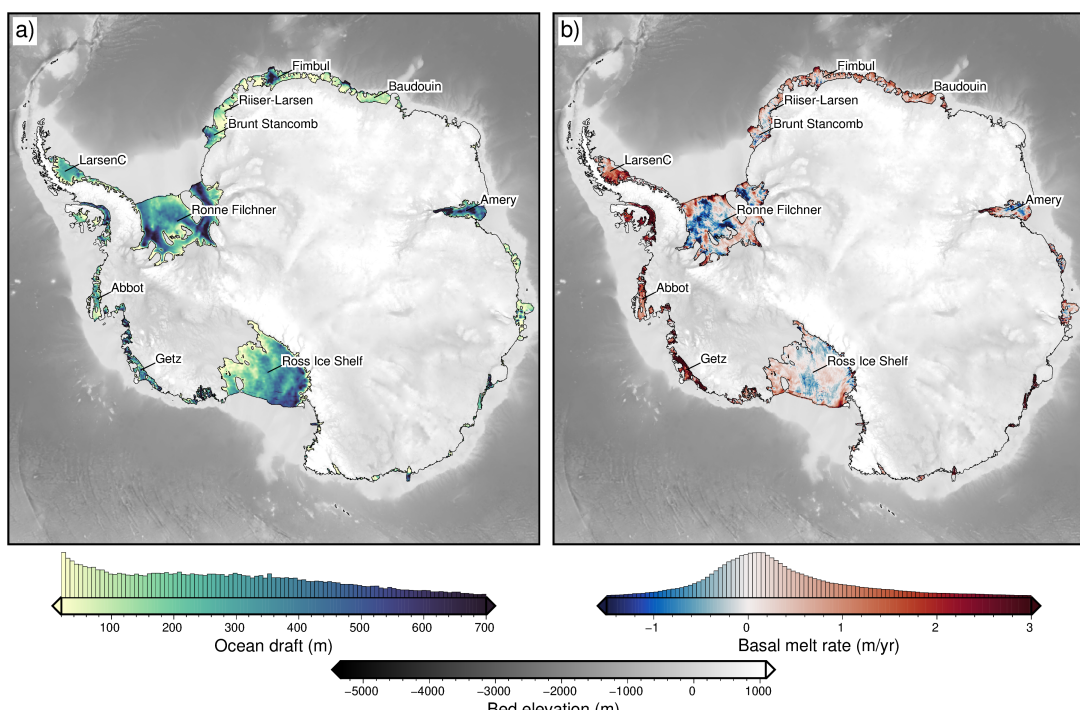


Figure 3.1: Ice shelves of Antarctica. **a)** Water column thickness beneath the ice shelves from Bedmachine data (Morlighem, 2022; Morlighem et al., 2020). **b)** Basal melt rate for the ice shelves from Adusumilli et al. (2020). Both plots show bed elevations in the gray colormap. 10 largest ice shelves are labeled.

While the elevation of the ice base for many of Antarctica's ice shelves is relatively well-constrained, the water depth is poorly known. The relatively good understanding of the ice base comes from a combination of airborne radar surveys (e.g. Das et al., 2020) and satellite altimetry measurements (e.g. Griggs & Bamber, 2011), in conjunction with the hydrostatic equilibrium assumption (Bamber & Bentley, 1994). Conversely, there is no equivalent fast and cheap technique to directly survey the bathymetry beneath floating ice shelves. Radar (ground or airborne) cannot image through the thick water, over-ice seismic surveys are slow and expensive, and numerous direct observations through drill holes are impractical. Due to the density contrast between the water and the sediment, the bathymetry surface produces a measurable gravity signal. This signal can be observed from airborne or ground-based gravity surveys, which provides a method, if used correctly, to model sub-shelf bathymetry. This method is a gravity inversion; a geophysical technique to take measurements of an energy source and estimate the physical properties responsible for these measurements (e.g., Menke, 2012; Oldenburg & Li, 2005; Tarantola, 2005). In this case, the energy source is Earth's gravitational field and the physical Earth property is the depth of the density contrast between the ocean and seafloor. This chapter will first introduce the gravity inversion technique in general, followed by the specific style of gravity inversion, a geometric inversion, which is used here. Next, a suite of synthetic models will be used to assess the performance and limitations of the inversion. The suite of models includes:

1. a simple synthetic topography.
2. a synthetic topography with a regional component of the gravity signal.
3. a semi-realistic model, using real Antarctic bathymetry and basement topographies to create the synthetic observed gravity.

With this suite of models, we will test the effects of various levels of noise, the data spacing of the observed gravity, the number of prior constraints, and various inversion methods and parameters. Finally, we will discuss the general limitations of using gravity inversions to recover bathymetry and will provide guidance for conducting gravity inversion for sub ice shelf bathymetry.

3.2 Methods

There are two fundamental types of geophysical modelling, forward modelling, and inverse modelling. Forward modelling is the process of simulating observed data from a model of physical properties. For a gravity application, this may be calculating the gravitational field resulting from a sedimentary basin of a given geometry and/or density model. In general, forward problems are well-posed, meaning there is a unique answer (Oldenburg & Li, 2005). In contrast, inverse modelling, or inversion, is the process of determining physical properties from observed data. For the previous example, this would entail using observed gravity data to predict the sediment thickness of a basin. Inverse problems are generally ill-posed. For a given set of gravity observations, there is a multitude of sedimentary basin configurations which reproduce the observed data with the same degree of accuracy. This is referred to as non-uniqueness and makes geophysical inversions a difficult procedure compared to forward modeling.

1075 3.2.1 Geophysical inversion

1076 In general, inversions consist of three components;

- 1077 1. Forward operator (f): This is a mathematical means of linking a physical
Earth property to the expected geophysical response. It accomplishes the task
1078 of forward modelling, as described above.
- 1080 2. Physical property model (p): This is a representation of the physical Earth
1081 property of interest. While real-world properties are continuous (i.e. a smoothly
1082 varying topography), computation often necessitates discretization (i.e. a
1083 DEM (digital elevation model), see section 3.2.2.1). The starting model (p_0)
1084 typically will include the prior geologic knowledge of the region. To discretize
1085 the topography we use a layer of adjacent, vertical right-rectangular prisms.
- 1086 3. Fit function (ϕ): This function describes the similarity between the observed
1087 data and the predicted data (resulting from the forward calculation of the
1088 property model ($f(p)$)). The goal of the inversion is to minimize this function
1089 so that $f(p)$ is as close to the observed data as possible.

1090 Here, a mathematical derivation of a generalized discrete inversion problem is
1091 shown, following closely to the derivation of Oliveira and Uieda (2014). The inversion
1092 problem can be framed as finding the set of physical parameters (\vec{p}) which when
1093 modeled with the forward operator (f) produce predicted data (\vec{d}^{pred}) as close
1094 to the observed data (\vec{d}^{obs}), as possible. This inversion is discrete because the
1095 topography is represent with a series of grid cells , instead of a continuous function.
1096 The difference between the observed and predicted data gives the misfit \vec{m} , where

$$\vec{m} = \vec{d}^{obs} - \vec{d}^{pred} = \vec{d}^{obs} - \vec{f}(\vec{p}). \quad (3.1)$$

1097 Here, the squared ℓ^2 -norm (mean squared error) of the misfit is the metric used
1098 to define the *closeness* between the predicted and observed data, where

$$\|\vec{m}\|_2^2 = \sum_{i=1}^N [d_i^{obs} - \vec{f}_i(\vec{p})]^2, \quad (3.2)$$

1099 where N is the number of observed data points.

1100 This is defined as the *fit function*, $\phi(\vec{p})$. The fit function can also be expressed
1101 as

$$\phi(\vec{p}) = \vec{m} \cdot \vec{m} = [\vec{d}^{obs} - \vec{f}(\vec{p})] \cdot [\vec{d}^{obs} - \vec{f}(\vec{p})]. \quad (3.3)$$

1102 In this context, the inversion problem is to determine a vector of parameters \tilde{p}
1103 of length M which minimizes $\phi(\vec{p})$. This minimum occurs where the gradient of
1104 $\phi(\vec{p})$ at the vector \tilde{p} has zero length. The gradient of $\phi(\vec{p})$ evaluated at any \vec{p} is
1105 an M -dimensional vector is defined as

$$\nabla \phi(\vec{p}) = \begin{bmatrix} \frac{\partial \phi(\vec{p})}{\partial p_1} \\ \frac{\partial \phi(\vec{p})}{\partial p_2} \\ \vdots \\ \frac{\partial \phi(\vec{p})}{\partial p_M} \end{bmatrix}. \quad (3.4)$$

Evaluating the gradient at the i^{th} element, using Equation 3.3 gives

$$\begin{aligned}\frac{\partial \phi(\vec{p})}{\partial p_i} &= \frac{\partial}{\partial p_i} \sum_j [d_j^{\text{obs}} - f_j(\vec{p})] \cdot [d_j^{\text{obs}} - f_j(\vec{p})] \\ &= \sum_j \frac{\partial}{\partial p_i} [d_j^{\text{obs}} - f_j(\vec{p})] \cdot [d_j^{\text{obs}} - f_j(\vec{p})] \\ &= -2 \sum_j \frac{\partial f_j(\vec{p})}{\partial p_i} \cdot [d_j^{\text{obs}} - f_j(\vec{p})]\end{aligned}\quad (3.5)$$

Substituting Equation 3.5 into the elements of Equation 3.4 gives

$$\nabla \phi(\vec{p}) = -2\mathbb{J}(\vec{p})[\vec{d}^{\text{obs}} - \vec{f}(\vec{p})], \quad (3.6)$$

where \vec{p} is the parameter vector of dimension M , \vec{d}^{obs} is the observed data vector of dimension N and \mathbb{J} is the Jacobian matrix of dimension $M \times N$, and is given by

$$\mathbb{J}(\vec{p}) = \begin{bmatrix} \frac{\partial f_1(\vec{p})}{\partial p_1} & \cdots & \frac{\partial f_N(\vec{p})}{\partial p_1} \\ \vdots & \ddots & \vdots \\ \frac{\partial f_1(\vec{p})}{\partial p_M} & \cdots & \frac{\partial f_N(\vec{p})}{\partial p_M} \end{bmatrix} \quad (3.7)$$

Each element of the Jacobian matrix is given by

$$\mathbb{J}_{ij} = \frac{\partial f_j(\vec{p})}{\partial p_i}, \quad (3.8)$$

which is the partial derivative of the j^{th} predicted data with respect to the i^{th} physical parameter. The *Jacobian* (\mathbb{J}) is a sensitivity matrix that describes how much the predicted data changes for an infinitesimal change in the physical parameter. For example, let's consider the case of a gravity inversion attempting to recover the density of subsurface cubes. The model consists of 100 cubes, and there are 10 observation points. The Jacobian would be a 100×10 matrix where $\mathbb{J}_{1,1}$ (the first entry) would be the 1st cube's gravitational derivative with respect to density at the first observation point. The Jacobian, therefore, describes how sensitive each pair of cubes and observations are to a change in density.

Once the Jacobian is created, a matrix equation of the form $Ax = b$ is set up, where A is the Jacobian, x is the unknown variable, and b is the data misfit.

$$\mathbb{J}\vec{x} = \vec{m} \quad (3.9)$$

A solution to this linear equation can be found directly, by finding the inverse or pseudo-inverse matrix of the Jacobian, or iteratively via a least-squares solver (Jacoby & Smilde, 2009). The solution gives the correction which when applied to the physical parameters of interest minimizes the misfit between the observed data and the starting model.

¹¹²⁹ **3.2.1.1 Non-Linear inversions**

¹¹³⁰ The derivative of the forward operator with respect to the parameter of interest
¹¹³¹ determines the linearity of an inversion. For a gravity inversion attempting to recover
¹¹³² rock density, the derivative of gravity with respect to density is constant, and thus
¹¹³³ the inversion is considered linear (Aster et al., 2018). Conversely, a gravity inversion
¹¹³⁴ attempting to recover the depth to a surface, or the thickness of a layer, is non-linear
¹¹³⁵ since the vertical derivative of gravity (derivative with respect to depth) is dependent
¹¹³⁶ on the depth. Non-linear inversion cannot be solved directly, with matrix inversion
¹¹³⁷ (Jacoby & Smilde, 2009). They must be linearized; which is the purpose of the
¹¹³⁸ Jacobian matrix. The Jacobian enables a minimum-norm solution to be found with
¹¹³⁹ an iterative solver, where at each iteration, the calculated corrections (\vec{x}) are applied
¹¹⁴⁰ to the starting model, the residuals (\vec{m}) are recalculated, the Jacobian is updated,
¹¹⁴¹ and Equation 3.9 is solved again, giving a new set of corrections. This is repeated
¹¹⁴² until $\phi(\vec{p})$ is suitably low.

¹¹⁴³ **3.2.1.2 Geometric inversions**

¹¹⁴⁴ Most gravity inversions aim to recover the distributions of densities in the subsurface.
¹¹⁴⁵ For this technique, the model domain is discretized into a series of polygons (for
¹¹⁴⁶ 2D) or polyhedrons (for 3D), and the inversion aims to predict the density of each
¹¹⁴⁷ polygon. This is widely used due to its relevance in mineral exploration (Oldenburg
¹¹⁴⁸ & Pratt, 2007). Less commonly used are gravity inversions which aim to recover
¹¹⁴⁹ the depth, shape, or volume of features. This style of gravity inversions are referred
¹¹⁵⁰ to as geometric inversions. They are typically used to estimate relief of the Moho
¹¹⁵¹ (e.g Borghi, 2022; Uieda & Barbosa, 2017) or the sediment-basement contact (e.g.
¹¹⁵² Barbosa et al., 2007; Santos et al., 2015). In this chapter, geometric inversions
¹¹⁵³ are used to recover the bathymetry. This use case of gravity inversion is unique
¹¹⁵⁴ to studying the cryosphere. In locations without ice cover, bathymetry data is
¹¹⁵⁵ typically collected with shipborne multi-beam echo sounding, airborne LiDAR, or
¹¹⁵⁶ satellite altimetry.

¹¹⁵⁷ **3.2.2 Forward modelling**

¹¹⁵⁸ To perform a geometric gravity inversion, first, the gravitational field produced by
¹¹⁵⁹ a topographic surface must be able to be calculated. This topography is approxi-
¹¹⁶⁰ mated as a constant density contrast between the overlying and underlying materials.
¹¹⁶¹ The topography is often modelled as a series of adjacent vertical right-rectangular
¹¹⁶² prisms. For a certain observation point, the gravitational field produced by this
¹¹⁶³ layer of prisms is the sum of the forward gravity of each prism. This forward gravity
¹¹⁶⁴ calculation of a prism is accomplished with the analytical solutions given by Nagy
¹¹⁶⁵ et al. (2000), as implemented in the Python package Harmonica (Fatiando a Terra
¹¹⁶⁶ Project et al., 2023).

¹¹⁶⁷ **3.2.2.1 Discretization**

¹¹⁶⁸ There are several options for discretizing a density contrast as a series of prisms
¹¹⁶⁹ (Figure 3.2). The most conceptually simple method is for the prisms to represent
¹¹⁷⁰ the true density and geometry of the material on either side of the surface (Figure
¹¹⁷¹ 3.2b). In this method, the topography is represented by the base of the above prisms,

and by the tops of the lower prisms. Alternatively, the contrast can be represented by a layer of prisms either above or below the surface, ending at an arbitrary reference, typically the minimum or maximum value of the surface (Figure 3.2c-d). For this, the prism's density values are relative to the medium on the other side of the surface (i.e. if prisms are below the surface, their densities are $\rho_{below} - \rho_{above}$). The last option is to choose a flat reference surface (typically the mean value of the surface or sea level) and create prisms between this and the surface (Figure 3.2e). Prisms above the reference are assigned a positive density contrast ($\Delta\rho = \rho_{below} - \rho_{above}$), and prisms below the surface a negative density contrast ($\Delta\rho = \rho_{above} - \rho_{below}$). All of these methods result in similar forward gravity calculations. Note that the absolute density option (Figure 3.2b) has twice as many prisms as the other options, significantly increasing its computational expense, regardless of whether or not a buffer zone is used.

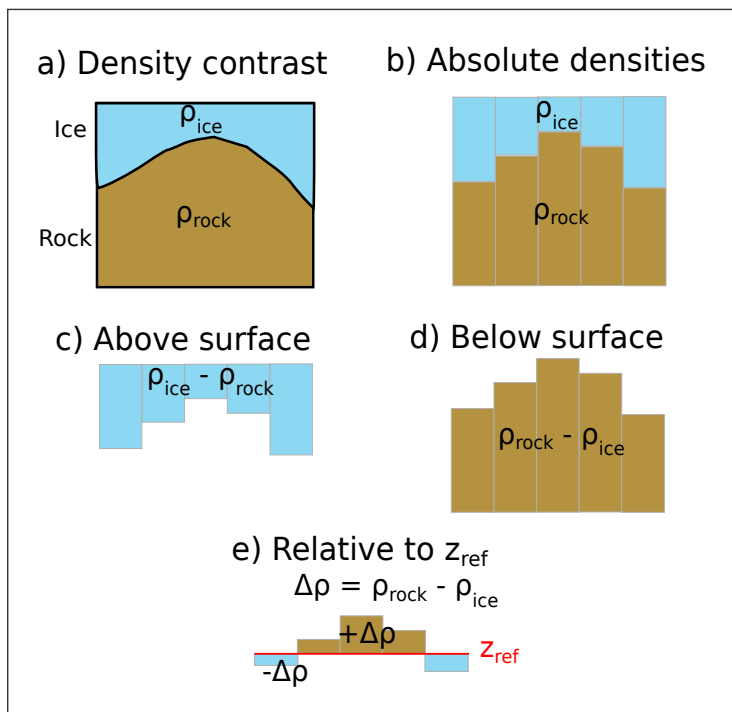


Figure 3.2: Equivalent methods of discretizing a density contrast (a) across a surface. b) Use absolute densities of the mediums above and below the reference, with prisms on either side. c-d) Use the density contrast across the surface, with prisms either above or below, and the sign of the density contrast reflecting whether they are above or below. e) Use a reference surface, with prisms above having a positive density contrast and prisms below a negative contrast.

3.2.2.2 Gravity edge effects

Any forward gravity calculation of a surface will include gravitational edge effects. These effects are typically a decay in the gravitational field towards the edges of the prism model due to the void space (density of 0) beyond the edge of the model. The magnitude of decay is dependent on the average thickness and density of prisms near the edge. Larger or denser prisms create a large contrast with the void space, resulting in a greater amount of decay. Therefore, the absolute density method of discretization (Figure 3.2b) produces the largest edge effects due to the high-density values and large total thickness of the prisms. The relative density methods (Figure 3.2c-d) produce a smaller edge effect, since the prisms are only above or below the

surface, reducing their total thickness. The density values are also less than in the absolute density method. The reference surface method (Figure 3.2e) produces the smallest edge effects due to both a) the mean prism thickness being smaller, and b) positive and negative density prisms having opposite edge effects, partially canceling each other out. This is only applicable if the reference level is located within the range of the values of the surface. Note that with a reference level completely above or below the surface, the reference method becomes identical to methods c) and d) of Figure 3.2.

A buffer zone can be used to reduce the impact of these edge effects by calculating forward gravity confined to an inner region, while the prism model extends beyond. This limits the majority of the edge effects to outside the region of calculation. Too large of a buffer zone will add an unnecessary amount of computation (more prisms), while too small of a zone will introduce unacceptably large edge effects to the calculations.

3.2.3 Isolating anomalies

For a successful geometric gravity inversion, the component of the observed gravity field resulting from the density contrast of interest must be isolated from all other gravity signals. This section describes the process of isolating the required anomaly. Since this section consists of synthetic gravity, the discussion of correcting raw gravity measurements and deriving the various gravity anomalies is omitted. See Chapter 4 for further discussion of gravity data processing. Here, *synthetic observed gravity* is taken to mean the gravity effect resulting solely from deviations between the true synthetic model, and a simple reference model, defined by a flat surface with a constant density above and a constant density below. This is considered a partial topo-corrected gravity disturbance, since the gravity effect of other layers, such as ice and water, if present, is assumed to have been corrected for. The misfit, \vec{m} , in Equation 3.1, is defined as this synthetic observed gravity minus the forward gravity effect of the starting bathymetry.

3.2.4 Regional vs. Residual gravity

The topography-free gravity disturbance is often simplified as consisting of two components, the regional and residual fields. The regional field typically dominates the signal and is often the result of deeper and broader structures, such as Moho variations. Superimposed on this signal is the residual field, which is typically the result of shallower structures. The terms residual and regional are relative; here, they are taken to mean the gravity effect of the bathymetry versus that of all deeper structures, respectively. In this inversion, the residual, regional, and misfit are related by

$$\vec{m} = \vec{m}_{res} + \vec{m}_{reg}, \quad (3.10)$$

where \vec{m} is the overall data misfit, from Equation 3.1. The residual misfit, \vec{m}_{res} , is the desired input into the inversion, and thus the regional component, \vec{m}_{reg} , must be removed prior to the inversion. This step proves to be one of the most challenging steps of a bathymetric inversion, especially in areas of limited

1238 constraints (Brisbourne et al., 2014). Removing an incorrect regional field, whether
1239 it is too much or too little, will directly impact the resulting bathymetry results.
1240 Regional-residual separation is also highly non-unique and benefits greatly from *a*
1241 *priori* constraints. Many methods of regional separation rely on the simplifying
1242 assumption that the regional field consists of longer-wavelength anomalies, while
1243 the residual field dominates the short-wavelength components. Here, four methods
1244 of estimating the regional component of gravity are described.

- 1245 1. Low-pass filter: With the assumption outlined above, a low-pass filter can be
1246 used to isolate the regional gravity. For this, a Gaussian wavelength filter is
1247 used and the filter width can be varied based on the expected regional anomaly
1248 wavelengths. This method requires the data to be gridded over the entire
1249 domain, which may be a problem for sparse surveys, or irregularly shaped
1250 domains. The choice of wavelength is subjective and needs to be carefully
1251 considered. See Eisermann et al. (2020) for a bathymetry inversion utilizing
1252 this method of regional separation.
- 1253 2. Trend removal: Similar to the low-pass filter method, a trend can be fit to the
1254 misfit data, representing the regional field. The order of the polynomial trend
1255 is subjective and can be varied to suit the data. Again, this parameter choice
1256 requires care.
- 1257 3. Equivalent source prediction: The equivalent sources technique is a method
1258 commonly used to grid, smooth, or upward-continue gravity data. It creates
1259 a set of point sources with densities, which when forward-modelled, reproduce
1260 the measured gravity data. These sources are then used to predict the gravity
1261 anomaly at any desired point. The source depths can be varied to achieve
1262 the desired regional component. This technique is beneficial over low-pass
1263 filter and trend removal in that it does not require the data to be gridded and
1264 can thus accommodate sparse surveys, or compilations of surveys at varying
1265 altitudes. It is computationally expensive compared to the above methods.
1266 Additionally, source depths are a subjective parameter, which needs to be
1267 carefully chosen. Past bathymetry inversions have used upward continuation
1268 as a means to define the regional field (e.g., Tinto et al., 2015).
- 1269 4. Constraint point minimization: The last method makes use of constraint points
1270 where the bathymetry depths are known. This inversion defines the residual
1271 component of the misfit as the gravity effect from deviations of the true
1272 bathymetry with respect to the starting bathymetry. At constraints, there is
1273 no deviation between the starting and true bathymetries, and thus the residual
1274 component of the misfit should be zero at the constraints. This means the total
1275 misfit value at the constraints is equal to the regional component (Equation
1276 3.10). By sampling the misfit at each constraint, and fitting a surface to these
1277 values, a regional component is estimated. This technique has a few advantages.
1278 It imposes a form of smallness regularization, where the inversion won't
1279 significantly alter the depth of the constraint points since the input residual
1280 at the points is ~ 0 mGal. Additionally, except for the gridding technique,
1281 this method doesn't require a subjective parameter, unlike the other methods.
1282 Similar to the low-pass filter and trend removal, this method requires gridded
1283 data. If this data is sparse, or the constraints are not located near gravity
1284 observation points, some inaccuracies will be introduced. This technique has

1285 been used in several bathymetry inversions (An et al., 2019a; Millan et al.,
 1286 2020; Yang et al., 2021).

1287 Other methods used to approximate the regional component include using high-
 1288 altitude (satellite) gravity data (Muto et al., 2016; Tinto et al., 2015), the forward
 1289 modelling of a geologic model, either inferred from 1) other geophysical data (Hodg-
 1290 son et al., 2019), 2) *a priori* geologic knowledge (Tinto & Bell, 2011), or 3) from an
 1291 approximated crustal density distribution (Cochran et al., 2020; Tinto et al., 2019).
 1292 Once estimated, the regional component is then removed from the total misfit, giv-
 1293 ing the residual misfit. This residual misfit ideally results solely from discrepancies
 1294 between the starting and true bathymetries.

1295 3.2.5 Running the inversion

1296 Here, the necessary steps for running an inversion are explained. First, the Jacobian
 1297 matrix is calculated (Equation 3.7). Next, the matrix equation (Equation 3.9) is
 1298 solved, giving the necessary corrections to apply to the bathymetry. Additionally,
 1299 this solution needs to be constrained to account for the inherent non-uniqueness
 1300 of the inversion. This is accomplished with various forms of regularization; i.e., a
 1301 unique solution is determined subject to minimize an additional objective function.

1302 3.2.5.1 Jacobian matrix

1303 The first step of the inversion is to calculate the sensitivity matrix, the Jacobian
 1304 (Equation 3.7). Each entry of the Jacobian (Equation 3.8) is the vertical derivative
 1305 of gravity of a prism relative to a single observation point. While a solution exists to
 1306 the analytical vertical gravity derivative of a prism, we use an approximation to limit
 1307 the computational expense (Nagy et al., 2000). Here two methods are derived for
 1308 approximating the vertical gravity derivative resulting from a prism; 1) an annular
 1309 approximation and 2) a finite differences approach.

1310 Annulus approximation

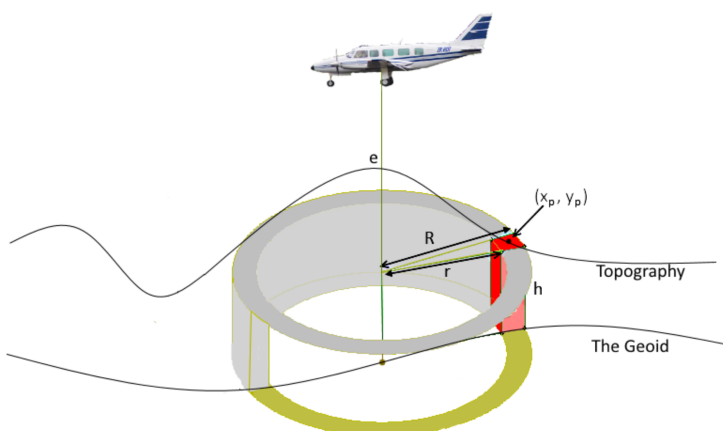


Figure 3.3: An illustration of an annulus of topography as an approximation for a vertical prism. From McCubbine (2016).

1311 A vertical prism can be approximated as a sector of an annulus (a cylindrical
 1312 shell), as in Figure 3.3. This approximation greatly simplifies the calculation of the
 1313 vertical derivative of the prisms' gravity. The vertical component of gravity of an
 1314 entire annulus (grey hollow cylinder in Figure 3.3) is defined by

$$\delta g = 2\pi G\rho(R - r + \sqrt{r^2 + h^2} - \sqrt{R^2 + h^2}) \quad (3.11)$$

1315 where ρ is the density, G is the gravitational constant, r and R are the inner and
 1316 outer radii, respectively, and h is the average height of the cylinder (Hammer, 1939).
 1317 r , R , and h are relative to the observation point, located in the center bottom of the
 1318 annulus. McCubbine (2016) provides an adaption of Equation 3.11 which isolates
 1319 the gravity of just a portion of this annulus (red section in Figure 3.3). This is
 1320 accomplished by adding an additional factor f , relating the area of the annulus to
 1321 the area of a sector of it:

$$f = \frac{\alpha^2}{\pi(R^2 - r^2)} \quad (3.12)$$

1322 where

$$r = \sqrt{x^2 + y^2} - \sqrt{\frac{\alpha^2}{2}} \quad (3.13)$$

$$R = \sqrt{x^2 + y^2} + \sqrt{\frac{\alpha^2}{2}} \quad (3.14)$$

1323 where α is the prism width, x , y , and z are coordinates of the prism center,
 1324 relative to the observation point. This factor f is then multiplied by Equation 3.11
 1325 to give the vertical component of gravity for a section of an annulus, $\delta g_{annulus} = f\delta g$.

1326 Taking the derivative of this with respect to h gives

$$\frac{\partial g}{\partial h} = 2f\pi G\rho h\left(\frac{1}{\sqrt{r^2 + h^2}} - \frac{1}{\sqrt{R^2 + h^2}}\right). \quad (3.15)$$

1327 While the approximation of a prism as a section of an annulus introduces some
 1328 errors, the calculation is efficient and simple to implement.

1329 Finite differences approximation

1330 Another option to calculate the vertical derivative for the Jacobian matrix is with
 1331 numerical differentiation. For this, a small prism is added above each existing prism,
 1332 its forward gravity is calculated and the result is divided by the small prism's height.
 1333 This approximates the vertical derivative of gravity at the surface of the prism, rel-
 1334 ative to the observation point.

1335 Both methods adequately determine the Jacobian. The annulus method is a
 1336 more simple calculation and is thus faster, but is likely less accurate and introduces
 1337 singularities. These singularities occur if the prism is directly beneath the observa-
 1338 tion point, so that either the inner or outer radii are negative (Figure 3.3). These
 1339 singularities are resolved by shifting the observation point to a prism edge. Con-
 1340 versely, the finite differences method, while it is a numerical approximation, uses
 1341 analytical solutions for calculating the forward gravity (Fatiando a Terra Project

1343 et al., 2023; Nagy et al., 2000), and thus is valid in the entire domain, with no singularities. This increased robustness makes the computation slower. Section 3.3.1.3
1344 compares the effectiveness and computation time of both of these methods.
1345

1346 **3.2.5.2 Least-squares solver**

1347 With the Jacobian matrix and the vector of gravity residuals, Equation 3.9 can be solved to find the set of surface correction values that minimize the fit function.
1348
1349 Here, the matrix equation $\mathbb{J}\vec{x} = \vec{r}$ is solved with an iterative damped least squares algorithm (LSQR Paige & Saunders, 1982). The algorithm gives the minimum-norm solution, where for a set of solutions that each fit the data with the same accuracy,
1350 the solution with the minimum $\|p\|^2$ is chosen. LSQR accepts a damping parameter,
1351 which helps regularize the problem, preventing the solution from becoming too large.
1352 The choice of the damping value is important as it directly affects the inverted results. The optimal value can be chosen with a cross-validation routine following
1353 that of Uieda and Barbosa (2017), as described below.
1354
1355
1356

1357 **3.2.5.3 Regularization**

1358 Regularization is a series of techniques used to help constrain ill-posed inversion problems (Aster et al., 2018). Most potential field inversions, due to their inherent non-uniqueness, are ill-posed, containing many solutions which equally satisfy the data. Here regularization is split into *smallness* and *smoothness*. *Smallness* deals with adhering to *a priori* constraints, i.e. having the inverted surface elevation match the previous bathymetry measurements (constraint points). *Smoothness* helps to achieve realistic topographic results, without major jumps or excessively steep slopes.
1359
1360
1361
1362
1363
1364
1365

1366 **Smoothness**

1367 To achieve a form of smoothness regularization, damping is applied at each iteration to the solver of the matrix equation. One method to choose an optimal damping value is cross-validation of the input gravity data (Uieda & Barbosa, 2017). An effective inversion should produce a topography that, when forward modelled, accurately recreates observed gravity data that weren't included in the inversion. This idea is the basis of the cross-validation routine. The observed gravity data is split into two sets, a *training* and a *testing* set. For an individual damping value, the inversion is run using only the training set. The final inverted bathymetry is then forward modelled onto the observation points of the testing set. The difference between the observed and forward gravity at these testing points is calculated. The root mean square (RMS) of the differences provides a metric for the effectiveness of the damping; this is referred to as the *score*. This process is then repeated for a suite of damping values, and the value which produces the lowest score is used as the optimal damping value. In this inversion, the gravity data, whether it is airborne flight lines or scattered ground stations, are interpolated onto a regular grid (see Section 3.3.1.5). To create the testing set of observed gravity data, the original data is interpolated onto a grid at half the desired grid spacing. This leaves the training set with the desired amount of points. This grid spacing configuration is shown in Figure 3.4.
1368
1369
1370
1371
1372
1373
1374
1375
1376
1377
1378
1379
1380
1381
1382
1383
1384
1385

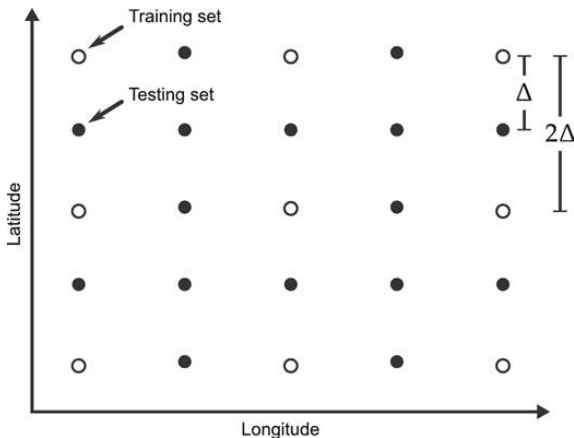


Figure 3.4: Configuration of observed gravity data observation points, split into training and testing sets. Reprinted from Uieda and Barbosa (2017).

1386 **Smallness**

1387 A form of smallness regularization is applied here to ensure the inversion results ad-
 1388 here to any *a priori* bathymetry constraints. A portion of this smallness regulariza-
 1389 tion is already accounted for when using the constraint point minimization method
 1390 of regional-residual separation. This method minimizes the residual component of
 1391 the gravity misfit at the constraint points by assigning the majority of the misfit to
 1392 the regional component. However, non-zero residual values near the constraints will
 1393 result in a non-zero correction of the prisms immediately surrounding the constraint.
 1394 For further smallness regularization, a weighting grid (Figure 3.5) is used to ensure
 1395 the surface correction values at each iteration are 0 at constraint points. If only
 1396 the prism immediately at the constraint point is fixed, a *pedestal* effect commonly
 1397 develops. This is where the nearby prisms' surfaces freely move during the inversion,
 1398 yet the constrained prism is fixed, resulting in either a pedestal or a hole. To avoid
 1399 this, the weighting grid smoothly decays from a value of 0 at the constraints, to a
 1400 value of 1 at a distance. To create this grid, the minimum distance between each
 1401 grid cell (prism) and the nearest constraint point is calculated. These values are
 1402 then normalized from 0 to 1 (Figure 3.5). At each iteration, the least squares solver
 1403 yields a grid of surface correction values. Before being added to the prism layer, the
 1404 grid is multiplied by this weighting grid. This results in surface corrections of 0 for
 1405 prisms located at constraint points, unmodified surface correction values far from
 1406 constraint points, and a smooth taper between these two endmembers.

1407

1408 The above sections outline a single iteration of the inversion. Once the surface
 1409 correction is calculated and the weights are applied, these values are added to the
 1410 starting bathymetry (or the last iterations inverted bathymetry). This is then re-
 1411 discretized into prisms. The updated prisms are then forward modelled to create a
 1412 new predicted gravity, \vec{d}^{pred} . This is subtracted from the observed gravity, \vec{d}^{obs} ,
 1413 to get a new misfit, \vec{m} . Using the same original regional component, the updated
 1414 residual gravity misfit, \vec{m}_{res} , is calculated. This is now the input into the second iter-
 1415 ation of the inversion. This process is repeated until a user-determined termination.
 1416 Next, we outline the four criteria for ending the inversion.

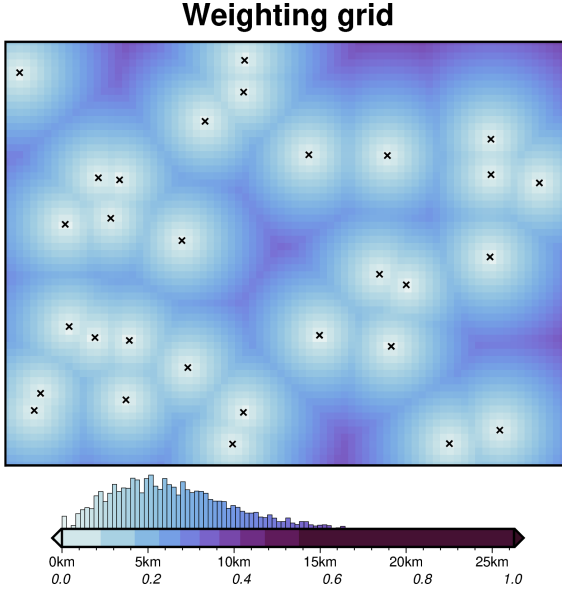


Figure 3.5: Weighting grid for the simple synthetic inversion, created from the minimum distance between each grid cell and the nearest constraint (black crosses). Grid values are normalized from 0 to 1 to produce the weighting grid (lower colormap annotations).

1417 3.2.6 Stopping Criteria

1418 The inversion is terminated on one of four stopping criteria:

- 1419 1. when the inversion reaches a maximum number of iterations (N)
- 1420 2. when the ℓ^2 -norm of the residual ($\|\vec{m}\|_2$, Equation 3.1) is less than a set ℓ^2 -
1421 norm tolerance
- 1422 3. if there is no significant variation in the ℓ^2 -norm between iterations (i.e. the
1423 $\Delta\|\vec{m}\|_2$ is less than a set tolerance)
- 1424 4. if the ℓ^2 -norm increases above a certain threshold of the starting ℓ^2 -norm.

1425 The maximum number of iterations is set as a safety margin to avoid excessively
1426 long-running inversions. The ℓ^2 -norm tolerance is used to end the inversion before
1427 excessive over-fitting of noise in the data. This should be set to the square root
1428 of the assumed noise level of the gravity data. The $\Delta\ell^2$ -norm tolerance is used to
1429 end inversions that have reached their limit of reducing the ℓ^2 -norm. Finally, the
1430 upper limit of ℓ^2 -norm terminates run-away inversions, which occurred during the
1431 development of the inversion due to coding errors but is retained here as a fail-safe.

1432 3.2.7 Software implementation

1433 The inversion algorithm described here is implemented within the Python program-
1434 ming language. The algorithm uses many open-source scientific libraries. These in-
1435 clude Harmonica for the forward gravity modelling of prisms and equivalent sources
1436 calculations (Fatiando a Terra Project et al., 2023; Soler & Uieda, 2021), Verde
1437 for various spatial operations (Uieda, 2018), PyGMT and Antarctic-Plots for figure
1438 creation (Tankersley, 2023; Uieda et al., 2021), Scipy for least squares regression
1439 (Virtanen et al., 2020), and Optuna for hyperparameter optimization (Akiba et al.,

2019). The majority of the experiments were run in Jupyter notebooks (Pérez & Granger, 2007), which are documented to explain the details of using the software. All source code, results, and figures involved in this chapter are made available in an online GitHub repository (https://github.com/mdtanker/RIS_gravity_inversion). See Section 1.6 for the hardware used in this study.

3.3 Synthetic models

To assess the performance of the inversion and showcase its use, it is applied to a suite of synthetic test models. Each model has three components; 1) the ‘true’ bathymetry surface, which the inversion is expected to model, 2) the ‘observed’ gravity data, and 3) the ‘starting’ bathymetry model, which is a low-resolution version of the true surface. The only inputs into the inversions are the observed gravity data and the starting bathymetry. The true bathymetry is only used to evaluate the performance of each inversion. The observed gravity data contains the forward gravity calculated from the true bathymetry, plus, in some cases, additional noise and other gravity signals such as a regional field. The starting bathymetry is created by sampling the true bathymetry at a set of points. These values are then used to re-grid the data for the entire region using a bi-harmonic spline interpolator (Uieda, 2018). This simulates the bathymetric knowledge of many ice shelves, where few direct measurements of bathymetry exist, such as drill holes, or single-point seismic surveys. These points are referred to as the constraints. The models tested here include:

1. A simple model (Section 3.3.1): This model sets a baseline performance expectation of the inversion, with no noise, dense gravity observation points, and no additional components included in the observed gravity. The synthetic bathymetry is created with Gaussian functions of various amplitudes and wavelengths. With this same simple model, the observed gravity data is re-gridded at a lower resolution, and random noise is added, to better simulate a gravity survey.
2. A simple model with a regional field (Section 3.4): Using the same model as above, a ‘regional’ component of the gravity field is added to the observed data.
3. A semi-realistic model (Section 3.5): This last model is created from real bathymetry data from Antarctica’s Ross Sea. This model tests the inversion’s capabilities with more realistic bathymetric features expected for sub-ice shelf environments.

3.3.1 Simple model

3.3.1.1 Model setup

Simulating typical sub-ice shelf bathymetry, this model (Figure 3.6a) has an average elevation of ~ -700 m and ranges between ~ -400 m and ~ -1000 m. It contains features of various wavelengths, amplitudes, and shapes; namely two circular features and two linear features. Overall, the grid is eastward deepening and contains a shallow and wide E-W trough through the center. The model domain is 80 km x

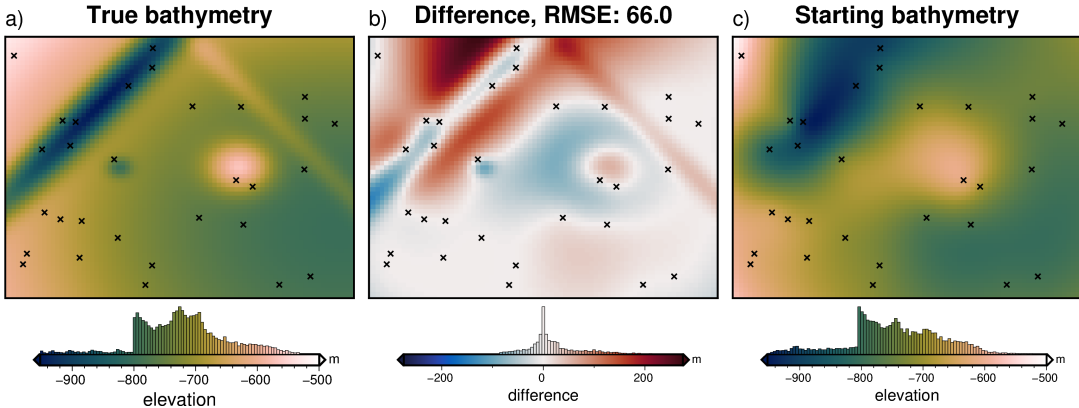


Figure 3.6: Simple synthetic model bathymetry. **a)** True bathymetry created from Gaussian functions, **b)** difference between a and c, and **c)** starting bathymetry, created from the sampling and re-gridding of the true bathymetry at 30 points (black crosses).

1482 60 km, with 1 km grid cells (4800 cells). A 6 km buffer zone in all directions was
 1483 included to limit gravitational edge effects. 30 randomly located constraint points
 1484 were used to create the starting bathymetry (Figure 3.6c). The starting bathymetry
 1485 has an RMS difference with the true bathymetry of 66 m.

1486
 1487 To forward model the gravity of the true bathymetry, a layer of adjacent verti-
 1488 cal right-rectangular prisms was created using the reference discretization method
 1489 (Figure 3.2e) with the mean elevation as the reference level. A density contrast of
 1490 $\Delta\rho = 1276 \text{ kg m}^{-3}$ (contrast between seawater (1024 kg m^{-3}) and sediment (2300 kg m^{-3})),
 1491 was used, with $+\Delta\rho$ for prisms above the reference, and $-\Delta\rho$ for prisms below
 1492 the reference. The forward gravity of this prism layer was calculated at a constant
 1493 height of 1000 m (roughly 1700 m above the bathymetry) on a regular grid at half
 1494 the grid spacing (500 m) of the bathymetry. This represents the observed gravity
 1495 data (Figure 3.7a) and consists of both the training and testing data sets used for
 1496 the cross-validation (Section 3.2.5.3, Figure 3.4).

1497
 1498 The low-resolution starting layer was discretized in the same method, and the
 1499 same density contrast was used. The forward gravity of these starting layer prisms
 1500 results in the predicted gravity (Figure 3.7c). To account for any offset between
 1501 the observed and predicted data, the observed data is DC-shifted to minimize the
 1502 differences at the constraint points. The difference between the shifted observed and
 1503 the predicted data gives the gravity misfit (Figure 3.7b). Since there is no regional
 1504 component in this synthetic model, the input into the inversion, the residual misfit,
 1505 is equal to this total misfit (Equation 3.10). This residual misfit describes the ability
 1506 of the starting model to predict the observed data.

1507 3.3.1.2 Cross validation

1508 To find the optimal value for the regularization damping parameter, the cross-
 1509 validation method of Uieda and Barbosa (2017) is used (Section 3.2.5.3). The full
 1510 set of observed data with a 500 m spacing ($N = 19481$), was separated into the
 1511 training ($N = 4941$) and testing set ($N = 14540$). With the grid configuration from
 1512 Figure 3.4, the resulting training data was on a regular 1 km grid, which matches
 1513 the grid of the bathymetry. This training data set was used as the input to 10
 1514 inversions. Each inversion used a different damping value between 10^{-4} and 10^{-1} .

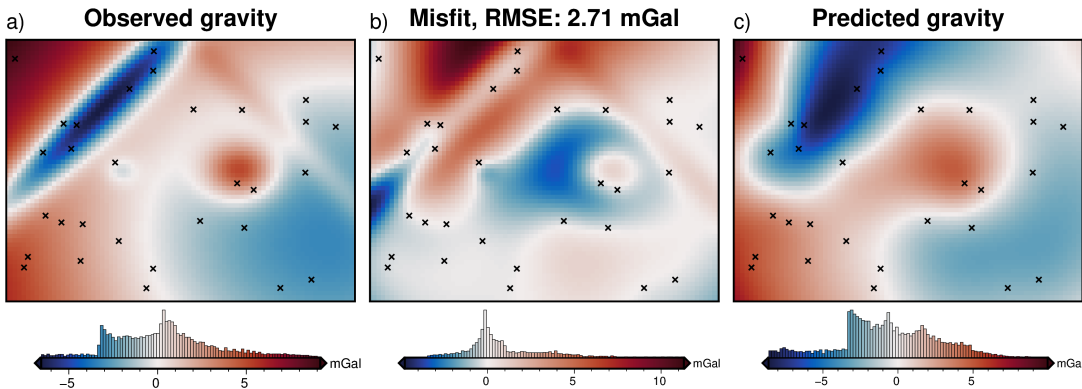


Figure 3.7: a) Synthetic gravity data generated from the true bathymetry, b) the residual anomaly, defined as the difference between a and c, and c) the predicted gravity from the starting bathymetry (Figure 3.6c).

1515 The resulting inverted bathymetry of each inversion was then forward modelled on
 1516 the observation points of the testing data set (not used in the inversion). The RMS
 1517 difference between the forward modelled gravity value and the initial residual misfit
 1518 values was calculated, giving the cross-validation score (Figure 3.9a). Of the 10
 1519 inverted bathymetry models, the model with the lowest score is retained.

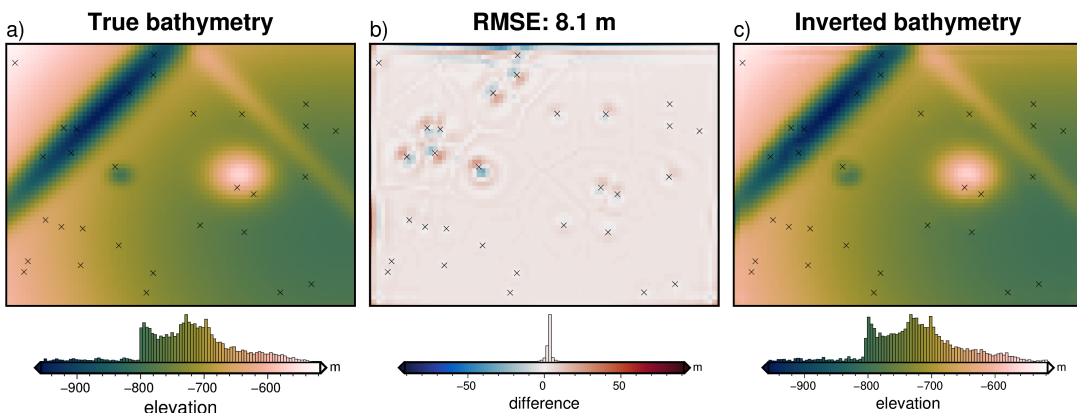


Figure 3.8: Inverted results with optimized parameters, using the annulus approximation method of calculating the Jacobian matrix. a) True bathymetry, b) difference between a and c, and c) final inverted bathymetry. Black crosses are constraint points. The RMS difference with the true bathymetry at these constraints is 1 m

1520 This model is shown in Figure 3.8c, and resulted from a damping value of 10^{-2} .
 1521 This inverted bathymetry has an RMS difference with the true bathymetry of 8 m
 1522 and an RMS difference at the constraint points of 1 m. Figure 3.9b shows a profile
 1523 across the model. The overlap of the true (red) and inverted (blue) bathymetry in the
 1524 first panel shows the effectiveness of the inversion at recovering the true bathymetry.
 1525 The lower panel shows the inversion's ability to minimize the misfit between the
 1526 observed gravity (red) and the forward response of the inverted bathymetry (blue).
 1527 The inversion was able to recover all the features of the true bathymetry, with only
 1528 minor errors along the edges of the domain, and adjacent to constraint points. For
 1529 this simple model, the inversion converged in 37 iterations, with a total computation
 1530 time of 30 seconds and a final RMS residual misfit of 0.022 mGal. It terminated due
 1531 to the ℓ^2 -norm decreasing between the set threshold of 0.15 (0.0225 mGal).

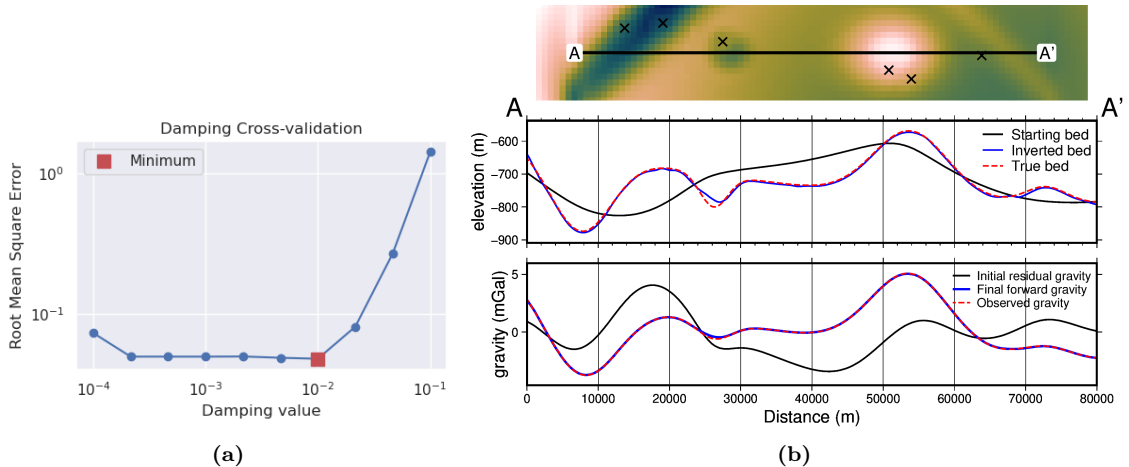


Figure 3.9: Cross-validation and profiles for the simple synthetic inversion. **a)** Cross-validation curve showing the optimal damping parameter (red square). Both axes are on a logarithmic scale. **b)** 2D profile of the inversion results. The top panel shows profile location and constraint points (black crosses). The middle panel contains topographic profiles of the starting, inverted, and true bathymetries. The bottom panel contains gravity anomaly profiles.

1532 3.3.1.3 Comparing vertical derivative methods

1533 Section 3.2.5.1 presented two methods for calculating the vertical derivative of gravity
 1534 of a prism. This vertical derivative is used to create the Jacobian matrix (Equation
 1535 3.9) and needs to be calculated at each iteration of the inversion. The above
 1536 cross-validation and inversion were performed using the *annulus approximation* of
 1537 the vertical derivative. Here, this process is repeated with the *finite differences*
 1538 method of the vertical derivative. Figure 3.10) shows the results of this inversion.
 1539 The optimal damping parameter was 10^{-2} , and the inversion resulted in an RMS
 1540 difference with the true bathymetry of 9 m, compared to 8 m for the annulus ap-
 1541 proximation. Figure 3.11 shows the inversion convergence curves for the inversion of
 1542 the annulus approximation and the finite differences methods. The inversion with
 1543 the annulus approximation was $\sim 500\%$ faster to converge than the finite differences
 1544 method (30 sec vs 169 sec). Because these vertical derivatives need to be recalcul-
 1545 ated at each iteration, a large portion of the inversion time is spent performing
 1546 these calculations. This comparison shows the annulus approximation is not only
 1547 significantly faster, but results in comparable, or slightly more accurate, inversion
 1548 results. For the remainder of this chapter, only the annulus approximation will be
 1549 used.

1550 3.3.1.4 Added noise

1551 To test the effect of noise in the gravity data, which is inevitable in data collection,
 1552 especially so in airborne surveying, the observed gravity was contaminated with
 1553 noise. The noise has a Gaussian distribution with a mean of 0 mGal and a standard
 1554 deviation of 2% of the max absolute value of the data ($\sim .16$ mGal). Similarly,
 1555 Rashidifard et al. (2021) used 5% noise in their synthetic gravity inversion while
 1556 Uieda and Barbosa (2017) use 5 mGal of noise, which for their synthetic application
 1557 equated to $\sim 1\%$ of the max absolute value. Using this noise-corrupted gravity data,
 1558 the same damping parameter cross-validation was run as previously (Figure 3.13a),
 1559 and the lowest score was achieved with a damping value of 10^{-2} . Figure 3.12 shows
 1560 the inversion results of this noise-contaminated model. The inversion converged in

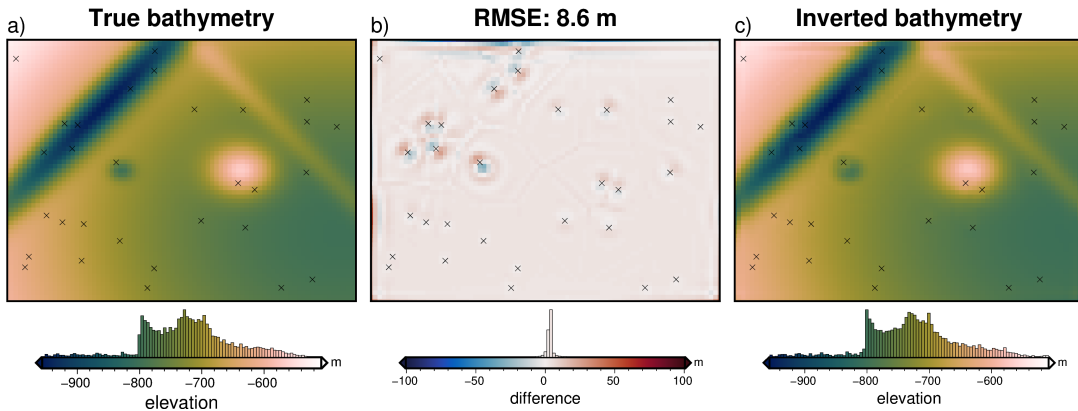


Figure 3.10: Inversion results with optimized parameters using the finite differences method. **a)** True bathymetry, **b)** difference between a and c, and **c)** final inverted bathymetry. Black crosses are constraint points. The RMS difference with the true bathymetry at these constraints is 1 m

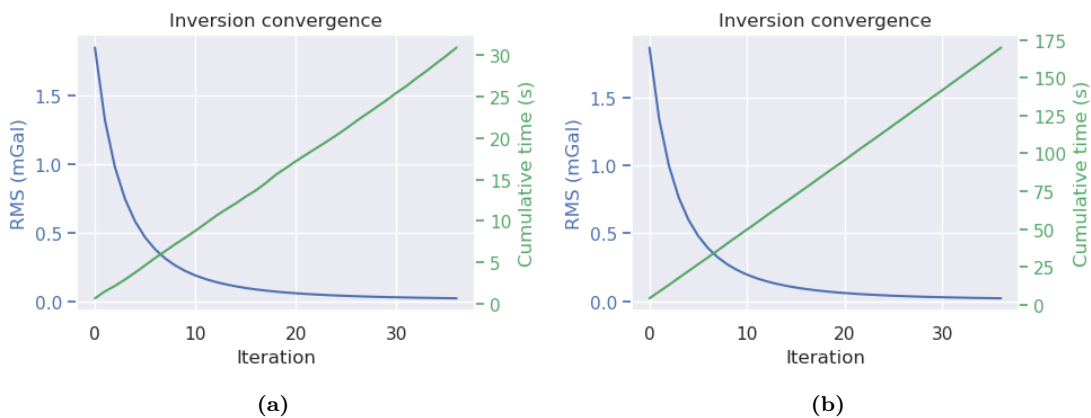


Figure 3.11: Inversion convergence curves for the two methods of creating the Jacobian matrix. Blue line (left y-axis) shows the RMS of the residual misfit at each iteration of the inversion. Green line (right y-axis) shows the cumulative time to complete the inversion. **a)** Results for the annulus approximation method of finding the vertical derivative. **b)** Results for the finite differences method.

1561 18 iterations, with a total computation time of 13 seconds and a final RMS residual
 1562 misfit of 0.16 mGal. It terminated after the ℓ^2 -norm became lower than the set
 1563 tolerance of 0.4 (0.16 mGal). This tolerance was set to match the known level
 1564 of noise. The inverted bathymetry had an RMS difference of 12 m with the true
 1565 bathymetry and an RMS difference of < 1 m at the constraint points. Figure 3.13b
 1566 shows the inversion is still able to reproduce the observed gravity (lower panel), but
 1567 a component of the noise was introduced into the final bathymetry (upper panel).
 1568 All major features of the true bathymetry are recovered, albeit not as accurately as
 1569 the no-noise model (Figure 3.8).

1570 3.3.1.5 Down-sampled data

1571 The previous two models used observed gravity data collected on a grid of observa-
 1572 tion points at the same grid spacing as the prism layer (1 km). This represents a
 1573 very dense gravity survey. Gravity surveys are often relatively sparse compared to
 1574 the resolution of the surface they are attempting to recover in an inversion. This
 1575 section tests the effect of changing the resolution of the gravity data, to simulate
 1576 a coarser gravity survey. Simply sampling the gravity data at a coarser resolution

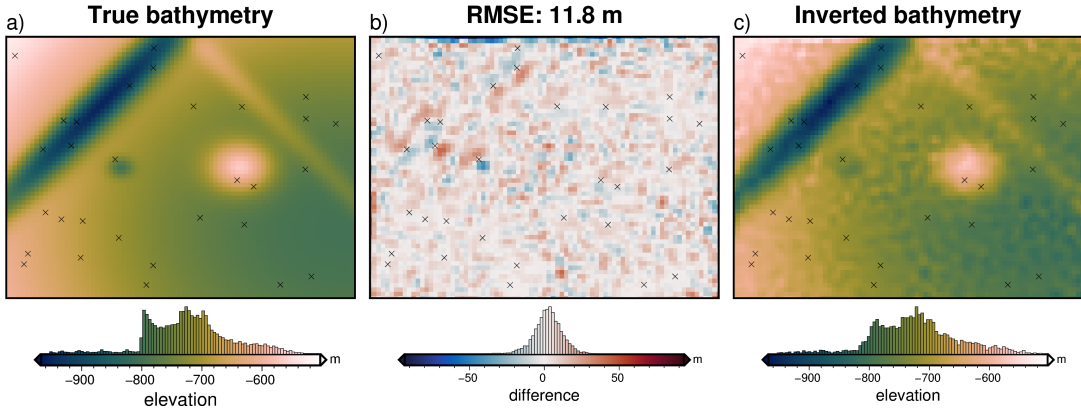


Figure 3.12: Simple synthetic model inversion results with 2% added noise (0.16 mGal). **a)** True bathymetry, **b)** difference between a and c, **c)** final inverted bathymetry. Black crosses are constraint points. The RMS difference with the true bathymetry at these constraints is < 1 m.

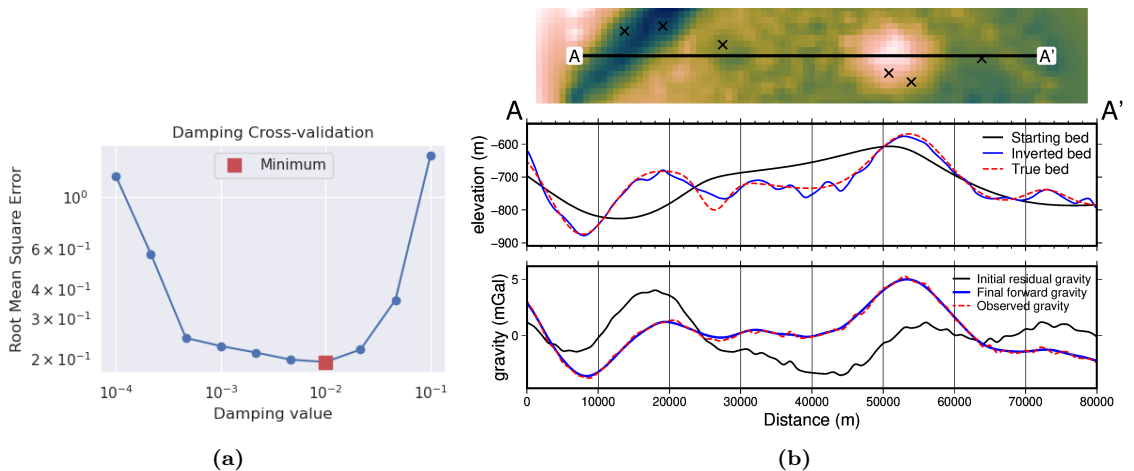


Figure 3.13: Cross-validation and profiles for the inversion with noise. **a)** Cross-validation curve showing the optimal damping parameter (red square). **b)** 2D profile of the inversion results. The top panel shows profile location and constraint points (black crosses). The middle panel contains topographic profiles of the starting, inverted, and true bathymetries. The bottom panel contains gravity anomaly profiles.

leads to a checker-boarding effect, where the inversion alters prisms nearby the gravity observations, but not prisms further away. For this reason, it is recommended here to re-grid the observed gravity data at a similar grid spacing to the prism layer. This can be accomplished with standard gridding techniques, such as minimum curvature or bi-harmonic splines (see section 3.4.2). However, these techniques aren't well suited for potential field data since they don't account for the variation in observation heights (Soler & Uieda, 2021). An alternative method of interpolating the gravity data onto a finer resolution grid is the equivalent sources technique (Dampney, 1969)¹.

1586

1587 Here, the original gravity data, on a 1 km grid, is sampled at a 6 km spaced grid
 1588 to represent a low-resolution survey with observations every 6 km. A series of point
 1589 sources are created at depth, and their densities are altered to best reproduce the
 1590 observed gravity data. Once this process of fitting the source parameters to the data

¹The equivalent sources technique is also used in this study as a means of regional separation (see section 3.2.4, this is a similar application but for different purposes).

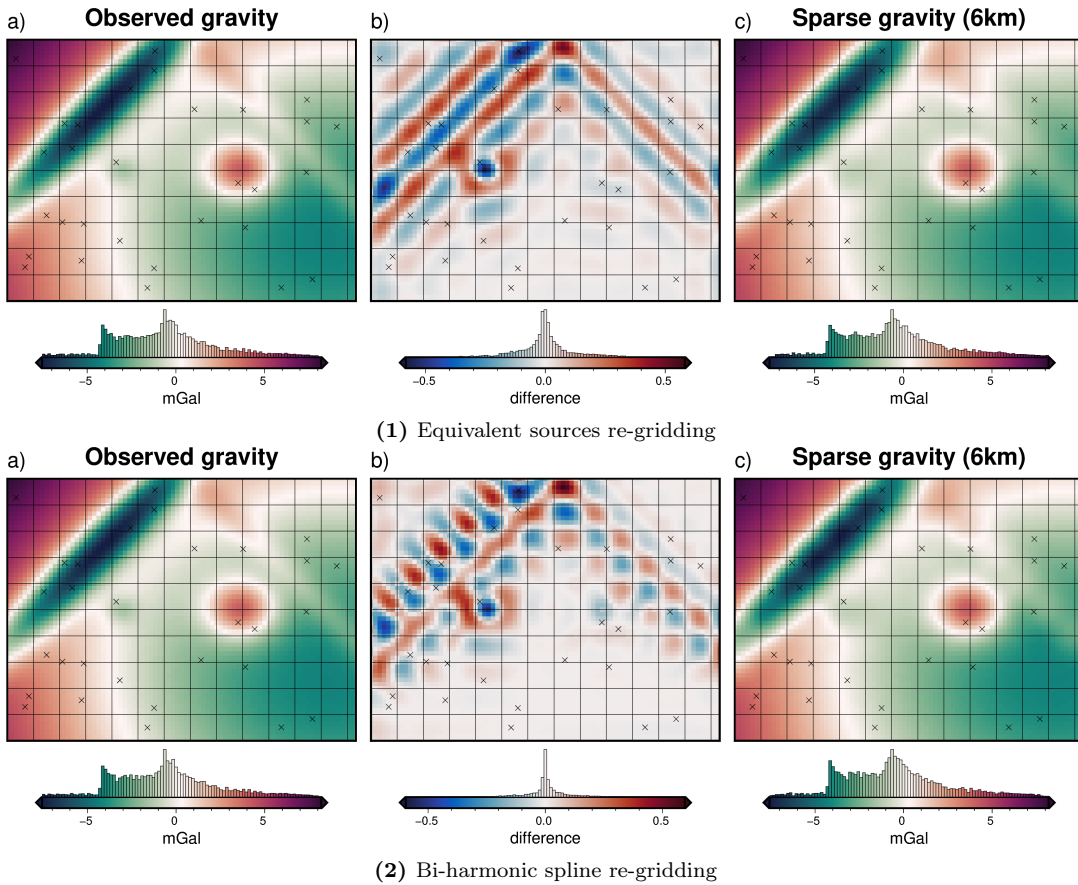


Figure 3.14: Creating a low-resolution observed gravity survey. **Top panel** shows results using the equivalent source technique of gridding gravity data. **Bottom panel** shows simple gridding using a bi-harmonic spline. **a)** Original observed data on a 1 km grid, **b)** gravity signal lost due to sampling and re-gridding, **c)** the low-resolution observed gravity (6 km spacing) re-gridded at 1 km with either equivalent sources (top) or a regular gridding algorithm (bottom). Black crosses show constraint points and black lines show 6 km grid.

is accomplished, the gravity field can be predicted anywhere. For this application, the equivalent sources are predicted onto an even 1 km grid, to match the spacing of the bathymetry. Figure 3.14 shows the results of this process (top panel) and the results using a simple gridding without equivalent sources (bottom panel). *Subplot a* shows the original observed gravity data (just training points) on a 1 km grid. This grid is sampled onto a 6 km grid (black grid lines) and re-gridded at 1 km (*subplot c*). *Subplot b* shows the difference, which represents the lost data resulting from the sparse survey. Typically the equivalent sources gridding technique is most beneficial to account for variations in observation heights. Here, even with constant elevations, there are noticeable differences between equivalent source gridding and simple gridding with bi-harmonic splines.

The equivalent-source resampled grid is used, with no added noise, in the same inversion procedure as the previous sections. The cross-validation (Figure 3.16a) resulted in an optimal damping value of 10^{-2} . The inverted bathymetry with this damping value is shown in Figure 3.15. The inversion was completed in 29 seconds and 38 iterations with a final RMS residual misfit of 0.019 mGal. The inversion was terminated due to the ℓ^2 -norm decreasing below the set threshold of $0.15 \text{ mGal}^{1/2}$. The inverted bathymetry had an RMS difference of 11 m with the true bathymetry

and an RMS difference of 1 m at the constraint points. While the overall difference from the true bathymetry is low, this inversion failed to fully recover the small circular depression. Figure 3.14 shows that the nearest observation point (intersection of gridlines) was on either side of this anomaly, and thus the sparse gravity survey used here failed to image the true magnitude of the feature. Figure 3.15b shows the absence of this feature in the inverted bathymetry.

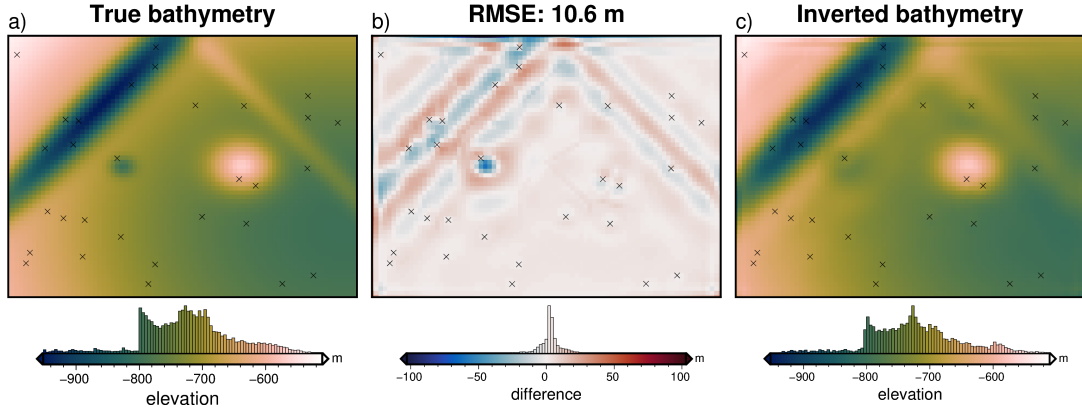


Figure 3.15: Simple synthetic model inversion results with input data resampled at 6x the bathymetry grid spacing (6 km). **a)** True bathymetry, **b)** difference between a and c, and **c)** final inverted bathymetry. Black crosses show constraint points. The RMS difference with the true bathymetry at these constraints is 1 m.

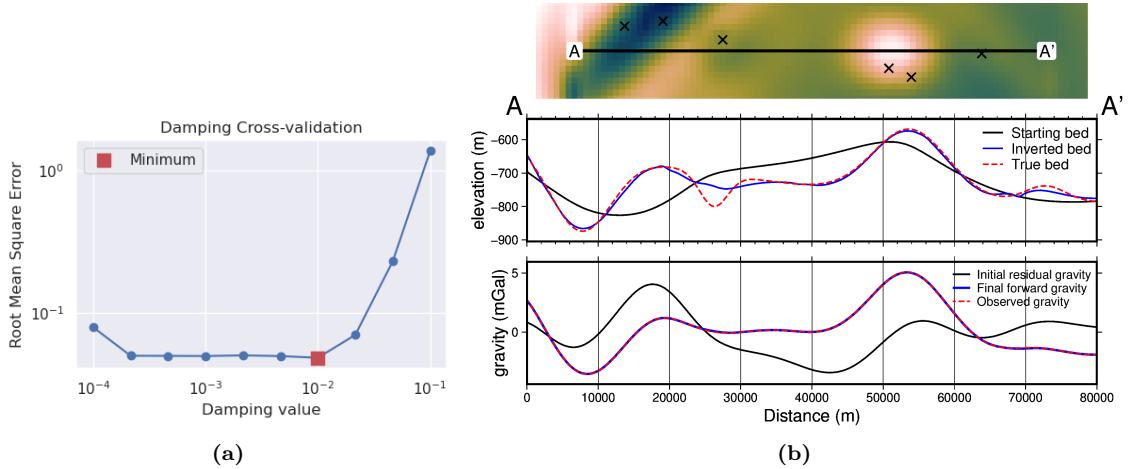


Figure 3.16: Cross-validation and profiles for the 6 km resampled inversion. **a)** Cross-validation curve showing the optimal damping parameter. **b)** 2D profile of the inversion results. The top panel shows profile location and constraint points (black crosses). The middle panel contains topographic profiles of the starting, inverted, and true bathymetries. The bottom panel contains gravity anomaly profiles.

3.3.2 Ensemble of Noise and Sampling values

To test the relative importance of the level of noise and the resolution of the gravity data (i.e. station/flight line spacing), an ensemble of 100 inversions was run, with 10 noise levels between 0 and 9%, and 10 gravity resolutions between 1 and 10 km. The noise level percentages are of the maximum absolute value of the data, equating to 10 levels between 0 and 0.85 mGal. The differing gravity resolutions were created with the sampling and re-gridding of equivalent sources outlined in the above section.

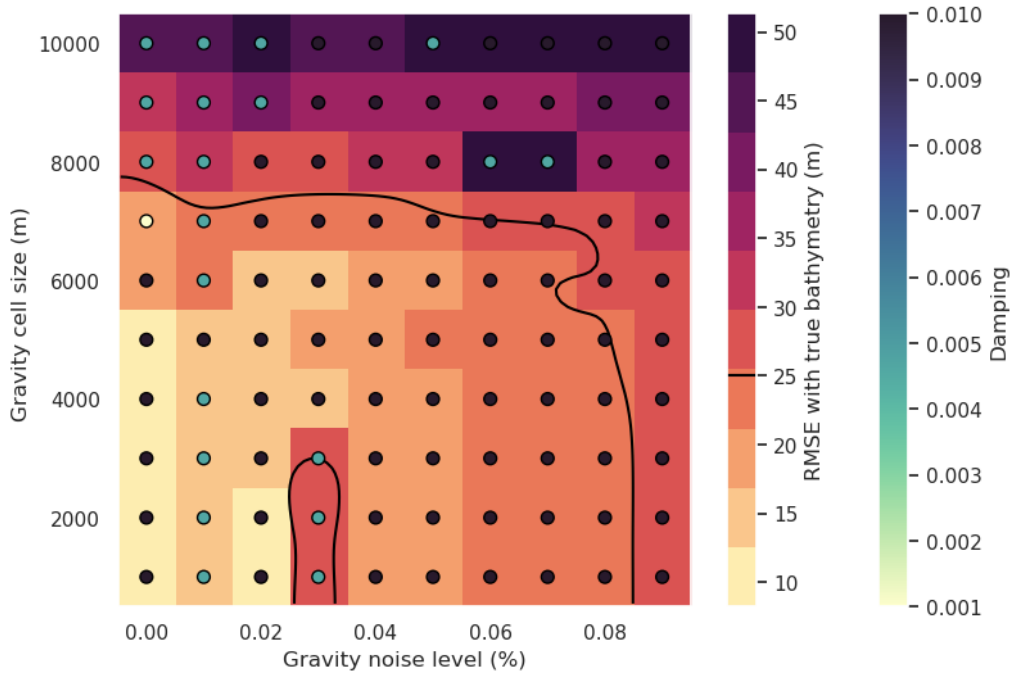


Figure 3.17: Ensemble of noise levels and gravity spacing for the simple synthetic model. Grid cell color indicates each inversion's RMS difference with the true bathymetry. Circles' color indicates the optimal damping value found for each inversion's cross-validation. Black line shows the 25 m RMSE contour, indicative of the amplitude of the smallest amplitude features.

For each set of noise and spacing values, the cross-validation routine was used to find the optimal damping parameters and associated inverted bathymetries. Each of these 100 inversions were then compared to the true bathymetry yielding an RMS difference for each.

Figure 3.17 shows the results of this ensemble of inversion. Each grid cell represents a single inversion, with the level of noise and gravity resolution for the inversion indicated by the x and y axis, respectively. The background color (warm colors) indicates each inversion's resulting RMS difference with the true bathymetry. Colored circles show the optimal damping value for each inversion found through cross-validation. This shows a general decrease in the inversion's accuracy with either more noise or lower-resolution gravity data. The smallest bathymetric features which this inversion ideally should recover have amplitudes of tens of meters (small circular depression and narrow ridge). The RMSE here indicates a base-level of error in the inversions, while the error in the vicinity of the short wavelength bathymetry features is likely higher (Figure 3.15b). Inversions with RMSEs of 10's of meters will likely fail to resolve these small features. For this inversion, an RMSE of 25 m (black contour in Figure 3.17) approximately equates to a gravity observation spacing greater than 8 times the prism layer spacing, and a noise level higher than 8% of the survey's max absolute value.

3.4 Adding a regional component

Now that the inversion has been demonstrated to adequately recover bathymetry with various levels of noise and resolutions of the input gravity data, an additional complexity is added. This complexity is a regional component of the observed

gravity field. To account for this, the inversion remains the same, but the regional component of the gravity misfit must be removed beforehand (Equation 3.10). In this section, first, the four methods of regional separation laid out in 3.2.4 are compared. Next, one of these methods, constraint point minimization, is further investigated. Lastly, the effects of noise and gravity survey spacing are explored.

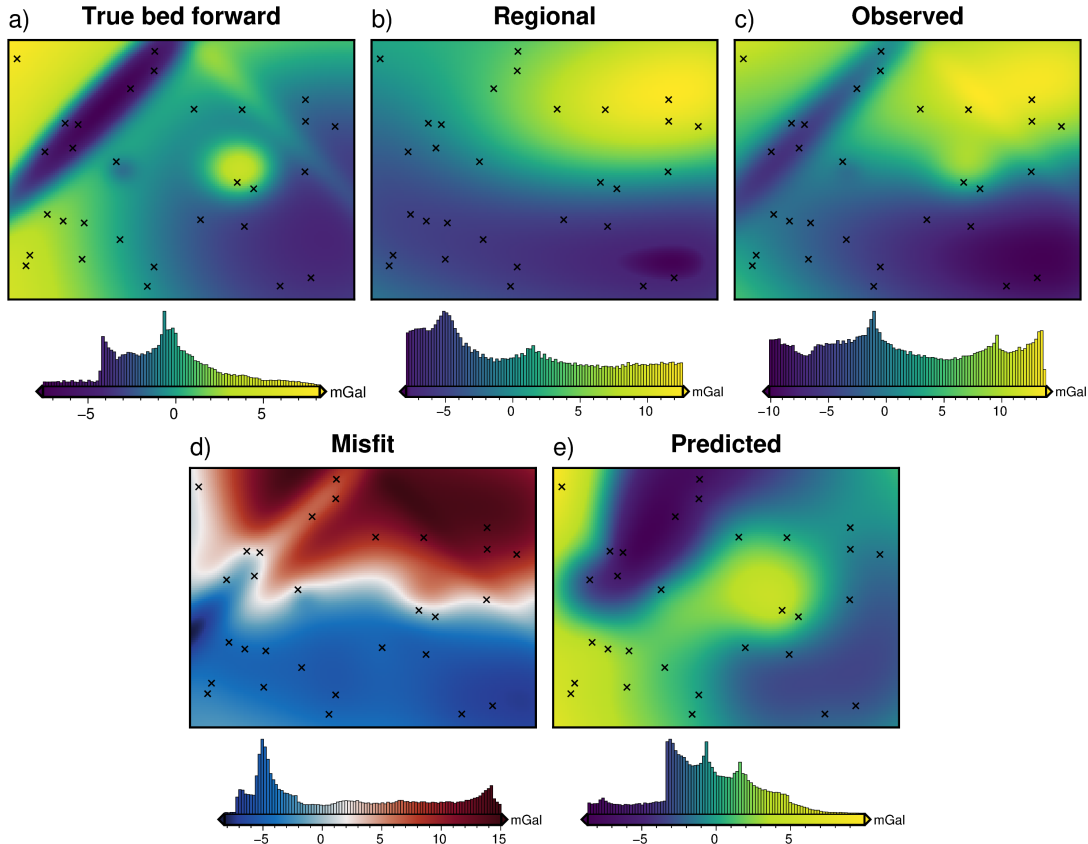


Figure 3.18: Gravity components and anomalies for the simple synthetic model with the addition of a regional field. **a)** the forward gravity of the true bathymetry, **b)** the regional component of gravity, **c)** the observed gravity from the combination of a and b, **d)** the gravity misfit from the difference between c and e, and **e)** the predicted gravity from the forward calculation of the starting bathymetry.

This model uses the same starting bathymetry (Figure 3.6) as the previous section, but the observed gravity includes a regional field, which represents the portion of observed gravity signal resulting from unknown crustal sources, such as anomalous bodies or crustal thickness variations. This component (Figure 3.18b) is calculated from a synthetic topography with a median elevation of -4300 m and a density contrast of 700 kg m^{-3} . Its range of gravity values is set to be the dominant signal in the observed gravity, but not large enough to fully mask the signal of the bathymetry signal. Figure 3.18 shows the various components of the gravity and resulting misfit for this model.

3.4.1 Regional separation methods

The four methods of regional separation discussed in section 3.2.4 each have at least one hyper-parameter which affects their calculation of the regional field. For each method these include

1. Low-pass filter: the distance width of the Gaussian filter.

- 1665 2. Trend removal: the degree of the polynomial trend fit to the misfit.
- 1666 3. Equivalent source prediction: the depth and damping parameters of fitting
1667 sources to the data (Soler & Uieda, 2021).
- 1668 4. Constraint point minimization: parameters for the associated gridding method,
1669 such as the tension factor for minimum curvature gridding (Smith & Wessel,
1670 1990) or the minimum distance and damping parameter for bi-harmonic spline
1671 gridding (Uieda, 2018).

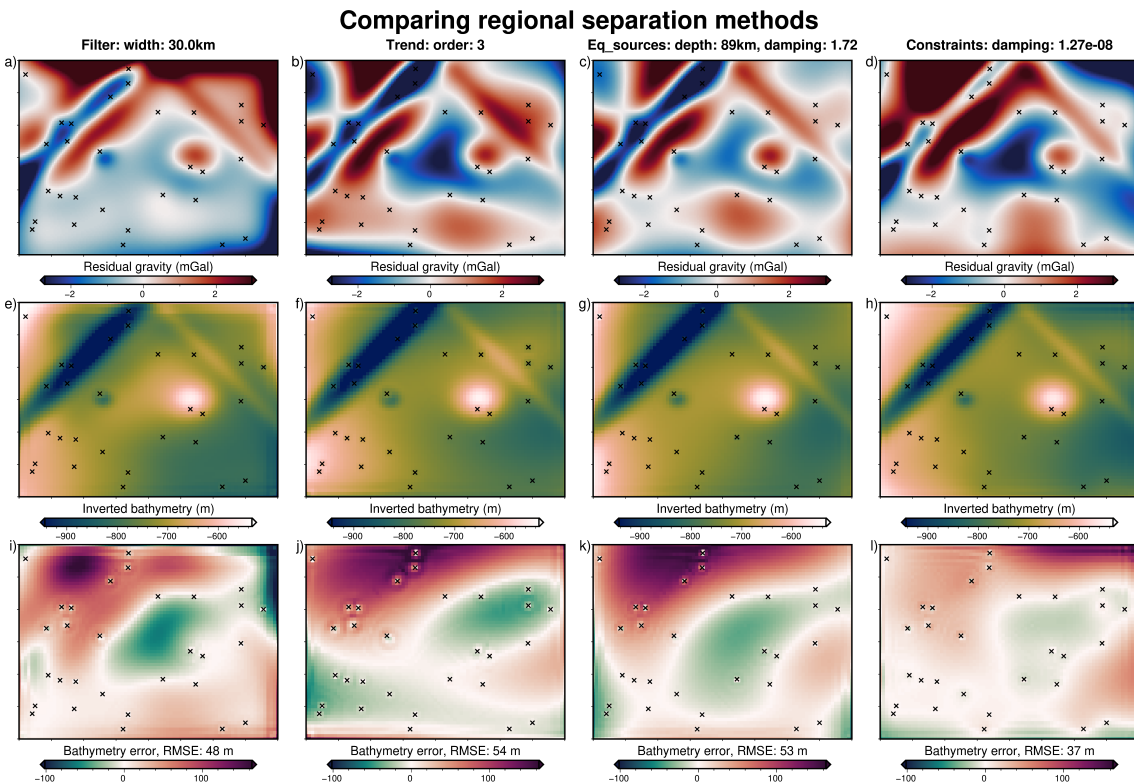


Figure 3.19: Comparison of inversions with 4 regional separation methods. First row (**a-d**) shows residual gravity misfit after regional separation. Second row (**e-h**) shows the inverted bathymetry for each method. Third row (**i-l**) shows the error of the inverted bathymetries with the true bathymetry. Constraint points are shown as black crosses. Colormaps are identical for each row. Profiles of these data are shown in Figure B.1 of Appendix B.

1672 Since for this synthetic model, the true regional field is known (Figure 3.18b), the
1673 effect of the parameters associated with each of the four methods can be explored.
1674 Excluding the constraint point minimization method, an optimization is run for
1675 each method, with the goal of finding the parameter values which minimize the RMS
1676 difference between the true and calculated regional gravity. Each optimization has 20
1677 trials. The constraint point minimization doesn't require optimization because the
1678 various gridding parameters won't significantly affect the RMS difference between
1679 the resulting regional field and the true field. However, the gridding parameters will
1680 affect the inversion itself; this is explored in the next section. For this comparison
1681 of the regional removal method, the constraint point minimization method uses bi-
1682 harmonic spline gridding, and the gridding damping parameter is chosen with a
1683 cross-validation (Uieda, 2018). The best regional field (lowest RMS with the true
1684 regional field) of each method was found with the following parameters:

- 1685 1. a 30 km filter width for the low pass filter method
- 1686 2. a 3rd order trend for the trend removal method
- 1687 3. source depth of 89 km and a damping value of 1.72 for the equivalent source
1688 technique
- 1689 4. an interpolator damping of 1.27×10^{-8} for the bi-harmonic spline interpolator
1690 of the constraint point minimization method.

1691 Each of these regional fields were then removed from the gravity misfit, producing
1692 the residual anomalies (Figure 3.19a-d). These resulting residuals were then input
1693 into an inversion, resulting in the inverted bathymetries of d-h of Figure 3.19, and the
1694 bathymetry error relative to the true bathymetry was found (Figure 3.19i-l). For
1695 these inversions, the same damping parameter cross-validation was conducted, as
1696 described in Section 3.3.1.2. This comparison of regional separation methods shows
1697 that the constraint point minimization method (Figure 3.19l) produces the best
1698 inverted bathymetry, both visually (Figure 3.19h), and based on the RMS difference
1699 with the true bathymetry (37 m). Figure B.1 in Appendix B shows a profile of
1700 the resulting regional fields and inverted bathymetries of these various methods of
1701 regional separation. The remainder of this section further examines the constraint
1702 point minimization method of regional separation.

1703 3.4.2 Constraint point minimization

1704 The constraint point minimization method assumes that at locations of known
1705 bathymetry there is no residual component of gravity misfit, and the regional com-
1706 ponent entirely equals the misfit. To implement this, misfit values at the constraints
1707 are sampled and used to create a region-wide grid of regional values. This grid is
1708 then removed from the misfit to get the residual misfit (Equation 3.10). This grid-
1709 ding can be accomplished by many techniques, which at an initial inspection appear
1710 to produce similar results. Here, two methods of gridding and their gridding param-
1711 eters are compared, and the impact on the inverted bathymetry are shown. These
1712 gridding methods are tensioned minimum curvature (Smith & Wessel, 1990) and
1713 bi-harmonic splines (Sandwell, 1987).

1714 3.4.2.1 Tensioned minimum curvature

1715 Tensioned minimum curvature gridding is a commonly used technique for gridding
1716 sparse data which fits the smoothest possible surface while still matching the data
1717 (Wessel & Bercovici, 1998). It allows variation in the location of maximum cur-
1718 vature through the tension factor parameter. A tension factor of 0 results in the
1719 minimum curvature solution (maxima and minima allowed anywhere), while a value
1720 of 1 localizes the curvature at the data points (maxima or minima only allowed at
1721 the data points) (Smith & Wessel, 1990). A tension of 0.25 is suggested for poten-
1722 tial field data (Wessel et al., 2019). Tensioned minimum curvature has been used in
1723 several bathymetric inversions for constraint point minimization (An et al., 2019a;
1724 Millan et al., 2020; Yang et al., 2021).

1725 **3.4.2.2 Bi-harmonic splines**

1726 The second method of gridding the sampled gravity misfit values uses bi-harmonic
 1727 splines. This method uses Green's functions and a least squares fit to the data
 1728 (Sandwell, 1987). Computation time for this technique is approximately propor-
 1729 tional to the cube of the number of data, making it computationally expensive for
 1730 large datasets (Deng & Tang, 2011). There is a damping parameter value that can
 1731 be adjusted, to smooth the resulting interpolation. As implemented in the *SplineCV*
 1732 class of the Python package Verde (Uieda, 2018), automated cross-validation of the
 1733 data can be used to identify the damping value which best predicts the data. Once
 1734 the parameter is determined, and the data is interpolated, the interpolation can be
 1735 predicted at any location, such as on the nodes of a uniform grid.

1736

1737 Despite its slow run time with large datasets, bi-harmonic spline gridding has
 1738 several advantages over tensioned minimum curvature gridding. It allows the in-
 1739 corporation of data uncertainties into the fitting via a weighting parameter. With
 1740 the use of cross-validation, there are no subjective parameters that can significantly
 1741 alter the results. Lastly, the predicted data don't need to be on a regular grid,
 1742 which is useful for irregularly shaped domains that don't adhere to a rectangular
 1743 region. In their bathymetry inversion, Millan et al. (2020) point out features in their
 1744 inverted bathymetry which likely result from the minimum curvature gridding tech-
 1745 nique. Apart from this, there appears to be little work related the how the gridding
 1746 procedure affects this aspect of a bathymetry inversion.

1747 **3.4.2.3 Gridding comparison**

1748 In this section, the effect which the gridding process has on the inverted bathymetry
 1749 is analyzed. Four sets of regional separations were conducted, three using the ten-
 1750 sioned minimum curvature technique, and one using the bi-harmonic spline tech-
 1751 nique. For the three minimum curvature separations, the tension factors used were
 1752 the end members, 0 and 1, and the suggested value for geopotential data, 0.25.
 1753 For the bi-harmonic spline, a cross-validation with 20 varying damping values was
 1754 conducted, and the best resulting damping value was used. For each of the four
 1755 calculated regional fields, the resulting residual fields (Figure 3.20a-d) were used as
 1756 inputs to an inversion. All four residual anomaly data were included in an inversion
 1757 damping parameter cross-validation, as described in Section 3.3.1.2. The difference
 1758 between the resulting inverted bathymetry and the true bathymetry of each model
 1759 is shown in Figure 3.20i-l. To help visualize the difference in the resulting residual
 1760 grids, 3.20e-h shows the vertical derivative of the residual fields. This highlights that
 1761 while the residual values at the constraints are all similar, the slope of the residual
 1762 in the vicinity of the grids is strongly dependent on the gridding method ². Addi-
 1763 tionally, the minimum curvature gridding is shown, in subplots a-c, to create large
 1764 artificial anomalies away from constraint points (low values in upper right corners).
 1765 These gridding artifacts result in large errors in the resulting bathymetry 3.20i-
 1766 k. The bi-harmonic spline interpolator (last column in 3.20) is shown to produce a
 1767 residual field that adheres to the constraints, has smooth curvature near constraints,
 1768 and doesn't create large artificial anomalies. The effectiveness of this interpolator

²Note that the gridding process creates the regional field (not shown in Figure 3.20), which when subtracted from the total misfit gives the residual field. The residual grid is affected by these gridding effects through the removal of the regional field.

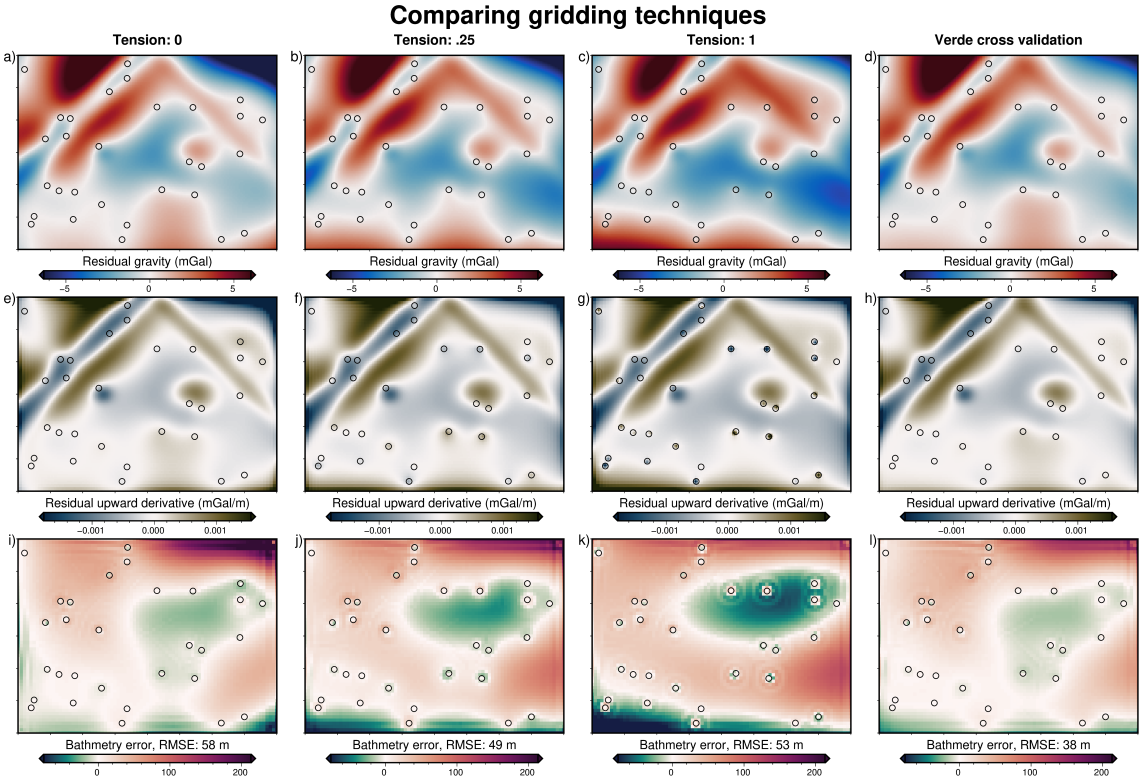


Figure 3.20: Comparison of gridding techniques for the constraint point minimization method of regional-residual separation. By sampling the misfit at constraints, and re-gridding over the entire domain, the regional component of the misfit is estimated. Gridding methods include minimum curvature gridding with tension factors of 0 (**column 1**), 0.25 (**column 2**), 1 (**column 3**), and cross-validated bi-harmonic spline gridding (**column 4**). Resulting gridded regional components were removed from the misfit grids to produce the residual grids (**a-d**). Second row (**e-h**) shows the vertical derivative of the residual, to highlight the gridding variations. Third row (**i-l**) shows the error of the inverted bathymetries with the true bathymetry. Constraint points are shown as open circles. Colormaps are identical across all columns. Profiles of these data are shown in Figure B.2 of Appendix B.

is confirmed by the low RMS difference between the inverted and true bathymetry (38 m). Figure B.2 in Appendix B shows a profile of the resulting regional fields and inverted bathymetries of these various gridding methods. With the bi-harmonic spline gridding techniques shown to be the most effective, the remainder of this chapter uses this gridding technique for the constraint point minimization method of regional separation.

3.4.3 Inversion results

Using the cross-validated bi-harmonic gridding method to separate the regional component of the gravity misfit, the resulting residual misfit was used in an inversion. The same gravity data cross-validation method of determining the optimal damping parameter is used (Figure 3.21). The optimal damping parameter was found to be $\sim 10^{-2.6}$. The resulting inversion is shown in Figure 3.22. The inverted bathymetry had an RMS difference with the true bathymetry of 37 m, and an RMS difference at the constraints of 2 m. The inversion was completed in 66 seconds, with 39 iterations and a final RMS residual of 0.022 mGal. The inversion was terminated due to the ℓ^2 -norm decreasing below the set threshold of $0.15 \text{ mGal}^{1/2}$. All four bathymetric features were recovered, but a lack of constraints in a few regions (the

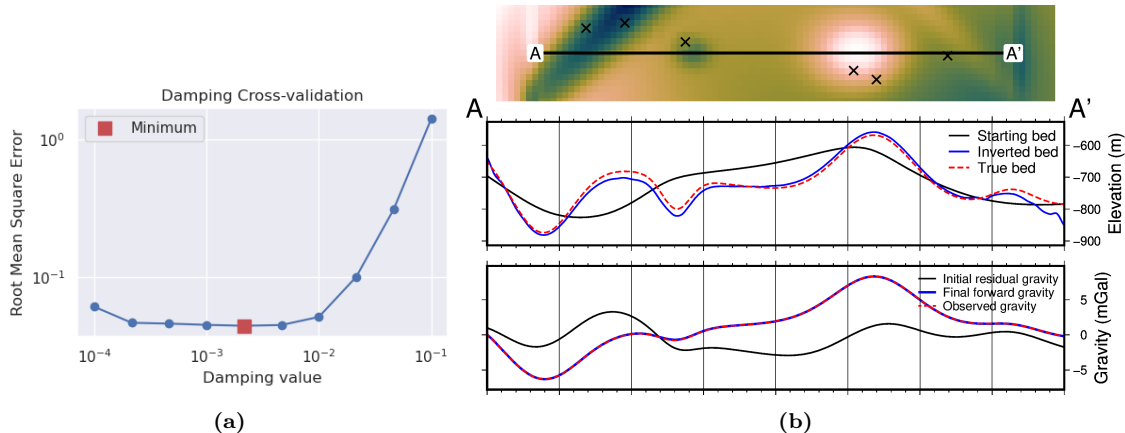


Figure 3.21: Cross-validation and profiles for the simple synthetic inversion with a regional component removed. **a)** Cross-validation curve showing the optimal damping parameter (red square). **b)** 2D profile of the inversion results. The top panel shows profile location and constraint points (black crosses). The middle panel contains topographic profiles of the starting, inverted, and true bathymetries. The bottom panel contains gravity anomaly profiles.

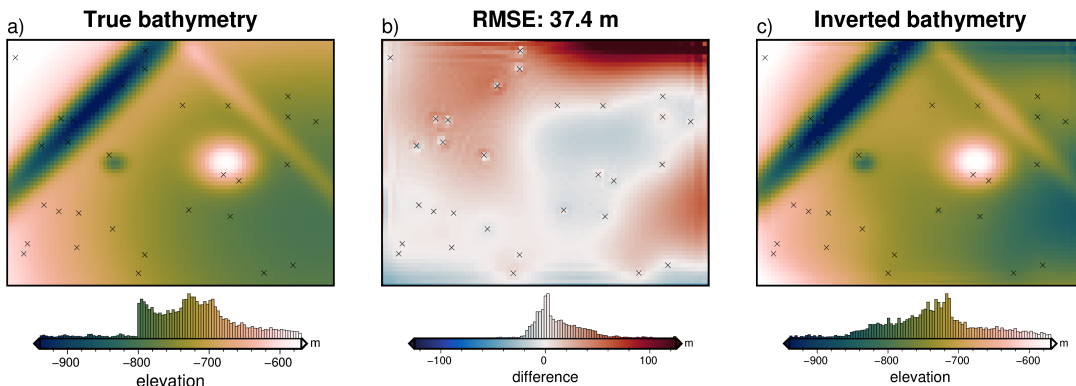


Figure 3.22: Simple synthetic model inversion with a removed regional component. **a)** True bathymetry, **b)** difference between a and c, **c)** final inverted bathymetry. Black crosses are constraint points. The RMS difference with the true bathymetry at these constraints is 2 m.

1786 upper-right corner) lead to a miscalculation of the regional field and a subsequent
1787 over-deepening of the bathymetry.

1788 The regional separation, parameter cross-validation, and inversion were repeated
1789 with additive noise and re-sampling of the gravity data to a coarser resolution (Ap-
1790 pendix B.1). As in section 3.3.2, this above workflow was also repeated for an
1791 ensemble of noise levels and gravity data grid spacings, as discussed next.

1792 3.4.4 Ensemble of Noise and Sampling values

1793 Following the method outlined in Section 3.3.2, an ensemble of 100 inversions with
1794 varying levels of noise and gravity observation spacings was conducted. The noise
1795 and gravity spacing changes were applied to the original observed data, and the
1796 forward calculation of the starting model, initial misfit calculation, and regional field
1797 removal were all repeated. Each model was then inverted with a cross-validation,
1798 and the resulting RMS differences with the true bathymetry are shown in Figure
1799 3.23.

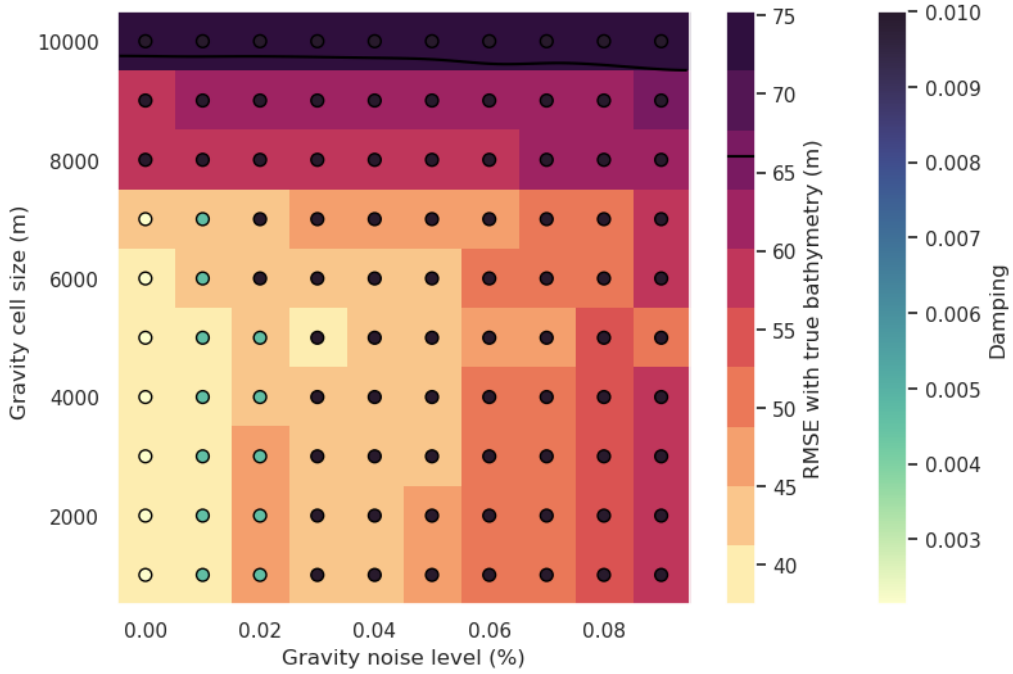


Figure 3.23: Ensemble of noise levels and gravity spacing for the simple synthetic model with a regional field. Grid cell color indicates each inversion’s RMSE with the true bathymetry. The circles’ color indicates the optimal damping value found for each inversion’s cross-validation. Black line shows the 66 m contour, representing the RMS difference between the true and starting bathymetry.

3.4.5 Simple model comparison

Table 3.4.5 compares the performance of each of the above inversions. The four inversions without a regional component of the gravity data (annulus approximation, prism approximation, with noise, and resampled), all recovered the bathymetry with an RMSE of ~ 10 m. With the regional component, the lowest RMS was raised to 37 m. The constraint point minimization method of regional separation produced significantly more accurate bathymetry models than the other methods. With these optimal methods and baseline performance standards, a new synthetic model is introduced which was created to emulate the expected bathymetry features and gravity anomalies associated with a sub-ice shelf environment.

Synthetic models statistics summary					
	RMS (m)	RMS at constraints (m)	Total time (hr:min:sec)	# iterations	Final residual RMS (mGal)
No regional component					
Starting bathymetry	66	0.04	—	—	2.7
annulus	8	1	00:00:30	37	0.022
finite differences	9	1	00:02:49	37	0.022
2% noise	12	< 1	00:00:13	18	0.16
6 km re-grid	11	1	00:00:29	38	0.019
With regional component					
Starting bathymetry	66	0.04	—	—	7.4
filter	48	—	—	—	—
trend	54	—	—	—	—
equivalent sources	53	—	—	—	—
constraint point minimization	37	2	00:01:06	39	0.022
2% noise	45	2	00:00:12	13	0.23
4 km re-grid	38	2	00:00:51	38	0.022

1810 3.5 Ross Sea model

1811 Here a semi-realistic model is introduced. In the past section, two synthetic topographies (bathymetry and a crustal layer) were used in forward modelling to
 1812 create synthetic gravity data. Here, real topographic data is used to create the synthetic gravity. This model is termed semi-realistic since the gravity is synthetically
 1813 calculated, but it results from geologically real surfaces. This model uses data from
 1814 Antarctica's Ross Sea (Figure 3.1, north of Ross Ice Shelf). The bathymetry data
 1815 is from the IBCSO v2 data compilation (Dorschel et al., 2022), resampled at a 5
 1816 km resolution (Figure 3.24a). This data is mostly from shipborne multi-beam echo
 1817 sounding. To create the regional component of gravity, basement depths from the
 1818 ANTOSTRAT compilation of shipborne seismic data have been used (Brancolini
 1819 et al., 1995), at a 5 km resolution (Figure 3.24b). The inversion domain is $320 \times$
 1820 420 km and a buffer zone of 40 km was included in all directions, resulting in 8000
 1821 grid cells per surface.
 1822

1823 3.5.1 Observed gravity

1824 The bathymetric and crustal surfaces were discretized with the reference discretization method (Figure 3.2e) with the mean elevation of each surface as its reference level. A density contrast of $\Delta\rho = 1276 \text{ kg m}^{-3}$ (contrast between seawater (1024 kg m^{-3}) and sediment (2300 kg m^{-3})), was used, with $+\Delta\rho$ for prisms above the reference, and $-\Delta\rho$ for prisms below the reference. For the basement, a density contrast of $\Delta\rho = 200 \text{ kg m}^{-3}$ was used, representing the contrast between sediment (2300 kg m^{-3}) and low-density basement rock (2500 kg m^{-3}). This contrast was set so that the resulting forward gravity of the basement was slightly greater in magnitude than that of the bathymetry. The forward gravity of each layer was calculated at a regular grid of observation points with a 5 km spacing, at a constant elevation of 1 km (Figure 3.24c-d). This created the full-resolution synthetic observed gravity dataset. To represent an airborne gravity survey, this grid is sampled along synthetic flight lines.

1825 This synthetic survey (Figure 3.25b) consisted of five N-S and 24 E-W flight lines.
 1826 Spacing between lines was 50 km for the N-S lines and 15 km for the E-W lines. One
 1827 N-S line and 3 E-W were omitted to represent missed flights. Along line spacing
 1828 of data was 5 km. This survey configuration is similar to other Antarctic airborne
 1829 surveys (Tinto et al., 2019). The full resolution gravity (Figure 3.25a) was sampled
 1830 at these flight line locations, and the resulting values were fitted with equivalent
 1831 sources. Gravity observations were then predicted from these sources on an even 5
 1832 km grid³ over the whole domain (Figure 3.25c). Lastly, the survey data was con-
 1833 taminated with noise from a Gaussian distribution, with a mean of 0 and a standard
 1834 deviation of 0.6 mGal (2% of the max absolute value of the full-resolution data).
 1835 The difference between the true gravity and this noise-contaminated synthetic sur-
 1836vey (Figure 3.25b) represents the typical loss of data resulting from a sparse airborne
 1837 survey. The RMS difference is 0.75 mGal. The largest differences are located within
 1838 the flight line data gaps.
 1839

³The gravity observations were actually interpolated onto a 2.5 km grid to account for the testing data.

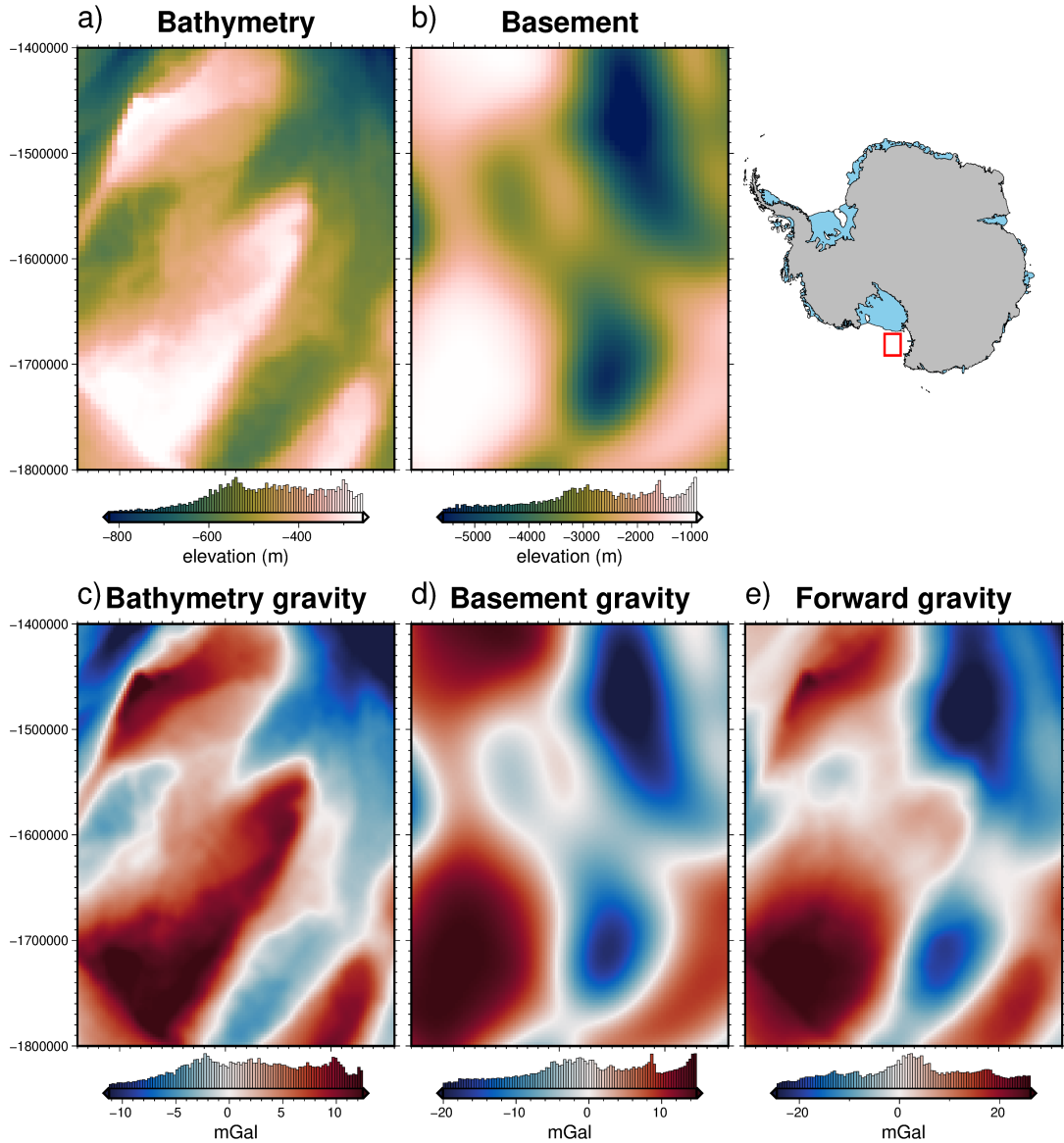


Figure 3.24: Ross Sea semi-synthetic model. **a)** Bathymetry data at 5 km resolution from IBCSO v2 (Dorschel et al., 2022), **b)** basement topography from the ANTOSTRAT project at 5 km resolution (Brancolini et al., 1995), **c)** forward gravity calculated at a regular 5 km grid at 1 km altitude for the bathymetry and **d)** for the basement. **e)** Total forward gravity from the combinations of c and d. Location of Ross Sea inversion domain shown as red box.

1854 3.5.2 Starting bathymetry

1855 The bed elevations around the borders of ice shelves are generally well-constrained.
 1856 Bathymetry depths from the open ocean portion of the ice shelf border can be
 1857 found through satellite altimetry or multi-beam sonar surveys. The remainder of
 1858 the ice shelf border consists of grounded ice. Bed elevations beneath grounded ice
 1859 can be efficiently imaged or modelled with methods such as airborne radar or mass-
 1860 conservation modelling (Morlighem et al., 2020). Many Antarctic ice shelves also
 1861 contain sparse direct measurements of bathymetry from seismic surveying. This re-
 1862 sulting configuration for many ice shelves is generalized by a very well-constrained
 1863 border with sparse constraints located within. Here, this configuration is mimicked
 1864 for a hypothetical ice shelf in the Ross Sea.

1865

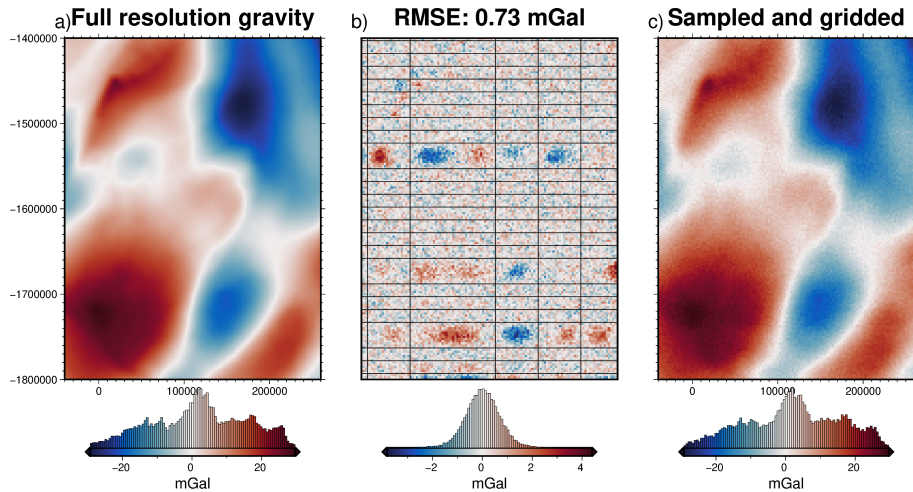


Figure 3.25: Ross Sea synthetic airborne survey. **a)** Full-resolution gravity data from the forward calculation of the bathymetry and basement. **b)** Difference between a and b, with black lines showing the synthetic airborne survey points. **c)** Gravity data from sampling along flight lines and re-gridded with equivalent sources.

Within the model domain, a polygon is created to represent the ice shelf border (Figure 3.26). Outside this border, constraint points are placed in each grid cell of the model ($N = 3503$, small black dots in Figure 3.26). Within the border, constraints are placed on a semi-regular grid. To represent a spatial constraint density similar to other Antarctic ice shelves⁴, 1 constraint per 2500 km^2 is used. This equates to 39 constraints. In the previous models, the true bathymetry was sampled at the constraints and the resulting values were gridded for the entire domain. Here, to represent measurement uncertainties for attaining the constraint point depths, after each point is sampled, Gaussian noise is added to the values before gridding.

1875

Points outside of the ice shelf are contaminated with noise from a Gaussian distribution with a standard deviation of 5 m. This represents the well-constrained methods associated with bed observations on either grounded ice or in the open ocean. Points within the shelf are contaminated with noise based on their depth. The Gaussian distribution used has a standard deviation of 2% of each point's depth. This simulates increasing measurement uncertainty with depth. Brisbourne et al. (2020) provide depth uncertainties for seismically imaged bathymetry beneath the Larsen C ice shelf, which have an average uncertainty as the percentage of depth from the surface of $\sim 2\%$. For our points, this equates to an RMS noise value of ~ 10 m for the ice shelf constraints. The uncertainty (the standard deviation of the Gaussian function used, not the actual value of the noise) of each point is shown in Figure 3.26a. This noise-contaminated sparse data is then gridded with a cross-validated bi-harmonic spline yielding the starting bathymetry. This interpolator takes the uncertainties of each point into account so that highly uncertain points don't introduce a bias into the interpolation (Uieda, 2018). The difference between the true and starting bathymetries had an RMS of 34 m over the whole grid, and an RMS at the constraint points of 10 m.

⁴The Ross Ice Shelf has ~ 1 constraint per 2200 km^2

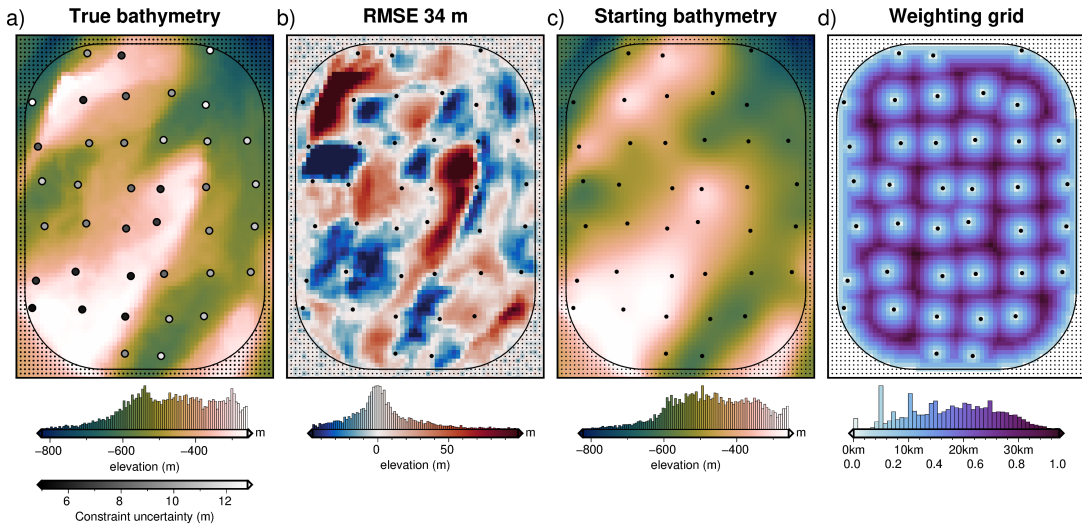


Figure 3.26: Gridding of the Ross Sea starting bathymetry. **a)** True bathymetry at 5 km resolution from the IBCSO v2 compilation (Dorschel et al., 2022). Constraint points (colored dots), show the uncertainty values of each point. These uncertainties were used as the standard deviations of the Gaussian function for contaminating the sampled data with noise before regridding. **b)** Difference between a and b, **c)** starting bathymetry from the sampling and gridding of the constraint points with added noise. **d)** Weighting grid used in the inversion. Grid colors show both the distance between each grid cell and the nearest constraint point and the weight values (0 - 1) from the normalization of these distances. Small black dots and large black dots indicate constraints outside and inside of the ice shelf border, respectively. Semi-rounded black line shows the outline of the synthetic ice shelf.

1893 3.5.3 Gravity misfit

1894 The starting bathymetry was discretized and forward modelled at the observation
 1895 points with a density contrast of 1276 kg m^{-3} . This forward gravity was then sub-
 1896 tracted from the observed gravity to get the gravity misfit (Figure 3.27a). Using
 1897 the constraint point minimization method, the regional field was estimated with a
 1898 bi-harmonic spline interpolator (Figure 3.27b), which was subsequently removed,
 1899 leaving the residual misfit (Figure 3.27c). As in the above section, the interpolator
 1900 takes the uncertainty of each constraint point into account to avoid overfitting the
 1901 regional field to highly-uncertain constraint points.

1902

1903 3.5.4 Inversion

1904 This residual misfit was then used in a cross-validation of 16 damping parameter
 1905 values (Figure 3.28a). The inversion with the lowest cross-validation score was then
 1906 chosen as the best model. During the inversions, a weighting grid was used to
 1907 constrain the bathymetry at the points of known depths(Section 3.2.5.3). This grid
 1908 (Figure 3.26d) is a normalized (0-1) grid of the minimum distance between each grid
 1909 cell and the nearest constraint point. The inversion result and the difference from
 1910 the true bathymetry are shown in Figure 3.29. The inversion had an RMS difference
 1911 with the true Ross Sea bathymetry of 21 m and an RMS at the constraints of < 1
 1912 m. The inversion converged in 12 seconds at 15 iterations and had a final residual
 1913 misfit of 0.43 mGal (Figure 3.28b).

1914

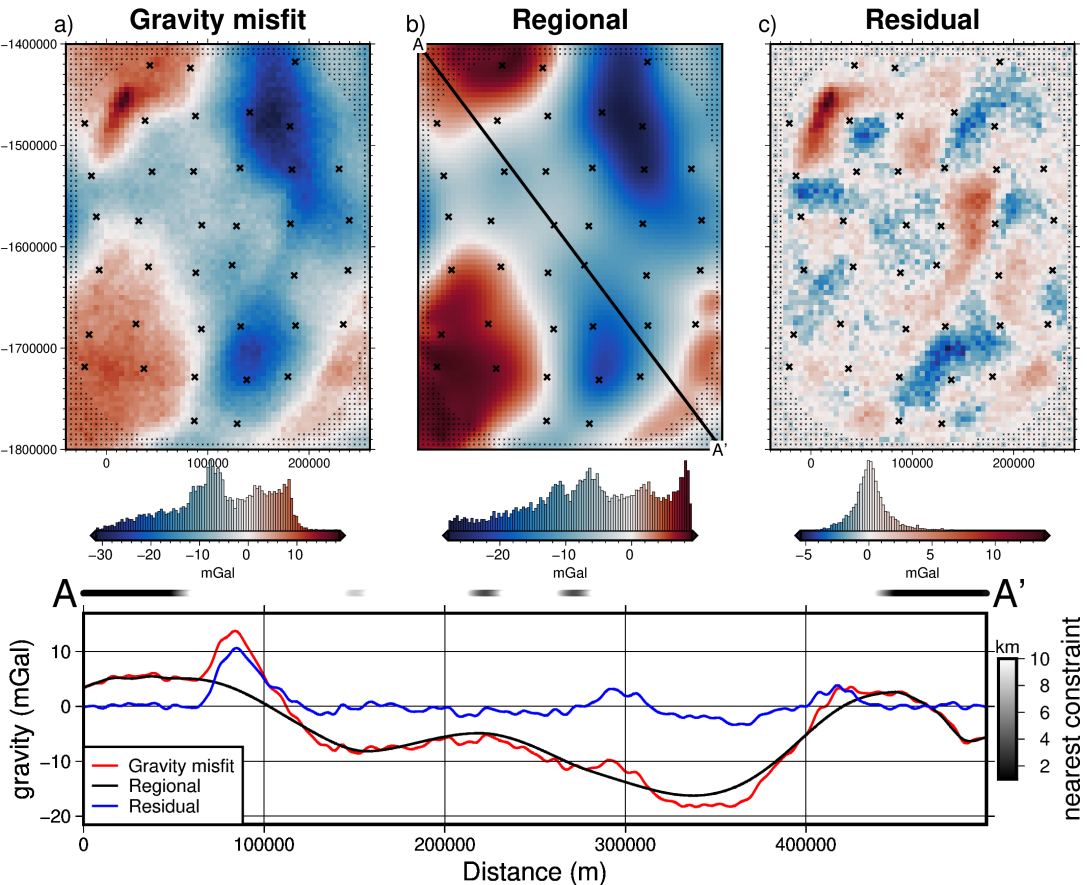


Figure 3.27: Ross Sea synthetic gravity anomalies. **a)** total gravity misfit, **b)** the estimated regional component using the constraint point minimization method, and **c)**, the residual misfit, as the difference between the total misfit and the regional component. Black crosses, large and small, show constraints inside and outside the ice shelf, respectively. **Lower panel** shows profile A to A' of gravity misfit and the regional and residual components. Distance to nearest constraint at each point along the profile shown in black to white colors at top of profile.

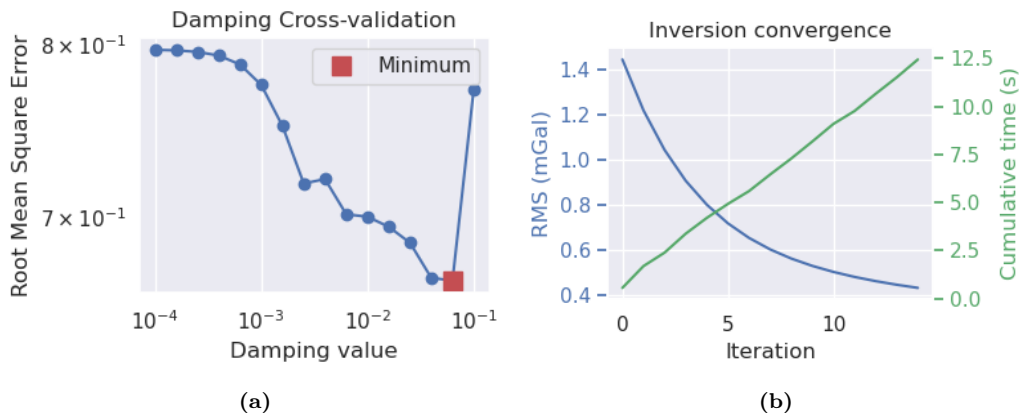


Figure 3.28: **a)** Cross-validation curve showing the optimal damping parameter (red square). **b)** Convergence of the inversion misfit. Blue line (left y-axis) shows the RMS of the residual misfit at each iteration of the inversion. Green line (right y-axis) shows the cumulative time to complete the inversion.

3.5.5 Uncertainty analysis

Since the true Ross Sea bathymetry for this inversion is known, a direct measurement of the spatial uncertainty of the resulting bathymetry is simple to calculate (Figure

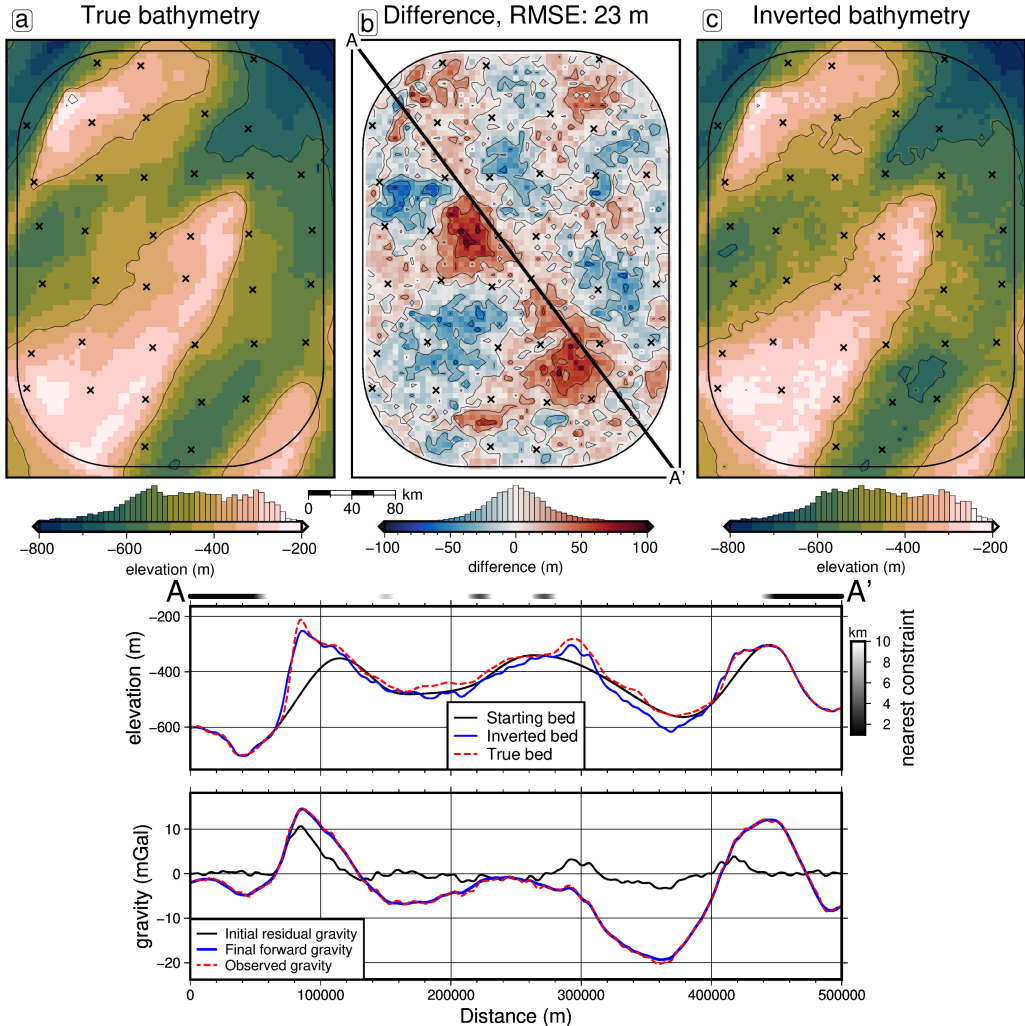


Figure 3.29: Ross Sea synthetic model inversion results. **a)** True bathymetry, **b)** difference between a and c, and **c)** final inverted bathymetry. Black crosses are constraint points. The RMS difference with the true bathymetry at these constraints is < 1 m. **Lower panel**) Profile from A to A'. The top panel contains topographic profiles of the starting, inverted, and true bathymetries. The bottom panel contains gravity anomaly profiles. Distance to nearest constraint at each point along the profile shown in black to white colors at top of profile.

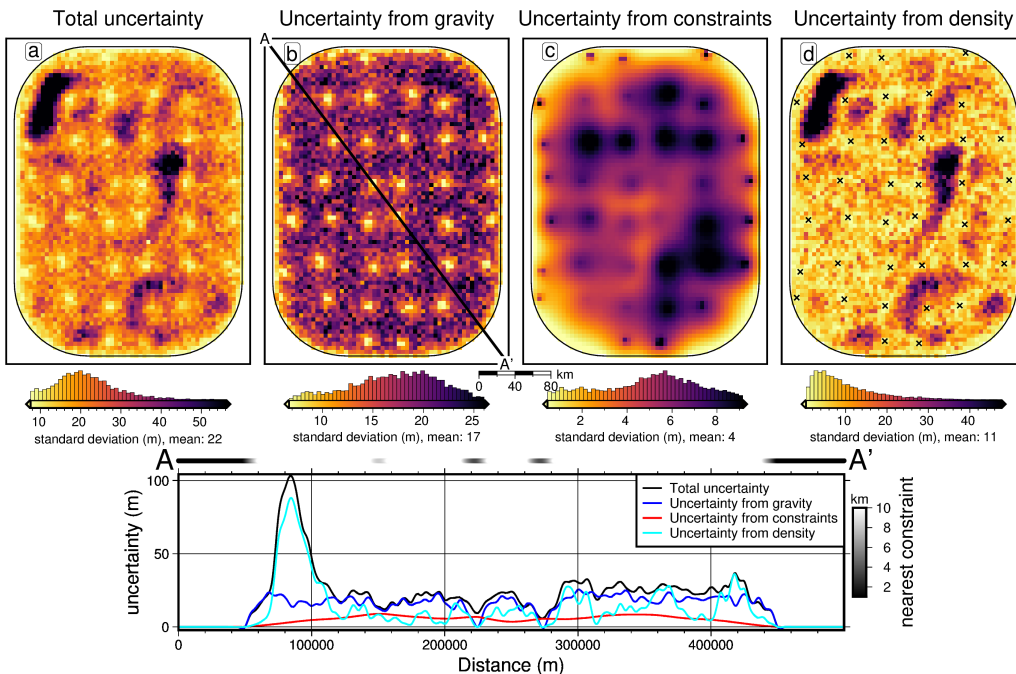
3.29b). This spatial uncertainty is useful to provide alongside the bathymetry results. It informs ocean modellers where results can be confidently interpreted and highlights regions to focus future data collection. Here, a method of uncertainty analysis for this inversion is proposed, and the resulting uncertainty is compared to the inversion error to get a sense of the accuracy of our calculation of uncertainty. This uncertainty analysis is accomplished with Monte Carlo simulations (Helton et al., 2006; Jansen et al., 1994).

Here, 20 inversions are run with the same damping parameter cross-validation as conducted previously. For each inversion the input parameters are sampled from distributions of their possible values. These prior distributions represent all plausible parameter values and thus the resulting inverted bathymetries should cover the range of plausible inversion outcomes. For each grid cell the weighted standard deviation of the 20 inverted bathymetry values of that grid cell was calculated. The weighting came from the inverse square of each inversion's RMS difference between the inverted grid values and the constraint point depths. This reduces the bias from

1934 inversions with large misfits to the actually constraint points (Schnaidt & Heinson,
 1935 Chapter 4 Section 4.2.4 contains a detailed description of those uncertainty
 1936 analysis methodology.

1937
 1938 The parameters included in the Monte Carlo sampling are:

- 1939 1. the observed gravity data, sampled from a normal distribution with a mean
 1940 equal to the observed values and a standard deviation of 0.6 mGal (2% of the
 1941 maximum absolute value).
- 1942 2. the constraint point depths, sampled from a uniform distribution with a center
 1943 as the measured point depth and bounds of ± 5 m for the points outside the
 1944 ice shelf, and $\pm 2\%$ depth for points within the shelf.
- 1945 3. the bathymetry density contrast. This is defined as the difference between the
 1946 densities of water and sediment. The mean value was taken to be 1276 kg m^{-3}
 1947 ($2300 - 1024 \text{ kg m}^{-3}$). A standard deviation of 400 kg m^{-3} was used.



1948 **Figure 3.30:** Monte Carlo simulation results for the Ross Sea synthetic inversion. Cell-wise
 1949 weighted standard deviations of all inversions in each simulation. **a)** Total uncertainty from
 1950 sampling of gravity data, constraint depths, and density contrast value. **b)** Sampling of only the
 1951 gravity data values. **c)** Sampling of only the constraint point depths. **d)** Sampling of only the
 1952 density contrast. To aid in interpretation, locations outside of the ice shelf have been masked.
 1953 Constraints within the ice shelf are shown as black crosses in **d**. **Lower panel)** Profile from A
 1954 to A' of the total uncertainty and individual components. Distance to nearest constraint at each
 point along the profile shown in black to white colors at top of profile.

1948 Four suites of Monte Carlo simulations were run and are shown in 3.30. Each
 1949 of the above parameters; gravity, constraints, and densities, were included in their
 1950 own Monte Carlo simulations, and the fourth simulation included all parameters
 1951 together. Simulations that included the sampling of the constraint depths required
 1952 the re-calculation of the starting bathymetry, the starting forward gravity, gravity
 1953 misfit, regional separation, and finally running the inversion. Simulations that in-
 1954 cluded sampling the density values required recalculating the forward gravity, misfit,

1955 regional separation, and running the inversion. Simulations that included the sam-
 1956 pling of gravity values only required recalculating the regional field and running the
 1957 inversion. These values were sampled from their respective distributions used Latin
 1958 hypercube sampling (Jansen et al., 1994). This allows an adequate coverage of the
 1959 parameter space with only 20 inversions. See Chapter 4 Section 4.2.4 for futher
 1960 details.

1961 3.5.6 Effects of constraint spacing

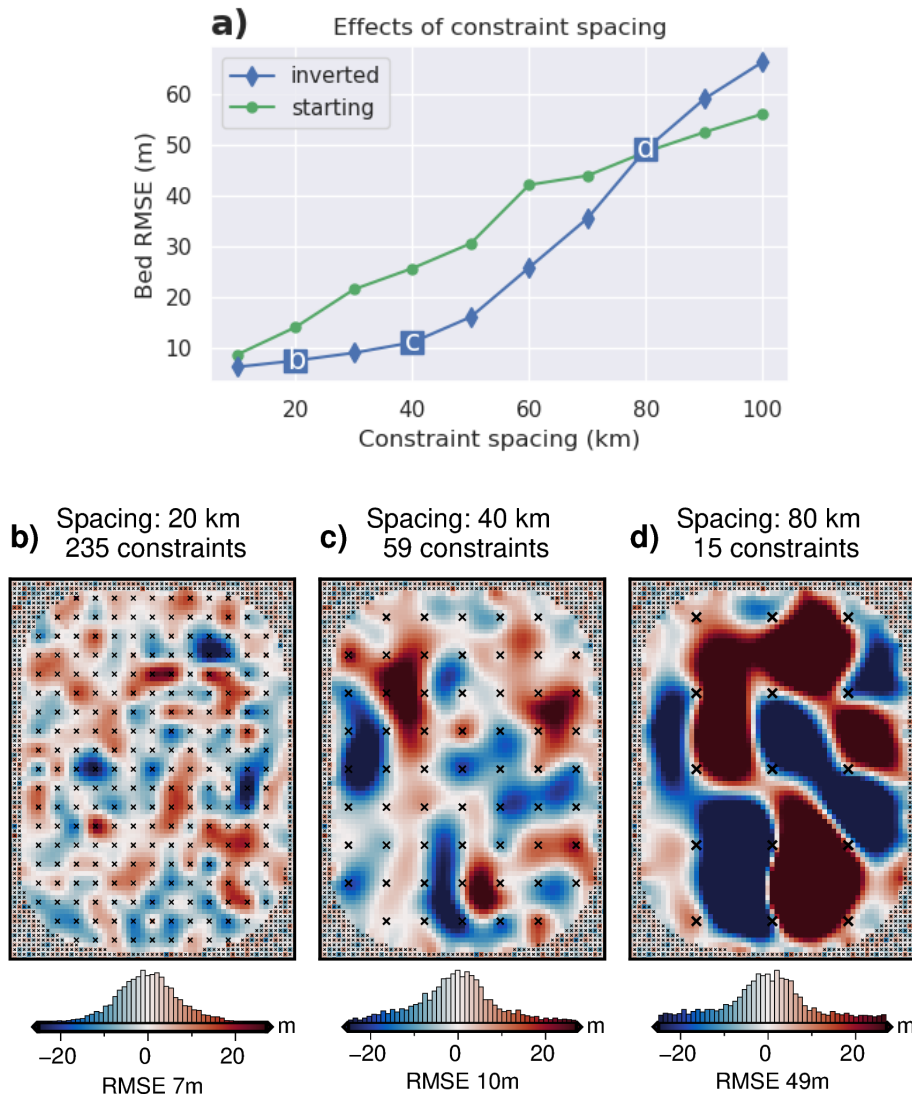


Figure 3.31: Effects of constraint spacing on inversion accuracy. **a)** Bathymetry error (RMSE) relative to the true bathymetry for 10 different constraint spacing. Green (circles) shows the starting error and blue (diamonds) shows the error after inversion. Labels b, c, and d refer to the three inversion error results shown as subplots. **b-d)** Inversion error grids for three of the ten configurations of constraints (labeled on a)). Note b-d use the same color map. Small black crosses show constraints outside the ice shelf, and larger black crosses show inside constraints with the corresponding constraint spacing.

1962 Here we test the effects of the number and spacing of constraint points on the
 1963 accuracy of the inversion. The constraints outside the ice shelf are kept as they have

been in the previous section, at the same grid spacing as the bathymetry (5 km). Constraints within the ice shelf are re-created on a regular grid, where the spacing of the grid, and thus the number of constraints, is varied from 10 km (959 constraints) to 100 km (9 constraints). The depth of the true bathymetry is sampled at each constraint. As in the previous section, points outside the shelf are contaminated with Gaussian noise with a standard deviation of 5 m. Noise for constraints within the ice shelf is relative to each point's depth (to simulate seismic survey uncertainties). These noise-contaminated constraint point depths are used in a bi-harmonic spline gridding to create the starting bed for each of the 10 constraint sets. The RMS difference between each of the starting beds and the true bed is shown as green dots in Figure 3.31a. From these starting beds the inversion workflow was conducted, as below:

1. the forward gravity of the starting beds were calculated,
2. the misfits with the observed gravity (Figure 3.25a) were calculated⁵
3. the regional component of the misfit was estimated and removed with the constraint point minimization method
4. the residual misfit was inverted with the cross-validation routine
5. the difference between each inverted bed and the true bed was found

Figure 3.31 shows the results of this analysis. Subplot a) shows the relationship between constraints spacing and the RMSE with the true bed of the starting bed (green circles) and the final inverted bed (blue diamonds). Three of the inverted bed errors are shown in subplots b-d. See Appendix B.2 for plots of the regional separation errors for these three inversions.

3.5.7 Effects of gravity data

As the above section analyzed the impact of the number of constraint points on the inversion's accuracy, here we investigate the impact of the quality and quantity of input gravity data. Following the methods of the two ensembles presented in the simple synthetic inversion (Figure 3.3.2 & 3.23), an ensemble of 100 inversions with varying levels of noise and gravity observation spacing's are conducted with this Ross Sea model. The observed gravity data was contaminated with noise as described in the past sections, with 10 levels between 0 and 9% of the max absolute value. To simulate a more spare gravity survey, the previous two ensembles sampled the full-resolution gravity data onto a coarser evenly spaced grid and then re-gridded the sparse data with equivalent sources back to the full resolution of the bathymetry. Here instead of evenly spaced grids, we use airborne flight lines.

We use a constant along-line observation spacing of 5 km but vary the spacing between flight lines. The N-S and E-W lines both use the same between-line spacing. The full-resolution gravity is then sampled at these points, and the sparse data is re-gridded to the full resolution (5 km) with equivalent sources. The noise and line spacing changes were applied to the original observed data, and the forward

⁵To isolate the effects of changing the constraint density, the full resolution observed gravity with no added noise was used here, instead of the synthetic survey gravity.

2005 calculation of the starting model, initial misfit calculation, and regional field removal
 2006 were all repeated. Each model was then inverted with a cross-validation, and the
 2007 resulting RMS differences with the true bathymetry are shown in Figure 3.32.

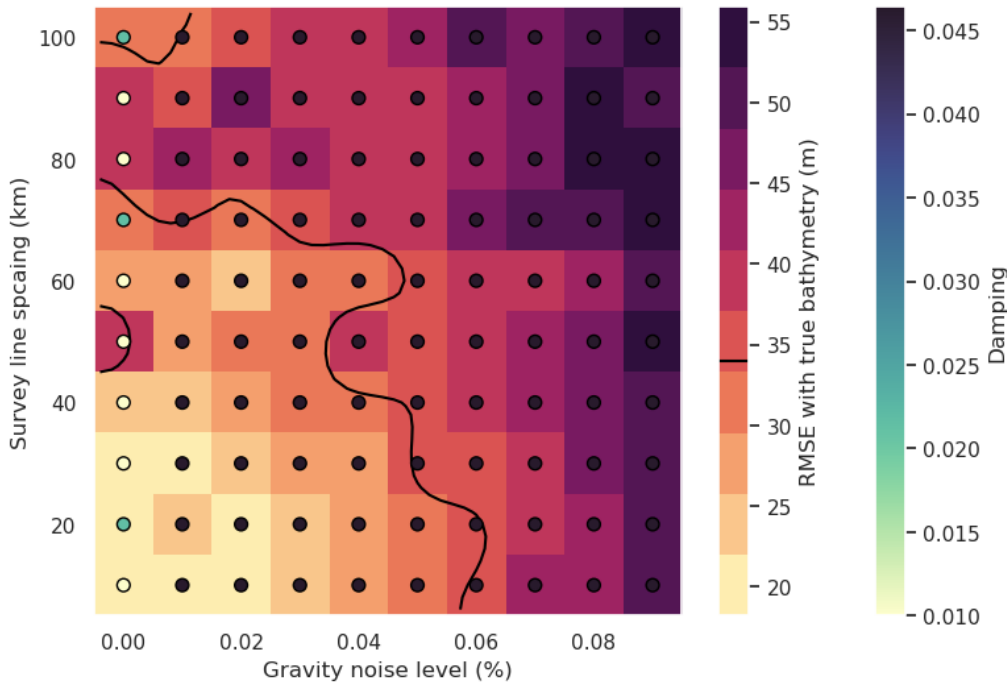


Figure 3.32: Ensemble of noise levels and airborne gravity line spacing for the Ross Sea synthetic model. Grid cell color indicates each inversion's RMSE with the true bathymetry. Circles' color indicates the optimal damping value found for each inversion's cross-validation. Black line shows the 34 m contour which represents the RMS difference between the true and starting bathymetry (Figure 3.26b).

2008 3.6 Discussion

2009 3.6.1 Simple synthetic model

2010 The simple synthetic model of Section 3.3.1 was introduced to 1) present the basic
 2011 workflow of the inversion, 2) determine the best options for various components of
 2012 the inversion and 3) demonstrate the capabilities and limitations of the inversion.
 2013 The starting bathymetry had an RMS difference with the true bathymetry of 66 m
 2014 (Figure 3.6). This error demonstrates the limitations of gridding sparse data. Even
 2015 with a very high spatial constraint density (1 constraint per 160 km^2) compared to
 2016 most ice shelves (Fretwell et al., 2013), simply gridding the constraints greatly misin-
 2017 terpreted the true bathymetry. To reduce this bathymetric error, we presented three
 2018 inversions, a noise-free full-resolution inversion, a noise-contaminated full-resolution
 2019 inversion, and a noise-free lower-resolution inversion.

2020 3.6.1.1 Inversion results

2021 All of these inversions (without a regional component) were able to reduce this
 2022 RMS difference with the true bathymetry to $\sim 10 \text{ m}$, and recover all bathymetric
 2023 features of interest. We demonstrated that the two methods of calculating the verti-
 2024 cal derivative of gravity produced similar results, but the annulus approximation was

significantly faster ($\sim 5\times$). Additionally, for each of these inversions, the weighting grid, based on the distance to the nearest constraints (Figure 3.5), successfully constrained the resulting inverted bathymetry at the points of prior bathymetry observations. Each inversion's constraint point RMS difference with the true bathymetry was $<\sim 2$ m, and the technique avoided any pedestal effect around the constraints in the resulting bathymetries. Interestingly, the inversion with low-resolution (6 km) gravity data yielded a very similar RMSE compared to the inversion with the full-resolution (1 km) data. This demonstrates that for recovering bathymetric features of wavelengths similar to those found in our synthetic model, high-resolution gravity surveys may not be necessary to achieve adequate results from an inversion.

3.6.1.2 Ensemble results

To test this theory further, we conducted an ensemble of 100 inversions with 10 levels of noise contamination and 10 gravity survey resolutions. The resulting RMS difference of each inversion with the true bathymetry is shown in Figure 3.17. All inversions in this ensemble, including the worst-case scenario of 9% noise and a gravity observation grid of $10\times$ the bathymetry spacing, still resulted in an RMS difference lower than that of the starting bathymetry (66 m). It is worth noting that this metric for the accuracy of the inversion, the root mean squared (RMS) difference with the true bathymetry, is used to give extra weighting to the outlier errors, as opposed to using a mean average error (MAE). These outliers typically include the features of interest in a bathymetry inversion. Figure 3.33a shows these ensemble results grouped by cell size. For each cell size value (colour of lines), the inverted bed RMSE for the range of noise levels is shown. This shows a roughly linear relationship between noise and RMSE, regardless of cell size. This means there is a continuous improvement in the inversion's accuracy with lower levels of noise. Conversely, figure 3.33b shows these ensemble results grouped by the noise level. For each noise level (colour of lines), the inverted bed RMSE for the range of cell sizes is shown. This shows an exponential relationship between gravity survey resolution and RMSE. This exponential relationship is strongest for low noise levels. This means inversion accuracy greatly benefits from increasing the survey resolution (decreasing the cell size), but this benefit diminishes once the survey resolution is at a certain point. Here, surveys at or below ~ 6 km resolutions have diminishing improvement in RMSE. The linear relationship between noise and RMSE, and the exponential relationship between resolution and RMSE can also be seen by the spacing of lines in either figure. The close spacing of the low-cell-size lines (purples) in Figure 3.33a show the diminishing improvements at small cell size surveys, while the continuous spacing of lines in Figure 3.33b shows the linear relationship.

In a typical gravity survey, there is often a trade-off between the number of observations made and the quality (noise) of the data. This is due to the time restrictions of both the total data collection period (i.e. the length of a field season in Antarctica), and the necessity to repeat base-station measurements to account for instrument drift. Collecting more data in the same time period inevitably results in increased noise. At a certain point, this increased noise will have a greater negative effect on the inversion results, than will be counteracted by the increased amount of data. These are important considerations for survey design. Figure 3.33b shows that for a given noise level, there is little benefit in increasing the gravity survey resolution from ~ 6 km to 1 km. For this survey domain (60×80 km),

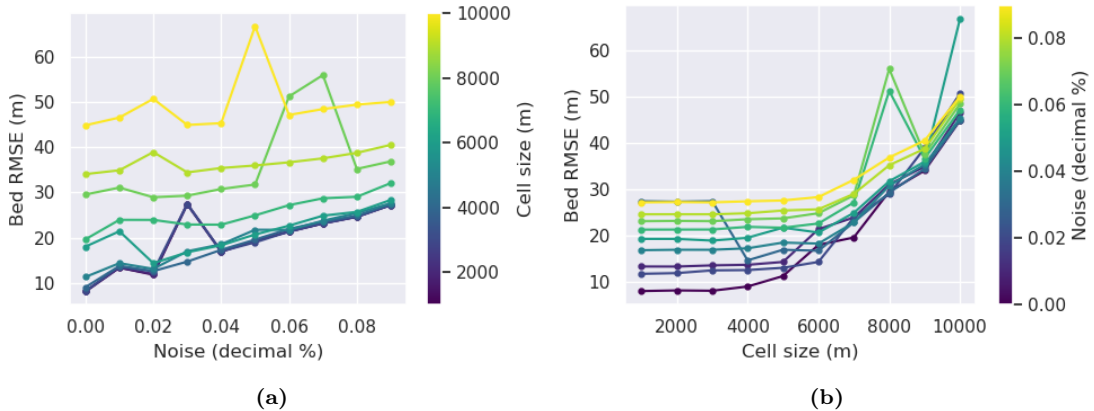


Figure 3.33: Ensemble results for the simple synthetic inversion, grouped by **a**) gravity survey cell size, and by **b**) noise level. Each line in a) corresponds to a row of Figure 3.17 and each line in b) corresponds to a column.

2073 a 6 km resolution results in \sim 130 gravity station, while with a 1 km resolution,
 2074 this increases to 4800 observation points. Simplistically speaking, if keeping total
 2075 survey time constant, this means at 6 km spacing as opposed to 1 km spacing, ei-
 2076 ther \sim 36 \times more area could be surveyed, or higher quality data could be collected,
 2077 with shorter base station loops, more repeated ties, and more careful measurements.
 2078

2079 The results from the noise-contaminated inversion (Figure 3.12 & 3.9b) show
 2080 that this gravity noise is directly reflected in the inversion results. For this reason,
 2081 data, either the observed data or the residual misfit, is typically low-pass filtered
 2082 prior to inversion (i.e. Boghosian et al., 2015; Yang et al., 2020a). This is typically
 2083 done with either a time-based filter for airborne surveys, or a spatial filter (Jordan
 2084 et al., 2010). With this filtering, there is a trade-off between removing the noise and
 2085 removing the true signal. Due to this, we have chosen to omit the filtering in these
 2086 synthetic examples.

2087 3.6.2 Simple model with a regional component

2088 3.6.2.1 Regional separation methods

2089 The addition of a regional component to the observed gravity data adds a major
 2090 complexity to the inversion workflow. The actual inversion remains the same, but
 2091 this regional component must be estimated and removed beforehand. We tested
 2092 four methods of regional estimation; 1) a low-pass filter, 2) fitting a polynomial
 2093 trend to the data, 3) predicting the data with a set of deep point sources, and 4)
 2094 attributing the entire misfit value to the regional field at constraint points and in-
 2095 terpolating between these values. Figure 3.19 compares the inversion results of each
 2096 of these methods. While each method recovered the short wavelengths bathymetry
 2097 features, the misestimation of the true regional field for each method introduced
 2098 long-wavelength errors in the inversion results. We show that the constrain point
 2099 minimization method most accurately estimated the region, and thus produced the
 2100 best inversion results. For the simple regional field used here, the filter and trend
 2101 methods achieved reasonable results, but the effectiveness of these methods is ex-
 2102 pected to be reduced with more complex regional fields associated with real data.
 2103

While the constraint point minimization worked best for this model, each of these methods may work better in specific scenarios. All the methods except the equivalent source method require the gravity data to be gridded over the entire region of interest. For sparse gravity surveys the interpolation required may introduce large errors. For this scenario, the equivalent source technique is likely the most appropriate. In scenarios with few bathymetry constraints and where the regional field is expected to be simple, the trend and low-pass filter methods are efficient and can be effective. However, if there are distributed bathymetry constraints, such as in this synthetic scenario, constraint point minimization is likely the best choice. This technique will only effectively remove regional anomalies with a wavelength equal to or greater than the average constraint spacing. If the constraints are sparse relative to the expected regional anomaly wavelengths, this method will underestimate the regional component. Lastly, if the bathymetry contains long-wavelength features which would result in long-wavelength anomalies, the trend, filter, and equivalent source techniques may include these in the regional removal. Therefore, the inverted bathymetry, while recovering the super-imposed short-wavelength bathymetry features, will underestimate the long-wavelength features. It is for these reasons that regional separation is perhaps the most important aspect of a bathymetry inversion.

3.6.2.2 Constraint point minimization

This constraint point minimization technique requires the gridding of sparse measurements of the regional field. We explored the impact of this gridding process on the resulting inversion. Figure 3.20 shows the results of four different gridding processes. Minimum curvature gridding without tension (tension of 0, Figure 3.20a) produces a smoothly varying surface at the constraints but introduces artificial minima and maximum at points far from any constraints. This erroneous effect is minimized with a higher tension factor. Using a tension factor of 1, figure 3.20c shows the limited erroneous minima and maxima, but this added tension results in high gradients in the surface immediately near the constraint points (Figure 3.20g). These high gradients in the resulting residual anomalies create a *ringing* effect in the inverted bathymetry (Figure 3.20k). For these reasons, an intermediate tension factor of 0.25 is suggested for potential field data. While this limits the negative effects of both low and high tension, there are still false minima and maxima (Figure 3.20b), and high gradients at the constraints (Figure 3.20f). The last gridding technique uses bi-harmonic splines. The optimal damping parameter associated with this technique is chosen from a cross-validation of the constraint points. This technique, while being more computationally expensive, solves both issues of tensioned minimum curvature.

3.6.2.3 Inversion results

With both the optimal regional separation method and the optimal gridding method determined, we performed a cross-validated inversion with the remaining residual misfit. This inversion was able to recover all the short-wavelength bathymetry features but introduced some long-wavelength errors. Figure 3.34 shows the inverted bathymetry error alongside the error in estimating the regional component of gravity. Comparing these shows that almost all of the inverted bathymetry error is tied to the inaccuracies of determining the regional component. the remaining error is all minor short-wavelength features, mostly around constraint points. They appear to

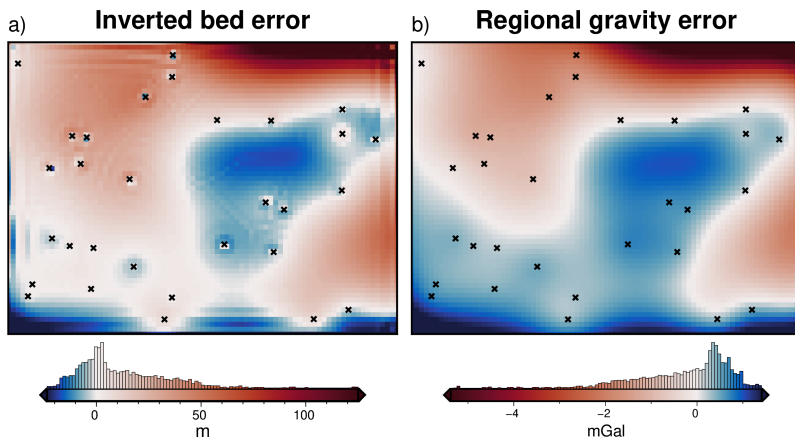


Figure 3.34: Source of inverted bathymetry error for the simple synthetic model with a regional field. **a)** Inverted bathymetry error from Figure 3.22b. **b)** Error in the estimation of the regional component of gravity from comparison with the true regional component (Figure 3.18b). Black crosses show constraint points. Colormaps are inverted to highlight the similarities and the median has been removed from the regional error.

result from the weighting grid implementation of regularization. Since the errors in the regional estimation are the dominant source of error in most inversions, as shown above, and by other Antarctic bathymetry inversions (Brisbourne et al., 2014), we have shown these details of the gridding process are a vital and often overlooked step in many studies.

3.6.2.4 Ensemble results

As with the simple model, an ensemble of noise and gravity survey spacing experiments were performed with this model containing a regional component. The lowest resulting RMS difference with the true bathymetry was raised from values of ~ 10 m for the inversion without the regional component, to a lowest value of ~ 40 m with the additional regional component. The black line in Figure 3.23 shows the 66 m contour, which represents the RMS difference between the true and starting bathymetries. Inversions that fall outside (above) of this line resulted in a worse bathymetry than the starting model. This shows that for this model, inversion is only worth conducting if the gravity survey has a spacing less than ~ 9 km ($\sim 9 \times$ the spacing of the desired bathymetry resolution). Figure 3.35 show these ensemble results grouped by cell size and noise level. There is a linear relationship between gravity noise and the resulting bathymetry RMSE, for all gravity survey spacings. There is an approximately exponential relationship between gravity survey resolution (cell size) and resulting bathymetry RMSE. The degree of this exponential relation decreases with increased noise.

2171

For this model, the *elbow* of the exponential curves in Figure 3.35b is at ~ 6 - 8 km survey resolutions (6 - $8 \times$ bathymetry resolution). This suggests that for a survey resolution finer than ~ 8 km, there is little benefit in collecting more data. This is supported by the close spacing of low-cell-size lines (purples) in Figure 3.35a. The effort would be better spent collecting data over a wider region, reducing noise in the data, or if possible collecting more bathymetric constraints.

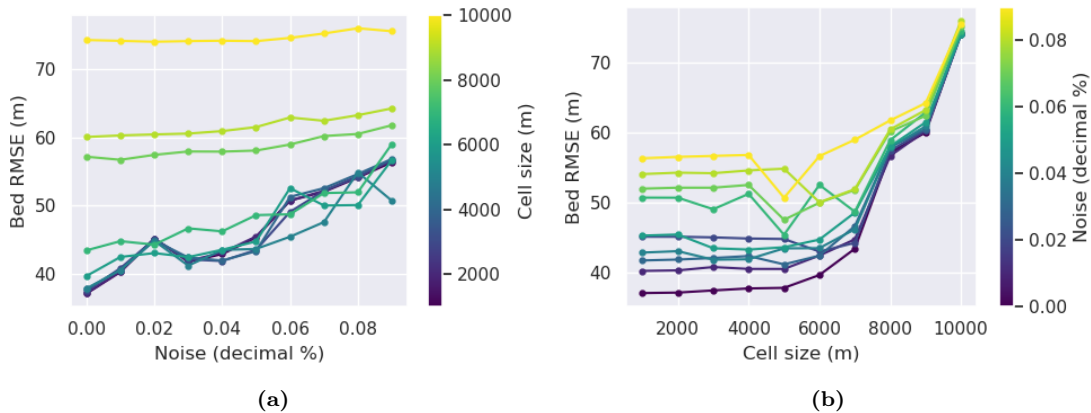


Figure 3.35: Ensemble results for the synthetic inversion with a regional component, grouped by a) gravity survey cell size, and by b) noise level. Each line in a) corresponds to a row of Figure 3.23 and each line in b) corresponds to a column.

2178 3.6.3 Ross Sea model

2179 The Ross Sea semi-realistic model was created to better emulate the gravity and
 2180 bathymetries expected for ice shelves. A few extra complexities were added to this
 2181 model compared to the purely synthetic models. An ice shelf border was included,
 2182 with a high density of constraints outside of the border, and sparse constraints
 2183 within. All the constraints had an associated uncertainty, instead of directly sam-
 2184 pling the true bathymetry depths. The observed gravity was calculated along the
 2185 flight paths of a typical airborne survey, instead of along a uniform grid. The main
 2186 inversion in this section had 2% noise added and had flight lines with 50 km N-S
 2187 spacing and 15 km E-W spacing. The inversion successfully reduced the starting
 2188 bathymetry error from an RMSE of 34 m to 23 m. The resulting bathymetry shows
 2189 a recovery of most of the lost bathymetry features, but some noise from the gravity
 2190 data has been introduced into the bathymetry. Sharp bathymetry features (upper
 2191 left corner) and smooth features were both recovered. The constraint points were
 2192 relatively evenly distributed (Figure 3.26d), resulting in a relatively even distribu-
 2193 tion of bathymetry misfits.

2194 Of these errors, the largest were located at the gaps in the synthetic survey
 2195 where there were missing flight lines (Figure 3.25b). To understand the cause of
 2196 the remaining errors, we compare the inverted bathymetry error with the regional
 2197 separation error (Figure 3.36). The strong correlation between these two grids shows
 2198 that the majority of errors in the inversion are tied to the miscalculation of the
 2199 regional field, as was seen in the simple synthetic inversion with a regional field.
 2200 The remaining errors appear to be from the flight line gaps and noise in the gravity
 2201 data.

2203 3.6.3.1 Effects of the gravity data

2204 The ensemble of gravity data noise levels and flight line spacings from Section 3.5.7
 2205 shows the relative importance of these two aspects of a gravity survey. As for the
 2206 previous ensembles, Figure 3.37 shows these results grouped by line spacing and by
 2207 the noise level. For the Ross Sea model, both factors have a roughly linear relation-
 2208 ship with inverted bathymetry error. The slopes for the lines of best fit for Figure
 2209 3.37a and b means the inversion RMSE increases by ~ 10 m for either a 4% increase

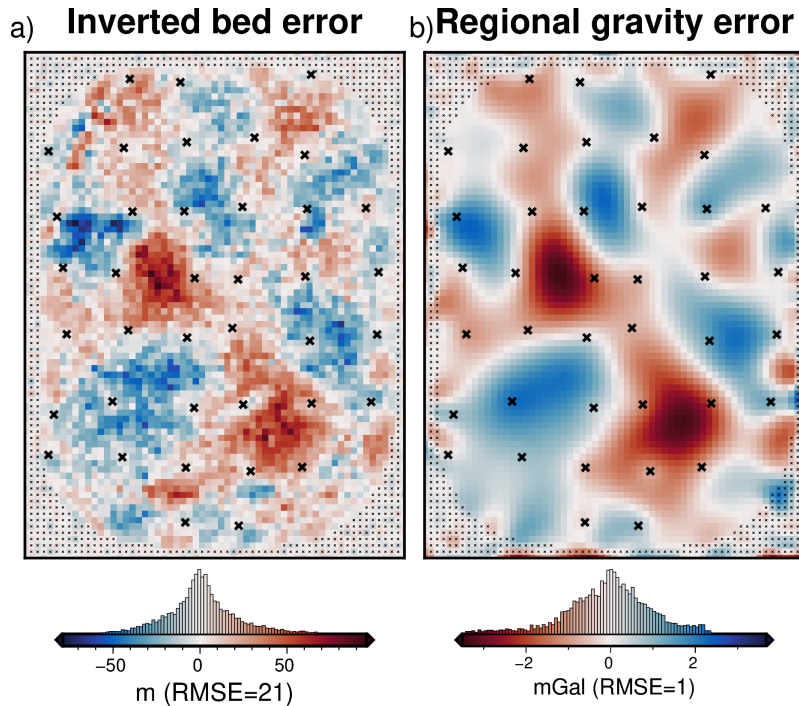


Figure 3.36: Comparison of the inverted bathymetry error and the error in the regional field estimation. **a)** Inverted bathymetry error from Figure 3.29b. **b)** Error in the estimation of the regional component of gravity from comparison with the true regional component (Figure 3.24d). Black crosses show constraint points. Colormaps are opposed to highlight the similarities and the median has been removed from the regional error.

in the noise level or a 60 km increase in the average flight line spacing. The inversions with a small line-spacing (purple lines) of Figure 3.5.7a are closely grouped, relative to the higher line spacings. This shows that at already low line spacings (40 km) there may be little benefit to reducing the line spacing further. Conversely, there is a larger spread for the low noise inversions (purple lines) in Figure 3.5.7b. This shows that even at low noise levels, further decreases may still provide important improvements to the inversion outcome. As in the previous ensemble results, for a field application, this demonstrates the important tradeoff between quantity and quality of gravity data.

These specific relationships between noise, line spacing, and inversion error, while not applicable to all survey configurations, show the importance of choosing an appropriate survey design. This analysis with synthetic data could be included in a pre-survey plan, to explore the effects of differing survey configurations.

3.6.3.2 Effects of the constraints

These synthetic inversions have shown that the removal of the regional field presents the biggest challenge for gravity inversions for bathymetry. The most robust technique for removing the regional field requires a distribution of points of known bathymetry across the inversion region. Since the largest errors in the inverted bathymetries occur at the largest distance to constraints, an even distribution of constraints will best be able to estimate the regional field. Section 3.5.6 explored the effects of varying the numbers of constraints, while keeping the remaining components of the inversion constant. Figure 3.31a shows the bathymetry RMSE with

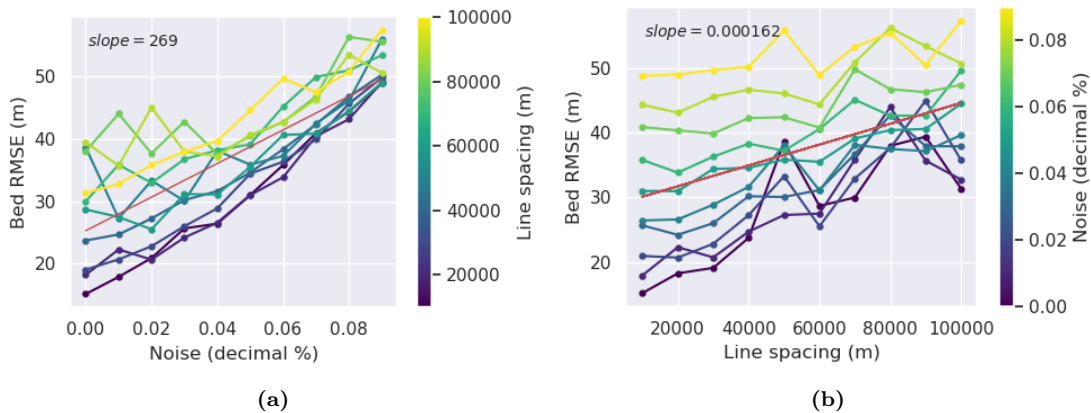


Figure 3.37: Ensemble results for the Ross Sea inversion, grouped by **a)** gravity survey line spacing, and by **b)** noise level. Each line in a corresponds to a row of Figure 3.32 and each line in b corresponds to a column. Red lines show the line of best fit, with their slopes shown in the upper left corners.

the true bathymetry both before (green) and after (blue) the inversion is conducted.

Figure 3.31a shows for this synthetic model that for average constraint spacing's less than ~ 20 km there is little improvement made by running an inversion. This is due to the starting bathymetry model already being relatively accurate, with the inversion only producing minor adjustments between constraint points. At the other end of the spectrum, with constraint densities greater than ~ 70 km, the inverted bathymetry has an error similar to or higher to the un-inverted bathymetry. This is due to the inaccuracies in calculating the regional field with only very sparse constraints. For these scenarios, the errors introduced by the inversion are greater than the errors of simply interpolating the constraint points. The inverted bathymetry error curve (Figure 3.31a) shows that for this survey, once below a certain constraint spacing (~ 30 km) there is little benefit to having additional constraints.

3.6.3.3 Uncertainties

We have demonstrated that the majority of the inverted bathymetry error is related to the estimation of the regional component of gravity. Without knowing the true regional component, as we do in these synthetic examples, estimating the uncertainty in the interpolation between constraint points of the regional field is difficult. The uncertainty of each grid cell is likely strongly dependant on the distance to the nearest constraint, as well as the depth uncertainties of these nearby constraints. While we show this to be true with our synthetic models, a quantitative method of predicting this uncertainty has yet to be implemented here. The field of conventional bathymetry surveying has developed uncertainty analysis tools that may be applicable to this (Bourgeois et al., 2016).

These tools are able to account for both the depth uncertainty of each measurement, and the distance of each grid cell to the nearest measurement. Future work will benefit from a quantitative assessment of the uncertainty of gridding the regional field from the constraint point values. While the uncertainty of the regional removal accounts for the majority of the uncertainty of the inverted bathymetry, it is technically completed before the inversion and is thus not a component of the

inversion uncertainty. To address the uncertainty resulting from the inversion process, we introduced a suite of Monte-Carlo simulations in Section 3.5.5. The results in figure 3.30 show a mean uncertainty for the entire region of 22 m. The majority of this uncertainty is attributed to the uncertainty in the gravity data, as shown by histograms of Figure 3.30. Here we discuss the significant of each component of the uncertainty analysis:

1. **Gravity uncertainty:** The uncertainties in the gravity data result in a relatively uniform bathymetry uncertainty across the region of 17 m. A simple calculation with the Bouguer slab formula with a density contrast of 1276 kg m⁻³ and our assumed gravity uncertainty of 0.612 mGal (%2 max absolute value) gives a value of 11.5 m ($\Delta g_{boug} = 4.18e-5\rho h$). This may show the conventionally used Bouguer slab approximation is underestimate the true uncertainty in inversions resulting from gravity data uncertainty. This uncertainty is lowest at the constraints, due to the use of the weighting grid in the inversion.
2. **Constraint depth uncertainty:** The contribution to the bathymetry uncertainty from the depth uncertainty of the constraint points is small, with a mean of \sim 4 m. This uncertainty resulting from the constraints is also concentrated around the constraint points. This shows improving the constraint point uncertainties will not greatly improve the inversion, and will only improve it in the immediate vicinity of constraints.
3. **Density uncertainty:** The bathymetry uncertainty component resulting from the prism densities is heterogeneous, with some spatially limited, but large values. The mean value is \sim 11 m, but some areas are up to 50 m. These high uncertainties are strongly correlated with the error in the starting bathymetry (Figure 3.26b). This is due to the change in density contrast resulting in a change in the total bathymetry correction calculated in the inversion. In other words, the residual misfit can be minimized by a large surface correction with a low-density contrast or a small surface correction with a large-density contrast.

The combined Monte-Carlo simulation (Figure 3.30a) shows the expected features of an uncertainty map. It has a base level uncertainty similar to the Bouguer slab thickness from the assumed gravity uncertainty, it is generally lowest at the constraints and highest in the large constraint gaps, and it is high where the inversion has produced a large change from the starting model.

3.7 Future work

Running this inversion with the various synthetic models gave us the ability to assess the inversion performance. From this assessment, we have determined several components which would benefit from additional investigation.

1. Implement an additional cross-validation routine to estimate the optimal density contrast, as in Uieda and Barbosa (2017). Here, we have used the same density contrasts for the creation of the observed gravity data and for the inversion itself. In a non-synthetic scenario, this contrast would need to be estimated.

- 2308 2. Test the effects of flight line orientation relative to the dominant trend of
2309 geologic structures.
- 2310 3. Implement a more robust method of enforcing the constraint points. This
2311 may likely be in the form of a bounded least squares solver or some form of
2312 manipulation of the Jacobian matrix.
- 2313 4. Quantify the uncertainty of the regional separation process. This will likely
2314 include techniques used in conventional bathymetry surveying (Bourgeois et
2315 al., 2016; Calder & Elmore, 2017), or a sequential Gaussian simulation (Perozzi
2316 et al., 2021).
- 2317 5. Testing the effects of pre-filtering the gravity data, either spatially or tempo-
2318 rally, to remove the effects of noise (Jordan et al., 2010).

2319 3.8 Conclusion

2320 With the goal of modelling the bathymetry beneath a floating ice shelf, we present
2321 a geometric gravity inversion that 1) adheres to prior bathymetry point measure-
2322 ments, within their uncertainties, 2) produces a smooth and realistic bathymetry,
2323 3) accounts for the regional gravity field and 4) is computationally efficient and
2324 fully-open source. To demonstrate the effectiveness, as well as the limitations, we
2325 conducted a series of inversions using synthetic and semi-realistic data. These in-
2326 versions showed the importance of accurately estimating and removing the regional
2327 component of gravity prior to the inversion. We showed that for the constraint ar-
2328 rangement for many Antarctic ice shelves, the optimal method for estimating this
2329 regional field is with a constraint-point minimization. In addition, we further ex-
2330 plored this method by testing various gridding (interpolation) techniques and found
2331 a clear increase in performance when using a cross-validated bi-harmonic spline in-
2332 stead of the typically used tensioned minimum curvature.

2333 Here we reiterate a few of the key findings from this chapter:

- 2335 1. Estimating and removing the regional component of gravity for typically in-
2336 version scenarios is the most important aspect of the inversion procedure. For
2337 typical bathymetry inversions, the optimal method for estimating the regional
2338 field is constraint point minimization.
- 2339 2. When collecting data for an inversion, it is best to aim for quality over quanti-
2340 ties for the gravity data, and conversely, quantity over quality for bathymetry
2341 constraint measurements.
- 2342 3. We provide general guidelines on the optimal ranges of constraint density, grav-
2343 ity survey line spacing, and gravity noise, for which conducting an inversion is
2344 suitable.

2345 Testing the various models with differing levels of gravity noise and numbers
2346 of gravity observation points highlights an important factor in planning a grav-
2347 ity survey. We show for the Ross Sea synthetic model, which likely emulates the
2348 scenario expected from many Antarctic ice shelves, **there are diminishing re-**
2349 **tURNS FOR AVERAGE FLIGHT LINE SPACINGS SMALLER THAN ~40 KM** if the goal is

2350 to recover bathymetry features typical of the Ross Sea. **However, the inverted**
2351 **bathymetry's accuracy is strongly affected by noise in the gravity data.**
2352 With this, the typically airborne survey focus on quantity of quality may need to be
2353 reassessed. If 40 km spaced flight lines produce similar results to 20 km lines, flying
2354 half the number of lines will save a significant amount of time. This time could
2355 be used to either expand the area of the survey or reduce the noise in the data.
2356 Reducing the data noise for an airborne survey may not always be feasible, but a
2357 few measures may be taken to attempt this, all of which are aided by the increased
2358 survey time allowed by reducing the number of flight lines. These include repeating
2359 lines or sections which are noisy, limiting flights to good weather windows, increasing
2360 the number of tie-lines, making shorter loops for base-station ties, or flying at
2361 lower altitudes and or ground speeds.

2362
2363 **The previous measurements of bathymetry, referred to as the constraints,**
2364 **are a vital part of an inversion for bathymetry.** Due to the non-
2365 uniqueness of an inversion, there are an infinite number of inverted bathymetry
2366 models which will equally match the observed data. These constraints provide the
2367 ground truth necessary to confidently chose a model out of these infinite choices.
2368 Additionally, if not more importantly, they provide the primary method of account-
2369 ing for the regional component of gravity. Since this is shown to be the largest
2370 source of uncertainty, the constraints are the most important aspect of the inver-
2371 sion. We tested the effects of varying the spatial density of the constraint points.
2372 The results (Figure 3.31) show the range of constraint point spacings for the Ross
2373 Sea synthetic model which justifies conducting a gravity inversion if the goal is to
2374 recover bathymetry with a 5 km resolution.

2375
2376 **The optimal constraint spacing is between ~20-70 km.** Smaller spacing
2377 values already have an adequate amount of information and little is gained over a
2378 simple interpolation of the data. At spacings larger than ~70 km, the errors in es-
2379 timating the regional field are larger than the improvements made by the inversion.
2380 These values, while specific to the Ross Sea scenario, provide an important context
2381 for the feasibility of conducting bathymetry inversions. Taken together with the
2382 above assessment of the relative importance of gravity data noise and density, some
2383 general guidelines are provided.

2384
2385 As long as the gravity data is on the order of magnitude of $2-4 \times$ the spacing of
2386 the desired bathymetry resolution, and the noise levels are low, **efforts should be**
2387 **focused on collecting more bathymetry measurements.** The uncertainty of
2388 these depth measurements is relatively unimportant (Figure 3.30c), meaning quan-
2389 tity over quality is acceptable here. The final spatial uncertainty of the inverted
2390 bathymetry is strongly tied to the distance to the nearest constraint. This suggests
2391 that an even distribution of the constraints is important. However, if specific re-
2392 gions of the survey are expected to have larger amplitude regional anomalies, an
2393 increased spatial density of constraints over this region would be beneficial. With
2394 these recommendations, future planning for Antarctic fieldwork should be able to
2395 collect data that prioritizes the accurate assessment of sub-ice shelf bathymetry.

2396
2397 Chapter 4 applies the inversion presented here to model the bathymetry beneath
2398 Antarctica's Ross Ice Shelf.

2399 **Chapter 4**

2400 **Ross Ice Shelf bathymetry inversion**

2401 **Abstract**

2402 Antarctica's Ross Ice Shelf buttresses large catchments of ice from both the East and
2403 West Antarctic Ice Sheets. Changes to the current stability of the ice shelf, likely
2404 through basal melt of the sensitive grounding zones or pinning points, will reduce this
2405 buttressing and accelerate the Antarctic Ice Sheet's contribution to global sea level
2406 rise. The distribution of basal melt is predominantly controlled by the ocean cavity
2407 thickness and the channelling of ocean waters by bathymetric features. Bathymetry
2408 is, however, poorly known for the Ross Ice Shelf. Here we use airborne gravity
2409 data and distributed seismic constraints across the ice shelf to create an updated
2410 sub-ice shelf bathymetry model. We accomplish this with a non-linear geometric
2411 gravity inversion, available as open-source Python code. Monte Carlo sampling
2412 of the inversion inputs provides a robust means of addressing spatial uncertainty
2413 and the relative significance of each component of the inversion. The resulting
2414 bathymetry closely matches the seismic constraints and reveals significant changes
2415 compared to past bathymetry models. We find several likely locations of past pinning
2416 points, locations where enhanced basal melting is likely, and sites of possible tectonic
2417 significance.

2418 **Key Points**

- 2419 1. We present a new bathymetry model beneath Antarctica's Ross Ice Shelf from
2420 a gravity inversion
- 2421 2. A Monte Carlo simulation provides a detailed spatial uncertainty analysis
- 2422 3. Results highlight locations where the updated bathymetry may impact ocean
2423 circulation models or where the shelf may have been recently grounded

2424 **4.1 Introduction**

2425 Much of Antarctica's coastline is fringed by floating extensions of the Antarctic Ice
2426 Sheet. These floating masses of ice, referred to as ice shelves, are connected to the
2427 grounded ice. Over 80% of Antarctica's grounded ice drains to the oceans through
2428 these ice shelves (Rignot et al., 2013). While they are floating, and thus already
2429 displace their mass equivalent of seawater, they are vital to the current and future
2430 contribution of the Antarctic Ice Sheet to global sea level rise (Fürst et al., 2016;

Jacobs et al., 1992). The ice shelves slow the flow of upstream ice into the ocean by imparting a resistive force, known as buttressing. This buttressing occurs from lateral drag along the sides of the ice shelves and resistive stresses incurred where they flow over pinning points (localized areas of grounded ice) (Dupont & Alley, 2005; Matsuoka et al., 2015). Changes to the geometry of the ice shelves can reduce their restraining effect on the flow of grounded ice, leading to an increased mass flux of ice across the grounding zone, thus increasing the ice sheet's contribution to global sea level rise (e.g., Pritchard et al., 2012; Scambos et al., 2004).

2439

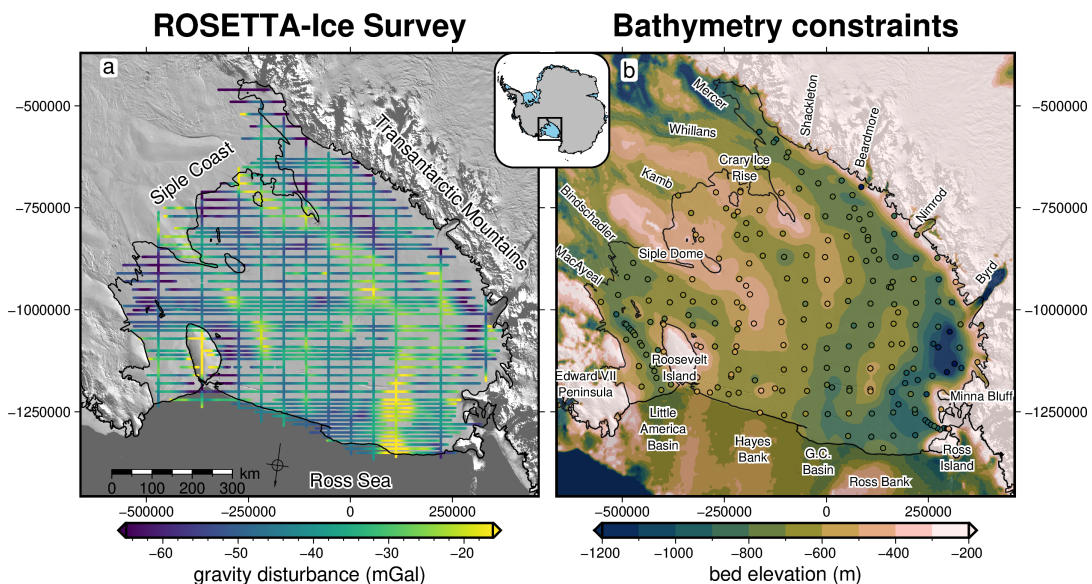


Figure 4.1: Input datasets for the Ross Ice Shelf bathymetry inversion. **a)** ROSETTA-Ice airborne gravity disturbance data (cleaned and re-levelled). **b)** Bedmap2 bed elevations in background, with individual constraint points within the ice shelf boundary (dots) on the same color scale. Black line in both figures shows the grounding line and ice front from Mouginot et al. (2017). Background imagery is from MODIS-MOA (Scambos et al., 2007). Regional names shown in **a** and specific location names shown in **b**, which include ice streams along the Siple Coast, outlet glaciers along the Transantarctic Mountains, and bathymetry features in the Ross Sea. The RMS difference between the constraint point values and the BedMap2 gridded values is 138 m.

The largest ice shelf is the Ross Ice Shelf (Figure 4.1, Fretwell et al., 2013). Situated in West Antarctica, along the boundary with East Antarctica, the Ross Ice Shelf comprises ice from both the East and West Antarctic Ice Sheets; a combined catchment totalling 11.6 meters of potential global sea level rise (Tinto et al., 2019). While the Ross Ice Shelf is in approximate steady-state, that is a near net-zero mass change (e.g., Moholdt et al., 2014; Rignot et al., 2013), geologic evidence shows rapid disintegration (Naish et al., 2009; Yokoyama et al., 2016) and extensive grounding line retreat (Spector et al., 2017; Venturelli et al., 2020) may have occurred as recently as the mid-Holocene (~ 7 kyr B.P.). Ocean forcing, specifically basal melting along the grounding zone, is thought to drive these rapid grounding line retreats (Lowry et al., 2019). The current stability of the ice shelf is in part attributed to the lack of warm Circumpolar Deep Water penetrating into the cavity (Dinniman et al., 2011; Tinto et al., 2019). Ocean waters that do penetrate the cavity, such as High Salinity Shelf Water, are dense and relatively cold. Despite their temperature, they are responsible for significant melting at the large depths of the grounding zone (Adusumilli et al., 2020) due to the pressure suppression of the freezing temperature

2456 of ice (Tinto et al., 2019).

2457

2458 This High Salinity Shelf Water is formed on the continental shelf from the cre-
2459 ation of sea ice. Due to their density and the reverse slope of the continental shelf,
2460 they flow into the cavity, guided by bathymetric troughs (Jacobs et al., 1992; Tinto
2461 et al., 2019). There are many examples of bathymetric features controlling the
2462 routing of these sub-shelf waters (e.g., De Rydt et al., 2014; Dutrieux et al., 2014;
2463 Gladish et al., 2015; Zhao et al., 2019). Additionally, ocean modelling sensitivity
2464 testing highlights the importance of bathymetric features to sub-shelf circulations
2465 and melt (De Rydt et al., 2014; Goldberg et al., 2020). Bathymetry, therefore, plays
2466 a key role in the stability of the Ross Ice Shelf through its likely control on the basal
2467 melt magnitude and distribution (Goldberg et al., 2019) and through the buttressing
2468 effect of bathymetric pinning points (Still et al., 2019).

2469

2470 Direct observations of the sea floor beneath the Ross Ice Shelf (excluding along
2471 its periphery) are limited to two drill holes. The first was the 1977 J9 drill hole north
2472 of Crary Ice Rise as part of the Ross Ice Shelf Project (Clough & Hansen, 1979). The
2473 second was the 2017 HWD2 drill hole near the centre of the ice shelf (Stevens et al.,
2474 2020). Apart from these two drill holes, all other inferences of sub-shelf bathymetry
2475 depths have been from seismic surveying, or the gravity inversion of Tinto et al.
2476 (2019). The majority of seismic surveys on the Ross Ice Shelf were accomplished
2477 during two projects, the International Geophysics Year traverses of the late 1950s
2478 and early 1960s (Crary et al., 1962; Crary, 1959; Crary & Robinson, 1962), and the
2479 Ross Ice Shelf Geophysical and Glaciological Survey (RIGGS, 1973-1974 Bentley,
2480 1984). These extensive surveys systematically covered the entire ice shelf, collecting
2481 223 observations of bathymetry with a mean spacing of approximately 40 km be-
2482 tween points (Figure 4.1b).

2483

2484 These seismic and drill hole depths have been included in various Antarctic bed
2485 and bathymetry products (Fretwell et al., 2013; Le Brocq et al., 2010; Timmermann
2486 et al., 2010). As discussed later, Tinto et al. (2019) conducted a gravity inver-
2487 sion over the entirety of the ice shelf with data from the Ross Ocean and ice Shelf
2488 Environment, and Tectonic setting Through Aerogeophysical surveys and modelling
2489 project (ROSETTA-Ice). This provided a significantly improved resolution over just
2490 the interpolation of the sparse seismic data. This gravity-inverted bathymetry was
2491 later incorporated in the BedMachine bed compilation (Morlighem, 2022; Morlighem
2492 et al., 2020). This chapter focuses on once again improving the sub-Ross Ice Shelf
2493 Bathymetry model. Following Tinto et al. (2019), we also use a gravity inversion of
2494 the ROSETTA-ice data to model the bathymetry. However, we conduct additional
2495 processing of the gravity data, and apply an entirely new gravity inversion algo-
2496 rithm, as described in Chapter 3. Additionally, our method provides an assessment
2497 of the spatial uncertainty of the resulting model, a useful component needed for the
2498 ocean modelling community (Goldberg et al., 2020).

2499

4.2 Methods

2501 Here we describe the three main methodologies of this chapter; 1) the gravity reduction
 2502 process (Figure 4.2a), 2) the bathymetric inversion process (Figure 4.2b), which
 2503 is explained in detail in Chapter 3 and briefly re-introduced here, and 3) the use of a
 2504 Monte Carlo simulation to quantify spatial uncertainty in the resulting bathymetry.

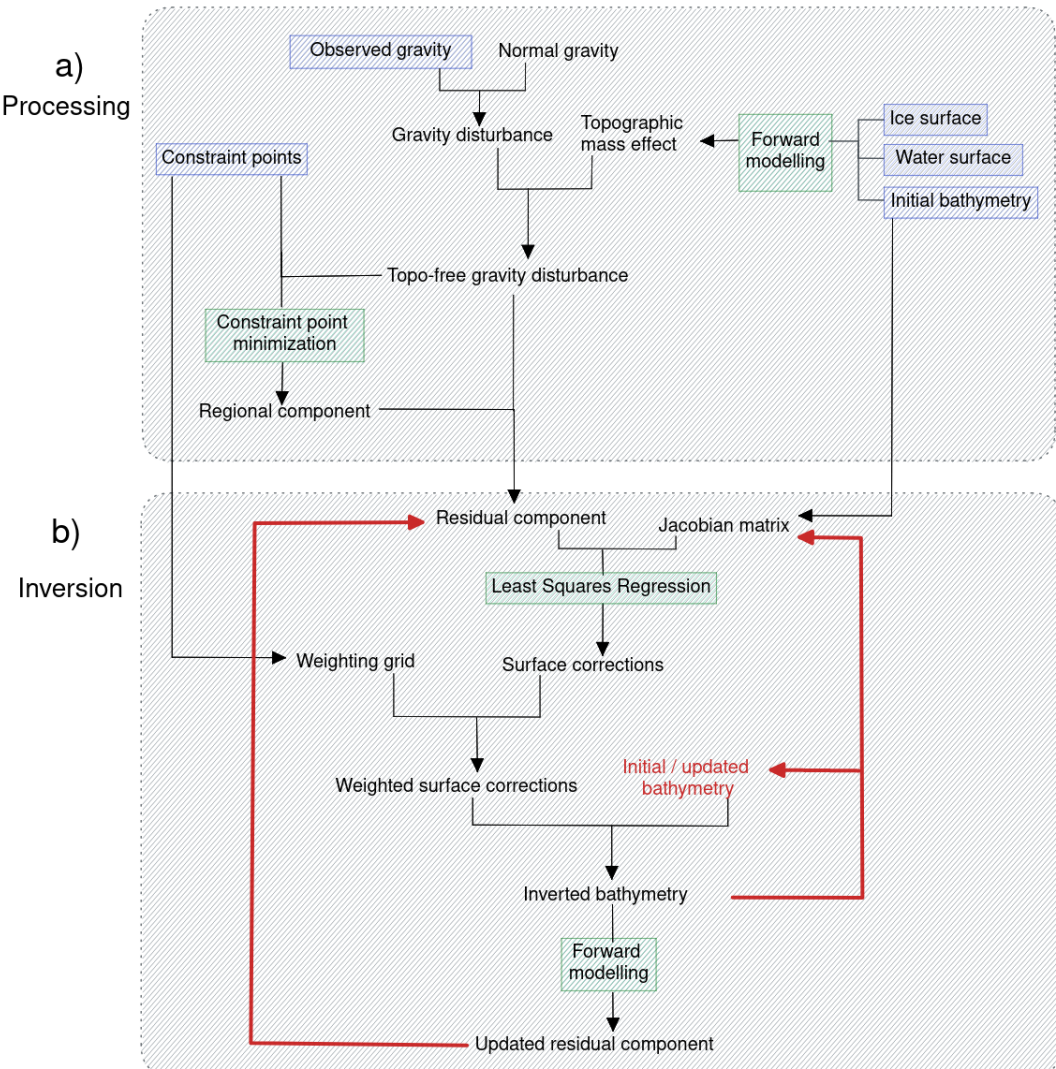


Figure 4.2: Schematic workflow diagram for a) gravity processing steps and b) running the inversion. Blue boxes show the input datasets, green boxes show the key processes and red lines signify iterative components of the inversion.

4.2.1 Gravity reduction

2505 A common task in geophysics is the removal of predictable noise to help amplify the
 2506 signal of interest. This is the basis of gravity reduction; the process of isolating the
 2507 desired gravity signal from the raw measurements of the Earth's gravitational field.
 2508 The magnitude of Earth's gravitational acceleration, which we will refer to as *gravity*
 2509 from here-on, ranges from $\sim 978,000$ to $\sim 983,000$ mGal, from the equator to the
 2510 poles, respectively (Hofmann-Wellenhof & Moritz, 2006). The range in these values,
 2511 approximately 5000 mGal, vastly outweighs the typical values of gravity anomalies
 2512

resulting from geologic features of interest. These anomalies of interest are typically on the order of magnitude of 10's of mGal. This exemplifies the issue of removing *noise* which has a significantly greater magnitude than the *signal* of interest.

Here, we start the gravity reduction process with observed gravity. We take observed gravity to be the signal which is produced by 1) the gravitational attraction of all massive bodies in Earth and 2) the rotation of the Earth. This means non-geological and time-dependent effects such as machine drift, tidal changes, aircraft manoeuvres and the effect of measuring gravity on a moving platform (Eötvös correction) have already been removed from the observed gravity (Hinze et al., 2005; Hinze et al., 2013). With this, observed gravity is defined as;

$$g_{obs}(p) = \gamma(p) + g_{geology}(p) \quad (4.1)$$

where, for an observation point p , $g_{obs}(p)$ is the observed gravity, $\gamma(p)$ is the attraction of the *normal* Earth and $g_{geology}(p)$ encompasses the gravity effects of all deviations between the *normal* Earth and the real Earth. This *normal* Earth is often taken as a single surface (here the reference ellipsoid) with a constant density above (ρ_{air}) and a constant density below (ρ_{crust}). Therefore, deviations between the *normal* and real Earth include 1) any masses above the ellipsoid which don't have the uniform density of air or 2) any masses below the ellipsoid which don't have the uniform density of crust. For a bathymetry inversion, the gravity signal of interest is a component of $g_{geology}$, which we must separate from γ .

4.2.1.1 Attraction of normal Earth

Observed gravity varies greatly due to the observation point's position, both based on latitude and elevation. Due to the oblate shape of the Earth, gravity is generally lower at low latitudes due to 1) increased distance from the center of Earth's mass, and 2) more importantly, the increased tangential velocity (Jacoby & Smilde, 2009). Additionally, there is a decay of gravity with increased elevation, due to an increased distance from the center of Earth's mass. These effects aren't related to the geologic variations of interest and thus should be removed. Historically, these effects of latitude and elevation were approximated separately, using the International Gravity Formula (*Latitude correction*) and the *Free-air correction*, respectively (Hinze et al., 2005). Alternatively, Li and Götze (2001) derived an analytical solution to the gravity effects of an ellipsoid, at any point on or above its surface¹. With this, the Latitude and Free-air corrections are combined, and their approximations are replaced with closed-form solutions. By subtracting the normal gravity from the observed gravity at each observation point the gravity disturbance is found, where

$$\delta g(p) = g_{obs}(p) - \gamma(p), \quad (4.2)$$

where for an observation point p , $\delta g(p)$ is the gravity disturbance, $g_{obs}(p)$ is the observed gravity, and $\gamma(p)$ is the normal gravity (*Understanding the Bouguer*

¹Note that the normal gravity calculation with this analytical solution is not valid below the ellipsoid. While this is irrelevant for most locations on Earth, West Antarctic has negative geoid elevations, meaning observations near sea level are likely below the reference ellipsoid, invalidating the normal gravity calculation. For these situations, the use of a quasi-ellipsoid is recommended (*Understanding the Bouguer Anomaly*, 2017; Vajda et al., 2008b)

2550 Anomaly, 2017).

2551

2552 The observation point, p , is defined by three coordinates; latitude, longitude, and
 2553 geometric height (ellipsoidal height). It is a common mistake in geophysical studies
 2554 for the normal gravity calculation to use the point p 's orthometric height (geoidal
 2555 height or mean sea level), instead of its geometric height (Oliveira et al., 2018). This
 2556 results in the calculation of normal gravity at a different point in 3D space relative
 2557 to the observation. This calculation, while truly determining the gravity anomaly
 2558 (a.k.a. free-air anomaly), is not well-suited for geological interests because the grav-
 2559 ity anomaly contains signal from centrifugal acceleration effects due to the different
 2560 locations of the points. Conversely, the gravity disturbance is defined as the differ-
 2561 ence between gravity and normal gravity at the same point, and thus only contains
 2562 signal resulting from geologic sources (Hofmann-Wellenhof & Moritz, 2006). The
 2563 difference between the gravity anomaly and the disturbance for Antarctica ranges
 2564 from -20 to +20 mGal (See Figure C.1 in appendix C for a comparison). It is com-
 2565 mon for studies to correctly use the gravity disturbance while referring to it as the
 2566 free-air anomaly to adhere to tradition. Combining Equations 4.1 and 4.2, shows
 2567 that the gravity disturbance, δg , results solely from deviations between the theo-
 2568 retical model of the Earth (the *normal* Earth) and the true density variations and
 2569 topography of the Earth (Vajda et al., 2004). Figure 4.3 compares observed grav-
 2570 ity, normal gravity, the gravity disturbance, and the gravity anomaly for Antarctica.

2571

2572 4.2.1.2 Topographic mass effects

2573 Typically, geophysical studies are interested in interpreting or inverting gravity sig-
 2574 nals resulting from subsurface features. To accommodate this, all other gravity
 2575 effects must be computed and removed from the gravity disturbance. These other
 2576 effects include the gravity resulting from masses bound by known surfaces, referred
 2577 to as *topographic* or *terrain masses*. These surfaces include, but are not limited to,
 2578 the rock surface (topography), the ocean surface (geoid), the seafloor (bathymetry),
 2579 and the ice surface. Together, the gravity resulting from these masses is referred to
 2580 as the *topographic mass effect*. Correcting the gravity disturbance for these topo-
 2581 graphic masses yields the *topo-free gravity disturbance* δg_{TC} , where

$$2582 \quad \delta g_{TC}(p) = \delta g(p) - g_{topo}(p). \quad (4.3)$$

2583 $g_{topo}(p)$ represents the summed topographic mass effect. δg_{TC} is sometimes re-
 2584 ferred to as the *Bouguer disturbance*, owing to the historic use of the *Bouguer
 2585 anomaly*. In accordance with Vajda et al. (2007), we refer to it as the *topo-free
 2586 gravity disturbance* to clarify that the ellipsoid has been used instead of the geoid
 2587 in all reduction steps. In the past, the topographic mass effect has been split into
 2588 the Bouguer slab correction and the terrain correction. The Bouguer slab correction
 2589 approximates the topographic masses as laterally infinite flat slabs, while the terrain
 2590 correction accounts for the overestimation of the Bouguer slab resulting from the
 2591 assumption of the flat slab. With modern computing able to efficiently calculate
 2592 the gravity resulting directly from a topographic surface (Fatiando a Terra Project
 2593 et al., 2023), there is no need for the separate two-step correction.

2593

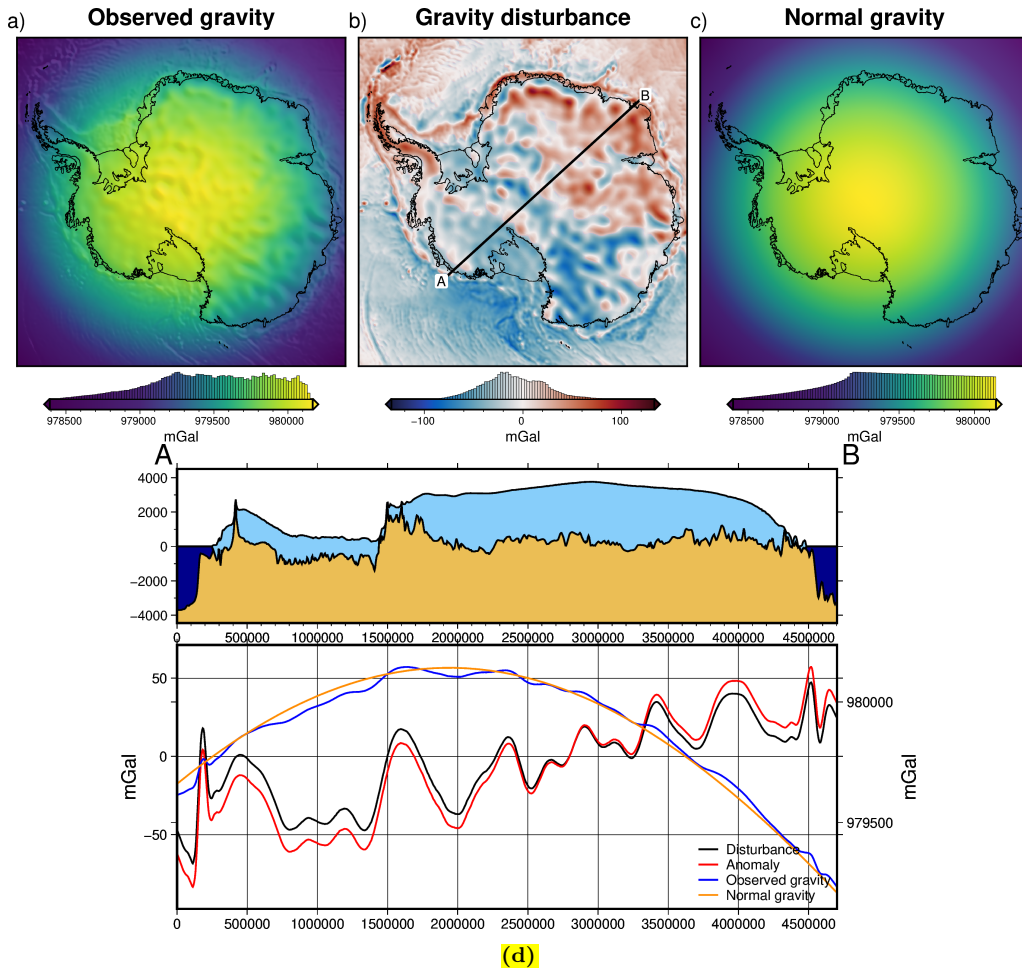


Figure 4.3: Observed gravity data reduction for Antarctica. **a)** Observed gravity data from Förste et al. (2014) at a geodetic observation height of 10 km. **b)** The gravity disturbance at 10 km height, defined as **a-c**. **c)** The normal gravity calculated at the same observation points as **a** using the closed-form equations of Li and Götze (2001). **d)** Profile A-B across Antarctica, location shown in **b**. Gravity disturbance (black) and anomaly (red) values are on the left y-axis, while observed (blue) and normal (orange) gravity values are on the right y-axis.

2594 The topographic mass effect reflects all topographic deviations (including topog-
 2595 raphy of the ice, water, and seafloor) between the *normal* Earth and the real Earth.
 2596 The *normal* Earth model is shown in Figure 4.4a, as defined by air above the ellipsoid
 2597 and crust below. A simplified model of the true Earth is shown in Figure 4.4b, and
 2598 contains air, ice, water, crust, and various geologic bodies within the crust. These
 2599 masses are separated in Figure 4.4c into components above and below the ellipsoid.
 2600 From this, the masses which are anomalous with respect to the *normal* Earth can
 2601 be distinguished, as shown in Figure 4.4d. These anomalous masses include water,
 2602 ice, and crust above the ellipsoid, and air, ice, water, and geologic bodies below the
 2603 ellipsoid. The gravitational effect of these anomalous masses can be approximated
 2604 by assuming each mass's density and setting it relative to the density of the com-
 2605 ponent of the *normal* Earth which the mass is replacing. These relative densities
 2606 are shown in the key of Figure 4.4d. Calculating and summing the gravity effect
 2607 of each of the components of Figure 4.4d (excluding the geologic bodies) gives the
 2608 topographic mass effect. Subtracting this from the gravity disturbance gives the
 2609 topo-free gravity disturbance².

²The use of the reference ellipsoid as the bounding surface of the topographic mass effect

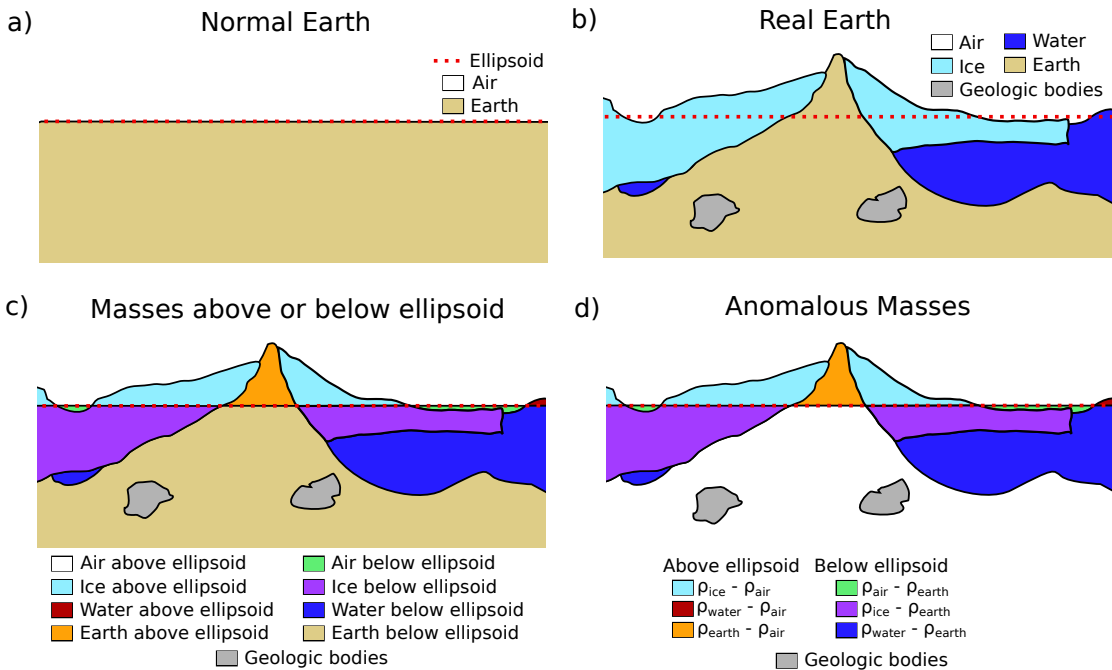


Figure 4.4: Components of the topographic mass effect and resulting topo-free gravity disturbance, or Bouguer disturbance. **a)** The normal Earth model, **b)** a simplified real Earth model. **c)** Topographic masses separated into components above and below the ellipsoid. **d)** Real Earth topographic masses which are anomalous with respect to the normal Earth. Note if the reference level (red dashed line) is switched from the ellipsoid to the geoid, this would result in a Bouguer anomaly.

2610

2611 To compute the topographic mass effect, the anomalous masses from Figure
 2612 4.4d are discretized into a series of vertical right-rectangular prisms. To achieve the
 2613 geometry and density configuration of Figure 4.4d, three sets of prisms are used, as
 2614 shown in Figure 4.5c-e.

- 2615 1. Prisms between the ice surface and the ellipsoid are assigned densities of $\rho_{ice} -$
 2616 ρ_{air} for prisms above the ellipsoid, and $\rho_{air} - \rho_{ice}$ for prisms below the ellipsoid.
- 2617 2. Prisms between the water surface (ice base) and the ellipsoid are assigned
 2618 densities of $\rho_{water} - \rho_{ice}$ for prisms above the ellipsoid, and $\rho_{ice} - \rho_{water}$ for
 2619 prisms below the ellipsoid.
- 2620 3. Prisms between the rock surface (topography onshore and bathymetry off-
 2621 shore) and the ellipsoid are assigned densities of $\rho_{rock} - \rho_{water}$ for prisms above
 2622 the ellipsoid, and $\rho_{water} - \rho_{rock}$ for prisms below the ellipsoid.

2623 This configuration of prisms correctly discretizes the topographic mass effect be-
 2624 cause the ice surface is equal to the water surface in areas of no ice thickness, and
 2625 the water surface is equal to the rock surface in areas of no water thickness. Due
 2626 to this, the overlap between the three sets of prisms, shown in Figure 4.5b gives the
 2627 appropriate densities, as defined in Figure 4.4d. From these three sets of prisms, the
 2628 topographic mass effect can be calculated at the gravity observation points using the
 2629 analytical solutions of Nagy et al. (2000). As a demonstration, the topographic mass

calculations results in a topo-free gravity disturbance while using the geoid as the bounding surface would result in a Bouguer anomaly (Vajda et al., 2006).

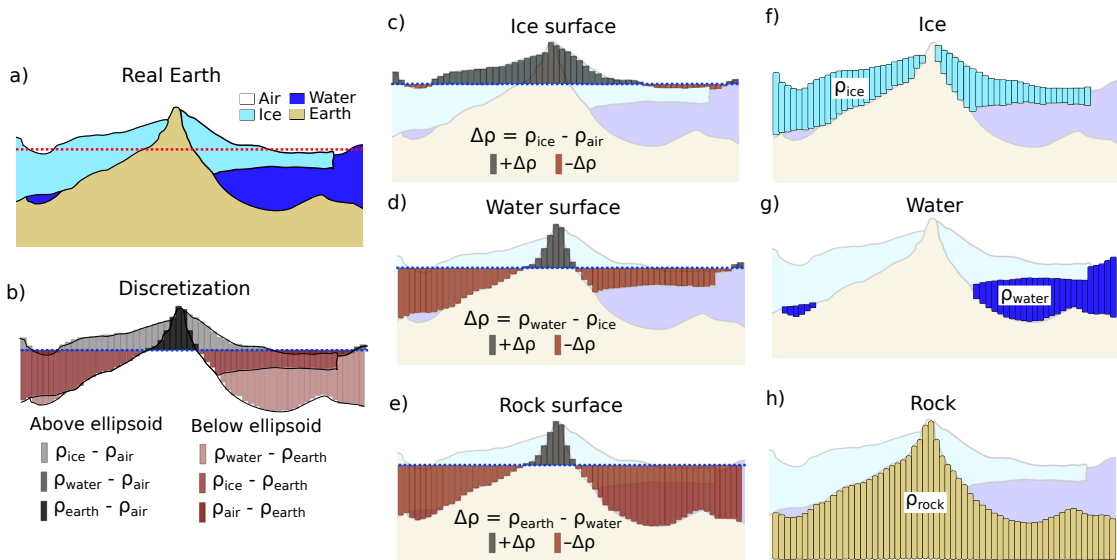


Figure 4.5: Discretizing the topographic mass effect. **a)** The simplified real Earth model, with air, ice, water, and earth. **b)** the resulting anomalous masses relative to the *normal* Earth, as shown in Figure 4.4d. **c)** Prisms between the ellipsoid and the ice surface, **d)** prisms between the ellipsoid and the water surface (ice base), and **e)** prisms between the ellipsoid and the rock surface (topography onshore and bathymetry offshore). Overlap of prisms from **c-e** creates the different shades shown in **b**. The alternative discretization approach, commonly used, is shown in **f-h** where the prism layers are bound both above and below by topographic layers, or arbitrary references (bottom of prisms in **h**), instead of by the normal Earth reference surface (ellipsoid). Additionally, density values of the prisms are related to the material they discretize and are not relative to the expected density of the normal Earth.

effect for Antarctica is calculated using topographic data from Bedmap2 (Fretwell et al., 2013), referenced to the WGS-84 ellipsoid. The observed satellite gravity data has a low spatial resolution, so the lower resolution of Bedmap2 over BedMachine v3 is insignificant. The calculated topographic mass effect, the gravity disturbance, the resulting topo-free gravity disturbance, and the topographic mass effect from the alternative method of discretization (Figure 4.5f-h) are shown in Figure 4.6.

The theoretical topo-free gravity disturbance is the gravity effect caused by and only by anomalous subsurface bodies, which have a density different from the assumed constant density of the crust. In reality, there are additional components of the topo-free gravity disturbance resulting from 1) noise in the observed data, 2) non-uniform densities used in the topographic mass effect calculation, and 3) inaccurate topographic data used for the topographic mass effect calculation. In most geophysical applications, the uncertainty of the topographic data is small compared to other uncertainties in the analysis, and thus component #3 is assumed to be zero. Conversely, for the case of a bathymetry inversion, this component of the topo-free disturbance resulting from the inaccuracies of the topography (bathymetry) data is the signal of interest. Next, we will isolate this component from the remainder of the topo-free gravity disturbance.

2649

2650 4.2.1.3 Regional separation

2651 Here, we separate the topo-free gravity disturbance into components resulting from
2652 1) subsurface geologic variations and 2) inaccuracies between the true bathymetry

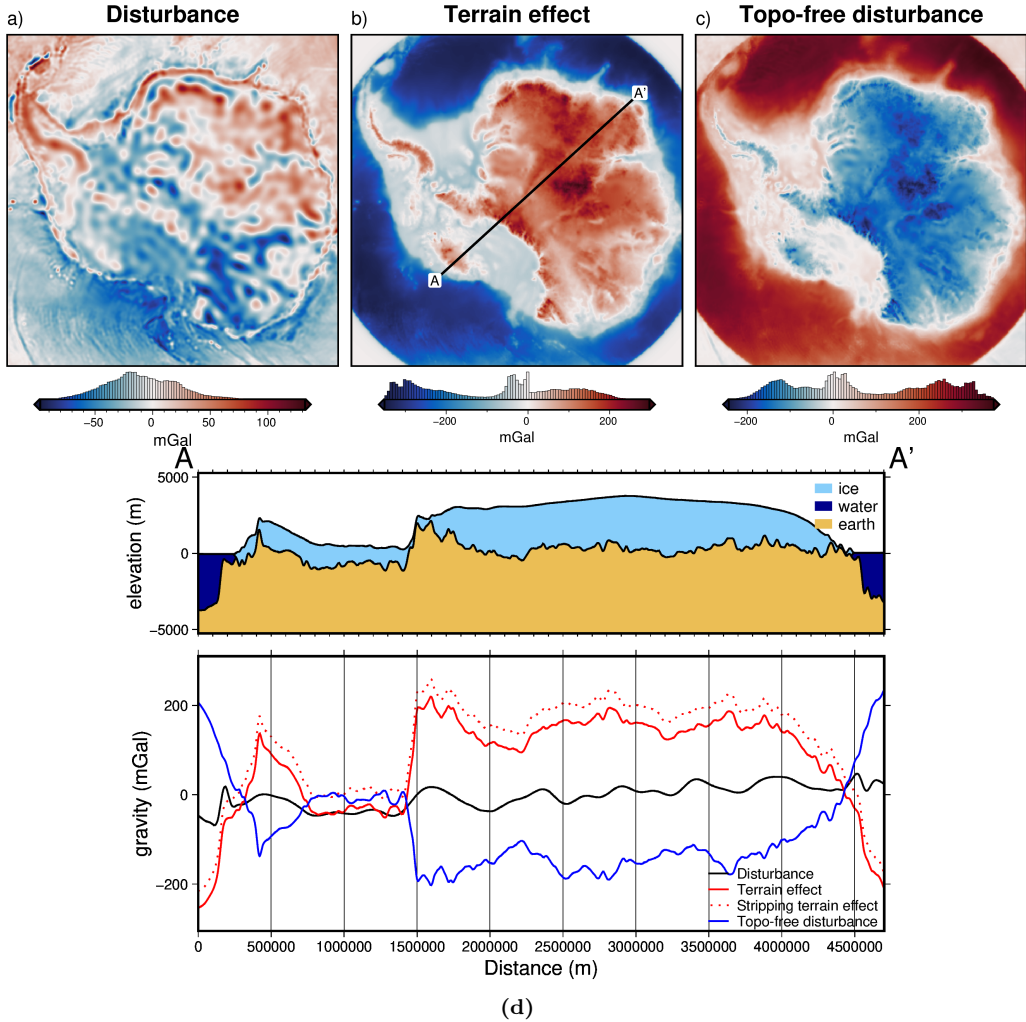


Figure 4.6: Topographic mass effect at 10 km height for Antarctica, from Bedmap2 topographic data (Fretwell et al., 2013). **a)** Gravity disturbance at a geodetic observation height of 10 km, from Figure 4.3b. **b)** The combined gravity effect of the anomalous masses defined in Figure 4.4d and discretized following 4.5b. **c)** The topo-free gravity disturbance, calculated as **a** - **b**. **d)** Profile A-A' across Antarctica, location shown in **b**. The dotted red line shows the terrain mass effect results of the alternative discretization method shown in Figure 4.5f-h. A DC shift was applied to attempt to remove the offset.

and the low-resolution bathymetry data used for the terrain mass effect. These are referred to as the regional and residual components, respectively. Chapter 3 highlighted the importance of accurately estimating and separating this regional component from the residual. The regional estimation was found to be the largest source of uncertainty in several synthetic bathymetry inversions, as well as other Antarctic bathymetry inversions (Brisbourne et al., 2014). While there are many techniques to estimate the regional component, we will use constraint point minimization due to its demonstrated effectiveness over the other methods (Section 3.2.4). This technique samples the topo-free gravity disturbance at points of known bathymetry depth, referred to as the constraint points. Since the depth is known here, the residual component of gravity should be near zero, and thus the regional component should entirely equal the topo-free gravity disturbance. Using these sampled values, the entire model domain is gridded with an interpolation, using either bi-harmonic splines (Uieda, 2018) or minimum curvature (Smith & Wessel, 1990). The resulting grid makes up the regional component, and when subtracted from the

2668 topo-free gravity disturbance gives the residual component. This residual compo-
 2669 nent is the input into the inversion.

2670

2671 4.2.2 Bathymetry inversion

2672 Here we start by briefly summarising the bathymetry inversion workflow described
 2673 in Chapter 3, and shown schematically in Figure 4.2b. Then we compare our method
 2674 to several other commonly used bathymetry inversion algorithms. The basis of mod-
 2675elling bathymetry with a gravity inversion is that the bathymetry surface, which is
 2676 a contrast between lower-density material (seawater) and higher-density material
 2677 (sediment) creates a measurable effect on Earth’s gravity. Our inversion begins by
 2678 computing the Jacobian matrix (Equation 3.7), which is a quantitative means of
 2679 describing the sensitivity of the residual gravity data to changes in the height of
 2680 each grid cell of bathymetry. In other words, the Jacobian quantifies the ratio be-
 2681 tween the amplitude of bathymetric features and the gravity anomaly resulting from
 2682 them. From this Jacobian matrix, the optimal change to apply to each bathymetry
 2683 grid cell to minimize the residual gravity data is estimated. This is in the form of
 2684 a surface correction grid, with a value for each grid cell of bathymetry. Since there
 2685 are locations of already known bathymetry depths (constraint points), this surface
 2686 correction grid should be zero at these points. To achieve this, a weighting grid is
 2687 calculated, which is based on the minimum distance between each grid cell and the
 2688 nearest constraint point. These distance values are then normalized from 0 to 1,
 2689 with 0 being the cells closest to the constraints, and 1 being the cells furthest. The
 2690 surface correction grid is multiplied by this weighting grid, to achieve a correction
 2691 value of 0 m at the constraints, smoothly tapering off to the full estimated correction
 2692 values at a distance.

2693

2694 With this weighted surface correction grid, the original bathymetry depths are
 2695 updated. To ensure the updated bathymetry doesn’t intersect the ice base, the ice
 2696 base topography is set as an upper-bounding surface. The forward gravity of this
 2697 updated bathymetry is then re-calculated, with the prism configuration and densi-
 2698 ties shown in Figure 4.5e. The updated forward gravity is used to recalculate the
 2699 topo-free gravity disturbance. Using the same regional component as calculated be-
 2700 fore the inversion (Section 4.2.1.3), an updated residual gravity is computed. This
 2701 is then input into the next iteration of the inversion (red lines in Figure 4.2b). Iter-
 2702 ations continue until a set of user-defined stopping criteria are met; 1) a maximum
 2703 number of iterations is reached, 2) a minimum value of the ℓ^2 -norm of the residual
 2704 is reached, or 3) there is no significant variation in the ℓ^2 -norm in two consecutive
 2705 iterations.

2706

2707 This process describes a single *inversion*. The critical step in this inversion, deter-
 2708 mining the surface correction values from the sensitivity matrix, includes a damping
 2709 parameter that controls the smoothness of the resulting inverted bathymetry. This
 2710 damping parameter value directly affects the resulting bathymetry model and needs
 2711 to be carefully chosen. For this, we follow the cross-validation routine described in
 2712 Chapter 3 from Uieda and Barbosa (2017). This involves running the entire inver-
 2713 sion for a suite of different damping parameter values. The input gravity data to
 2714 these inversions is split into a *testing* set and a *training* set. The inversion only

uses the *training* set. After each inversion, the forward gravity effect of the updated bathymetry model is calculated at the points of the *testing* set. The root mean squared difference between the testing gravity values and the forward gravity values gives the *score* of each cross-validation. The damping parameter which produces the lowest score is chosen as the optimal value.

2720

2721 4.2.3 Starting bathymetry

2722 An initial bathymetry model for the inversion is needed to compute the topographic
2723 mass effect and to run the inversion. The weighting grid constrains the inversion
2724 from changing the starting grid values at the constraint points. For this reason,
2725 the starting model should be carefully created. As discussed in the previous chapter
2726 (Chapter 3, Section 3.4.2), there are several methods of creating the starting
2727 model from the sparse measurements at the constraint points. Here, we use and
2728 compare two techniques for interpolating these constraint point values over the en-
2729 tire domain; tensioned minimum curvature (Smith & Wessel, 1990) and bi-harmonic
2730 splines (Sandwell, 1987). See Chapter 3 Section 3.4.2 for the details of these gridding
2731 techniques. Figure 4.1b

2732

2733 4.2.4 Uncertainty quantification

2734 A major component missing from many bathymetry inversions is assessing the spa-
2735 tially variable uncertainty in the resulting bathymetry depths. This uncertainty
2736 arises from a multitude of sources, including uncertainty in 1) the gravity data mea-
2737 surements, 2) constraint point depths, 3) user-defined variables, such as ice, water,
2738 or sediment density, and 4) uncertainties associated with the various methodologies
2739 of the inversion. Here we use a sampling-based approach to estimate the uncertainty,
2740 where the uncertainty of the *inputs* is used to assess the uncertainty of the *output*,
2741 in this case, the inverted bathymetry. This general method of uncertainty analysis
2742 is referred to as Monte Carlo sampling (Jansen et al., 1994).

2743

2744 For a generalized problem of inputs \mathbf{x} and a function $y(\mathbf{x})$, Monte Carlo sim-
2745 ulation provides a means to answer the two following questions; 1) what is the
2746 uncertainty in $y(\mathbf{x})$ given the uncertainty in \mathbf{x} ? and 2) what are the relative im-
2747 portance of the various components of \mathbf{x} with respect to $y(\mathbf{x})$ (Helton et al., 2006)?
2748 While there are many components that contribute to the overall inversion uncer-
2749 tainty, here we will examine 1) uncertainty in the gravity data values, 2) depth
2750 uncertainty of the constraint points, 3) uncertainty in the chosen density values
2751 used for ice, water, and earth, and 4) uncertainties related to user-chosen parameter
2752 values in the inversion. Uncertainties that are not covered here as those which relate
2753 to processes of the inversion which don't have associated measurable input uncer-
2754 tainties. This includes the use of spatially non-variable density values for ice, water,
2755 or earth, or the effects of discretizing a real topographic surface as a series of prisms.

2756

2757 The Monte Carlo simulation consists of sampling the input parameters N times
2758 from their respective distributions (Figure 4.7b) and running the entire inversion
2759 workflow for each of the N parameter sets (Figure 4.7c). For each bathymetry grid

cell, the weighted standard deviation of the N resulting inverted bathymetries is found (Figure 4.7d). This grid of cell-specific standard deviations show where the input parameters have a large effect on the bathymetry results. This grid is used as our estimate of the spatial uncertainty in the inversion. The grid of cell-specific weighted median values is then taken to be the optimal inversion result. These cell-specific statistics are weighted by the inverse square of each inverted bathymetry's RMS difference with the constraint point depths (Figure 4.7d). This reduces the bias of inversions in the ensemble which performed poorly, as defined by not adhering to the constraints (Schnaidt & Heinson, 2015). To assess the relative importance of the input parameters, in addition to the complete Monte Carlo simulation, additional simulations are run where each parameter's effect is isolated. For these, only a singular parameter is sampled from its distribution, so that the resulting spatial standard deviation is due solely to the uncertainty of that parameter.

2773

The parameters included in the Monte Carlo sampling are; 1) the gravity disturbance data, 2) the constraints point depths, 3) the gridding parameters to create the starting bathymetry, 4) the density of ice, 5) the density of water, 6) the density of sediment, and 7) gridding parameters for the constraint point minimization technique of regional gravity estimation (Figure 4.7b). For the full Monte Carlo simulation, with all the above inputs sampled from their respective distributions, the entire inversion workflow needs to be repeated with each of the N parameter sets. This includes 1) creating the starting bathymetry model from the constraint points (Section 4.2.3), 2) calculating the terrain mass effect to get the topo-free gravity disturbance (Section 4.2.1.2), 3) estimating the regional component of the disturbance and removing it (Section 4.2.1.3), and 4) running the damping parameter value cross-validation (Section 4.2.2) to obtain the inverted bathymetry (Figure 4.7). For the individual Monte Carlo simulations, only portions of this workflow need to be repeated. For example, if only the gravity disturbance is sampled, only the regional field and inversion need to be re-run. The starting bed and topographic mass effect calculated during the baseline inversion are re-used.

2790

Due to the computational demand of a full inversion workflow, the total number of inversions in each Monte Carlo simulation is limited. To ensure the uncertainty distributions of the inputs are adequately sampled with this limited number of possible runs, we have used Latin hypercube sampling where possible (Jansen et al., 1994). This sampling technique is well suited for computationally demanding tasks since it ensures proper coverage of the uncertainty distributions of the sampled values, despite a low number of samples Helton et al., 2006. To accomplish this, for a Monte Carlo simulation of N runs, the given distributions are split into N intervals of equal probability and one value is chosen from each interval. The N values for each parameter are then randomly paired to get N sets of sampled input parameter values (Helton et al., 2006). Since the gravity data and constraint points are each sampled on a point-by-point basis, Latin hypercube sampling is unnecessary and random sampling is used. Figure 4.8 shows a $N = 9$ comparison of random sampling and Latin hypercube sampling for a two-parameter simulation.

2805

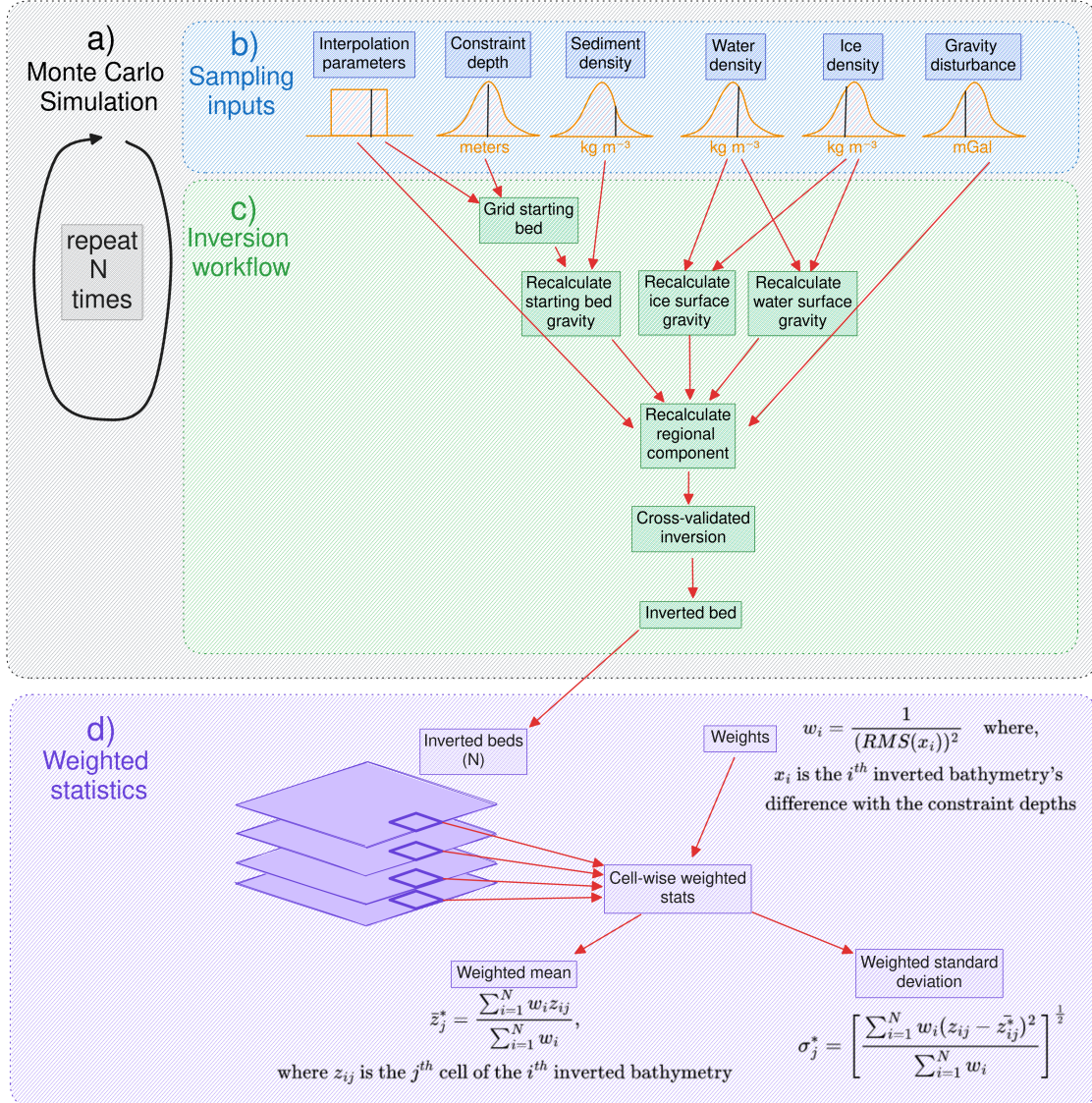


Figure 4.7: Schematic workflow diagram for the Monte Carlo uncertainty analysis. **a)** The Monte Carlo simulation, consisting of **b)** sampling the inputs from their respective distributions, and **c)** implementing the various components of the workflow, depending on which inputs have been sampled. This process is repeated N times, yielding N inverted bathymetry grids. **d)** Weighted cell-specific statistics are computed. Each inverted bathymetry grid (large purple boxes) is weighted by the respective inversion's constraint depth RMSE. These weights are used to compute the weighted mean and weighted standard deviation of each grid cell (bold purple square).

2806 4.3 Relation to past bathymetry inversions

2807 The fundamental theory in all bathymetry inversions is based on the fact that the
 2808 density contrast across the bathymetry surface produces a measurable gravity ef-
 2809 fect. This phenomenon gives rise to several techniques to convert observed gravity
 2810 data into bathymetric depths. This by definition is a geophysical inverse problem
 2811 (Oldenburg & Li, 2005), but the methods chosen to solve it vary from 3D rigorous
 2812 inversions to iterative 2D forward modelling. Our inversion method follows a clas-
 2813 sical least-squares approach to solving the inverse problem, while our uncertainty
 2814 and sensitivity analysis follows a Bayesian approach (Aster et al., 2018). Here, we
 2815 compare our inversion method and workflow to other bathymetry inversions. We
 2816 attempt to include all past studies related to Antarctica, as well as several from

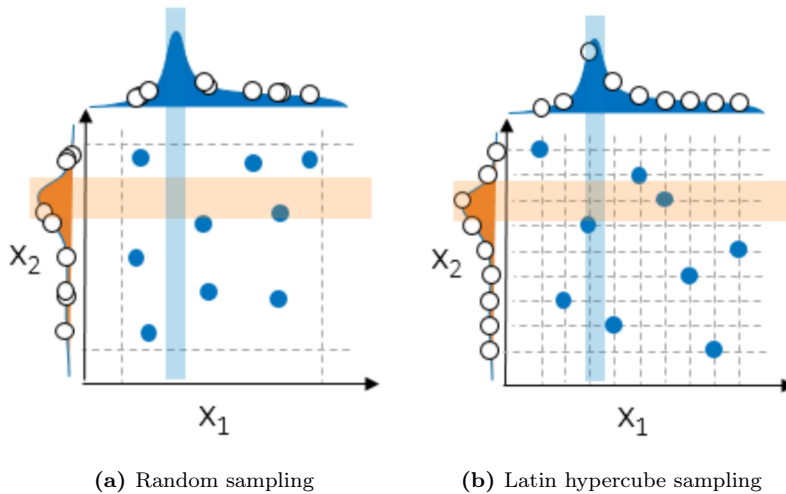


Figure 4.8: Comparison of sampling methods for a Monte Carlo simulation of two variables (X_1 and X_2) with 9 samples drawn from each. **a)** Random sampling, where values are drawn at random from each variable's distribution, and **b)** Latin hypercube sampling, where values are drawn from equal-probability intervals. Note the effective coverage of the distributions in **b** relative to **a**. The figure is adapted from Koch et al. (2017).

2817 Greenland. We start by comparing our technique for the gravity reduction process,
 2818 followed by differences in the actual inversion, and finally by differences in our as-
 2819 sessment of uncertainty.

2820

2821 4.3.1 Gravity reduction comparison

2822 One of the largest differences between our method and past studies is the gravity
 2823 reduction process. We employ a rigorous terrain mass effect calculation to obtain
 2824 a topo-free gravity disturbance, often referred to as a Complete Bouguer Anomaly
 2825 (Vajda et al., 2007). Theoretically, this gravity signal contains only effects due to
 2826 subsurface density anomalies and inaccuracies in calculating the terrain mass effect.
 2827 Our method isolates the gravity effect of this inaccuracy since it is due to the de-
 2828 viations between the starting model of bathymetry and the true bathymetry. This
 2829 is referred to as our residual component of the topo-free gravity disturbance. While
 2830 most other bathymetry inversion studies achieve a similar residual anomaly, they
 2831 complete this procedure in a theoretically different way, which may be introducing
 2832 unnecessary errors. The differences arise from other studies ignoring the reference
 2833 surface (the ellipsoid) for all calculations after the normal gravity correction.

2834

2835 The sign of a gravity disturbance value informs the interpreter as to whether
 2836 the true Earth has either excess or deficient mass at that location with respect to
 2837 the normal Earth. Therefore, the absolute level of gravity disturbance data should
 2838 be retained, even though direct offsets (DC shifts) don't alter the amplitude of
 2839 the gravity anomalies. For this reason, the reference surface used in the normal
 2840 gravity calculation (here the ellipsoid) should be continued to be used in all further
 2841 calculations of topographic masses, including in the forward calculation made during
 2842 the inversion, as shown in Figure 4.5 b. Many studies instead have discretized the
 2843 ice, water, and starting bathymetry surfaces into prism layers which either have
 2844 arbitrary references or density values not relative to the normal Earth model. This

alternative discretization is shown in Figure 4.5f-h. For example, the gravity effect of ice, if not just ignored (e.g., Cochran & Bell, 2012; Jordan et al., 2020b; Millan et al., 2017; Yang et al., 2020b), is typically removed via a "stripping" technique (Vajda et al., 2008a), (e.g., Greenbaum et al., 2015; Millan et al., 2020; Muto et al., 2013a; Yang et al., 2021). This stripping involves calculating the forward gravity of prisms with tops defined by the ice surface, bottoms defined by the ice base, and densities defined by the assumed density of ice (Figure 4.5f). Additionally, the prisms which comprise the starting bathymetry model for many inversions are bound above by the starting bathymetry, and below by an arbitrary constant depth (Figure 4.5h) (e.g., Muto et al., 2013a; Tinto et al., 2019). The forward gravity calculations of this style of discretization can introduce several errors:

1. The largest of these errors is an offset in the mean value of the forward gravity relative to the observed gravity. This offset needs to be estimated and removed prior to comparison with the observed data. The DC-shift used to remove the offset is typically estimated by finding a value that minimizes the difference between the observed and predicted data at locations of known bathymetry (e.g., Boghosian et al., 2015; Cochran et al., 2020; Constantino et al., 2020; Eisermann et al., 2020; Millan et al., 2017; Muto et al., 2013a). This additional step, referred to as "pinning", is unnecessary in our implementation, due to adhering to a rigorous determination of the terrain mass effect. If an incorrect DC shift is applied, the significance of the zero level of the topo-free gravity disturbance is lost. The value of 0 signifies that the simplified model of the Earth (i.e. the starting bathymetry model) is equal to the true Earth density distribution. Shifting this zero-level due to errors in estimating the DC-shift may lead to a shift in the inverted bathymetry, especially if the inversion domain isn't well constrained. The DC-shifted terrain mass effect and the rigorous terrain mass effect for Antarctica are compared in Figure 4.6d.
2. The forward gravity calculation with this style of discretization results in slightly different amplitude anomalies compared to the true terrain mass effect. This difference is due to the different densities assigned to the prism layer between the two techniques (Figure 4.5). While this difference is likely below the range of uncertainties in the gravity error, it is an unnecessary addition of error to the gravity reduction process.
3. The last drawback to using this alternative discretization is an increased gravitational edge effect. As shown in Figure 4.5, the average densities and prism heights are larger with this technique. This increases the overall decay of calculated gravity at the edges of the model space, due to the contrast with the void-space beyond the model domain. To account for this, a larger buffer zone is needed, which can significantly increase the computational requirements during forward modelling (see Chapter 3 Section 3.2.2.2).

4.3.1.1 Regional separation

The last step in the gravity reduction process for bathymetry inversion is separating the regional and residual signals, where the residual signal should theoretically be entirely a result of the bathymetry surface. Some techniques commonly used for this are described in Chapter 3 Section 3.2.4. Past bathymetry inversions have used a variety of these techniques, as summarized below;

- 2891 1. Zero or uniform adjustment; For small inversion domains the regional field
 2892 is sometimes assumed to be minimal. In these scenarios, past studies have
 2893 either limited the inversion domain to where the regional field is assumed small
 2894 (Boghosian et al., 2015; Cochran & Bell, 2012), have used a uniform value for
 2895 the regional component (Muto et al., 2013b), or have found a constant density
 2896 value for the starting model which minimize the gravity misfit (An et al., 2017;
 2897 Millan et al., 2018; Millan et al., 2017).
- 2898 2. Low-pass filtering; for inversion domains with an expected regional field slightly
 2899 larger than the above scenario, low-pass filtering of the gravity data can ap-
 2900 proximate the regional component (Eisermann et al., 2020; Hodgson et al.,
 2901 2019).
- 2902 3. Geologic modelling; To account for the regional field, some studies create ge-
 2903 ologic models of varying density to estimate the regional field. These models
 2904 are typically informed from other geophysical data (Greenbaum et al., 2015;
 2905 Hodgson et al., 2019), *a priori* geologic knowledge (Cochran et al., 2014b; Con-
 2906 stantino et al., 2020; Tinto & Bell, 2011), or from an approximated crustal
 2907 density distribution (Cochran et al., 2020; Eisermann et al., 2021; Tinto et al.,
 2908 2019; Wei et al., 2020).
- 2909 4. Upwards continuation / high altitude surveys; This technique estimates the
 2910 long-wavelength regional component by either upward continuing the gravity
 2911 data to large altitudes, using separate gravity data collect from high-altitude
 2912 surveys (Muto et al., 2016), or a combination of both (Tinto et al., 2015)
- 2913 5. Constraint point minimization; the last commonly used technique utilizes the
 2914 assumption that the desired residual component is near-zero at points of known
 2915 bathymetry. From this assumption, the regional component at these con-
 2916 straints is entirely equal to the gravity anomaly value. To estimate the regional
 2917 field, the gravity values are sampled at the constraints and interpolated over
 2918 the region. This technique has been used in several recent inversions where
 2919 sparse constraints are available (An et al., 2019a; An et al., 2019b; Jordan
 2920 et al., 2020b; Millan et al., 2020; Vaňková et al., 2023; Yang et al., 2021; Yang
 2921 et al., 2020a). While implemented in a different method, this constraint point
 2922 minimization follows the same concept as several studies which use the con-
 2923 strained locations to derive a spatially variable density model, accounting for
 2924 the regional field (Eisermann et al., 2021; Tinto et al., 2019; Wei et al., 2020).

2925 Here, we use the constraint point minimization technique for estimating and
 2926 removing the regional component of the topo-free gravity disturbance.

2927 4.3.2 Inversion comparison

2928 We have developed a conventional non-linear geometric gravity inversion algorithm,
 2929 as often used in modelling density contrasts, such as sedimentary basins (e.g., Mar-
 2930 tins et al., 2010; Santos et al., 2015), or the Moho (e.g., Pappa et al., 2019; Uieda
 2931 & Barbosa, 2017). This algorithm is similar in concept to inversions used in other
 2932 bathymetric studies but differs in its implementation. Past inversion techniques
 2933 used for bathymetry modelling can be grouped into several categories;

- 2934 1. algorithmic approaches. This method termed the "topographic shift method"
2935 (Hodgson et al., 2019; Jordan et al., 2020b), while not a formal inversion,
2936 calculates the equivalent rock thickness from the residual component of gravity,
2937 adds this to the starting bathymetry model, and constrains the results by the
2938 locations of known bathymetry.
- 2939 2. 2D profile inversions. Using the method of Talwani et al. (1959), and often
2940 implemented within the commercial software Geosoft Oasis Montaj, these inv-
2941 ersions retain the 2D nature of the airborne flight lines and invert only along
2942 the path of the flight (Boghosian et al., 2015; Cochran et al., 2014b; Cochran
2943 et al., 2020; Constantino & Tinto, 2023; Tinto & Bell, 2011; Tinto et al., 2015;
2944 Wei et al., 2020).
- 2945 3. 3D frequency-based inversions. This category of inversion uses a Fourier trans-
2946 formation to calculate the forward gravity effect of a continuous topographic
2947 surface, forgoing the need to discretize the topography into vertical prisms
2948 (Oldenburg, 1974; Parker, 1972). This Fourier transform is then iteratively
2949 modified to minimize the misfit to the observed gravity. This method, par-
2950 ticularly its implementation within the commercial software Geosoft Oasis
2951 Montaj, is frequently used for bathymetry inversions (An et al., 2017; An et
2952 al., 2019a; An et al., 2019b; Cochran & Bell, 2012; Eisermann et al., 2020;
2953 Eisermann et al., 2021; Greenbaum et al., 2015; Millan et al., 2018; Millan
2954 et al., 2017; Millan et al., 2020; Studinger et al., 2004b).
- 2955 4. Simulated Annealing. This global optimization technique (Kirkpatrick et al.,
2956 1983) performs many forward calculations of possible bathymetry surfaces and
2957 slowly converges on a model which minimizes the misfit with the observations.
2958 This method, similar to our Monte Carlo uncertainty analysis, has the benefit
2959 of providing an uncertainty estimate of the resulting bathymetry based on the
2960 uncertainty in the inversion inputs. This has been used in several bathymetric
2961 inversions (Filina et al., 2008; Muto et al., 2013a; Muto et al., 2016; Roy et al.,
2962 2005; Yang et al., 2021; Yang et al., 2018; Yang et al., 2020a)
- 2963 5. Regularized least-squares inversions. This style of inversion is the conven-
2964 tional approach to solving non-unique inverse problems (Aster et al., 2018).
2965 While this method is commonly used for other geometric gravity inversions
2966 (e.g., Moho and basement), to our knowledge it is only applied to bathymetry
2967 inversions here, and in Vaňková et al. (2023).

2968 4.3.3 Uncertainty comparison

2969 Here we compare our uncertainty analysis to those from other bathymetry-gravity
2970 inversion studies. Most of these past studies provide an estimation of uncertainty,
2971 but only a few provide spatially variable uncertainties (e.g., An et al., 2019a; Muto
2972 et al., 2016). Typically, these inversion uncertainties are assumed to result from
2973 three sources.

- 2974 1. Uncertainty in the gravity data. The uncertainties resulting from the gravity
2975 data uncertainty are typically estimated using a Bouguer slab approximation,
2976 with an assumed density of the contrast between rock and water ($\sim 1600 \text{ kg m}^{-3}$), and a gravity uncertainty approximated from the RMS crossover values

2978 of the airborne gravity survey (e.g., Boghosian et al., 2015; Constantino et al.,
 2979 2020; Tinto et al., 2019). Alternatively, a simple conversion factor has been
 2980 proposed of 100 m of inversion uncertainty per 5 mGal of gravity uncertainty
 2981 (An et al., 2019a; An et al., 2019b).

- 2982 2. Assumptions of the geologic structure. The uncertainty resulting from as-
 2983 sumptions of the geologic structure is typically simplified as uncertainties in
 2984 the choice of the constant density contrast between sediment and seawater.
 2985 This uncertainty is sometimes approximated as a ratio of change in density to
 2986 change in inverted relief as a percentage (e.g., $\sim 3\%$ relief for 50 kg m^{-3} Tinto
 2987 et al., 2019) or by altering the density and comparing the results (Boghosian
 2988 et al., 2015).
- 2989 3. Uncertainties in the past measurements of bathymetry (constraints). Lastly,
 2990 constraint point measurement uncertainties are typically assumed to result in
 2991 a 1:1 uncertainty in the inverted bathymetry (e.g., Boghosian et al., 2015;
 2992 Tinto et al., 2019).

2993 Our uncertainty analysis, through Monte Carlo simulation, provides robust spa-
 2994 tial uncertainty estimates for each of these three sources of uncertainty. Similar to
 2995 the above methods, Monte Carlo simulation only addresses uncertainties related to
 2996 the uncertainty of the inputs to the inversion.

2997 4.4 Results

2998 Here we apply the above-described methods to recover a higher resolution bathymetry
 2999 beneath Antarctica's Ross Ice Shelf. First, we show the results from an individ-
 3000 ual workflow, as depicted in Figure 4.2. This includes the starting bathymetry
 3001 model, the topo-free gravity disturbance calculations, and the resulting inverted
 3002 bathymetry. Next, we present the Monte Carlo simulation results, where this entire
 3003 workflow is repeated many times with varying values of input data and parameters.
 3004

3005 4.4.1 Starting bathymetry

3006 Existing options for a starting bathymetry model for the sub-Ross Ice Shelf include
 3007 Bedmap2 (Fretwell et al., 2013) or BedMachine v3 (Morlighem, 2022; Morlighem
 3008 et al., 2020). BedMachine v3 for the Ross Ice Shelf contains the gravity-inverted
 3009 bathymetry results from Tinto et al. (2019). To avoid over-interpretation of the
 3010 gravity data (starting an inversion with the results of a separate inversion) we opted
 3011 to not use BedMachine for the starting model. Bedmap2 bed elevations for the Ross
 3012 Ice Shelf were created through the interpolation of the point constraints (Fretwell et
 3013 al., 2013). These point constraints within the ice shelf (Figure 4.1b) were compiled
 3014 from several surveys, including the early traverses of the 1950s and 60s (Crary et al.,
 3015 1962; Crary, 1959; Crary & Robinson, 1962)³, and the Ross Ice Shelf Geophysical
 3016 and Glaciological Survey (RIGGS, 1973-1974 Bentley, 1984) ($N = 223$). However,

³These surveys included the Ross Ice Shelf Traverse (1957-1958), the Little America Station Byrd Trail Traverse (1958), the Victoria Land Traverse (1958-1959), and the Discovery Deep Traverse (1960), see Bennett (1964) for the data and descriptions.

3017 the gridding algorithm used (ArcGIS Topogrid), while producing smooth results for
3018 the Ross Ice Shelf, didn't strictly adhere to the constraint point depths. This can
3019 be seen through the comparison of constraint point depths and Bedmap2 grid val-
3020 ues at the same location (Figure 4.1b). The RMS difference between the constraint
3021 depths and the grid depths within the ice shelf is 138 m. The largest differences are
3022 concentrated along the Transantarctic Mountain Front, where Bedmap2 grid values
3023 are much shallower than the constraint points. Due to this over-smoothing of the
3024 constraints, we have opted to create our own starting bathymetry model.

3025

3026 Our starting model was created from the combination of various seismic survey
3027 constraint points on the ice shelf, and bed data from BedMachine v3 (Morlighem,
3028 2022; Morlighem et al., 2020) outside of the ice shelf. To create this, the BedMachine
3029 v3 bed elevations, relative to the WGS-84 ellipsoid, were masked within the Ross
3030 Ice Shelf, based on the MEASUREs v2 Ross Ice Shelf boundary (Mouginot et al.,
3031 2017; Rignot et al., 2013). These data were converted from gridded data into point
3032 data and merged with the various bathymetry data within the ice shelf. A contin-
3033 uous grid of bathymetry depths at a 5 km cell size was then interpolated from the
3034 combined data inside and outside the shelf. The interpolation can be accomplished
3035 with two gridding methods, bi-harmonic splines (Sandwell, 1987), and minimum
3036 curvature (Smith & Wessel, 1990). While the bi-harmonic spline method appears to
3037 have several advantages over minimum curvature (Chapter 3 Section 3.4.2), such as
3038 the ability to apply weights to the data, interpolating the above Ross Ice Shelf data
3039 resulted in significant unconstrained minima and maxima. Initial inversion results
3040 showed these erroneous features carry through to the final inverted bathymetry.
3041 Due to this, we have opted to interpolate the data to create the starting bathymetry
3042 model using tensioned minimum curvature. This method resulted in less extreme
3043 un-constrained minima and maxima.

3044

3045 To test the importance of the tension value used in the minimum curvature grid-
3046 ding, we performed 6 interpolations, with tension values of 0, 0.2, 0.4, 0.6, 0.8, and
3047 1 (Figure 4.9a-f). From these six resulting bathymetry models, we calculated the
3048 standard deviation (Figure 4.9g) and the cell-specific mean (Figure 4.9h). These
3049 statistics were weighted, in the same method described in Figure 4.7d. The weight
3050 value used for each grid was the inverse square of the RMS difference between
3051 the constraint point depth values and the resulting grid values at the same points.
3052 These RMS values are shown in the figure titles of Figure 4.9a-f. This weighted
3053 mean starting model is compared to Bedmap2 bathymetry (Figure 4.9i). Note that
3054 while low tension factors result in models that closely match the constraints, they
3055 also produce local maxima and minima away from the data, which is not ideal since
3056 these features can be seen to carry through the inversion to the final bathymetry,
3057 as discussed later. Alternatively, higher tension values produce models that don't
3058 match the constraints as well (higher RMS values), but they don't have as many
3059 erroneous features. For this reason, we use the cell-specific mean of the six models
3060 as our starting bathymetry (Figure 4.9h). This model has an RMS difference from
3061 BedMap2 within the ice shelf of 95 m.

3062

3063 From these constraint points used to create the starting bathymetry, a weighting
3064 grid was created (Figure 4.10). This grid was calculated from the distance between
3065 each grid cell and the nearest constraint point. This minimum constraint distance

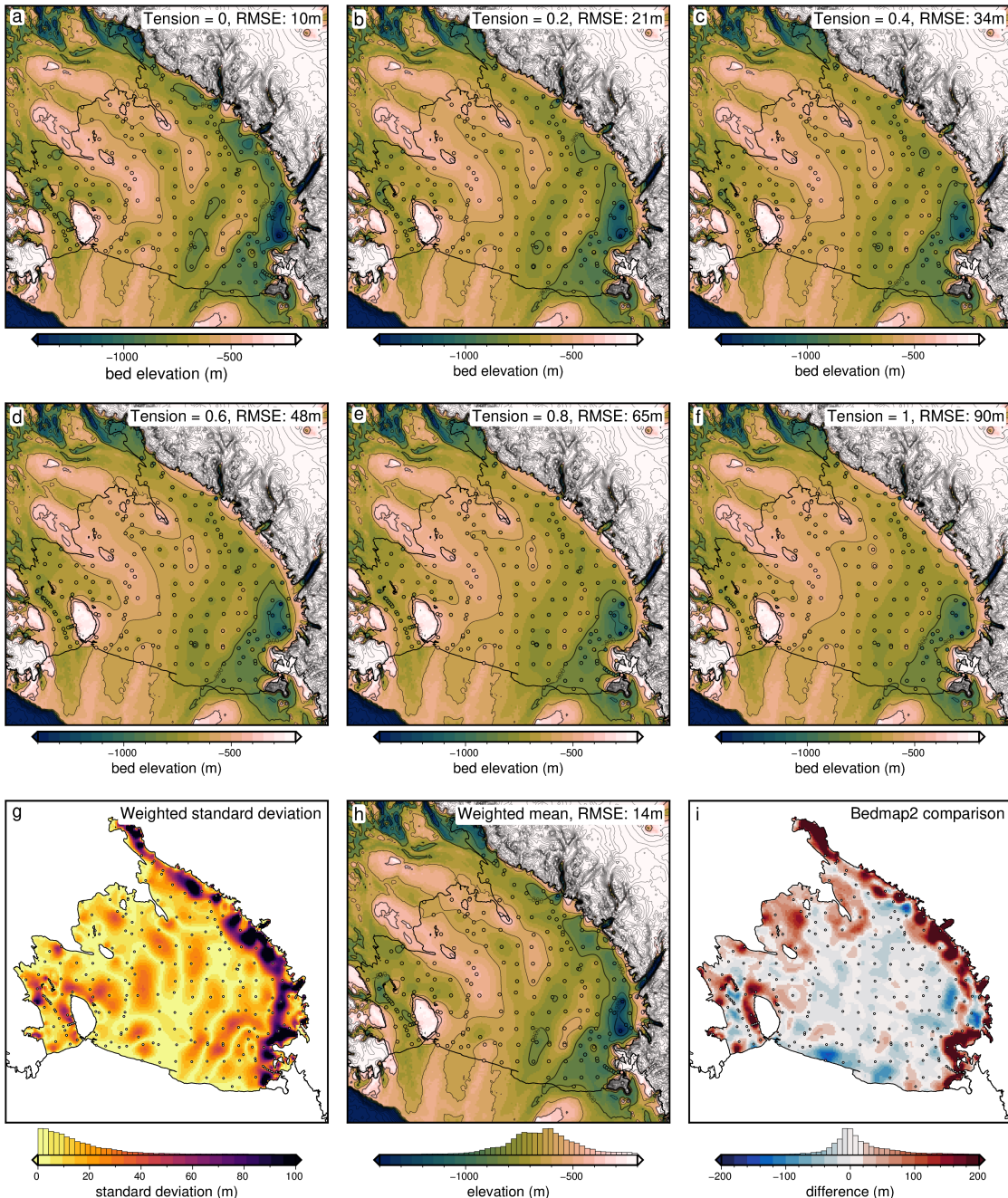


Figure 4.9: Starting bathymetry models from the interpolation of constraint points within the ice shelf and BedMachine v3 gridded data outside of the shelf (Morlighem, 2022; Morlighem et al., 2020). The ice shelf border, from Mouginot et al. (2017), is shown as the solid black line, representing the grounding line and the calving front. **a-f)** Bathymetry models resulting from 6 varying tension factor values of minimum curvature interpolation. Contours shown at 400m intervals. **g)** The cell-specific weighted standard deviation of the six models (**a-f**). **h)** The cell-specific weighted mean bed elevation from the six models. **i)** The difference between Bedmap2 bathymetry and the mean model (**h**). The RMS difference is 95 m. Blues show where the mean model is shallower than Bedmap2, while reds show where the mean model is deeper. Root mean square error (RMSE) values in the plot titles are between the constraint point depths and the values at those points on the interpolated grids.

3066 (top annotations of Figure 4.10 colorbar) was then normalized between 0 and 1 to
 3067 create the weighting grid (bottom annotations of Figure 4.10 colorbar). As all grid
 3068 cells outside of the ice shelf border are considered constraint points non-zero weights
 3069 and minimum constraint distances are confined to within the ice shelf border. The

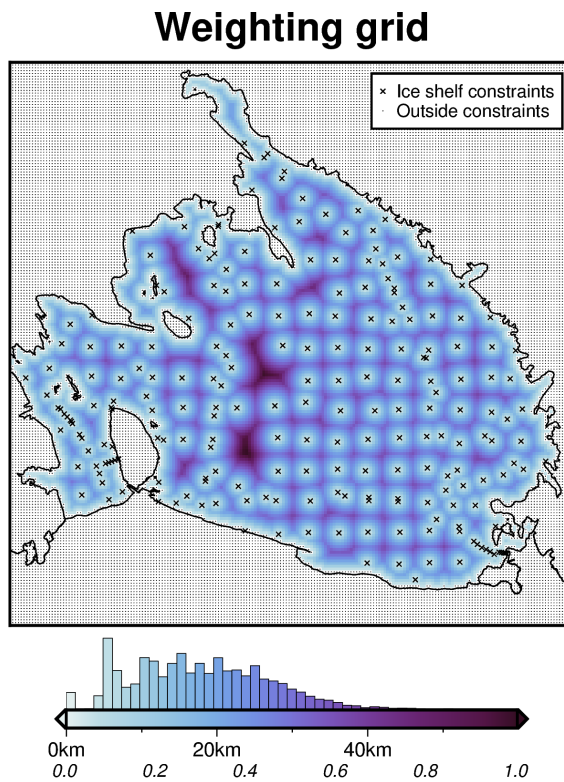


Figure 4.10: Weighting grid used in the Ross Ice Shelf bathymetry inversion. Grid colors show both the distance between each grid cell and the nearest constraint point and the weight values (0 - 1) from the normalization of these distances. Constraint points are defined as either direct measurements of bathymetry within the ice shelf (black crosses), or any grid cell outside of the ice shelf (small black dots). The ice shelf border, from Mouginot et al. (2017) is shown as the solid black line, representing the grounding line or the calving front.

3070 colorbar histogram shows a mean minimum constraint distance within the ice shelf
 3071 of approximately 20 km, and an upper limit of approximately 60 km. Within the
 3072 shelf, there are 223 constraint points. Over an area of $\sim 480,000 \text{ km}^2$ (Mouginot et
 3073 al., 2017), this equates to a constraint density of ~ 1 constraint per $46 \times 46 \text{ km}$ (2154 km^2).
 3074

3075

3076 4.4.2 Gravity processing results

3077 We use airborne gravity data from the Ross Ocean and ice Shelf Environment, and
 3078 Tectonic setting Through Aerogeophysical surveys and modelling project (ROSETTA-
 3079 Ice). This project was created with the goal of investigating the interactions between
 3080 ice, ocean, and earth of Antarctica's Ross Ice Shelf (Tinto et al., 2019). The survey
 3081 consisted of 3 field seasons (2015-2017) of airborne geophysical surveying with a
 3082 survey design consisting of E-W flight lines, at a nominal spacing of 10 km, and
 3083 N-S tie lines with a nominal spacing of 55 km (Figure 4.1a). Flights were flown
 3084 at an average of 750 m above the ice surface and a speed of 180 knots (93 ms^{-1}),
 3085 The survey was designed to maximize the overlap between the flight lines and the
 3086 past bathymetry constraints across the ice shelf from the RIGGS seismic surveys
 3087 (Bentley, 1984). The data collection and initial processing were performed by Tinto
 3088 et al. (2019) and are briefly summarized here. The gravity data were collected with
 3089 a combination of a LaCoste and Romberg gravimeter upgraded with a ZLS UltraSys

control system, an iMAR inertial measurement unit, and a DgS gravimeter. The ZLS data was tied to an absolute gravity reference station at McMurdo Station. Poor-quality data from the ZLS was replaced with the iMAR or DgS values. The accelerations of the aircraft were calculated from GPS data and removed from the gravity signal. The Eötvös correction was applied, to account for measuring gravity on a moving platform (Harlan, 1968). At each observation point, the effects of the normal earth were calculated and removed, giving the gravity disturbance values (See Section 4.2.1.1). Levelling was then performed using the cross-over values between E-W flight lines and N-S tie lines.

3099

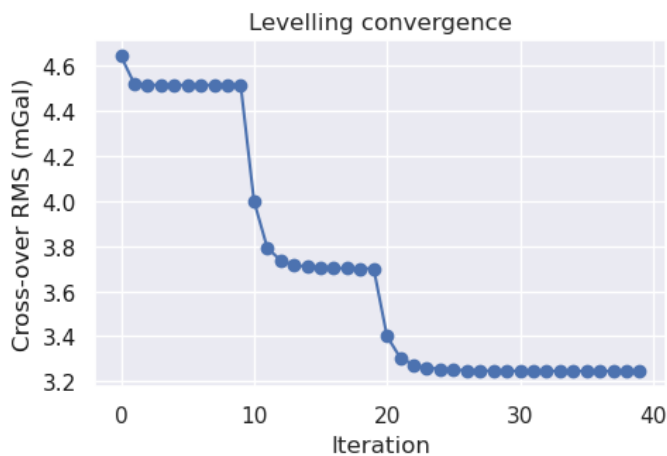


Figure 4.11: Re-levelling of the ROSETTA-Ice gravity data. First, flight lines were individually upward continued, them cross-over point misties were found. These were used in 0th, 1st, and 2nd order iterative levelling, alternative between levelling flight lines to tie lines and vice versa at each iteration. The RMS cross-over errors at each iteration are shown. The major steps show the 0th, 1st, and 2nd order stages of levelling.

Since this bathymetry inversion is strongly influenced by noise in the gravity data, as demonstrated in Chapter 3 Section 3.6.3.1, we have performed additional processing to the published ROSETTA-Ice dataset. Erroneous sections of flight line data were manually removed, and the dataset was re-levelled. The levelling procedure utilizes the gravity difference between E-W and N-S flight lines at cross-over points. While the flight paths intersect in 2-D space, their altitudes typically differ, meaning there is no true cross-over point in 3-D space. To account for this, the flight lines are individually upward continued to a constant elevation of 1 km (ellipsoidal height). The mean elevation of the cleaned data was \sim 790 m, and 1 km was greater than 96% of the data. This limited the amount of downward continuation while retaining a spatial resolution close to the original data. This continuation was calculated using the equivalent source technique (see Section 3.3.1.5 Dampney, 1969; Soler & Uieda, 2021). Since the cross-over points are now true 3-D intersections, the difference between E-W and N-S lines at these points (mis-ties) can be used to re-level the dataset. Here, we alternate between levelling the E-W lines to the N-S lines, and vice versa. We start with a 0-th order levelling, where only DC shifts are applied. Followed by a 1st and 2nd order levelling, where 1 and 2-degree polynomials, respectively, are fit to the mis-ties, and used to level the lines. The results of this levelling procedure are shown in Figure 4.11. For each order of levelling several iterations are performed. The step-wise convergence of the RMS mis-tie values shows the 0th, 1st, and 2nd order levelling stages. The re-levelling procedure brought

3121 the RMS mis-tie from ~ 4.8 mGal to ~ 3.2 mGal.

3122

3123 Finally, this re-levelled gravity disturbance line data were gridded onto a regular
3124 grid at 2.5 km spacing, using equivalent sources. Since the inversion only affects
3125 the bathymetry within the ice shelf border, as implemented with the weighting grid
3126 (Figure 4.10), the interpolated gravity grid is masked beyond 10 km outside of the
3127 ice shelf border (Figure 4.11b). This 2.5 km gridded data ($N = 85,914$) consists of
3128 both the *testing* ($N = 64,435$) and *training* ($N = 21,479$) sets used in the cross-
3129 validation. With the grid configuration shown in Chapter 3 Figure 3.4, the *training*
3130 data used in the actual inversion are on a regular 5 km grid.

3131

3132 4.4.3 Gravity reduction results

3133 The terrain mass effect was calculated at each of the gridded gravity data points. For
3134 this calculation, the three layers of prisms shown in Figure 4.5c-e were created from
3135 BedMachine v3 (Morlighem, 2022; Morlighem et al., 2020) ice surface and water
3136 surface data and the mean starting bathymetry from Figure 4.9h. All data are ref-
3137 erenced to the WGS-84 ellipsoid. The ice surface elevations used from BedMachine
3138 v3 are in ice equivalent, meaning they have had a firn depth correction applied,
3139 making for a slightly lower surface elevation to account for spatially variable firn
3140 thickness (Morlighem et al., 2020). An ice equivalent surface is suitable for calculat-
3141 ing the terrain mass effect since it gives the estimated thickness of the ice shelf with
3142 a density of ice, instead of the true ice shelf thickness, with a layer of low-density
3143 firn above. Comparing the forward gravity calculated from the true geometry of ice
3144 shelf thickness, the ice equivalent thickness, and a 2-layer model with firn and ice,
3145 show minimal differences, and thus we use the ice equivalent thickness in the terrain
3146 mass effect. The densities used in the terrain mass effect calculations were 1 kg m^{-3}
3147 for air, 915 kg m^{-3} for the density of ice, 1024 kg m^{-3} for the density of seawater
3148 (Griggs & Bamber, 2011), and 2300 kg m^{-3} for the density of the seafloor. Since we
3149 use a single value for the density of the seafloor, it should represent the expected
3150 average density of the seafloor over the entire region. Chapter 2 showed a continu-
3151 ous drape of sediment over the seafloor. We chose 2300 kg m^{-3} to be in the middle
3152 between unconsolidated sediment ($\sim 1900 \text{ kg m}^{-3}$) and low-density crystalline rock
3153 ($\sim 2700 \text{ kg m}^{-3}$) (Schön, 2015). The inversion domain was 1 million km^2 ($1000 \text{ km} \times$
3154 1000 km). To avoid gravitational edge effects in the forward calculations, the prism
3155 layers were extended in all directions by a 40 km buffer zone, resulting in 120,000
3156 prisms. The resulting terrain mass effect was subtracted from the gravity distur-
3157 bance to get the topo-free gravity disturbance. These data are shown in Figure 4.12.

3158

3159 The topo-free gravity disturbance was subsequently separated into the regional
3160 and residual components. This was accomplished with constraint point minimiza-
3161 tion (Chapter 3 Section 3.2.4). While the synthetic data of the past chapter showed
3162 a clear benefit of using a bi-harmonic spline interpolation over a minimum curvature
3163 interpolation, we use minimum curvature here. As with the interpolation for the
3164 starting bathymetry model, bi-harmonic spline interpolation led to excessive uncon-
3165 strained maximum or minima. The resulting regional and residual components are
3166 shown in Figure 4.12.

3167

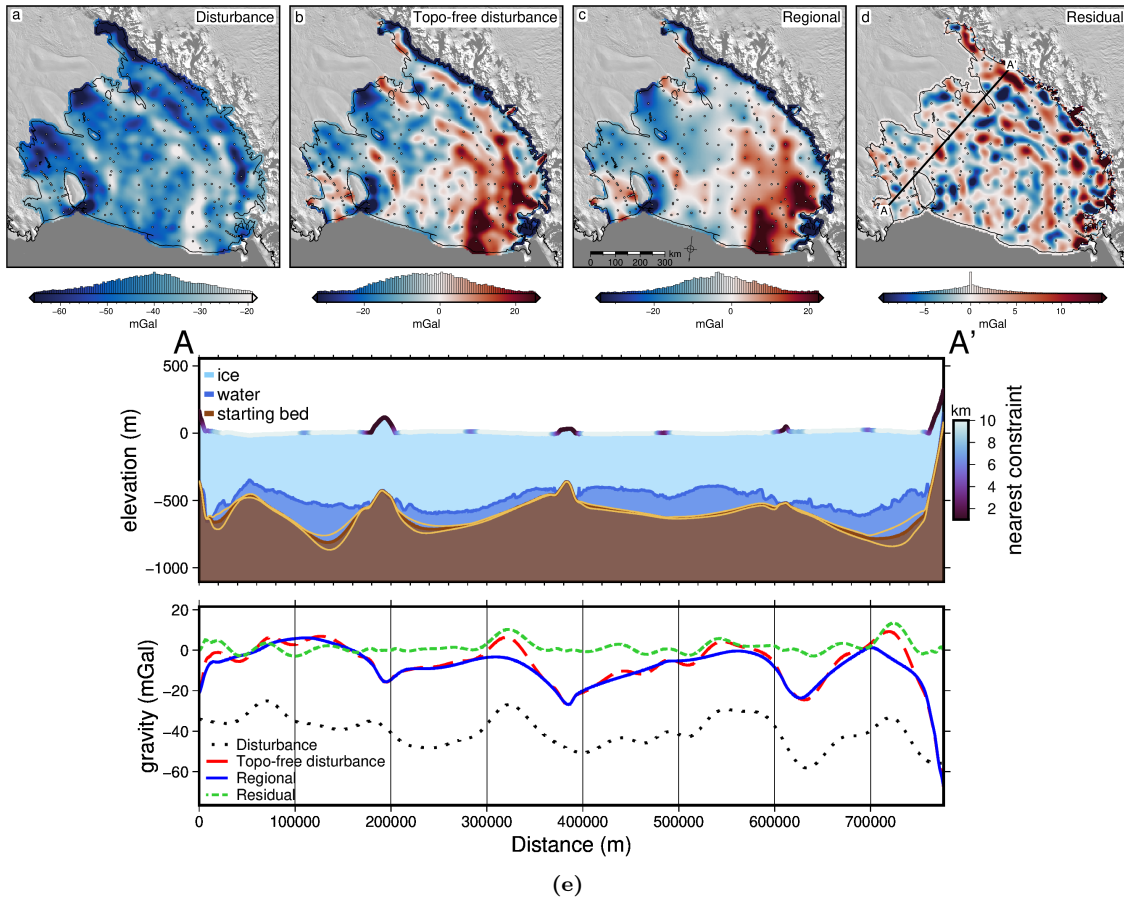


Figure 4.12: Gravity reduction results for the Ross Ice Shelf. **a)** Gravity disturbance, **b)** topo-free gravity disturbance, after the removal of the terrain mass effect, **c)** regional component of the topo-free disturbance, estimated with constraint point minimization, and **d)** residual component of the topo-free disturbance, as the difference between **b** and **c**. Background imagery is from MODIS-MOA (Scambos et al., 2007) and grounding line and coastlines are from (Morlighem, 2022). Constraint points within the ice shelf are shown as dots. **e)** Profile from A to A', location shown in **d**. **Upper panel** shows cross-section, with ice surface and ice base from BedMachine v3 (Morlighem, 2022; Morlighem et al., 2020). Brown layer shows the mean starting bed model with bounding uncertainty (light brown lines) from the standard deviation of the various starting bed models in Figure 4.9. Color of ice surface shows distance to nearest constraint point. **Lower panel** shows data from **a-d** along the profile.

3168 4.4.4 Inversion results

3169 With the residual component of the topo-free gravity disturbance as the inversion
 3170 input (Figure 4.12d), we ran 10 inversions with varying levels of damping. Each inver-
 3171 sion used a density of 1024 kg m^{-3} for ocean water and 2300 kg m^{-3} for the density
 3172 of the seafloor. For each value of the damping parameter, the cross-validation score
 3173 was calculated by forward modelling the gravity effect of the resulting bathymetry
 3174 model onto the locations of the testing gravity data. The RMS difference between the
 3175 residual component of the topo-free gravity disturbance and the forward-modelled
 3176 results at these testing points gave the score. These scores are shown in Figure
 3177 4.13a. The lowest score was achieved with a damping value of 10^{-2} .

3178
 3179 This inversion took 8 iterations and 135 seconds⁴ and converged due to a lack of
 3180 change in the ℓ^2 -norm between subsequent iterations (Figure 4.13b). The RMS of

⁴See Appendix 1.6 for a description of the hardware used.

³¹⁸¹ the residual gravity started at 6.1 mGal prior to the inversion and was reduced to
³¹⁸² 4.0 mGal (Fig 4.13b).

3183

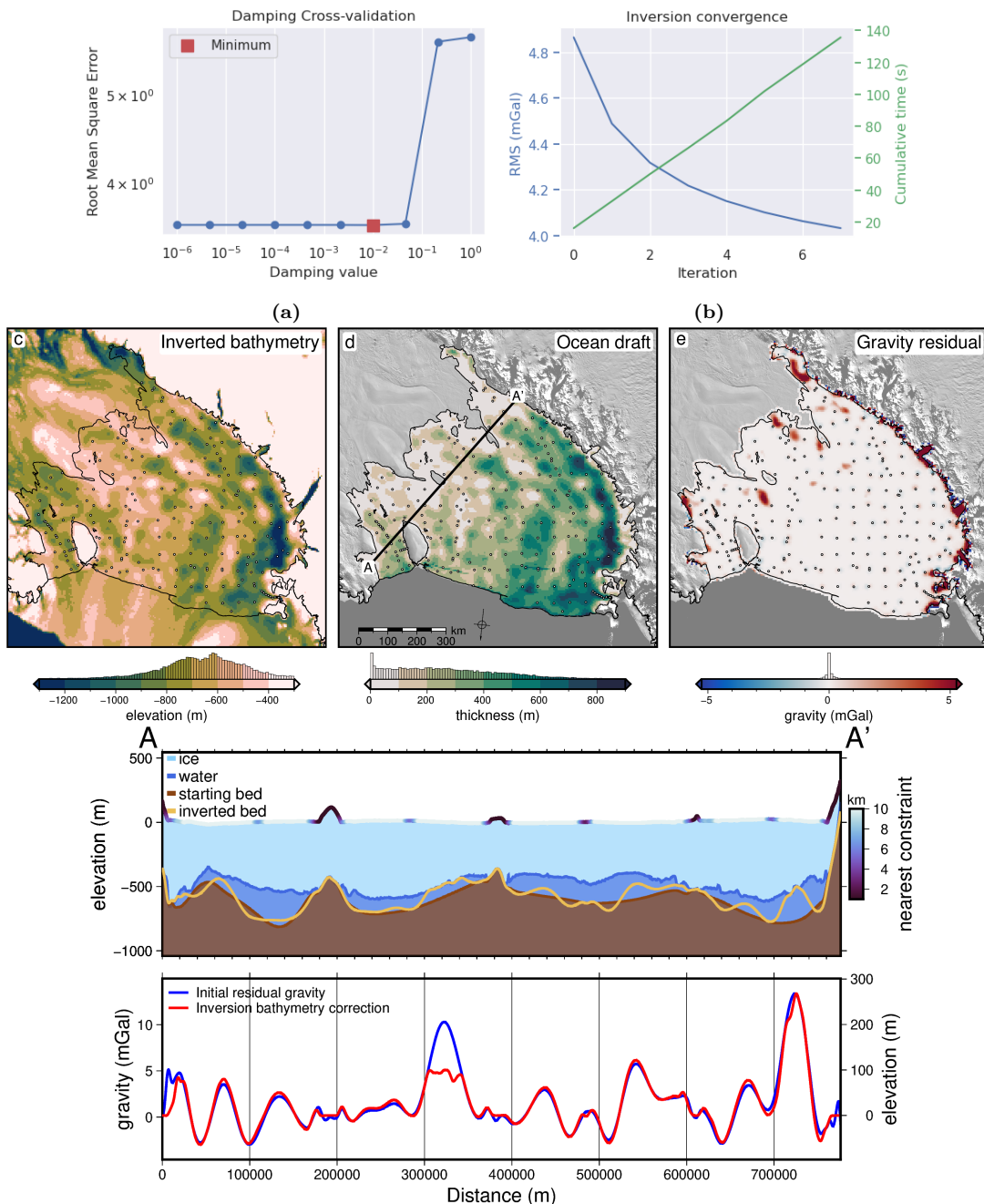


Figure 4.13: Ross Ice Shelf singular bathymetry inversion results. **a)** Damping parameter cross-validation with the lowest score shown in red. **b)** Convergence curve and cumulative inversion time for the optimal inversion. Blue line (left y-axis) shows consecutive iteration's RMS residual component of the topo-free gravity disturbance. Green line (right y-axis) shows cumulative time to run the inversion. **c)** Inverted bathymetry, **d)** water column thickness between the inverted bathymetry and Bedmachine v3 icebase (Morlighem, 2022; Morlighem et al., 2020), **e)** final residual component of the topo-free gravity disturbance. **Profile A to A'**. **Upper panel** shows ice surface and icebase from BedMachine v3, both the starting bathymetry (dark brown) and the inverted bathymetry (light brown). Color of ice surface shows distance to nearest constraint point. **Lower panel** shows the initial residual gravity used as input to the inversion (blue line, left y-axis), and the total correction (red line, right y-axis) applied to the starting bathymetry surface during the inversion to get the inverted bathymetry.

The inverted bathymetry model for the sub-Ross Ice Shelf, at a 5km resolution, is shown in Figure 4.13c. Note that this is just the result of a single inversion. Our final inverted bathymetry model is achieved through the Monte Carlo simulation, as described below. The RMS difference between the inversion results and the starting model at the constraints is 16 m. The thickness of the water column, defined as the difference between BedMachine v3 ice base and the inverted bathymetry, is shown in Figure 4.13d.

3191

3192 4.4.5 Uncertainty

3193 We used a series of Monte Carlo simulations (Figure 4.7) to assess both the spatial
 3194 uncertainty of the resulting inverted bathymetry and the importance of the various
 3195 components and parameters of the inversion. By varying the inputs of the inversion
 3196 within their ranges of uncertainties, we can gather a range of the possible bathymetry
 3197 results, which when compared shows where the inversion results are more or less
 3198 certain. The inputs and their respective uncertainty distributions included in the
 3199 sampling are:

- 3200 1. gravity disturbance data, sampled from a normal distribution with a mean of
 3201 the data point, and a standard deviation of the RMS mis-tie of the line data
 3202 after levelling (3.3 mGal),
- 3203 2. constraint point depths, sampled from a normal distribution with a mean of
 3204 the measured depth, and a standard deviation of 10 m for points outside of
 3205 the ice shelf, and 5% of depth from the ice surface for points within the ice
 3206 shelf (mean of 36 m),
- 3207 3. the density of ice, water, and sediment, all from normal distributions with
 3208 means of 915 kg m^{-3} , 1024 kg m^{-3} , and 2300 kg m^{-3} respectively, and standard
 3209 deviations of 5 kg m^{-3} , 5 kg m^{-3} , and 400 kg m^{-3} . The small standard deviations
 3210 of ice and water compared to sediment reflects the relative certainty of the
 3211 value and spatial heterogeneity of the density of ice and water, compared to
 3212 those of the material comprising the sea floor. For the Ross Ice Shelf, the entire
 3213 region is likely to be draped in at least 10's of meters of sediment (Chapter 2,
 3214 Tankersley et al., 2022). With a mean of 2300 kg m^{-3} and a standard deviation
 3215 of 400 kg m^{-3} , these values span the range from unconsolidated sediment to
 3216 low-density crystalline rock (Schön, 2015).
- 3217 4. the tension factor used in minimum curvature gridding for interpolating both
 3218 the starting bathymetry model and the regional component of gravity. The
 3219 tension factor values were sampled from a uniform distribution between 0 and
 3220 1.

3221 Figure 4.14 shows the results of the Latin hypercube sampling of the 5 input
 3222 variables (not including the gravity and constraints data). The correlations between
 3223 each set of variables show that pairwise correlation was minimal. This is ideal since
 3224 these inputs are unrelated, and therefore their sampled values should be uncorre-
 3225 lated (Helton et al., 2006). This also shows that with only 10 samplings, the Latin
 3226 hypercube sampling was able to provide adequate spatial coverage of the individual
 3227 distributions (4.14b) as well as all the pairwise distributions combinations (4.14a).

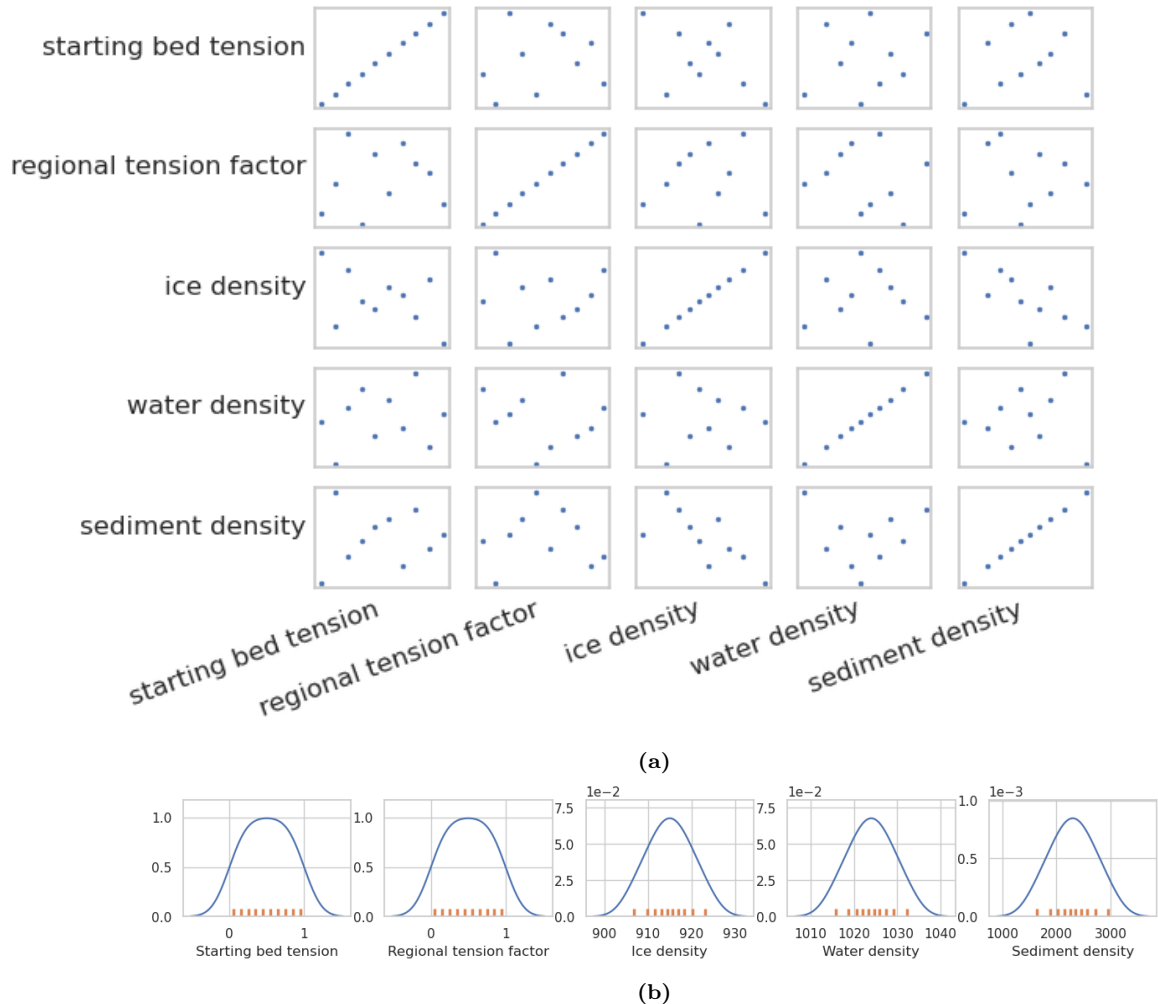


Figure 4.14: Latin hypercube sampling results for the 10 inversions of the full Monte Carlo simulation. **a)** Correlations between each pair of the 5 sampled input parameters. **b)** Resulting distributions of the 10 sampled values of each parameter. Blue line shows kernel density estimates fit to each set of sampled values, which are shown as orange ticks.

3228 Each simulation consisted of 10 runs. We performed a *full* simulation, where
 3229 each of the above inputs were sampled (Figure 4.15). We performed five additional
 3230 simulations (Figure 4.16) where 1) only the gravity data was sampled, 2) only the
 3231 constraint point depths were sampled, 3) only the density values of ice, water, and
 3232 sediment were sampled, 4) only the tension factor for interpolating the starting
 3233 bathymetry model was sampled, and finally 5) only the tension factor for interpo-
 3234 lating the regional component of gravity was sampled. Each simulation results in a
 3235 series of inverted bathymetries. Finding the cell-specific weighted standard deviation
 3236 of the bathymetry depths for each of these simulations gives an estimation of the
 3237 uncertainty resulting from the associated parameter. The cell-specific statistics of
 3238 these simulations were low-pass filtered to remove high-frequency noise induced by
 3239 the random sampling. For the full simulation (Figure 4.15b) the weighted mean of
 3240 the resulting bathymetries gives the final inverted bathymetry results of this study
 3241 (Figure 4.15a). Note that this final bathymetry model resulting from the Monte
 3242 Carlo simulation is similar, but distinct from the inverted bathymetry resulting
 3243 from a single inversion without the Monte Carlo simulation, shown in Figure 4.13c.

3244

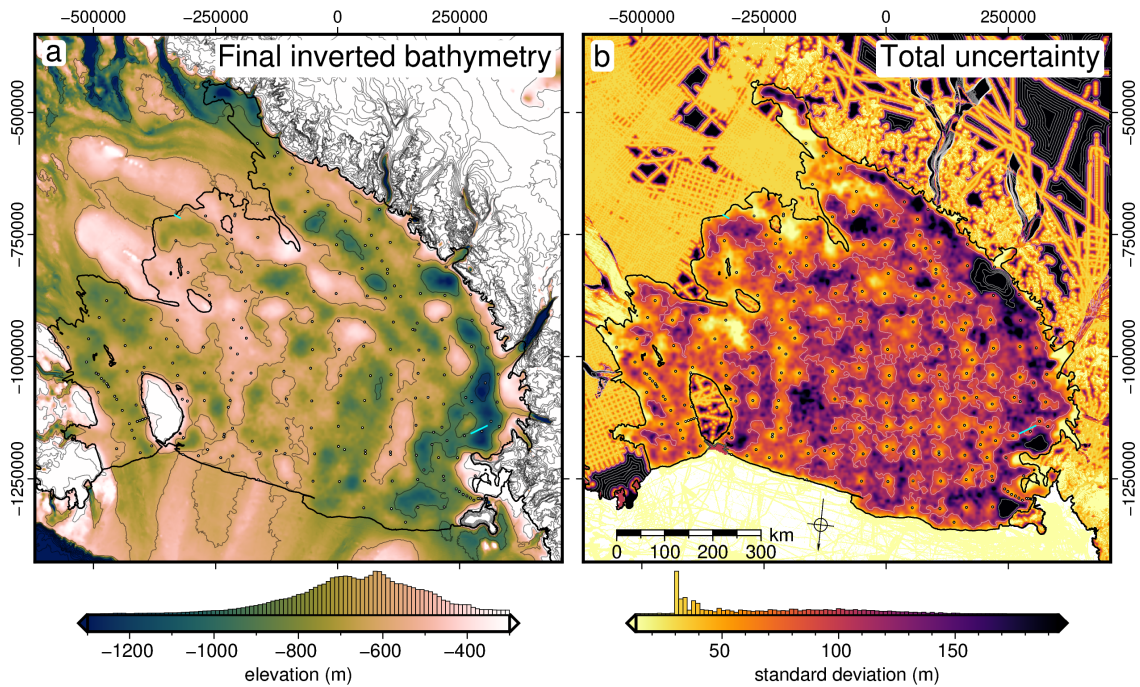


Figure 4.15: Final bathymetry depths and uncertainties from the full Monte Carlo simulation, merged with 500m resolution elevation and uncertainty data outside of the shelf from BedMachine v3 (Morlighem, 2022; Morlighem et al., 2020). **a)** Final inverted bathymetry model, calculated as the weighted mean of the full Monte Carlo simulation. Shown with 300 m contours. **b)** Uncertainty estimation of the inverted bathymetry from the cell-specific weighted standard deviation of the inverted bathymetry results from the full Monte Carlo simulation. Shown with 100 m contours. Constraints within the ice shelf are shown as dots in **a**. Grounding line and coastline are shown in black (Morlighem, 2022). Background imagery is from Scambos et al. (2007). Cyan lines show Discovery Deep and Kamb Ice Stream seismic surveys.

3245 The final bathymetry and uncertainty grids were resampled to a resolution of
 3246 500 m, from their original 5 km resolutions, masked outside of the ice shelf, and
 3247 merged to the 500 m resolution bed and uncertainty data of BedMachine v3. This
 3248 final bathymetry has a mean elevation of ~ 700 m within the ice shelf. The deepest
 3249 point is $\sim -1370 \pm 187$ m, located near the Byrd Glacier outlet (Figure 4.1b). Bathymetric
 3250 features appear to have continuity with features from BedMachine v3 data
 3251 outside of the ice shelf. The RMS difference between the bathymetry and the origi-
 3252 nal constraint point depths is 44 m. Subtracting the bathymetry from the ice base
 3253 elevations of BedMachine v3 (Morlighem, 2022; Morlighem et al., 2020) gives the
 3254 water column thickness, as shown in Figure 4.18b. Without ice base uncertainty es-
 3255 timates from BedMachine v3, we use the bathymetry uncertainty as our uncertainty
 3256 for the water column thickness, acknowledging that this is a minimum uncertainty.
 3257 Within the ice shelf boundary, this water column thickness has a mean value of 260
 3258 m and a maximum of 1000 m, located near the Nimrod Glacier outlet. Here, the
 3259 bathymetry has an uncertainty of ± 800 m. Outside of this region, the thickest ocean
 3260 cavity is $\sim 940 \pm 180$ m, located at the Byrd Glacier outlet. The similarity between
 3261 the bathymetry depth and the water column thickness shows that the ocean cavity is
 3262 predominantly controlled by bathymetry and that the ice base topography is smooth
 3263 compared to the bed. The uncertainty in the bed elevation ranges from $\sim 10 - 850$ m,
 3264 with a mean of 95 m (Figure 4.13b). It has an approximately normal distribution,
 3265 with a slight skew to the higher values. In general, the uncertainty is lowest at the
 3266 constraint points and highest far from constraints. There are elevated uncertain-

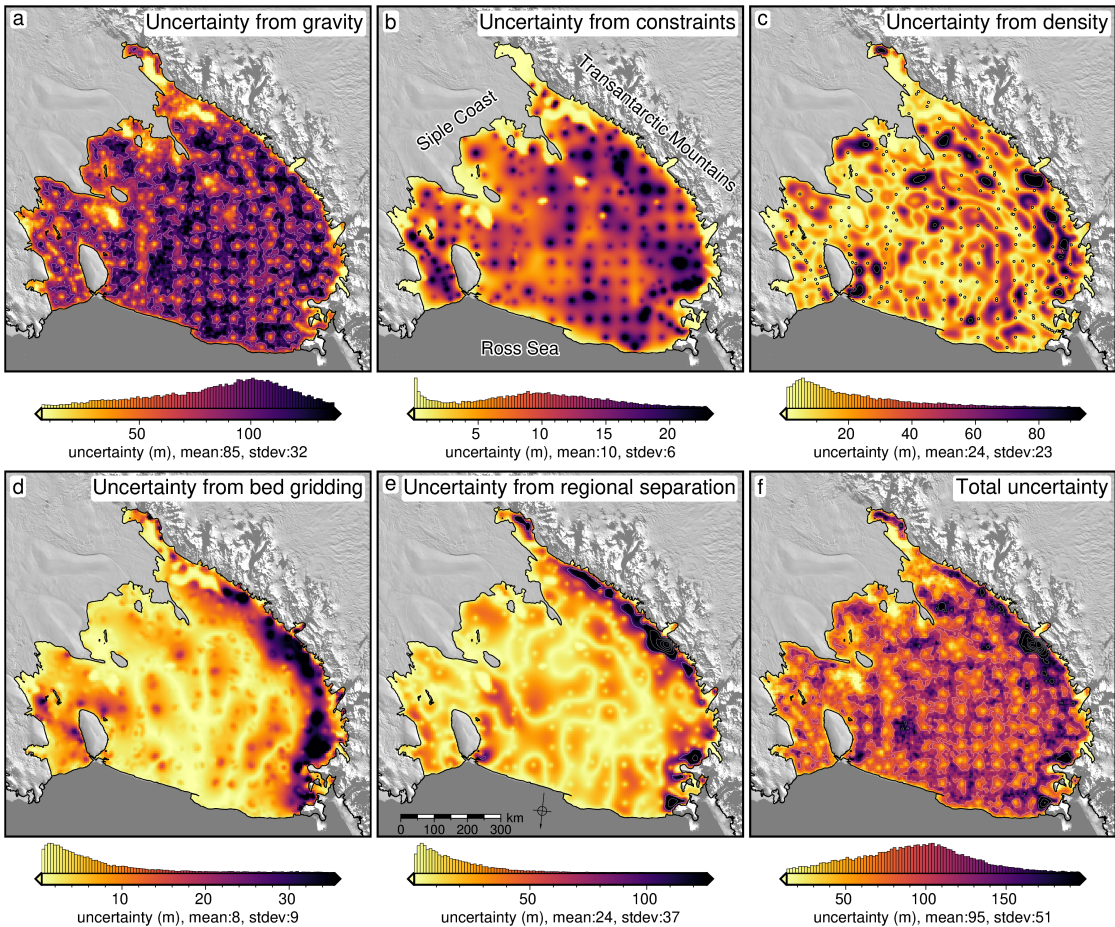


Figure 4.16: Sensitivity analysis for the inversion input data and parameters. Cell-specific weighted standard deviations of the inverted bathymetry results from Monte Carlo simulations with sampling the uncertainties of the **a)** gravity data, **b)** constraint points depths, **c)** ice, water, and sediment density values, **d)** starting bed interpolation tension factor, and **e)** tension factor for interpolating the regional gravity component. **f)** The total uncertainty from the full simulation. 100 m contours in white. Constraints within the ice shelf are shown as dots in **c)**. Grounding line and coastline shown in black (Morlighem, 2022). Background imagery is from Scambos et al. (2007).

ties in several spots, with the largest being along the Transantarctic mountain front.
3267
3268

3269 4.4.5.1 Partitioning uncertainty

3270 The uncertainty in the inverted bathymetry which arises from the uncertainty in
3271 gravity data (Figure 4.16a) is relatively spatially uniform, with a mean of 85 m. It
3272 is lowest immediately at the constraints, and generally highest far from constraints.
3273 The uncertainty from the constraints point depths (Figure 4.16b) is also generally
3274 spatially uniform, with a mean of 10 m. Conversely, it is highest at the constraints,
3275 and lowest far from constraints. The uncertainty resulting from the choice of den-
3276 sity values (Figure 4.16c) displays a more heterogeneous spatial distribution than the
3277 previous two uncertainties. It is lowest at the constraints and has a mean of 24 m.
3278 The largest values are located at the gaps between constraints. The uncertainty
3279 resulting from the interpolation of the starting bed (Figure 4.16d) has a distinct
3280 spatial distribution. It is highest along the Transantarctic mountain front, with val-
3281 ues up to 40 m, but it has an overall mean of 7 m. Lastly, the uncertainty resulting

Study	Inverted bathymetry uncertainty (m)			
	total	from gravity	from geology	from constraints
This study ($\bar{x} \pm 1\sigma$)	95±51	85±32	48±30	10±6
Eisermann et al. (2021)	220	84	116	20
Tinto et al. (2015)	160	26	124	10
Constantino et al. (2020)	133	34	90	5-10
Boghosian et al. (2015)	110	10-28	50-70	10
Tinto and Bell (2011)	70	34	10-15	20
Constantino and Tinto (2023)	69-123	32-39	27-74	10
Tinto et al. (2019)	68	48	10	10
Eisermann et al. (2020)	175-225	-	-	10
Jordan et al. (2020b)	100	23	-	-
An et al. (2019a)	60	60	-	-
Studinger et al. (2004b)	250	-	-	-
Wei et al. (2020)	246	-	-	-
Greenbaum et al. (2015)	190	-	-	-
Brisbourne et al. (2014)	160	-	-	-
Hodgson et al. (2019)	100	-	-	-
Yang et al. (2021)	68	-	-	-
An et al. (2017)	60	-	-	-
Millan et al. (2017)	50-65	-	-	-
Millan et al. (2018)	30-50	-	-	-
Millan et al. (2020)	45	-	-	-
Filina et al. (2008)	-	19	-	-
Mean	117 (N = 25)	40 (N = 13)	57 (N = 11)	12 (N = 10)

Table 4.1: Reported inverted bathymetry uncertainties and the various components. Our reported geologic uncertainty is the combination of uncertainties resulting from the density values and the tension factor used in grinding the regional field.

from the estimation and removal of the regional component of gravity, prior to the inversion, (Figure 4.16e), also shows highest values along the mountain front, with values over 200 m (up to 700 m at the Nimrod Glacier outlet). The mean value is 24 m. The reported uncertainties and their components from a wide range of past studies are shown in Table 4.1.

3287

3288 4.5 Discussion

3289 Here we discuss the results of our Ross Ice Shelf bathymetry model from the in-
 3290 version of airborne gravity data. First, we describe the results of the uncertainty
 3291 and parameter sensitivity analysis. Then we compare our results with two past
 3292 bathymetry models beneath the Ross Ice Shelf and discuss the differences. Lastly,
 3293 we discuss various implications of this updated bathymetry model, including how
 3294 the findings relate to geology, tectonics, and ice sheet dynamics.

3295 4.5.1 Uncertainties and parameter importance

3296 The results of our Monte Carlo simulations provide answers to several important
3297 questions; 1) how confident are we in the inverted bathymetry depths? 2) where
3298 are we most and least confident about the bathymetry depth? 3) what are the
3299 specific sources of this uncertainty? and finally, 4) what can be done to limit the
3300 uncertainty? Figures 4.15b and 4.16f show the resulting spatial uncertainty of the
3301 inverted bathymetry, providing an answer to the first two questions. To determine
3302 the sources of this uncertainty, the individual inputs to the inversion were isolated
3303 and their effects on the estimated uncertainty were found (Figure 4.16).

3304

3305 4.5.1.1 Gravity component

3306 The largest contributor to the overall uncertainty of the inversion is the uncertainty
3307 of the gravity data (Figure 4.16a). This uncertainty resulting from the gravity data
3308 results in a base-level bathymetry uncertainty of ~ 85 m and is relatively spatially
3309 uniform. This is because each gridded gravity data point is contaminated with
3310 independent noise of varying levels during the Monte Carlo sampling. It is this
3311 point-by-point random noise that creates the noisy component in the final inverted
3312 bathymetry. In reality, the uncertainty of nearby gravity data is likely correlated,
3313 where entire lines, or sections of lines have similar uncertainty values, due to chang-
3314 ing data collection conditions, like turbulence, or mis-levelling, causing values of
3315 entire lines to be offset, or tilted. Here our estimate of gravity uncertainty is entirely
3316 dependent on cross-over mistakes; likely an oversimplified estimation of uncertainty
3317 for an entire survey. This suggests that the true uncertainty resulting from the
3318 gravity data likely has a different spatial distribution and may be larger than we re-
3319 port; a finding which is not surprising, since the entire method depends on this data.

3320

3321 4.5.1.2 Constraints component

3322 The uncertainty in the other data input to the inversion, the constraint point depths,
3323 has only a small effect on the results (Figure 4.16b). It is worth noting that while
3324 the uncertainty resulting from the constraint point measurement uncertainty is low,
3325 the constraints themselves are fundamental to the inversion. These constraints feed
3326 into all the components of the inversion and thus affect the uncertainty of each
3327 component, including the uncertainty from the gravity data. This is shown by the
3328 correlation between uncertainty and the distance to the nearest constraint (Figure
3329 4.10) of all the components of Figure 4.16. Our Monte Carlo sensitivity analysis only
3330 tests the effects of estimated noise in the inputs, and not their overall importance for
3331 the inversion. Since the uncertainty in the constraints only impacts the inversion
3332 in the immediate vicinity of the constraint, for constraint data collection, efforts
3333 should be focused on quantity over quality, assuming the uncertainty can be limited
3334 to a reasonable amount. In practice, for over-ice seismic surveying, this may lead to
3335 the choice of fast and efficient systems as opposed to high-resolution systems. For
3336 example, towable snow streamers and sources such as surface detonations or vibro-
3337 seis (e.g., Hofstede et al., 2020; Smith et al., 2020b) can collect data very efficiently
3338 (~ 20 km/day), compared to higher-resolution surveys with buried geophone arrays
3339 and drill-emplaced explosives (e.g., Horgan et al., 2013). The remaining sources of

3340 uncertainty are related to user-defined inversion parameters.

3341

3342 4.5.1.3 Density component

3343 The choice of density values for the ice, water, and sediment results in a mean un-
 3344 certainty in the bathymetry model of 24 m (Figure 4.16c). The ranges of densities
 3345 tested in the Monte Carlo simulation were $\sim 905 - 925 \text{ kg m}^{-3}$ for ice⁵, $\sim 1015 -$
 3346 1035 kg m^{-3} for seawater, and $\sim 1600 - 3000 \text{ kg m}^{-3}$ for the seafloor. We only test
 3347 homogeneous changes in the density values.

3348

3349 The uncertainty arising from the choice in density values has a strong spatial cor-
 3350 relation with the absolute value of the inversion's input gravity, the residual gravity
 3351 (Figure 4.12d). This correlation can be explained by the inverse relation between
 3352 the amplitude of the corrections applied to the bathymetry during the inversion,
 3353 and the density contrasts used in the inversion. For the same gravity anomaly, a
 3354 smaller density contrast results in a larger amplitude correction while a larger den-
 3355 sity contrast results in a smaller correction. This means that changes in the density
 3356 values just affect the amplitude of the correction applied to the bathymetry. Often,
 3357 spatially variable density is used as a means to account for the regional component
 3358 of gravity (e.g., Constantino et al., 2020; Tinto et al., 2019). We note that there
 3359 is an additional benefit to incorporating spatially variable densities. If adequate
 3360 *a priori* information is known to justify a density distribution, this can be used
 3361 to allow differing amplitudes of corrections across the inversion domain. In other
 3362 words, if the seafloor truly is denser in one region of the inversion compared to the
 3363 seafloor elsewhere, for a similar gravity anomaly, the inversion correction should be
 3364 of smaller amplitude in the high-density region. However, due to a lack of geologic
 3365 knowledge beneath the ice shelf, we use constant density values. We propose Monte
 3366 Carlo sampling of a wide range of possible density values as a robust and feasible
 3367 method to avoid biasing the resulting bathymetry model to either too high or too
 3368 low correction amplitudes, to achieve both the most realistic results and an estima-
 3369 tion of the uncertainty.

3370

3371 4.5.1.4 Interpolation component

3372 The final components of the overall uncertainty are related to interpolation con-
 3373 ducted during two stages of the inversion; 1) the interpolation of the starting model
 3374 from the sparse constraint point depths, and 2) the estimation of the regional field
 3375 from the interpolation of gravity values at the constraint points. Here, we have used
 3376 a minimum curvature gridding algorithm (Smith & Wessel, 1990), which accepts a
 3377 tension factor for the interpolation which can range from 0 to 1. Figure 4.9 shows
 3378 the results of six different values of this tension factor for creating the starting bed
 3379 model. These figures show that low values of tension are able to accurately reproduce
 3380 the data with a smooth interpolation, but can result in unconstrained local maxima
 3381 or minima. Conversely, high tension values produce smooth surfaces without false
 3382 oscillations but don't adhere to the data as well. For these issues associated with

⁵We note that the maximum density of meteoric ice is 917 kg m^{-3} , however, the inclusion of marine ice may raise this value (Fricker et al., 2001)

3383 the two end members, intermediate values of 0.25 and 0.35 are often suggested for
3384 potential field data and topographic data, respectively. We suggest a more robust
3385 alternative to using these suggested values is the Monte Carlo sampling approach
3386 we have used. This runs the inversion with a variety of tension factors and uses
3387 the standard deviation of the resulting bathymetry models as a means to estimate
3388 the uncertainty associated with the choice of the tension factor. While tensioned
3389 minimum curvature gridding has been used in several past inversions (e.g., An et al.,
3390 2019a; Millan et al., 2020; Yang et al., 2021), the choice of the tension values has
3391 not been discussed for these applications.

3392
3393 The uncertainties arising from the choice of tension factors are shown in Figure
3394 4.16d and e. The tension factor for gridding the starting bed model results in a
3395 relatively low uncertainty with a mean of 7 m. The resulting uncertainty for the
3396 regional separation is comparatively high, with a mean of 24 m. Both of these re-
3397 sults show large spatial heterogeneity, with significantly larger uncertainties along
3398 the Transantarctic Mountain front. This is likely related to the poor performance
3399 of this gridding algorithm for high-gradient data. This region along the mountain
3400 front has both steep topography and high amplitude gravity anomalies.
3401

3402 4.5.1.5 Reducing uncertainties

3403 Of the various components of the uncertainty analysis, only some can feasibly be
3404 reduced. Reducing the uncertainty resulting from the interpolation parameters may
3405 be possible with future method development, but this is beyond the discussion of this
3406 research. To our knowledge, there is no robust method of determining a spatially
3407 variable density distribution to be used in the inversion, without the collection of in-
3408 situ data. This leaves the data inputs, gravity and constraints, as viable components
3409 of a bathymetry inversion where further reductions of uncertainties can occur. We
3410 propose a favorability of quantity over quality for constraint data, since typical bed
3411 elevation uncertainty is already relatively low, and therefore more data of mediocre
3412 quality should be prioritized over high quality but spatially limited data. In order
3413 to reduce the uncertainty component resulting from the gravity data, first we must
3414 be able to estimate the realistic spatial uncertainty of the gravity data itself. A
3415 simple cross-over analysis is too simple to cover the effects of turbulence, chang-
3416 ing flight speed and altitude, and errors in processing steps, such as base station
3417 ties and levelling. The areas of largest uncertainty are generally a function of 1)
3418 distance to the nearest constraint point (Figure 4.10) and 2) proximity to steep gra-
3419 dients of topography and/or gravity (Figure 4.16d and e). This highlights the entire
3420 Transantarctic Mountain front of the Ross Ice Shelf and the two major constraint
3421 gaps in the central-east portion of the ice shelf (Figure 4.10) as locations that would
3422 greatly benefit from additional seismic surveying.

3423 4.5.1.6 Past estimations of uncertainty

3424 Our comprehensive uncertainty and sensitivity analysis is shown to be similar to the
3425 approximated uncertainties reported for other ice shelves (Table 4.1). Some differ-
3426 ences include; our reported uncertainty resulting from the gravity data uncertainty
3427 is the highest reported, while our values resulting from other sources, and the total
3428 uncertainty, were similar to those of other studies. Our larger reported uncertainty

resulting from the gravity data likely shows that the simple Bouguer slab approximation used by the other studies underestimates the component of uncertainty resulting from the gravity data uncertainty. We take the uncertainties resulting from geologic variations to be the combination of our reported uncertainties from the chosen density values (Figure 4.16c) and from the regional separation gridding (Figure 4.16e) since these both affect the estimation of the regional component. The uncertainty resulting from the constraint point measurement uncertainty was very similar across all studies.

From this, we propose future bathymetry inversions undertake similar uncertainty analysis through the Monte Carlo sampling of the input parameters. This technique not only provides similar uncertainty estimates to past studies, but it accomplishes it in a systematic and reproducible method. Additionally, this technique provides a spatial distribution of the uncertainties, instead of a single value. Once the inversion workflow is set up, the sampling and re-running of the inversion is a simple procedure, and with the use of Latin hypercube sampling, we have shown that with only 10 runs, the parameter space of all the inputs is adequately sampled (Figure 4.8).

3447

4.5.2 Past bathymetry models

Our gravity-inverted bathymetry model for the sub-Ross Ice Shelf reveals significant differences with previous bathymetry models. However, a portion of these differences are not related to the inversion, but to the creation of the starting model. First, we will discuss the differences between our starting bathymetry model and another interpolation-based bathymetry model, then we will compare our inversion results with two past models. These past models include Bedmap2 (Fretwell et al., 2013) and Bedmachine v3 (Morlighem, 2022; Morlighem et al., 2020). The Bedmap2 model for the Ross Ice Shelf region is created from the interpolation of the same constraint points within the ice shelf as used in this study, as well as grounded ice thickness measurements and limited rock outcrop elevation data (Fretwell et al., 2013; Le Brocq et al., 2010; Timmermann et al., 2010). BedMachine v3 used these point measurements and applied additional methods to increase the resolution of the bed. For outside of the ice shelf, this included mass conservation for areas of fast-moving ice (outlet glaciers and ice streams), streamline diffusion for regions of slow-moving ice, as well as minimum curvature gridding to interpolate the remaining gaps (Morlighem et al., 2020). Within the ice shelf, BedMachine used the gravity inversion results of Tinto et al. (2019).

3466

4.5.2.1 Starting model comparison

Figure 4.9 shows the series of six starting bed models we created from the interpolation of the sparse constraints. These were created with six levels of tension applied to a minimum curvature interpolation. The cell-specific standard deviation of these six models shows the uncertainty associated with this interpolation (Figure 4.9g), and the mean of the six grids is our chosen starting model (Figure 4.9h). This is compared with the Bedmap2 model in (Figure 4.9i). The RMS difference between the two grids, within the ice shelf, is 95 m. Our starting bed is deeper proximal to

3475 the entire grounding zone, while it is shallower along the ice front and throughout
3476 the center of the ice shelf. However, these differences of up to 200 m do not suggest
3477 our starting model is inaccurate. Sampling the grid values at the constraint points
3478 and comparing them with the constraint depths shows that our model was signif-
3479 icantly better at adhering to these constraints, compared to Bedmap2. The RMS
3480 of the difference with our model was 14 m, while the RMS of Bedmap2 was 138 m
3481 (Figure 4.1).

3482
3483 These large differences for Bedmap2 are concentrated along the Transantarctic
3484 Mountain front, where the interpolation algorithm used in Bedmap2 resulted in ex-
3485 cessively shallow bathymetry. This interpolation appears to have favoured smooth-
3486 ness over accuracy for this location of steep terrain. This has resulted in a "leakage"
3487 of the high elevations within the mountains into the bathymetry interpolation, as
3488 pointed out in this region (Le Brocq et al., 2010), as well as for other ice shelves
3489 (Brisbourne et al., 2020). This over-smoothing and "leakage", while strongest along
3490 the mountain front, can be seen along the entire grounding zone. This is the reason
3491 why Bedmap2 was more shallow than our starting model along the grounding line.
3492 This shows that care needs to be taken when picking or creating a starting model for
3493 an inversion, especially in regions of steep topography. The re-creation of the start-
3494 ing model from the point data allows the choice of interpolation techniques better
3495 suited for the region of interest, compared to techniques determined most suitable
3496 for a continent-wide study.

3497

3498 4.5.2.2 Inversion result comparisons

3499 Bedmap2 comparison

3500 Figure 4.17 compares our final bathymetry results with the models of Bedmap2 and
3501 BedMachine v3. Additionally, several profiles across different regions are shown in
3502 Figure 4.18, comparing the various models. Interestingly, the inversion has raised
3503 the RMS difference with Bedmap2, compared to the starting model. But due to the
3504 issues with the Bedmap2 grid along the mountain front, this increased difference is
3505 expected. The differences between our inverted bed and Bedmap2 have a normal
3506 distribution (Figure 4.17d). Our results introduce many small-scale features, as ex-
3507 pected since Bedmap2 is an inherently smooth product. However, there are several
3508 noticeable large-scale differences with Bedmap2. Proximal to the grounding line,
3509 our results are generally deeper, as seen with the starting model comparison (Figure
3510 4.18g). Many of the regions where our results are deeper are related to the issue of
3511 over-shallow interpolation of Bedmap2. Portions of the grounding zone along the
3512 Siple Coast are over 200 m deeper, including the Kamb (Figure 4.18c) and Mercer
3513 ice stream grounding zones.

3514

3515 Another notable difference is an NW-SE oriented trough which appears in our
3516 results but is essentially absent in Bedmap2. This feature begins at the southern
3517 end of the Crary Ice Rise grounding zone and continues ~ 300 km, paralleling the
3518 mountain front (Figure 4.18c). This feature is the southwestern-most of a series of
3519 2 or 3 parallel troughs and ridges, as shown in Figure 4.18d. These features are
3520 oriented at a high angle to both E-W and N-S flight lines, increasing their likelihood
3521 as true features of the bathymetry and not flight line levelling artifacts. While they

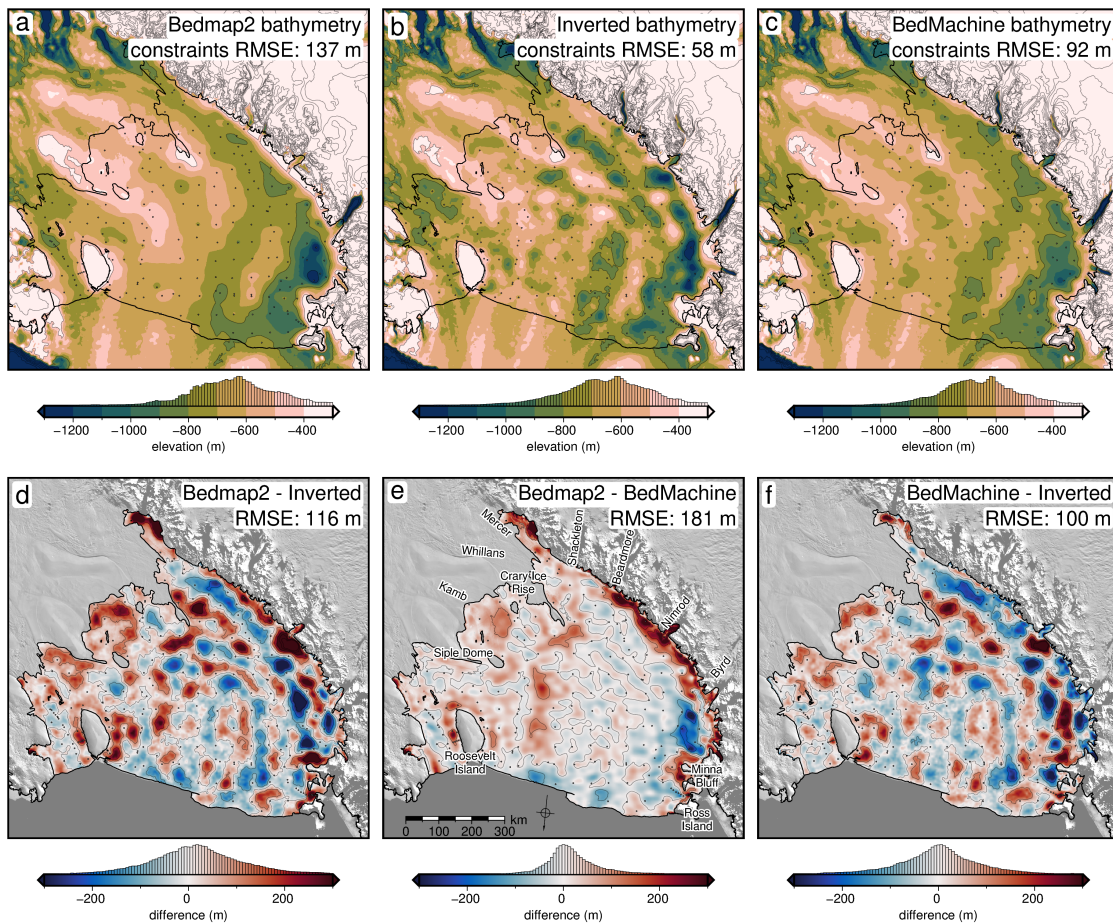


Figure 4.17: Comparison of our inverted bathymetry with past models. **a)** Bedmap2 bathymetry, **b)** our inversion results, from the weighted mean of the full Monte Carlo simulation, and **c)** BedMachine bathymetry. All three share the same colour scale and are contoured at 400 m intervals. RMS difference with the constraint points for each model is stated on the maps. **d)** Difference between our model and Bedmap2, **e)** difference between Bedmap2 and BedMachine v3, and **f)** difference between our model and BedMachine v3. Grids share a colour scale and are contoured at 100 m intervals. Blue regions in **d** and **f** indicate where our results are shallower, while red regions indicate where our results are deeper than the past models. Blue regions in **e** indicate where BedMachine is shallow, while red regions indicate where BedMachine is deeper than Bedmap2. RMS differences are stated on the maps. Grounding line and coastline are shown in black (Morlighem, 2022). Background imagery is from Scambos et al. (2007). Elevations are referenced to the WGS-84 ellipsoid.

are subtle, their presence alters the general *texture* in the region from a primary N-S / NNE-SSW to an NW-SW orientation. This switches the general trend of bathymetry features in the region to be aligned with Siple Coast ice flow, rather than the Transantarctic outlet glacier ice flow. Whether these bedforms are tectonic in nature, revealing the tectonic fabric, or are erosion/depositional, and thus revealing the past flow directions of the previously grounded ice sheet is unknown. The last major difference with Bedmap2 is a significantly deeper bathymetry along the western edge of Roosevelt Island (Figure 4.18a)

3520
3521
3522
3523
3524
3525
3526
3527
3528
3529

3530 **Bedmachine comparison**

3531 Comparing our results to Bedmachine v3 provides a unique opportunity to evaluate
3532 the differences resulting from different gravity inversion algorithms. The gravity
3533

3534 inversion results of Tinto et al. (2019), which comprise the Bedmachine v3 data be-
3535 neath the ice shelf, used similar input datasets (gravity data and constraint points),
3536 suggesting that differing inversion algorithms and workflows are likely responsible
3537 for the majority of the differences shown in Figure 4.17f. However, some of the
3538 differences may arise from re-processing the gravity data, and a different method of
3539 gravity reduction applied here, as compared in Section 4.3.

3540

3541 To remove the regional component of gravity, Tinto et al. (2019) used a smoothly
3542 varying density model in their inversion. To create this density model, they created
3543 an initial prism layer with prisms extending from their starting bathymetry to a
3544 depth of 60 km. With the gravity disturbance, they performed a density inver-
3545 sion to recover the density of each prism. This spatially variable density was then
3546 low-pass filtered, with a 50km cutoff. Incorporating this remaining long-wavelength
3547 gravity signal within the density model removed the regional component from the
3548 gravity input to the inversion. This technique is conceptually similar to high-pass
3549 filtering the gravity data to remove the long-wavelength component. For the in-
3550 version, Tinto et al. (2019) used the commercial software Geosoft Oasis Montaj.
3551 Limited information is available from Geosoft as to the specifics of this inversion
3552 procedure.

3553

3554 Comparing our bathymetry (Figure 4.17f), there is a normal distribution of dif-
3555 ferences, centred on zero. The RMS difference between the two grids is \sim 100 m.
3556 Comparing each grid to the constraint point depths, the BedMachine grid has an
3557 RMS difference of 92 m, compared to our RMS of 44 m. Generally, our results
3558 are approximately 50-100 m deeper proximal to most of the Siple Coast ground-
3559 ing line. Conversely, our results are approximately 50-100 m shallower along the
3560 Transantarctic Mountain front. This could be due to our inability to fully fix the
3561 issue of overly-shallow interpolation of data along the mountain front in the creation
3562 of our starting model, as discussed.

3563

3564 Alternatively, the differences could be a result of the different gravity reduction
3565 steps. Figure 4.12b and e show that correcting the gravity disturbance for the terrain
3566 mass effect results in a large negative topo-free disturbance along the Transantarc-
3567 tic mountain front (dark blues in **b**). During the regional field estimation, fitting
3568 a spline to these large negative values would bring down the nearby regional field,
3569 resulting in an underestimation of the regional (more negative), and thus an over-
3570 estimation of the residual (positive values). This is shown by the profile of Figure
3571 4.12e. On the right side, along the mountain front, in an attempt to fit the negative
3572 values of the topo-free disturbance (red dashed line), the regional field (blue) has
3573 been underestimated, leaving a large positive residual anomaly (pink dashed). This
3574 positive residual results in a shallowing of the inverted bathymetry.

3575

3576 These shallower depths along the mountain front, instead, could be revealing
3577 a flaw in the constraint point minimization assumption of the residual being 0 at
3578 constraints. While the constraint point itself doesn't contribute to the residual sig-
3579 nal, since the actual bed is equal to the starting bed at those points, deviations
3580 between the actual bed and the starting bed in the vicinity of the constraints may
3581 lead to a non-zero residual at the constraint. In this case, the interpolation of the
3582 regional field attempts to smoothly connect extremely negative values at the moun-

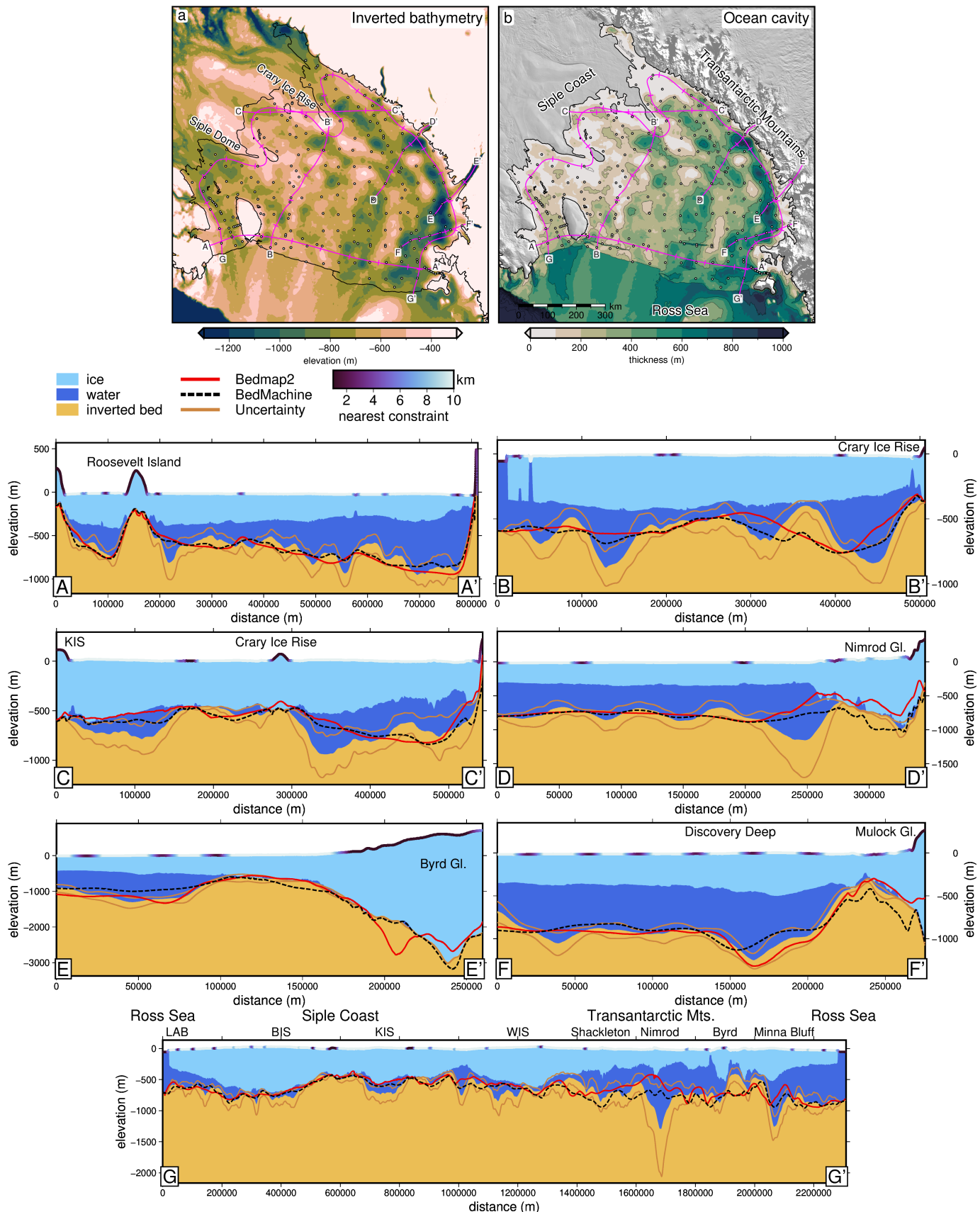


Figure 4.18: **Upper panel)** Ross Ice Shelf inverted bathymetry (left) and water column thickness (bed to ice base) relative to Bedmachine v3 ice base (Morlighem, 2022). Pink lines show profile locations with ticks every ~100 km. Grounding line and coastline in black (Mouginot et al., 2017). Constraint points shown as dots. **Profiles A-G)** Various cross-sections showing the ice layer (light blue), water layer (darker blue), and bathymetry (yellow), with uncertainties (brown). Red and black lines show Bedmap2 and BedMachine v3 bathymetry, respectively. Color of ice surface indicates distance to nearest constraint. Legend and colorscale shown above profile A.

tain front, and high values at the nearby constraints. This high gradient leads to poor interpolation. This can be seen in 4.12e where the regional (blue line) is force exactly equal to the topo-free disturbance (red dashed line) at the constraint point at 700 km along the profile. In reality, the residual gravity at that constraint is likely non-zero. A non-zero value may allow the regional field to closer match the large positive topo-free disturbance located at 720 km.

3589

The remaining major differences between our results and BedMachine v3 include the same series of alternating NW-SE troughs and ridges as discussed above, an ~ 100 m deeper region on the west side of Roosevelt Island, and a significantly deeper (~ 250 m) trough spanning from the south side of Minna Bluff to the outlet of the Byrd Glacier. The deepest depths we model in this trough are $\sim 1350 \pm 100$ m, located offshore of the Byrd Glacier Outlet. Preliminary results of a seismic survey at Discovery Deep, just south of Minna Bluff (cyan line Figure 4.15), in the 2021/2022 field season report depths up to 1450 m (pers. comm. Prof. A. Gorman). These findings confirm the presence of depths of this range, but our deepest bathymetry is approximately 100 km north of our deepest results. This seismic data was not included in this inversion. An additional comparison  a seismic survey can be made proximal to the Kamb Ice Stream grounding zone (cyan line Figure 4.15). Horgan et al. (2017) image bathymetry depths along a ~ 20 km seismic survey with a mean depth of ~ 605 m. Sampling our bathymetry and uncertainty along this profile yields a mean depth of $\sim 608 \pm 45$ m, while sampling BedMachine v3 bathymetry and uncertainty yields a mean depth of $\sim 572 \pm 79$ m.

3606

Comparing the various difference maps of Figure 4.17 shows that our inversion has resulted in more varied topography across the ice shelf compared to Tinto et al. (2019). This increased amplitude is likely due to the differences in densities used between the inversions. Tinto et al. (2019) used a spatially variable density model, which ranged from $\sim 2600 - 2800$ kg m $^{-3}$, with a mean of ~ 2700 kg m $^{-3}$. While we used a spatially-constant density value, in the Monte Carlo analysis the density was varied between $\sim 1800 - 3000$ kg m $^{-3}$, with a mean of ~ 2400 kg m $^{-3}$. This ~ 300 kg m $^{-3}$ difference between the mean density values would result in a more subdued inverted bathymetry from the (Tinto et al., 2019) model. While the Tinto et al. (2019) density model does a good job of removing the regional field prior to the inversion, whether or not the density values used are representative of the seafloor is questionable. The lowest values in their model of approximately 2600 kg m $^{-3}$ represent the upper end of sedimentary rock densities (Schön, 2015), and are significantly greater than expected densities of unconsolidated sediments. For a region with an expected continuous drape of seafloor sediments (Chapter 2, Tankersley et al., 2022), we believe the densities used in (Tinto et al., 2019) to be too high. This explanation for the differences between the inversion results is supported by the strong correlation between our bathymetry uncertainty resulting from the choice in density (Figure 4.16c) and the difference between the inversion results (Figure 4.17f). This shows the importance of picking a plausible density value, and the added benefit of testing many values to estimate the uncertainty related to the chosen density value.

3628

4.5.2.3 Ocean cavity comparison

Due to the smoothness of the base of an ice shelf, relative to bathymetry, the water column thickness beneath many ice shelves is predominately determined by the bathymetry. We use BedMachine v3 ice base elevations and our updated bathymetry to calculate the water column thickness beneath the Ross Ice Shelf and compare the results to the water column thicknesses of Bedmap2 and BedMachine (Figure 4.19). These differences are very similar to those described above, due to the smooth nature of the ice base. Notable areas where our results show a thicker ocean cavity (within uncertainty ranges) compared to past models include;

1. nearby the Kamb grounding zone ($\sim 100 \pm 50$ m thicker, Figure 4.18c near km 100)
2. the west side of Crary Ice Rise ($\sim 300 \pm 150$ m thicker, Figure 4.18c near km 350)
3. the south side of Minna Bluff ($\sim 300 \pm 200$ m thicker, Figure 4.18g near km 2100)
4. the west side of Roosevelt Island ($\sim 200 \pm 100$ m thicker, Figure 4.18a near km 220))

Notable areas where our results show a thinner cavity include;

1. the mountain front north of Byrd Glacier ($\sim 300 \pm 50$ m thinner, Figure 4.18g near km 2000))
2. three 50 km wide regions in the central ice shelf, which are up to 200 ± 50 m thinner
3. several points approximately 50 km off of the Transantarctic Mountain front which are up to 400 ± 50 m thinner (Figure 4.18c near km 150)



4.5.3 Implications

Here, we discuss several of the important implications of our updated sub-RIS bathymetry. These implications relate to the stability of the Ross Ice Shelf, geology, and tectonics.

4.5.3.1 New pinning points

We have identified several areas of thin water column thickness (< 20 m) with our updated results beneath the Ross Ice Shelf. These areas are shown by the 20 m water column thickness contour, in bright blue in Figure 4.19a. These include a $\sim 100 \times 100$ km region SW of Roosevelt Island, several $\sim 50 \times 50$ km regions on the north flank of Crary Ice Rise (Figure 4.18g at km ~ 900), and a widespread region south of Crary Ice Rise (Figure 4.18g at km ~ 1350). Thin water depths south of Crary Ice Rise have also been modelled by a local gravity survey along the Whillans Ice Stream grounding zone (Muto et al., 2013b). Additionally, two smaller regions of sub-20 m water column thickness are found nearer the centre of the ice shelf. One is approximately 100 km off the point of Crary Ice Rise and is ~ 400 km² (Figure

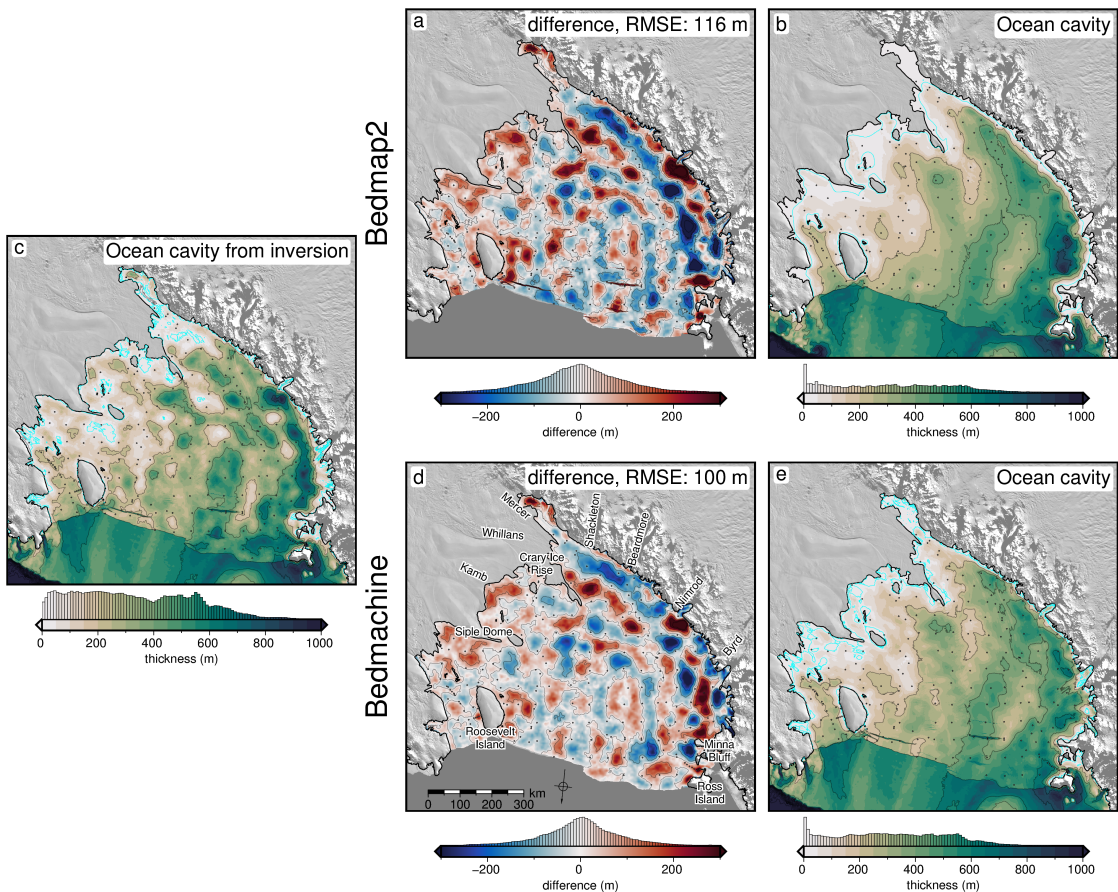


Figure 4.19: Comparison of our updated water column thickness with past models. **a)** Difference between our model and the water column thickness from Bedmap2, and **b)** the Bedmap2 water column thickness. **c)** Water column thickness calculated as the difference between BedMachine v3 icebase and our inverted bathymetry. **d)** Difference between our model and the water column thickness from BedMachine v3, and **e)** the BedMachine v3 water column thickness. Blue regions in the difference maps indicate where our results' water column is thinner, while red regions indicate where our results are thicker than the past models. Grounding line and coastline are shown in black (Morlighem, 2022). Background imagery is from Scambos et al. (2007). Water column thickness grids are contoured at 200 m intervals, and the 20 m contour is shown in bright blue. The difference grids are contoured at 100 m intervals. Water column thickness grids and difference grids share common colour scales.

3668 4.18c at km \sim 200). The second is \sim 200 km north of Crary Ice Rise and is slightly
 3669 smaller (Figure 4.18b at km \sim 350). None of these shallow water column regions are
 3670 present in either of the past models. Interestingly, these regions coincide with some
 3671 of the lowest uncertainties we report \sim 20 m. A portion of this low uncertainty may
 3672 be related to the inversion constraining the bathymetry to the ice base, which in
 3673 regions of thin water column will reduce the variability of the suite of inversions in
 3674 the Monte Carlo simulation which were used to define the uncertainty.

3675

3676 These new-identified shallow regions highlight where the Ross Ice Shelf was likely
 3677 grounded in the recent past, or could likely become re-grounded in the future. While
 3678 some of these regions are small, analysis of pinning points on the Ross Ice Shelf has
 3679 shown some of the smallest pinning points can create the largest effective resistance
 3680 on the ice shelf (Still et al., 2019). Additionally, some of these locations (north side
 3681 of Crary Ice Rise) are predicted to have on the order of 1 m/yr of basal accretion
 3682 (Adusumilli et al., 2020). An already thickening shelf within \sim 20 m of the bed will

likely affect the ice sheet dynamics as part of future projections of the ice shelf. Incorporation of these localities of likely past pinning points may aid in resolving the ongoing debate of the style of grounding line retreat and readvance of the Ross Ice Shelf throughout the Holocene (Kingslake et al., 2018; Lowry et al., 2019; Venturelli et al., 2020).

3688

3689 4.5.3.2 Basal melting

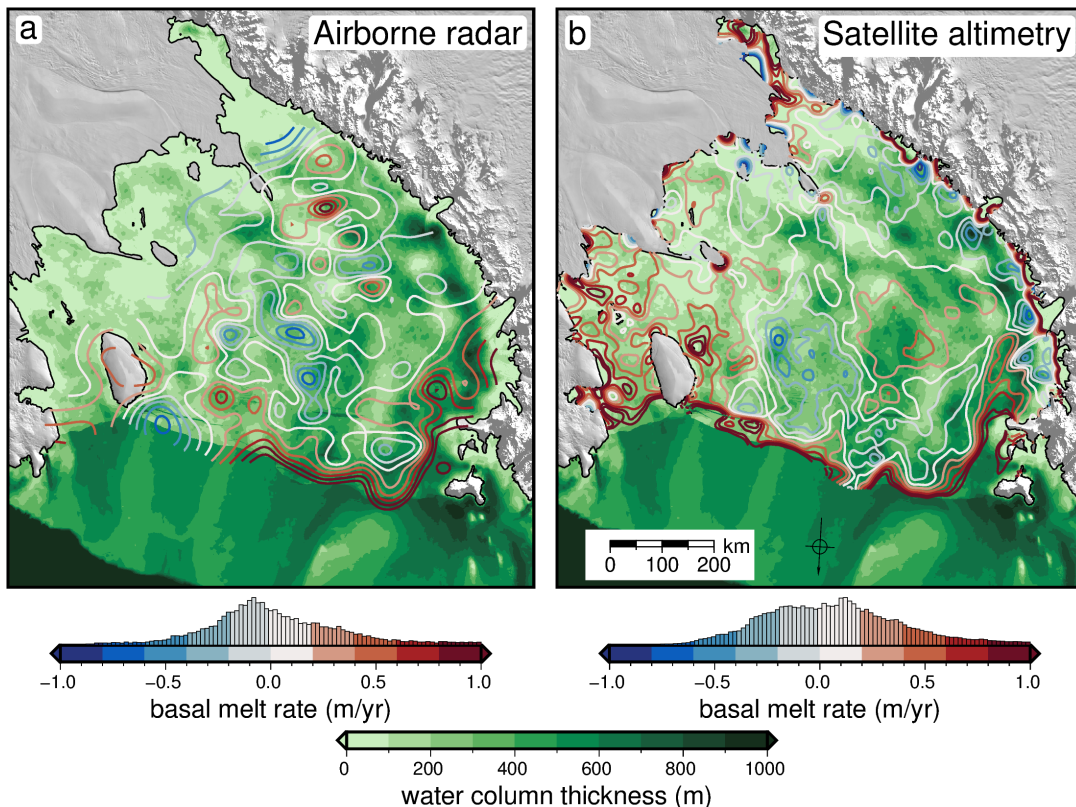


Figure 4.20: Basal melt rate and water column thickness compared for the Ross Ice Shelf. **a)** Blue to red contours show interpolated basal melt rate from Das et al. (2020) derived from ROSETTA-ice airborne ice-penetrating radar. Background shows water column thickness from this study. **b)** Same as **a** but with basal melt rate from Adusumilli et al. (2020) derived from satellite altimetry. Black line is the grounding line from Mouginot et al. (2017). Background imagery is from MODIS-MOA (Scambos et al., 2007).

Our updated bathymetry, water column thickness, and uncertainty maps provide additional information vital to understanding the distribution of basal melt beneath the ice shelf. Melt beneath the Ross Ice Shelf is thought to predominantly occur 1) along the ice front, where Antarctic Surface Water causes rapid melting in the summer (Figure 4.20 Horgan et al., 2011; Moholdt et al., 2014), and along the deep grounding zones of the Transantarctic Mountain front, where contact with High Salinity Shelf Water induces melting (Figure 4.20b Adusumilli et al., 2020; Tinto et al., 2019). Throughout the centre of the ice shelf are zones of refreezing (Figure 4.20 Adusumilli et al., 2020; Das et al., 2020). Overall basal melting of the Ross Ice Shelf is thought to be low compared to other shelves due to the blocking of warm Circumpolar Deep Water from entering the cavity. This blocking is from a layer of dense High Salinity Shelf Water (Dinniman et al., 2011; Tinto et al., 2019). The

3702 Hayes Bank (Figure 4.1b) has been identified as one location where the Circumpolar
3703 Deep Water is able to penetrate the ice shelf cavity and induce melting, but this
3704 penetration is thought to be limited to the region near Roosevelt Island (Das et al.,
3705 2020; Tinto et al., 2019). Our ocean cavity is ~ 100 m thicker than Tinto et al.
3706 (2019) immediately to the west of Roosevelt Island (Figures 4.18a and 4.19d). This
3707 region should be investigated with sub-shelf circulation models using our updated
3708 bathymetry. Our larger cavity allowing the inflow of warm Circumpolar Deep Water
3709 beyond Roosevelt Island could help explain the relatively large basal melt rate found
3710 in the region as shown by satellite altimetry (Figure 4.20b).

3711
3712 The high melt rates measured along the Transantarctic Mountain front (Adusumilli
3713 et al., 2020) are caused by the inflow of High Salinity Shelf Water (Tinto et al.,
3714 2019). This water is thought to be guided by bathymetric troughs and is able to
3715 induce melting only at large depths, due to the pressure suppression of the melting
3716 temperature of ice. Figures 4.20 show a comparison of both airborne radar and
3717 satellite altimetry-derived basal melt rates to the updated water column thickness
3718 resulting from our bathymetry inversion. The deeper bathymetry proximal to the
3719 Transantarctic Mountain front found in both our inversion and (Tinto et al., 2019),
3720 compared to the depths of Bedmap2, help explain the high melt rates measured
3721 there. The other locations we report with deeper bathymetry near grounding zones,
3722 such as the south side of Minna Bluff, and the far southern end of the ice shelf, at the
3723 Mercer Ice Stream grounding zone, may be potential locations where High Salinity
3724 Shelf Water is able to induce basal melt. Additionally, some of the very shallow
3725 water column thicknesses (< 20 m) we find (Figure 4.19c), for instance to the south
3726 of Crary Ice Rise, correspond with low basal melt rates (Figure 4.20). This may
3727 be due to the lack of stratification in the water column, which occurs due to tidal
3728 mixing possible only in thin water columns (Holland, 2008; Muto et al., 2013b).

3729 4.5.3.3 Geologic and tectonic significance

3730 While there are many interesting implications to explore in this new dataset, we
3731 limit our discussion to several sub-Ross Ice Shelf bathymetric features of possible
3732 importance to solid-Earth investigations. These features include the bathymetry
3733 along the Transantarctic Mountain front, a deep feature on the south-west flank of
3734 Crary Ice Rise, and a newly identified orientation of bathymetry features, aligned
3735 with the Siple Coast ice streams.

3736 Transantarctic Mountain front

3737 The Transantarctic Mountains (Figure 4.1a) make up the world's largest rift shoul-
3738 der. Despite their prominence, the uplift mechanisms are still debated (Goodge,
3739 2020). It is likely that these mechanisms vary along-strike, and consist of some com-
3740 bination of thermal, flexural, or isostatic support (Goodge, 2020). For the central
3741 TAM, a mechanism of cantilevered flexure is proposed for the uplift of the moun-
3742 tains (Wannamaker et al., 2017; Yamasaki et al., 2008). This theoretically should
3743 be accompanied by a deep trough parallel just offshore the range front, and an
3744 outer bathymetric high, approximately 200 km from the range front (Stern & ten
3745 Brink, 1989). These features have not yet been observed (ten Brink et al., 1993;
3746 Wannamaker et al., 2017). Our results show a deep trough along the range front
3747 between the Nimrod Glacier and Minna Bluff, with bathymetry highs further off-

shore. These features may support the theory of flexural uplift along this portion of the TAM (Wannamaker et al., 2017). Further south, where the trough disappears, the mechanism of flexural uplift is not required, since the mountains have a crustal root, which likely provides the uplift mechanism, via Airy isostasy (Block et al., 2009; Wannamaker et al., 2017).

3753 Fault bound Crary Ice Rise

3754 Figure 4.18c shows a profile of the updated bathymetry model across the Crary Ice
 3755 Rise. Our results show a steep drop off the south flank of the ice rise (at km \sim 320),
 3756 to depths up to \sim 1000 \pm 200 m. This steep drop-off is aligned with a NW-SE fault
 3757 proposed by Muto et al. (2013b) from a local gravity survey along the Whillan Ice
 3758 Stream grounding zone. Depth to basement analysis from magnetic data (Chapter
 3759 2, Tankersley et al., 2022) also highlights this north flank of Crary Ice Rise as a
 3760 likely location for faults. We believe this steep bathymetry feature adds evidence to
 3761 the proposition of the Crary Ice Rise as a fault-bound horst (Muto et al., 2013b).
 3762 This would imply the current grounding of the Ross Ice Shelf along the Crary Ice
 3763 Rise is in part controlled by regional tectonics.

3764 New bathymetric trend

3765 From the gridding of point data, the bathymetry of the central Ross Ice Shelf is
 3766 dominated by a N-S - NNE-SSW trend, aligned with the flow directions of the outlet
 3767 glaciers of the Transantarctic Mountains (Figure 4.1). Our updated bathymetry
 3768 model (Figure 4.15a) adds an overprinted NW-SE trend to the bathymetry features
 3769 of the central portion of the ice shelf. This trend is prevalent, but subtle, in the
 3770 inversion of Tinto et al. (2019). The features comprising this trend are a series of
 3771 2-3 ridges and troughs of \sim 100 m amplitudes and \sim 50 km wavelengths, as shown
 3772 in Figure 4.18d. These features are oblique to flight lines, adding to their validity,
 3773 and are well-aligned with the Crary Ice Rise and the general ice flow direction of the
 3774 Siple Coast ice streams. This trend could signify several things; 1) the most recently
 3775 grounded ice in this region had a flow direction aligned with the Siple Coast ice
 3776 streams, leaving behind erosional or depositional features with these orientations, 2)
 3777 these features are tectonic in origin, and are the surface expressions of rift structures.
 3778 These structures overprint the large bathymetric depression which runs from the
 3779 Nimrod glacier to the calving front. If these are features left behind from the most
 3780 recent grounding line retreat, they might inform the style of retreat. As seen in the
 3781 Ross Sea, physiography of the sea floor exerts the primary control on ice stream flow
 3782 and the patterns of retreat (Halberstadt et al., 2016).

3783 4.6 Conclusion

3784 Here we present an updated model of bathymetry depths beneath Antarctica's Ross
 3785 Ice Shelf, as modelled from airborne gravity data. Our inversion algorithm provides
 3786 a comprehensive spatial uncertainty analysis and parameter sensitivity estimation.
 3787 This uncertainty highlights regions of high uncertainty that would benefit from addi-
 3788 tional seismic constraints. These regions include the entire Transantarctic Mountain
 3789 front and two points near the centre of the shelf which are up to 40 km from the
 3790 nearest constraints. We summarize some key findings from the research below;

- 3791 1. Monte Carlo sampling is a robust method of uncertainty quantification and
3792 parameter sensitivity analysis for bathymetric gravity inversions.
- 3793 2. Sensitivity analysis shows that gravity data is the largest contributor to bathymetry
3794 uncertainty, followed by assumptions of the geology of the region.
- 3795 3. Our updated bathymetry model better matches *a priori* sub-ice shelf measure-
3796 ments compared to past models.
- 3797 4. Compared to Bedmap2, our results are deeper proximal to the grounding line
3798 and shallower along the ice front.
- 3799 5. Differences with the inversion of Tinto et al. (2019) (BedMachine v3) are
3800 mostly due to different chosen density contrasts.
- 3801 6. Newly identified potential past pinning points are found along the Siple Coast
3802 and in the central Ross Ice Shelf.
- 3803 7. Thick ocean cavity is found along the west flank of Roosevelt Island, where
3804 Circumpolar Deep Water flows under shelf and may highlight a region of im-
3805 portance for ocean circulation modelling.
- 3806 8. Possible tectonic implications including a fault-bound Crary Ice Rise and a
3807 flexural trough associated with Transantarctic Mountain uplift.

3808 Our results provide the datasets necessary to begin answering key questions re-
3809 garding the role of the Ross Ice Shelf in various components of the Earth system.
3810 These questions include; 1) where are melt-inducing bodies of water guided beneath
3811 the ice shelf? 2) where was the ice shelf grounded in the recent past, and what was
3812 the geometry of Holocene grounding line retreat and re-advance? Are the modern
3813 bathymetry features remnants of the last grounding line retreat, or are they tec-
3814 tonic in origin? While we don't provide direct answers to these questions, without
3815 adequate knowledge of the sea floor morphology and the associated uncertainties, in-
3816 vestigators won't have the relevant boundary conditions to answer these questions.
3817 All of the research conducted here is published as open-source Python code (see
3818 Chapter 1 Section 1.6), with hopes that the methods presented here can be used by
3819 researchers to better model the bathymetry and uncertainty of other Antarctic ice
3820 shelves.

³⁸²¹ Chapter 5

³⁸²² Synthesis

³⁸²³ Improving decadal to centennial projections of global sea level rise is of utmost im-
³⁸²⁴ portance for mitigating future environment and socio-economic impacts (Durand
³⁸²⁵ et al., 2022). Antarctica's projected contributions to global sea level rise by the
³⁸²⁶ end of the century under a high-emission scenario is between 0.03 and 0.28 m (RCP
³⁸²⁷ 8.5, Intergovernmental Panel on Climate Change (IPCC), 2022). This wide range
³⁸²⁸ of possible values expresses the uncertainty of the Antarctic Ice Sheet's response to
³⁸²⁹ a warming world. Over 80% of ice loss from Antarctica occurs through ice shelves
³⁸³⁰ (Rignot et al., 2013), highlighting their importance in reducing the uncertainty in
³⁸³¹ sea level rise projections. Antarctica's largest ice shelf, the Ross Ice Shelf, is fed
³⁸³² from both the East and West Antarctic Ice Sheets. Its catchment contains a total
³⁸³³ volume of ice equivalent to 11.6 m of global sea level rise (Fretwell et al., 2013;
³⁸³⁴ Rignot et al., 2011; Tinto et al., 2019). While the Ross Ice Shelf is relatively stable
³⁸³⁵ currently (Moholdt et al., 2014; Rignot et al., 2013), geologic evidence shows the
³⁸³⁶ rapid destabilization of the ice shelf within the past ~7,000 years (e.g., Naish et al.,
³⁸³⁷ 2009; Venturelli et al., 2020).

³⁸³⁸
³⁸³⁹ The destabilization of the ice shelf is thought to have been primarily caused
³⁸⁴⁰ by ocean forcings (Lowry et al., 2019), as bathymetric troughs guide the inflow of
³⁸⁴¹ melt-inducing ocean circulations (Tinto et al., 2019). The subsequent grounding
³⁸⁴² line retreat however is predominantly controlled by the physiography, geology, and
³⁸⁴³ glaciological feedbacks (Halberstadt et al., 2016). This highlights the solid earth,
³⁸⁴⁴ through its bathymetric control on basal melt and its effects on grounding line re-
³⁸⁴⁵ treat dynamics, as an important component of the dynamics of the Ross Ice Shelf.
³⁸⁴⁶ To reliably understand the contribution of the Ross Ice Shelf to future sea level rise,
³⁸⁴⁷ we must provide ocean and ice modellers with the necessary geologic boundary con-
³⁸⁴⁸ ditions. This thesis aimed to provide both these boundary conditions and estimates
³⁸⁴⁹ of their uncertainties to the modelling community. A series of research questions
³⁸⁵⁰ were proposed; as restated below:

- ³⁸⁵¹ 1. What is the geologic structure of the upper crust beneath the Ross Ice Shelf?
³⁸⁵² If there are sediments, what is their thickness and distribution? Where are
³⁸⁵³ the major faults likely located?
- ³⁸⁵⁴ 2. How can bathymetry beneath an ice shelf best be modelled? Are there further
³⁸⁵⁵ improvements that can be made to the gravity-inversion process? What are
³⁸⁵⁶ the predominant sources of uncertainty, and how can these be limited?

- 3857 3. How deep is the bathymetry beneath the Ross Ice Shelf and where are we most
3858 and least certain about it?
- 3859 4. What are the geologic controls on the Ross Ice Shelf's stability?

3860 Here we draw from the various research chapters to provide answers to these
3861 questions.

3862 5.1 Investigating geologic structures

3863 Research question 1

3864 To address research question 1 we sought to model the depth of the crystalline base-
3865 ment rock beneath the ice shelf. We accomplished this with a depth-to-magnetic
3866 source technique, which used airborne magnetic data and was calibrated to seismi-
3867 cally imaged basement depths of the Ross Sea. Our resulting basement topography
3868 revealed large-scale, fault-controlled extensional basins throughout the sub-Ross Ice
3869 Shelf crust (Figure 5.1f). Above this basement sits various sediments, likely rang-
3870 ing from coherent sedimentary rock to unconsolidated recent glacial and marine
3871 deposits. While there is a continuous drape of sediments across the entire ice shelf,
3872 we also image several distinct depocenters; the Western Ross Basin, covering the
3873 East Antarctic half of the ice shelf, and several basins on the West Antarctic side,
3874 including the Siple Dome Basin and the Crary Trough (Figure 5.1f). These results
3875 were incorporated into an Antarctic-wide review of sedimentary basins (Figure 5.1a
3876 Aitken et al., 2023b), showing the widespread distribution of similar basins across
3877 much of Antarctica. From our findings, we were able to draw a wide range of imp-
3878 lications, ranging from tectonic influence on ice dynamics along the Siple Coast to
3879 the buried and subsided remnants of an above-sea-level Oligocene mountain range,
3880 which likely accommodated alpine glaciers. These results provided the first view of
3881 the upper crust beneath the entirety of the Ross Ice Shelf.

3882

3883 5.2 Developing a gravity inversion

3884 Research question 2

3885 To provide modellers with accurate bathymetry depths beneath the Ross Ice Shelf,
3886 we utilized a gravity inversion technique. While there is an existing gravity-inverted
3887 bathymetry model for the Ross Ice Shelf (Tinto et al., 2019), the reported uncertain-
3888 ties were spatially uniform. To provide spatial uncertainties, we chose to develop
3889 a new gravity inversion algorithm. In addition, since the majority of gravity inver-
3890 sions use proprietary and expensive software, in an effort towards open-source and
3891 reproducible science, we chose to develop our gravity inversion using Python and
3892 release the code in an online repository.

3893

3894 Chapter 3 described this algorithm in detail. Extensive testing of various syn-
3895 thetic and semi-realistic datasets revealed several intricacies of performing a gravity
3896 inversion to attain a bathymetry model. The estimation and removal of the regional
3897 component of gravity, which occurs in the data reduction steps before the inversion,
3898 accounts for the majority of the error in the model. There are various techniques to

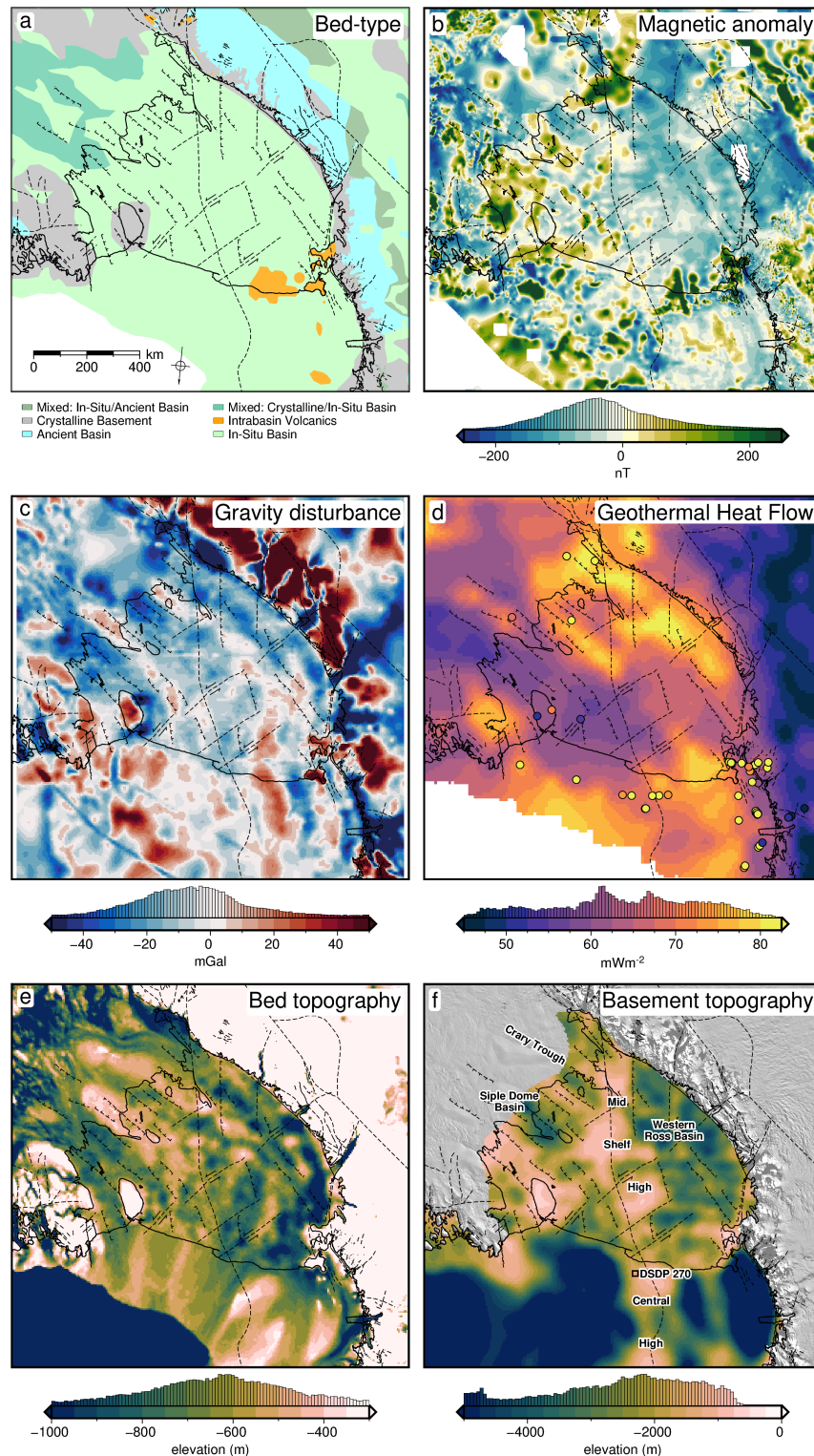


Figure 5.1: Summary of southern Ross Embayment geophysical and geologic information. **a)** Generalized geologic classification of the bed from Aitken et al. (2023a), **b)** ROSETTA-Ice airborne magnetic anomalies (Tinto et al., 2019) merged with ADMAP2 magnetic anomaly compilation (Golynsky et al., 2018), **c)** Gravity disturbance compilation from Forsberg (2020), include ROSETTA-Ice data. **d)** Geothermal heat flux from a seismically-derived model (Shen et al., 2020), and point measurements compiled from Burton-Johnson et al. (2020). **e)** Inverted bathymetry from Chapter 4, **f)** Basement topography from Chapter 2. Solid black line shows the grounding line and ice front from Mouginot et al. (2017). Fainter black lines show inferred (dashed) and exposed (solid) faults from a combination of Chapter 2 and Cox et al. (2023). Background imagery in **f** from MODIS-MOA (Scambos et al., 2007).

remove the regional field. We explore several of these methods and provide recommendations to best reduce the errors. Our uncertainty analysis highlighted regions of either steep topography or high gradient gravity anomalies as key regions where additional bathymetry measurements will make a significant contribution to reducing uncertainties. These suggestions of where to collect additional data should be considered alongside key regions of investigation identified through ocean modelling. Our findings suggest the quantity of bathymetry measurements is more important for reducing inversion uncertainty than the quality of these measurements. Conversely, we show larger sensitivity of the inversion results to the noise in the gravity data, relative to the density of gravity data collected. This suggests optimizing quantity over quality for bathymetry constraints while optimizing quality over quantity for gravity observation data. We hope these suggestions are able to better inform future Antarctic data collection for the goal of improving sub-ice shelf bathymetry models.

As part of Chapter 4, we compared our methods, of both the gravity reduction process and the inversion procedure, to all past bathymetry models conducted in Antarctica, as well as several from Greenland. Several other inversions have used a regional separation method similar to ours, however, none of these have provided an assessment of the associated uncertainties related to this method, which we found to be significant. We also found that all other inversions utilized a non-rigorous method of correcting the gravity data for the effects of ice, water, and topography. While the error introduced is likely small, with modern computing, applying this correction correctly is trivial.

From the other studies, excluding those with undocumented inversion algorithms, we found only one study which used a conventional regularized least-squares approach, similar to ours. Comparing our uncertainty analysis to past inversions revealed only two studies that report spatially variable uncertainties of their bathymetry model. It is our hope that the improvements made for the gravity inversion process are incorporated in future inversions in order to attain better estimates of uncertainties.

3930

5.3 Modelling Ross Ice Shelf Bathymetry

Research question 3

With the gravity inversion methodology laid out in Chapter 3, we created a new model of sub-Ross Ice Shelf bathymetry (Figure 5.1e). This model highlighted some important differences from past bathymetry models. In general, our model has more varied topography, compared to the smooth Bedmap2 model, and the intermediate BedMachine model. Compared to Bedmap2, we report significantly deeper bathymetry proximal to the entire grounding zone, including notably deeper areas near the Kamb Ice Stream, along the west side of Roosevelt Island, and south of Minna Bluff. Compared to the past inverted bathymetry (Tinto et al., 2019), our results are deeper along the Siple Coast but vary between deeper and shallower along the Transantarctic Mountain front. Our uncertainty analysis identified gravity data quality as the largest component of the overall uncertainty, while the distance from the nearest constraint and interpolation parameter values contributed significantly

3945 to the spatial variability of the uncertainty. From this, the largest uncertainties were
3946 found either far from constraints, or along the steep topography of the Transantarctic
3947 Mountains. This highlighted several locations where future seismic surveys would
3948 be able to effectively reduce uncertainties.

3949 5.4 Geologic controls on Ross Ice Shelf Stability

3950 Research question 4

3951 Next, we synthesize our findings which relate to the geologic influence on the Ross
3952 Ice Shelf, in an attempt to answer research question 4. We start with the controls
3953 on the ice shelf as it is today, before speculating on what these geologic controls
3954 were in the past or will be in the future.

3955 5.4.1 Present controls

3956 5.4.1.1 Basal melt

3957 Basal mass loss of the Ross Ice Shelf is dominated at the deep grounding zones,
3958 where relatively cool High Salinity Shelf Water is able to induce melting due to the
3959 high pressure at depth (Adusumilli et al., 2020; Tinto et al., 2019). These inflows of
3960 cold and dense water occur along the seafloor and are guided south beneath the ice
3961 shelf by bathymetric features (Holland, 2008). Tinto et al. (2019) model the domi-
3962 nant inflow of High Salinity Shelf Water starting near Ross Island, flowing south
3963 along the mountain front, where at the southern flank of Crary Ice Rise the flow
3964 turns north and flows back to the ice front through the centre of the ice shelf. This
3965 inflow is responsible for much of the basal melting of the Ross Ice Shelf (Adusumilli
3966 et al., 2020; Tinto et al., 2019). Our bathymetry model (Figure 5.1e) confirms the
3967 presence of a deep trough ranging from the western ice front along the Transantarctic
3968 Mountain front which accommodates this High Salinity Shelf Water inflow. Our
3969 mountain front trough however is both narrower and deeper than past models. At
3970 the Nimrod Glacier outlet our trough steps to the east by ~ 100km, and eventually
3971 ends along the south flank of Crary Ice Rise.

3972
3973 This eastward step is likely important for two reasons. 1) South of Nimrod
3974 Glacier, we model a shallow bathymetric shelf proximal to the grounding line. This
3975 likely blocks grounding line access to southward flowing High Salinity Shelf Water,
3976 limiting basal melt for the southernmost outlet glaciers. 2) The eastward step likely
3977 re-directs southward flowing High Salinity Shelf Water closer to the Siple Coast
3978 grounding zone, particularly the south flank of Crary Ice Rise. In this region, past
3979 bathymetry models show a continuous bathymetric ridge for ~ 300 km off the edge
3980 of Crary Ice Rise which blocks the inflow of High Salinity Shelf Water to the Siple
3981 Coast north of Crary Ice Rise (Tinto et al., 2019). Our results however show this
3982 ridge being dissected by two low saddles. If included in ocean circulation models,
3983 the lack of a continuous ridge and the presence of these low saddle may allow the
3984 inflow of circulations to the Siple Coast; a scenario which should be further explored.

3985
3986 The Hayes Bank, to the west of Roosevelt Island, has been identified as the
3987 primary location of inflow of warm Circumpolar Deep Water (Das et al., 2020;

3988 Tinto et al., 2019). We model a region of deeper-than-previously seen bathymetry
 3989 along the west edge of Roosevelt Island and propose this as a location that may
 3990 allow the incursion of this ocean water with a high potential for melt. Additionally,
 3991 along the Shirase Coast, south of Roosevelt Island, we model a thicker ocean cavity
 3992 than past estimates. This may allow further penetration of water which enters the
 3993 shelf near Hayes Bank. To address these highlighted regions of importance for basal
 3994 melt, future ocean circulation models should incorporate our bathymetry model.
 3995 Further, to test the sensitivity of sub-shelf circulations to bathymetry, the upper
 3996 and lower bounds of uncertainty should be used in separate circulation models to
 3997 test the range of possible sub-shelf circulations.

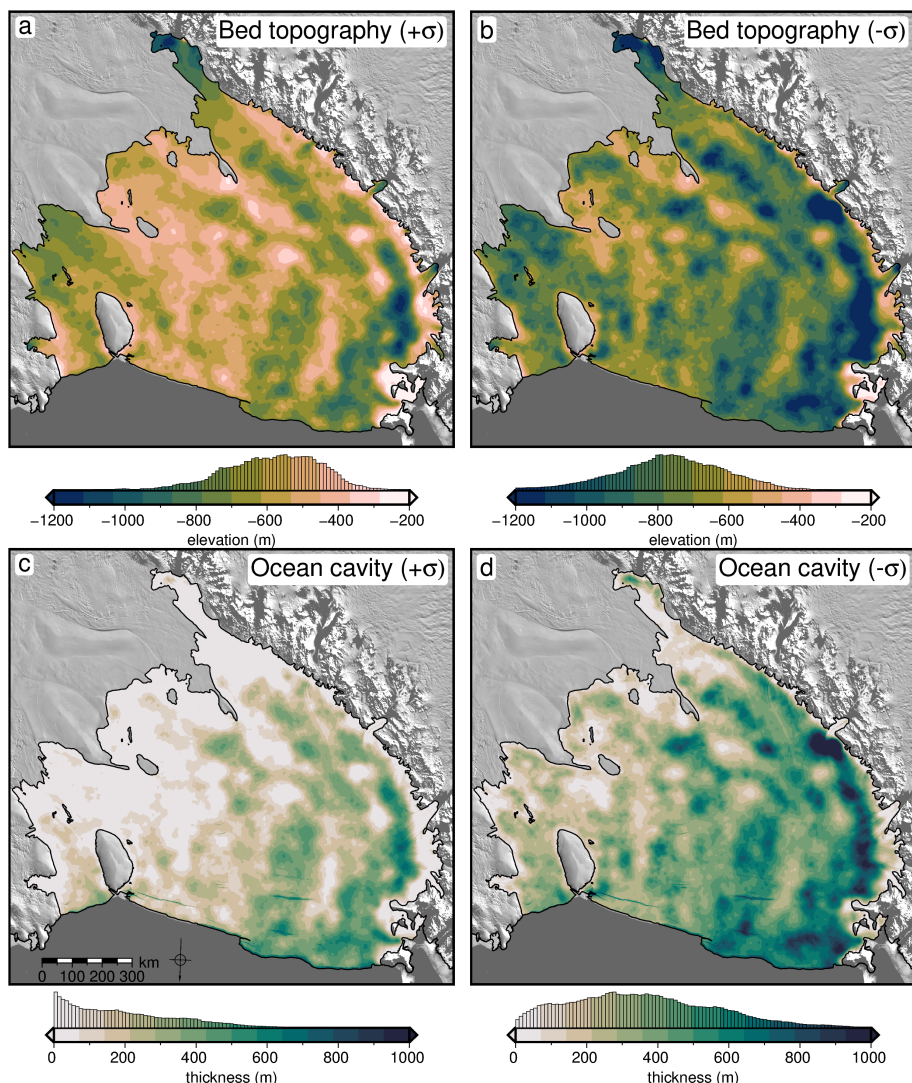


Figure 5.2: Lower and upper uncertainty bounds of Ross Ice Shelf bathymetry and ocean cavity thickness. **a)** Upper bathymetry uncertainty bound, **b)** lower bathymetry uncertainty bound, **c)** upper ocean cavity uncertainty bound, **d)** lower ocean cavity uncertainty bound.

3998 5.4.1.2 Modern pinning points

3999 Analysis of Ross Ice Shelf's pinning points has shown that the effective resistance as
 4000 well as the temporal persistence of pinning points are not tied solely to their size, but
 4001 are strongly influenced by the competency of the bedrock (Still et al., 2019; Still &
 4002 Hulbe, 2021). A really small pinning points which exert large effective resistance are

assumed to be grounded on bed with a high friction coefficient, while large pinning points which exert only minor resistance are assumed to be grounded on an easily deformable substrate. Based on the ratio of area to effective resistance, Still et al. (2019) suggested the bed beneath the Shirase Coast Ice Rumples, to the south-east of Roosevelt Island (Figure 5.3), is likely composed of competent bedrock with a high friction coefficient. Conversely, they suggest pinning point #14, just north of Crary Ice Rise, to be grounded on easily deformable till. The downstream extent of streaklines from pinning points provides an estimate of the temporal persistence of these features. Based on these streaklines, the Shirase Coast Ice Rumples and the Crary Ice Rise have likely been grounded for hundreds of years, while the large Steershead Ice Rise, just west of Siple Dome, only became grounded within the last 400 years (Fahnstock et al., 2000; Still et al., 2019).

4015

4016 Persistent pinning points

Our basement and sediment thickness results provide support for many of these observations of ice dynamics. The Shirase Coast Ice Rumples, predicted to have been long-lasting and grounded on competent bedrock, are shown in our basement results to sit upon a large basement high, with thin sedimentary cover. This implies both that the bedrock beneath the pinning point is either crystalline basement, or very coarse sediment from minimally re-worked basement material, and that the elevation of the bed is stable. This stability is likely due to both the tectonic nature of the bed as a fault-bound horst, and the higher strength of the bedrock, able to resist erosion by the overriding ice. Similarly, the persistence of Crary Ice Rise in the glaciologic record may be owed to its location above a basement ridge. Of the areas of possible recent grounding we identified, the region to the south of Crary Ice Rise, and the smaller area \sim 200 km north of Crary Ice Rise, both are located on similar large basement highs with thin sedimentary cover. When grounded, these past pinning points likely imparted a large effective resistance on the overriding ice.

4031

4032 Recent pinning points

The predicted deformable substrate of both Steershead Ice Rise and pinning point #14 (Still et al., 2019), as well as the recent grounding of Steershead Ice Rise (Fahnstock et al., 2000), are supported by our observations of these features being located over thick fault-bound sedimentary basins. These thick sediments provide material that is easily weathered into glacial till by the overriding ice, which lowers the effective resistance of the pinning point. If the basin bounding faults we predicted in Chapter 2 are truly active, they could accommodate local vertical bed movements associated with glacial isostatic adjustment following changing ice loads (Peltier et al., 2022; Steffen et al., 2021). For the very low-viscosity upper mantle and thin lithosphere beneath West Antarctica (Chen et al., 2018; Pappa et al., 2019), these solid earth responses to changing ice thickness may occur on decadal timescales (Barletta et al., 2018). This may help explain the short-lived history of these pinning points. One of the possible recent pinning points we identified is within the same sedimentary basin as Steershead Ice Rise (between Steershead Ice Rise and Roosevelt Island), and when grounded, likely shared these qualities. With these observations, we support the notion of a strong geologic control on the buttressing ability and persistence of pinning points throughout the Ross Ice Shelf. As the West Antarctic

4050 Ice Sheet thins, swift glacial isostatic rebound may lead to re-grounding; a response
4051 which may promote stability of the ice sheet (Barletta et al., 2018; Coulon et al.,
4052 2021; Kachuck et al., 2020). Accurate bathymetry beneath the Ross Ice Shelf is
4053 vital for knowing where this re-grounding may occur, and thus where new pinning
4054 points will develop.

4055 **5.4.1.3 Sediment distribution**

4056 The dynamics of Siple Coast ice streams are intrinsically tied to the bed which
4057 they flow over. The presence of sediments and sedimentary basins allows for several
4058 mechanisms to achieve the fast flow seen in these ice streams. 1) The sediments are
4059 able to deform in response to the shear stress of the overriding ice, allowing faster
4060 flow (Alley et al., 1986), 2) groundwater stored within the sedimentary basins both
4061 lubricates the ice base, reducing basal friction and increases till deformation, through
4062 increased pore-fluid pressure (Tulaczyk et al., 2000). Our results of Chapter 2 show
4063 a continuous drape of sediments across the ice shelf including along the Siple Coast
4064 grounding zone. The presence of these sediments helps explain the fast-flowing ice
4065 along this region. Additionally, we image several large sediment basins beneath the
4066 Siple Coast (Figure 5.1f). The groundwater storage capabilities of such basins could
4067 provide up to half of the groundwater in the subglacial system of West Antarctica
4068 (Christoffersen et al., 2014). The southernmost of these sedimentary basins has been
4069 confirmed by a recent magnetotelluric survey, which identified >1 km of sediments
4070 with extensive groundwater storage (Gustafson et al., 2022). The other two basins
4071 we imaged, the Siple Dome Basin, and the Crary Trough (Figure 5.3), could be key
4072 drivers on subglacial hydrology beneath the Siple Coast.

4073 **5.4.1.4 Geothermal heat flux at Siple Coast**

4074 **Spatial control on geothermal heat**

4075 The last main geologic control on Ross Ice Shelf stability we propose is the distribu-
4076 tion of geothermal heat along the Siple Coast (Figure 5.1d). Geothermal heat flux
4077 is one of the least constrained boundary conditions for Antarctica (Larour et al.,
4078 2012; Pollard et al., 2005; Seroussi et al., 2017). High geothermal heat supplied to
4079 the ice base can accelerate flow by 1) increasing englacial temperatures, reducing ice
4080 viscosity, 2) increasing basal lubrication through meltwater production and 3) in-
4081 creasing the ability of subglacial tills to deform, through water-saturation (Golledge
4082 et al., 2014; Pollard et al., 2005). While we don't provide any direct measurements
4083 of geothermal heat flux, our fault-bound sedimentary basins along the Siple Coast
4084 provide important insights into the temporal and spatial variability expected for
4085 geothermal heat flux along the Siple Coast.

4086
4087 Measurements and predictions of geothermal heat flux along the Siple Coast are
4088 shown to vary significantly, even between nearby (within ~ 100 km) measurements
4089 (Figure 5.1d, Begeman et al., 2017; Fox Maule et al., 2005). This high spatial
4090 variability is attributed to the localization of heat due to upper crustal structures
4091 (Begeman et al., 2017). Faults and basement margins act as efficient fluid conduits,
4092 which can localize the already regionally elevated heat (e.g., Burton-Johnson et al.,
4093 2020; Fox Maule et al., 2005), resulting in vastly enhanced heat flow to the ice
4094 base (Gooch et al., 2016), which is likely the cause of the anomalously high heat

4095 flow measured at Subglacial Lake Whillans (285 mW/m^2 , Fisher et al., 2015). We
4096 hypothesized in Chapter 2 that these faults not only provide a spatial control on
4097 geothermal heat flux, but a temporal control as well.

4098

4099 Temporal control on geothermal heat

4100 As ice thickness has varied throughout the Holocene, the changing ice overburden
4101 pressure on the subglacial sediments drives the discharge and recharge of these sedi-
4102 mentary aquifers (Gooch et al., 2016; Li et al., 2022). This fluid movement is
4103 accommodated along fault-damage zones and impermeable basement margins (Fig-
4104 ure 5.1 Jolie et al., 2021). This may present a positive feedback, where thickening
4105 ice drives groundwater into the aquifers, advecting heat away from the ice base,
4106 which slows the flow of ice, leading to increased thickness. Similarly, as ice thins,
4107 the reduced overburden on the aquifers results in water discharge to the ice base and
4108 an associated localization of heat. The resulting increased flow speed and thinning
4109 of the ice further reduces the overburden pressure. These mechanisms express how
4110 crustal structures often thought of as static on a millennial timescale from the view-
4111 point of ice dynamics may enable rapid changes in ice dynamics. The co-location of
4112 highly dynamic ice streams (Bougamont et al., 2015; Catania et al., 2012), extensive
4113 groundwater reservoirs (Christoffersen et al., 2014; Gustafson et al., 2022), elevated
4114 geothermal heat flux (Burton-Johnson et al., 2020; Shen et al., 2020), and fluid
4115 pathways (Chapter 2), highlight the Siple Coast as an ideal study site to investigate
4116 these possible relations between changes in ice thickness, groundwater discharge,
4117 and the advection of geothermal heat. We now discuss various implications of our
4118 geologic findings for understanding past and future ice dynamics of the Ross Ice
4119 Shelf region.

4120

4121 5.4.2 Constraining past and future ice sheet behaviour

4122 While the above geologic controls on the ice sheet likely existed in the past and will
4123 continue into the future, our study has implications that are exclusive to past or
4124 future ice sheet configurations. The pinning points we discussed, and the regions of
4125 thin draft, were all likely pinning points during periods of thicker ice. Since the Last
4126 Glacial Maximum ($\sim 22 \text{ kya}$) retreat of the grounding line from the outer shelf edge
4127 has been primarily controlled by the physiography of the bed, as well as its geologic
4128 composition (Anderson et al., 2019; Halberstadt et al., 2016). While the retreat
4129 dynamics have been well studied in the Ross Sea, where the open ocean conditions
4130 allow seismic and high-resolution multi-beam sonar surveying (Anderson et al., 2019;
4131 Halberstadt et al., 2016), and drill cores provide sedimentary records (McKay et al.,
4132 2016), under the Ross Ice Shelf there has been very little investigation on retreat
4133 dynamics, apart from modelling studies (Kingslake et al., 2018; Lowry et al., 2020).
4134 Here we have provided the physiography of the region, through the sub-Ross Ice
4135 Shelf bathymetry model, enabling insight into the retreat dynamics throughout the
4136 Holocene.

4137

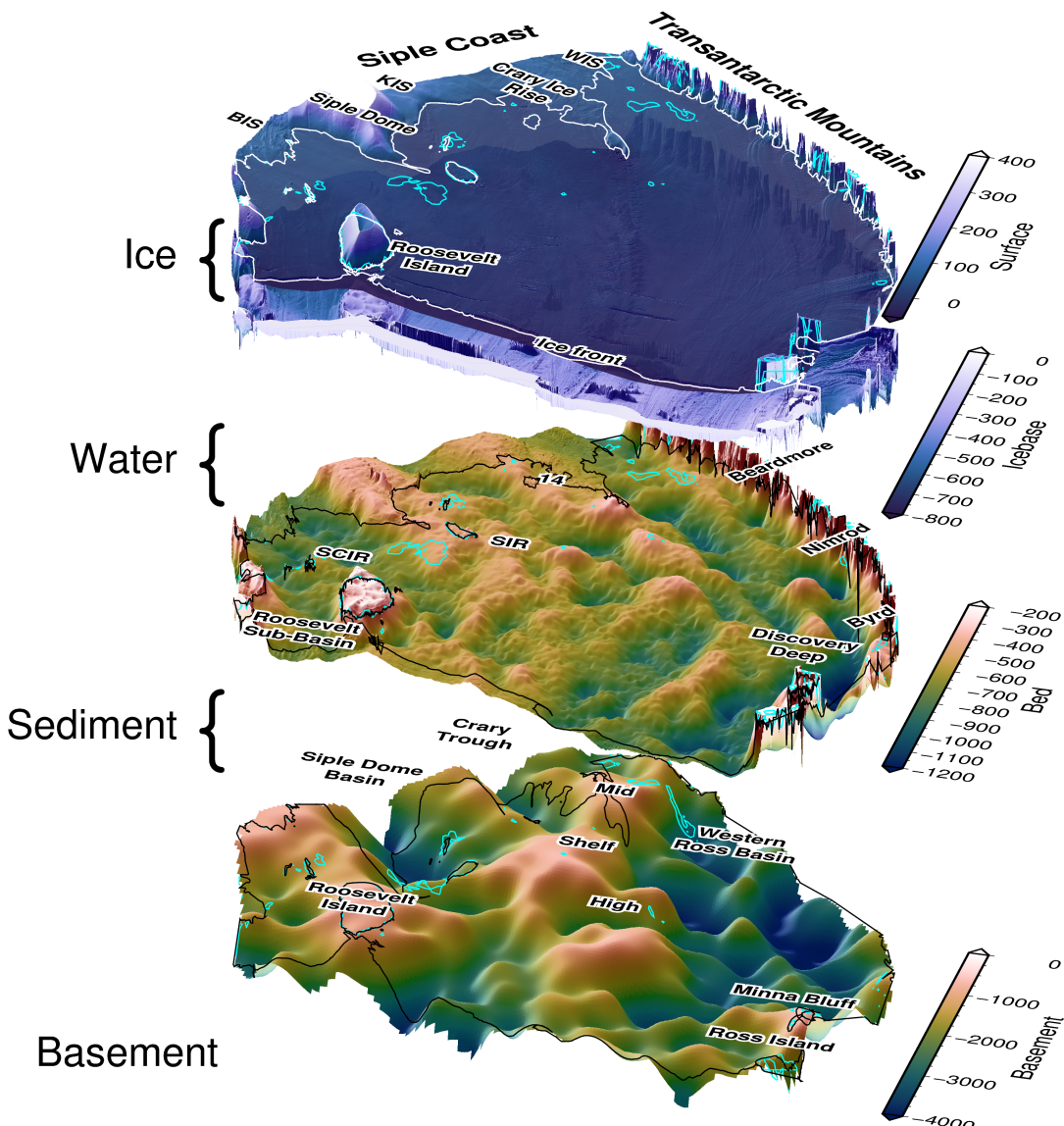


Figure 5.3: A 3D perspective view of the structure of the Ross Ice Shelf. Starting at the top, ice surface, and ice base from BedMachine v3 (Morlighem, 2022; Morlighem et al., 2020), inverted bathymetry results from Chapter 4, and basement topography from Chapter 2. Grounding line shown in all layers if from Morlighem (2022). Bright blue contour shows 20 m water column thickness. Note each layer has an independent vertical exaggeration to aid in visualization.

4138 5.4.2.1 Retreat dynamics

4139 While we don't constrain the age of the sea floor sediments, the general physiography
 4140 of the sea floor can provide some insights. The eastern side of the ice shelf, apart
 4141 from Roosevelt Island, shows similar physiography to the eastern Ross Sea, with
 4142 relatively flat bathymetry without major banks or troughs (Figure 5.1e). There,
 4143 the subdued bathymetry likely resulted in a stepwise style of grounding line retreat
 4144 throughout the Miocene, with the stabilizing build-up of grounding zone wedges, fol-
 4145 lowed by decoupling and rapid retreat of 10's of kilometres (Anderson et al., 2019;
 4146 Bart et al., 2017). The bathymetry of the western Ross Ice Shelf, characterized by
 4147 depth troughs and shallow banks, is similar to that of the western Ross Sea (Figure

4148 5.1e). There, the retreat style, also controlled by the bathymetry, was continuous
4149 and complex, as ice streams followed the bathymetry in a continuous retreat back to
4150 the outlet valleys in the Transantarctic Mountains (Anderson et al., 2019; Halber-
4151 stadt et al., 2016). In the western Ross Sea, repeated cycles of advance and retreat
4152 within these confined bathymetry troughs led to the scouring of sediments from the
4153 inner shelf, and an over-deepened, landward sloping inner shelf (Anderson et al.,
4154 2019). These contrasting styles of retreat proposed for the eastern and western Ross
4155 Ice Shelf may be in part responsible for the varied bathymetry found on either side
4156 of the ice shelf. The above section discussed our bathymetry results in relation to
4157 past and future ice dynamics. Next, we discuss the implication of our basement
4158 topography on the glacial history of the region.

4159

4160 5.4.2.2 Glacial initialization

4161 During the Oligocene, the Ross Embayment contained a long and broad mountain
4162 range emergent above sea level, trending N-S from the Ross Sea through the ice
4163 shelf. This feature was first recognized from the drill cores of DSDP (Deep Sea
4164 Drilling Project) site 270 in the Ross Sea (Figure 5.1f, Leckie, 1983), where a 400 m
4165 sedimentary sequence with depositional environments ranging from above sea level
4166 to \sim 500 below sea level was found, dating from late Oligocene to early Miocene
4167 (Kulhanek et al., 2019). Beneath this sequence was crystalline basement. The broad
4168 dome-like shape of this basement high was revealed by shipborne seismic surveys
4169 (Brancolini et al., 1995), which imaged a similar basement high further north. These
4170 basement features were termed the Northern and Southern Central High. Seismic
4171 data also revealed small U-shaped channels within the acoustic basement, which
4172 were attributed to alpine glaciation (De Santis et al., 1995). Off the flanks of these
4173 fault-bound basement highs, wider troughs in the basement were imaged and at-
4174 tributed to the erosion of ice streams flowing off these basement highs. During the
4175 late Oligocene, ice caps nucleated on these subaerial basement features (De San-
4176 tis et al., 1995; Olivetti et al., 2023). Thermal subsidence following the onset of
4177 mid-Cretaceous West Antarctic Rift System extension (Karner et al., 2005; Wilson
4178 & Luyendyk, 2009) gradually submerged these basement highs (De Santis, 1999;
4179 Olivetti et al., 2023). In addition to the North and South Central High features
4180 in the Ross Sea, paleotopographic reconstructions of the Oligocene (Paxman et al.,
4181 2019; Wilson et al., 2012) have predicted the continuation of this broad subaerial
4182 mountain range under the Ross Ice Shelf. Our depth to magnetic basement (Chap-
4183 ter 2) provided the first observations of the feature, which we termed the Mid Shelf
4184 High, beneath the Ross Ice Shelf (Figure 5.1f).

4185

4186 The strong continuity of the Mid Shelf High with the Ross Sea's Central High
4187 suggests that these features have similar histories. We propose the three blocks of the
4188 Mid Shelf High were emergent and hosted ice caps in the Oligocene. Following their
4189 submersion, likely in the latest Oligocene (Olivetti et al., 2023) these features would
4190 have acted as major bathymetry pinning points, similar to the modern Roosevelt
4191 Island. We suggest this chain of shallow basement blocks formed a long-lasting
4192 catchment divide of both sediment transport and ice flow between East and West
4193 Antarctica. This divide has been predicted as far back as the Paleogene, from
4194 distinct microfossil assemblages on either side of the Ross Embayment (Coenen et
4195 al., 2019). Since the Last Glacial Maximum, the Central High has been thought to

⁴¹⁹⁶ be an ice flow divide, separating ice originating from the East and West Antarctic
⁴¹⁹⁷ Ice Sheets (Li et al., 2020; Licht et al., 2014; Licht et al., 2005). The prominent Mid
⁴¹⁹⁸ Shelf High / Central High appears to have played a central role in the history of the
⁴¹⁹⁹ Ross Embayment since the Oligocene.

⁴²⁰⁰ 5.5 Future work

⁴²⁰¹ Here we provide several suggestions for future research and fieldwork related to this
⁴²⁰² thesis. A primary piece of future work resulting from this thesis should be the incor-
⁴²⁰³ poration of the updated bathymetry into a sub-ice shelf circulation model. To access
⁴²⁰⁴ the sensitivity of sub-shelf circulations to bathymetry, models should be run for our
⁴²⁰⁵ mean bathymetry model, as well as the upper and lower ranges of our uncertainties,
⁴²⁰⁶ as defined by the mean model plus and minus the spatial uncertainty we present
⁴²⁰⁷ (Figure 5.2). To better improve the bathymetry model and reduce uncertainties, we
⁴²⁰⁸ suggest three alternatives for field seasons on the Ross Ice Shelf.

- ⁴²⁰⁹ 1. Collect additional seismic depth measurements along the Transantarctic Moun-
⁴²¹⁰ tain front. This would serve to lower uncertainties in the bathymetry associ-
⁴²¹¹ ated with the nearby steep topography. A traverse-style field season would be
⁴²¹² best for this to accommodate the linear nature of the grounding zone. Collect-
⁴²¹³ ing occasional cross lines, running perpendicular to the grounding line, would
⁴²¹⁴ likely image the range front faults, commonly inferred by only rarely imaged.
- ⁴²¹⁵ 2. A seismic survey of the central block of the Mid Shelf High (Figure 5.1f).
⁴²¹⁶ This survey would accomplish several goals. First, it would fill one of the
⁴²¹⁷ two major gaps in bathymetry measurements in the central ice shelf, reducing
⁴²¹⁸ the bathymetry uncertainty. Secondly, it would inform on the nature of the
⁴²¹⁹ Mid Shelf High as a past pinning point and nucleation site of Oligocene ice
⁴²²⁰ caps. Lastly, it would act as a site survey for potential sea-floor drilling. The
⁴²²¹ thin sedimentary cover of the Mid Shelf High may provide a good target for
⁴²²² future drilling since a temporally wide-ranging sequence may be concentrated
⁴²²³ into a thin sedimentary package. Additionally, sampling of the crystalline
⁴²²⁴ basement, trace element and provenance analysis will give further insights into
⁴²²⁵ 1) the proposed East-West Antarctic geologic boundary along the middle of the
⁴²²⁶ Ross Embayment (Tinto et al., 2019), 2) the region's Cretaceous extensional
⁴²²⁷ history (Olivetti et al., 2023), and 3) the region's Oligocene to Miocene climatic
⁴²²⁸ evolution (Olivetti et al., 2023).
- ⁴²²⁹ 3. Conduct a regional seismic survey across portions of the Siple Coast to better
⁴²³⁰ image the sedimentary basins and basin bounding faults, especially where the
⁴²³¹ faults proposed in Chapter 2 may interact with the ice streams.

⁴²³² We make several suggestions for future inversions based on our comprehensive re-
⁴²³³ view of past Antarctic bathymetry gravity inversions. To test the inversion method
⁴²³⁴ developed here, it would be useful to perform another inversion for an ice shelf that
⁴²³⁵ has been previously inverted. The three best options would be the Getz Ice Shelf,
⁴²³⁶ the Thwaites Glacier, and the Pine Island Glacier. The bathymetry beneath each of
⁴²³⁷ these ice shelves has been inverted three separate times, allowing the comparison of
⁴²³⁸ several different methods. The Getz Ice shelf bathymetry has been inverted in 2D
⁴²³⁹ (Cochran et al., 2020; Wei et al., 2020), and with a 3D frequency-based inversion

(Millan et al., 2020). The Thwaites cavity has also been inverted in both 2D (Tinto & Bell, 2011) and 3D, with both the "topo-shift method" (Jordan et al., 2020a), and a frequency-based method (Millan et al., 2017). Lastly, the Pine Island Glacier bathymetry has been inversion twice with Simulated Annealing (Muto et al., 2013a; Muto et al., 2016), and once with a frequency-based inversion (Millan et al., 2017). To compare to a wider range of methods, the Thwaites glacier would be optimal. To gain insights into the effectiveness of our uncertainty analysis, Pine Island Glacier should be chosen since spatially variable uncertainty estimates exist from the studies which used Simulated Annealing.

4249

Of the major Antarctic ice shelves, there are four that stand out as prime candidates for a future inversion if the goal is to increase our sub-ice shelf bathymetric knowledge. These include the Larse C Ice Shelf, the Ronne Filchner Ice Shelf, the Riiser-Larsen Ice Shelf, and the Shackleton Ice Shelf.

4254

1. Larsen C is the largest ice shelf on the Antarctic Peninsula, yet bathymetry knowledge beneath it is still limited. A bathymetry inversion has been conducted (Cochran & Bell, 2012), but comparison with seismic constraints revealed large uncertainties in the model. A recent constraint compilation and new seismic data (Brisbourne et al., 2020) make this an ideal candidate without needing any field work. Additional gravity data has also been collected over the ice shelf during 2016, 2017, and 2018 Operation Ice Bridge flights ("IceBridge Sander AIRGrav L1B Geolocated Free Air Gravity Anomalies, Version 1", 2020).

4263

2. The Ronne Filchner is the second-largest ice shelf, yet has not been included in a gravity inversion. An extensive array of seismic constraints, similar to the RIGGS survey of the Ross Ice Shelf exists (Fretwell et al., 2013; Rosier et al., 2018), and gravity data from compiled from Russian airborne and ground-based surveys (Aleshkova et al., 2000; Studinger & Miller, 1999) is accessible as part of the continent-wide AntGG gravity compilation (Scheinert et al., 2016).

4270

3. and 4. The Riiser-Larsen and the Shackleton Ice Shelves are the 5th and 7th largest ice shelves, respectively. To our knowledge, there is no bathymetry knowledge beneath the entirety of either shelf. Gravity data exists for both shelves from the AntGG compilation (Scheinert et al., 2016). Performing inversions for these shelves would require extensive seismic data acquisition to be adequately constrained.

4276

Lastly, we highlight a few alternative use cases and limitations for our gravity inversion algorithm. While this has been developed for a regional-scale sub-ice shelf application, at its core the inversion is a standard geometric (sometimes referred to as structural) inversion. Therefore, this code can be used to invert any topographic surface of a user-defined density contrast based on input gravity anomaly data. It is compatible with domains ranging from small-scale, local areas, to large domains such as ours (1000×1000 km). However, domains significantly larger than ours (continental scale) will introduce inaccuracies due to our use of vertical right-rectangular prisms, which makes assumptions of a planar Earth. For these continental to global scale inversions, vertical prisms should be replaced with spherical prisms (tesseroids), as implemented by (Uieda & Barbosa, 2017). With this, our

4287 inversion will work for other applications, such as predicting regional Moho depths,
4288 the sediment-basement contact, or determining bed depths beneath grounded ice,
4289 under subglacial lakes, or in the open ocean. We hope this code is used by others
4290 for these various applications.

4291 5.6 Concluding remark

4292 The primary aim of this thesis was to use existing airborne geophysical data to better
4293 characterize the geology and physiography beneath Antarctica's Ross Ice Shelf. We
4294 used and developed several geophysical techniques to accomplish this. We first used
4295 variations in Earth's magnetic field measured over the ice shelf to model the spatial
4296 distribution and thickness of sediments beneath the ice shelf. We then developed
4297 and extensively tested a geophysical inversion, which uses measurements of Earth's
4298 gravity field to model the depth to the seafloor. With this, we created an updated
4299 model of the bathymetry beneath the ice shelf.

4300

4301 From this geophysically informed knowledge of the upper crust of the sub-Ross
4302 Ice Shelf, we were able to draw inferences on the complex interactions between the
4303 solid Earth, ocean, and ice for the Ross Embayment. We highlighted the Siple
4304 Coast as a location with strong geologic control on ice dynamics, through 1) the
4305 distribution of sediments, which control the competency of bedrock material beneath
4306 grounded ice, and 2) the location of deep sedimentary basins, which likely supply
4307 the ice base with lubricating water and localize the geothermal heat delivered to the
4308 ice. Our bathymetry model confirms the findings of past models which show a deep
4309 trough spanning from the ice front near Ross Island south along the Transantarctic
4310 Mountain Front. This trough likely guides High Salinity Shelf Water from the ice
4311 front to the deep grounding zone of the Transantarctic Mountain outlet glaciers,
4312 where it induces significant basal melting. Our spatial uncertainty results highlight
4313 the Transantarctic Mountain Front as the least-certain portion of the sub-ice shelf
4314 bathymetry model. Combined with this region's importance for basal melt, we
4315 suggest future seismic surveys target the mountain front. This thesis provides the
4316 necessary boundary conditions and estimates of their uncertainties for ice and ocean
4317 modellers to better characterize the Ross Ice Shelf's response to past, present, and
4318 future changes in the climate.

4319 Appendix A

4320 This appendix section provides supplementary information to Chapter 2, and is
4321 tasked directly from the published supplementary materials of Tankersley et al.
4322 (2022).

4323 A.1 Introduction

4324 This supplement provides additional information on the assumptions behind the
4325 process of determining basement depth from magnetic anomalies (Section A.2), the
4326 collection and processing of aeromagnetic line data (Section A.3), the methodolo-
4327 gy of tying ROSETTA-Ice magnetic basement to ANTOSTRAT acoustic base-
4328 ment (Brancolini et al., 1995), through the use of Operation IceBridge (OIB) mag-
4329 netic data (Cochran et al., 2014a) (Section A.4 & A.5), the gridding, merging,
4330 and filtering of the resulting basement grid (Section A.6), the calculation of sedi-
4331 ment thickness and β -factors for the region (Section A.7), and our quantification
4332 of uncertainties and comparison with points of previously measured sediment thick-
4333 ness (Section A.8). Sediment thickness comparisons with past seismic surveys are
4334 included in Table S1. Also included are supplementary figures showing various
4335 additional Ross Ice Shelf grids (Figure A.1), the Werner deconvolution solutions
4336 of OIB flight 403.3 (A.2), several selected ROSETTA-Ice flight lines with Werner
4337 deconvolution solutions (A.3), unfiltered basement solutions with flight line loca-
4338 tions and individual Werner deconvolution solutions (A.4), uncertainties applied to
4339 basement and sediment thickness results (A.5), and misfit distributions between
4340 OIB, ANTOSTRAT, and ROSETTA basement models (A.6). Python code, within
4341 a Jupyter notebook, documents our workflow and figure creation and is accessi-
4342 ble here: <https://zenodo.org/badge/latestdoi/470814953> or at the GitHub reposi-
4343 tory: https://github.com/mdtanker/RIS_basement_sediment. Results in the form
4344 of netCDF's and csv's are available at <https://doi.pangaea.de/10.1594/PANGAEA.941238>, including figures of all ROSETTA-ice flight line basement solutions.
4345

4346 A.2 Depth to basement assumptions

4347 Our resulting basement grid is the depth to the shallowest magnetic signal. It is
4348 assumed that the crystalline basement in this region produces significantly larger
4349 magnetic anomalies compared to the overlying sediment fill. Note that in some
4350 instances, such as igneous bodies intruded into sedimentary basin fill, Werner de-
4351 termined solutions fall upon the crest of the intrusion, and the actual top of the
4352 crystalline basement could be at a deeper level. Intrusions of small lateral extent

will have small widths, resulting in small values of parameter S (susceptibility \times width) and therefore will be removed by our filter (Section A.4). For larger intrusions into existing basins, (i.e. Ross Island and Minna Bluff Cox et al., 2023), the modelled magnetic basement surface will be shallower than the bottom of the sedimentary basin. While this underestimates sediment volume, it better characterizes the competency of the substrate from an ice dynamics perspective. This is similar to how extensive intrusions into basins would be imaged by seismic surveys as shallow basement. However, these extensive regions of late-Cretaceous-Cenozoic magmatism are not expected to be prevalent under the RIS (Andrews & LeMasurier, 2021).

4362 A.3 Magnetic data collection, processing, and Werner 4363 deconvolution

4364 Both ROSETTA-Ice and OIB data sets were collected with a Scintrex CS3 Ce-
4365 sium magnetometer. Average flight speeds were 123 m/s and 93 m/s for OIB and
4366 ROSETTA-Ice respectively. Altitudes for the sections of OIB flight 403 used here
4367 average around 400 m above sea level, while ROSETTA-Ice altitude averaged at 750
4368 m above the ice sheet surface. OIB data were resampled from 20 Hz to 1 Hz to
4369 match the frequency of the ROSETTA-Ice data. Both datasets have been despiked,
4370 diurnally corrected, and had the International Geomagnetic Reference Field model
4371 removed. See Tinto et al. (2019) for more details of the ROSETTA-Ice survey and
4372 flight line locations. Due to variable flight elevations, both between and within the
4373 datasets, all magnetic data were upward continued to 1000 m above sea level. To
4374 avoid artifacts of downwards continuing, any data with flight elevations above 1000
4375 m were removed ($\sim 10\%$ of the data).

4376
4377 Here we use 2D Werner deconvolution Werner (1953), applied to aeromagnetic
4378 line data, to image the shallowest magnetic signals in the crust. Assuming that the
4379 overlying sediments produce smaller magnetic anomalies than the crystalline base-
4380 ment, we treat the resulting solutions as a depth to the magnetic basement. During
4381 Werner deconvolution, moving and expanding windows are passed over the mag-
4382 netic anomaly line data. Within each window, after linearly detrending the data,
4383 the source parameters of the anomalies are estimated with a least-squares approach,
4384 assuming the source bodies are infinite-depth dikes or contacts. The source param-
4385 eters include position (distance along profile and depth), magnetic susceptibility,
4386 and source geometry (contact or dike). Solutions are considered valid between 1200
4387 m and 20 km of upward continued flight elevation (approx. 200 m - 19 km bsl).
4388 Windows ranged from 500 m - 50 km, with a window shift increment of 1 km and
4389 an expansion of 1 km.

4390
4391 Due to passing over the data many times with varying window widths, Werner
4392 deconvolution produces a depth-scatter of solutions, which tend to cluster vertically
4393 beneath the true magnetic sources. Each of these solutions consists of location,
4394 depth, susceptibility (S), window width (W), and a simplified source geometry (dike
4395 or contact). For contact-type solutions, parameter S is the estimated magnetic
4396 susceptibility of the body, while for dike-type solutions, S is the product of suscep-
4397 tibility and dike width. During filtering (Sections A.4 & A.5), a cut-off based on
4398 parameter S is used to remove shallow solutions. Since the value of parameter S for

4399 contact solutions are typically much smaller than for dike solutions (since they are
4400 not multiplied by dike width), only dike solutions have been considered here. To
4401 achieve a basement surface from this resulting depth-scatter of solutions, we have
4402 utilized parameter-based filtering and clustering, described in Sections A.4 & A.5.
4403 This Werner deconvolution process was the same for both OIB and ROSETTA-Ice
4404 magnetics data. Werner deconvolution was performed in Geosoft's Oasis Montaj and
4405 subsequent processing of these results was performed in Python, and is included in
4406 a Jupyter notebook; <https://zenodo.org/badge/latestdoi/470814953>.

4407

4408 This magnetic basement approach has been used to map sedimentary basins
4409 throughout Antarctica, including the Ross Sea Karner et al. (2005), western Marie
4410 Byrd Land (Bell et al., 2006), and Wilkes Subglacial Basin (Frederick et al., 2016;
4411 Studinger et al., 2004a). Our approach is similar to past studies, but our proximity
4412 to well-constrained offshore seismic basement depths (Brancolini et al., 1995) allows
4413 us to develop the method further. Most studies display their results as 2D profiles
4414 with the depth-scatter of solutions mentioned above, and simply use the tops of the
4415 clusters as the basement depth. By comparison with seismic basement, we have
4416 developed a reliable, automated method of 'draping' a surface over these depth-
4417 scattered solutions to produce a 3D surface. This process is described below.

4418 **A.4 Tying magnetic basement to seismic basement**

4419 To validate the method described in Section A.3 and address uncertainty we per-
4420 form Werner deconvolution for OIB magnetics data (Figure 2.1b, Cochran et al.,
4421 2014a) over the Ross Sea. Here, ice-free conditions have permitted shipborne seis-
4422 mic surveys to image basement depths in the region. These have been compiled by
4423 the Antarctic Offshore Acoustic Stratigraphy project (ANTOSTRAT) (Brancolini
4424 et al., 1995) (Figure 2.1b). The basement was not imaged for the deeper portions
4425 of the basins and data coverage of actual basement reflectors, versus interpolation
4426 between basement reflectors, is not reported. Werner deconvolution (Section A.3)
4427 produces a series of many solutions (black dots in Figures 2.2 & A.2) at each window
4428 along the line.

4429

4430 To achieve a basement surface, instead of a depth-scatter of solutions, solutions
4431 were filtered based on Werner window width (W) and the product of magnetic sus-
4432 ceptibility and body width (parameter S). Filtered solutions (black circles, scaled to
4433 parameter S in Figures 2.2 & A.2) were then horizontally binned with variable bin
4434 sizes (parameter B) (vertical grey lines in Figures 2.2 & A.2). Bins with a minimum
4435 count of solutions (parameter C) were retained, and the depth of the bin center was
4436 set to the 95th-percentile depth of the solutions in the bin. This removed spurious
4437 shallow solutions, while effectively retaining the 'top' of the magnetic signal. These
4438 bin centers (orange crosses in Figures 2.2 & A.2) were then interpolated, producing
4439 our model of magnetic basement depths (orange line in Figures 2.2 & A.2). The
4440 above filtering techniques removed the solutions above the basement, and the clus-
4441 tering technique fitted a surface over the remaining points, which represents the
4442 top of the basement. This interpolated line allowed a direct comparison between
4443 ANTOSTRAT seismic basement and OIB magnetic basement.

4444

4445 We varied each of the four parameters (W, S, B, and C) with 21 different values

and conducted the above procedures for all unique combinations of them on OIB line 403, segments 1 and 3, in the Ross Sea (location in Figure 2.1b). This resulted in 194,481 iterations, for each of which we calculated a mean absolute difference at points every 5 km between ANTOSTRAT seismic basement and the resulting OIB magnetic basement. We found the parameter values which produced the closest match between OIB magnetic basement and ANTOSTRAT seismic basement, as shown in Figures 2.2 & A.2. These resulting values were a maximum Werner deconvolution window width (parameter W) of 10 km, a minimum product of magnetic susceptibility and body width (parameter S) of 1.0, a horizontal bin width (parameter B) of 36 km, and a minimum number of solutions per bin (parameter C) of 6. The median absolute misfit between OIB and ANTOSTRAT basement for the two line-segments was 480 m (260 m for Line 403.1 (Figure 2.2), and 1040 m for Line 403.3 (Figure A.2)). This equates to 11% of average ANTOSTRAT depths for the two lines. The close fit between the OIB magnetic basement and the ANTOSTRAT seismic basement both supports the validity of this method and gives us the parameters necessary to repeat this method for data over the RIS.

A.5 Tying Ross Sea magnetic basement to Ross Ice Shelf magnetic basement

Having optimized our method to match OIB magnetic basement to ANTOSTRAT seismic basement in the Ross Sea (Section A.4, Figures 2.2 & A.2), we now optimize the method to match ROSETTA-Ice magnetic basement to OIB magnetic basement. This additional optimization is necessary due to differences in processing and survey design, including flight elevations, speed, aircraft, mounting equipment used, and frequency of recording. With the optimized parameters for OIB data (Section A.4), we calculate magnetic basement for OIB flight 404 over the ice shelf. We treat this as the 'true' basement and update the filtering and clustering parameters (Section A.3) to minimize the misfit between OIB basement and the resulting ROSETTA-Ice basement. This tuning was performed on ROSETTA-Ice lines 590 and 650, which were coincident with segments from OIB line 404 (location in Figures 2.1b & A.4). Optimal parameters to match ROSETTA-Ice solutions to OIB basement are found to be $W < 26$ km, $S > 1.2$, $B = 36$ km, and $C > 40$, resulting in a median absolute misfit between OIB basement and ROSETTA-Ice solutions of 400 m (630 m for line 404.590 (Figure A.3e) and 310 m for line 404.590 (Figure A.3f)). This equates to 18% of OIB depths for the two lines. With these parameters which best match ROSETTA magnetic basement to OIB magnetic basement, we performed the same procedure on all the ROSETTA-ice flight lines. A selection of these lines, and the two ties to OIB 404, are shown in Figure A.3. All ROSETTA-ice flight line solutions are available as images at the PANGAEA link.

A.6 Gridding, merging, and filtering

The above processes were performed on all ROSETTA-ice flight lines (white lines in Figure A.4), including the N-S tie lines at ~ 55 km spacing. Where the tie lines crossed over the E-W flight lines, some resulting basement solutions (black dots in Figure A.4) are nearby those from the crossing line. Since we are interested in the

shallowest magnetic signals, we have retained only the shallowest solution with 8 km cells across our region. Since bin widths (parameter B) were set to 36 km, the nearest solutions along individual lines were further apart than the 8 km cell. The closest spacing of E-W flight lines was 10 km, so this process only affected solutions at the crossover between N-S and E-W lines. These points were then gridded with a 5 km cell size and a minimum curvature spline with a tension factor of 0.35 Smith and Wessel, 1990 (Figure A.4). This grid was then merged with a Ross Sea seismic basement grid. The Ross Sea grid, while mostly ANTOSTRAT data, was sourced from a regional compilation of sediment thicknesses (Lindeque et al., 2016; Wilson & Luyendyk, 2009) we have subtracted from bathymetry depths (Morlighem et al., 2020) to achieve basement depths. Where the grids overlap near the ice shelf edge, we retain our RIS values. To aid in the merging at the overlaps, and to match RIS basement wavelengths to the characteristic basement wavelengths of ANTOSTRAT, we filtered the merged grid with an 80 km Gaussian filter (Figure 2.3a). This filtering was performed with a variety of wavelengths (20-120 km), where we found filters <80 km didn't significantly alter the regional basement, while filters >80 km excessively smoothed the basement topography. A few locations with anomalously shallow basement were set equal to BedMachine bathymetry.

4507 **A.7 Sediment thickness and β -factor calculations**

With the regional basement model (Figure 2.3a) including RIS magnetic basement and offshore seismic basement, we calculated sediment thickness (Figure 2.3b) by subtracting the grid from BedMachine bathymetry depths (Figure 2.1a & A.1e, Morlighem et al., 2020). Previous estimates of sediment thickness for the sub-RIS come from the extrapolation of gravity anomalies with bathymetry trends (Wilson & Luyendyk, 2009). These were included in the Lindeque et al. (2016) compilation (Figure A.1d). Eocene Oligocene boundary paleotopographic reconstructions (Paxman et al., 2019; Wilson et al., 2012) assumed this sediment estimate was post-Eocene and used it as their maximum sub-RIS sediment thickness, incorporated into their minimum surface reconstruction. The thickness of sediment affects onshore erosion estimates, surface raising due to deposition, and isostatic surface subsidence due to loading. For their maximum paleotopographic reconstructions, they used a thinner sediment model, with the same general trends (Wilson & Luyendyk, 2009). Figure A.1 (c, d, & f) shows the comparison between the sediment thickness models. Figure A.1f colorbar histogram shows the distribution, with our values having a mean thickness ~ 115 m greater than the past model. Yet, along the Siple Coast, we show much greater discrepancies, up to 2 km thicker. β -factor, the ratio of initial crustal thickness to final crustal thickness, is useful for quantifying the thinning of crust in extensional settings. We calculate a distribution of β -factors beneath the RIS by assuming a uniform initial crustal thickness and dividing it by current crustal thickness. We pick an initial crustal thickness of 38 km, which represents a global average for un-thinned plateau-type crust (Mooney et al., 1998), and has been used for the West Antarctic Rift System β -factor calculations (Müller et al., 2007). For the final (current) crustal thickness, we use a continent-wide Moho model from surface wave observations to define the bottom of the crust (An et al., 2015). For the top of the crust, we use our resulting RIS basement grid.

Name	Reference	Seismic sediment thickness (m)	Magnetic sediment thickness (m)	Absolute difference (m)
CIR	(Rooney et al., 1987)	400	514	114
I10S	(Robertson & Bentley, 1989)	750 ± 100	1281	818
J9DC	(Greischar et al., 1992)	1350	770	580
BC	(Robertson & Bentley, 1989)	1900 ± 400	1082	818
RI	(Greischar et al., 1992)	850	822	28
C49	(Crary, 1961)	754	1162	408
LAS	(Crary, 1961)	1325	1799	474
Q13	(Greischar et al., 1992)	255 ± 145	721	466

Table A.1: Previous seismic sediment thickness results for the Ross Ice Shelf. Stations names are labelled in Figure 2.3b. Magnetic sediment thickness column shows our sampled results at the location of each station. Comparing the seismic estimates with our sediment thickness at the eight stations gives a median absolute misfit of 470 m.

4534 A.8 Uncertainties

4535 We estimated a representative uncertainty for our basement model by examining
 4536 the misfit of our modelled basement compared to offshore seismic basement depths
 4537 (Brancolini et al., 1995). We did this by sampling our OIB magnetic basement
 4538 estimate and the coincident ANTOSTRAT basement at 1 km intervals along lines
 4539 403.1 and 403.3 (Figures 2.2 and A.2) and compared the values. The resulting ab-
 4540 sorlute values of the differences don't exhibit a normal distribution (Figure A.6a);
 4541 therefore, we use the median of the absolute misfit (± 480 m) as the basement model
 4542 uncertainty. This equates to 22% of average basement depths for the sub-RIS. We
 4543 performed a similar analysis between OIB magnetic basement and ROSETTA-Ice
 4544 magnetic basement for coincident lines 590 and 650 (Figure A.3 e & f). This resulted
 4545 in a median absolute misfit of 400 m (Figure A.6b). Tinto et al. (2019) report an un-
 4546 certainty of 68 m for their bathymetry model. Incorporating this with our basement
 4547 model gives an uncertainty of 550 m (37% of average thickness) for our sediment
 4548 thickness results. Comparison with sub-RIS sediment thickness and distribution re-
 4549 sults from a variety of methods, including active source seismic surveys (Table A.1
 4550 and references within), seismic radial anisotropy (Zhou et al., 2022), geophysical
 4551 machine learning (Li et al., 2022), and magnetotelluric surveying (Gustafson et al.,
 4552 2022), all show general agreement with our results.

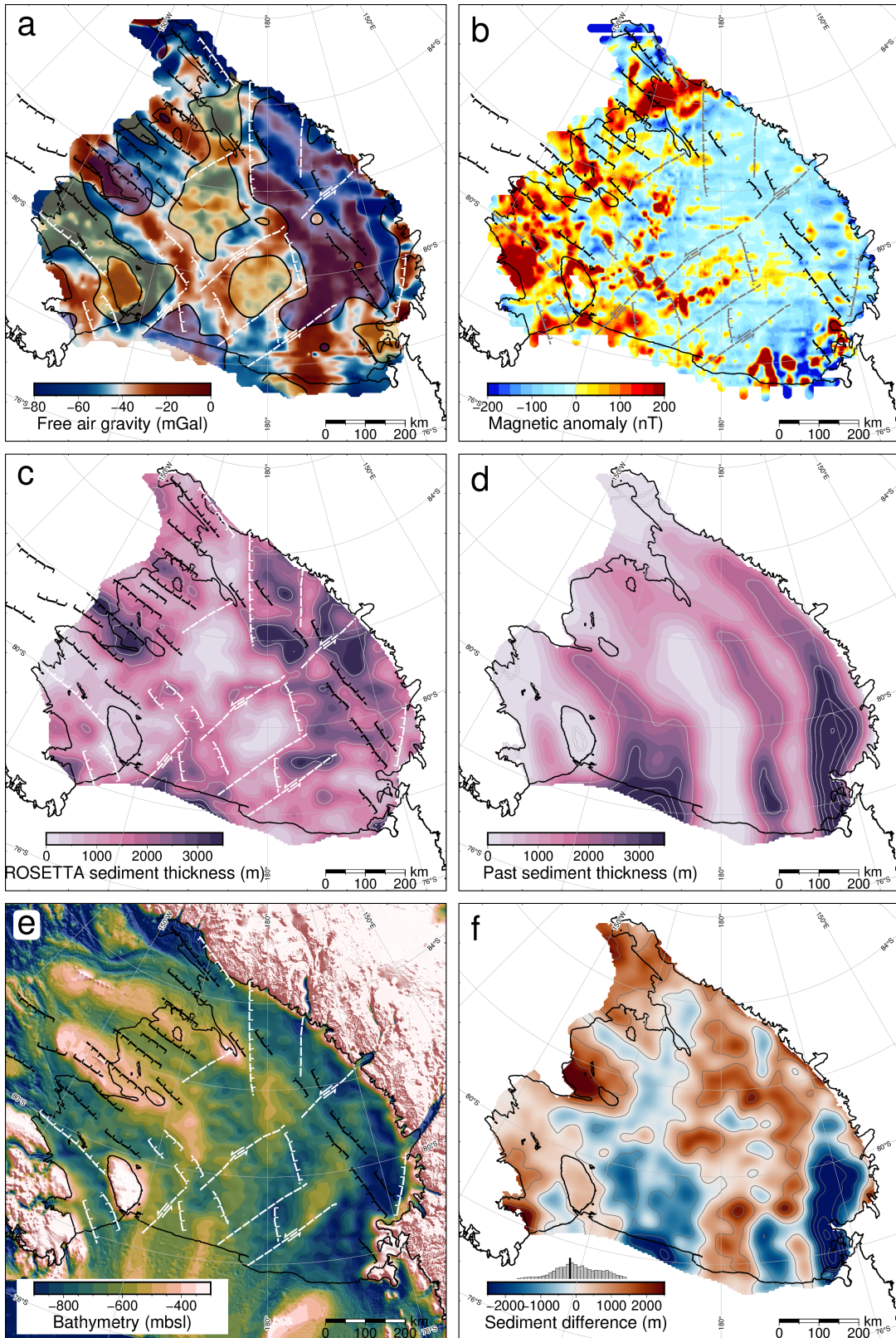


Figure A.1: **a)** ROSETTA-Ice free air gravity (Tinto et al., 2019). Shaded yellow regions are shallow basement ($<\sim 1600$ mbsl), shaded blue regions are deep basement ($>\sim 2600$ mbsl). **b)** ROSETTA-Ice airborne magnetic anomaly data (Tinto et al., 2019). **c)** Sediment thickness from this study (same as Figure 2.3b), with 1 km contours. **d)** Sediment thickness from a regional compilation (Section A.7, Lindeque et al., 2016; Wilson & Luyendyk, 2009), with 1 km contours. **e)** BedMachine2 bathymetry (Morlighem et al., 2020), from which sediment thickness in c) was calculated. **f)** Difference between c) and d). Red signifies our results have more sediment, while blue signifies our results have less sediment. Histogram shows data distribution, with mean value (black) at 115 m. Inferred faults in a), b), c), and e) same as Figure 2.4a. Grounding line and coastlines in black (Rignot et al., 2013). Projection is Antarctic Polar Stereographic: EPSG 3031.

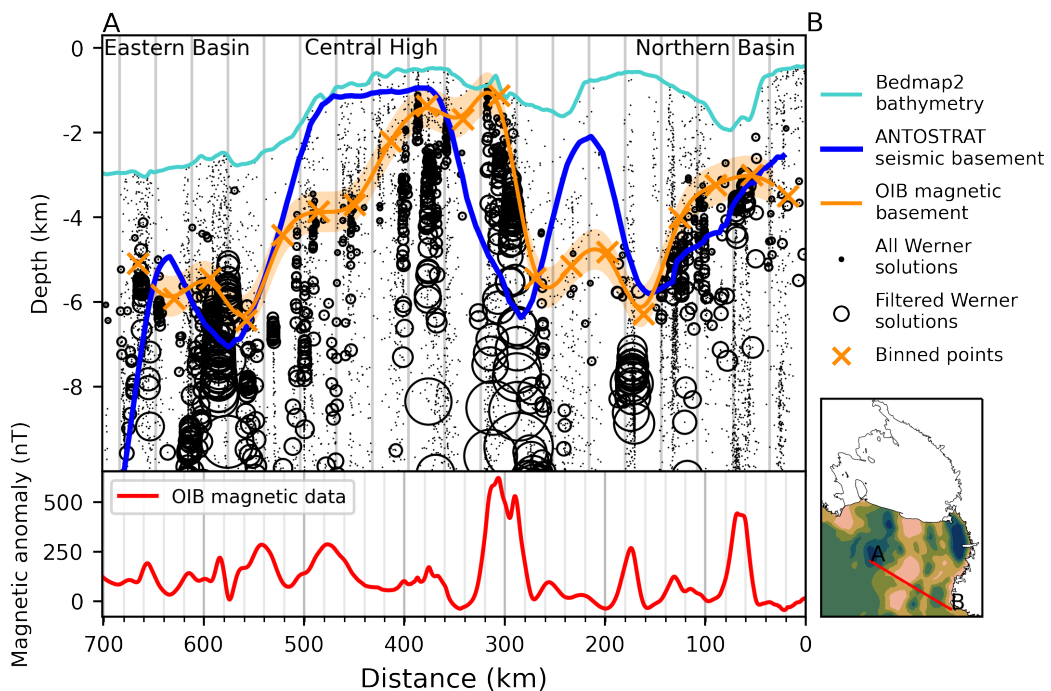


Figure A.2: Ross Sea magnetic and seismic basement comparison. Operation IceBridge airborne magnetic data (lower panel) from segment 403.3 (Figure 2.1b). Small dots show Werner deconvolution solutions, which were filtered based on parameters S and W (Section A.3) to produce black circles, which are scaled to parameter S. These circles were binned at a width equal to parameter B, shown by the vertical grey lines in the upper panel. Orange crosses show bin centers, which were fitted to a line to facilitate the comparison between the magnetic basement (orange line) and seismic basement (blue line). Orange band shows ± 480 m uncertainty for the basement model. Ross Sea basement features are labeled on top.

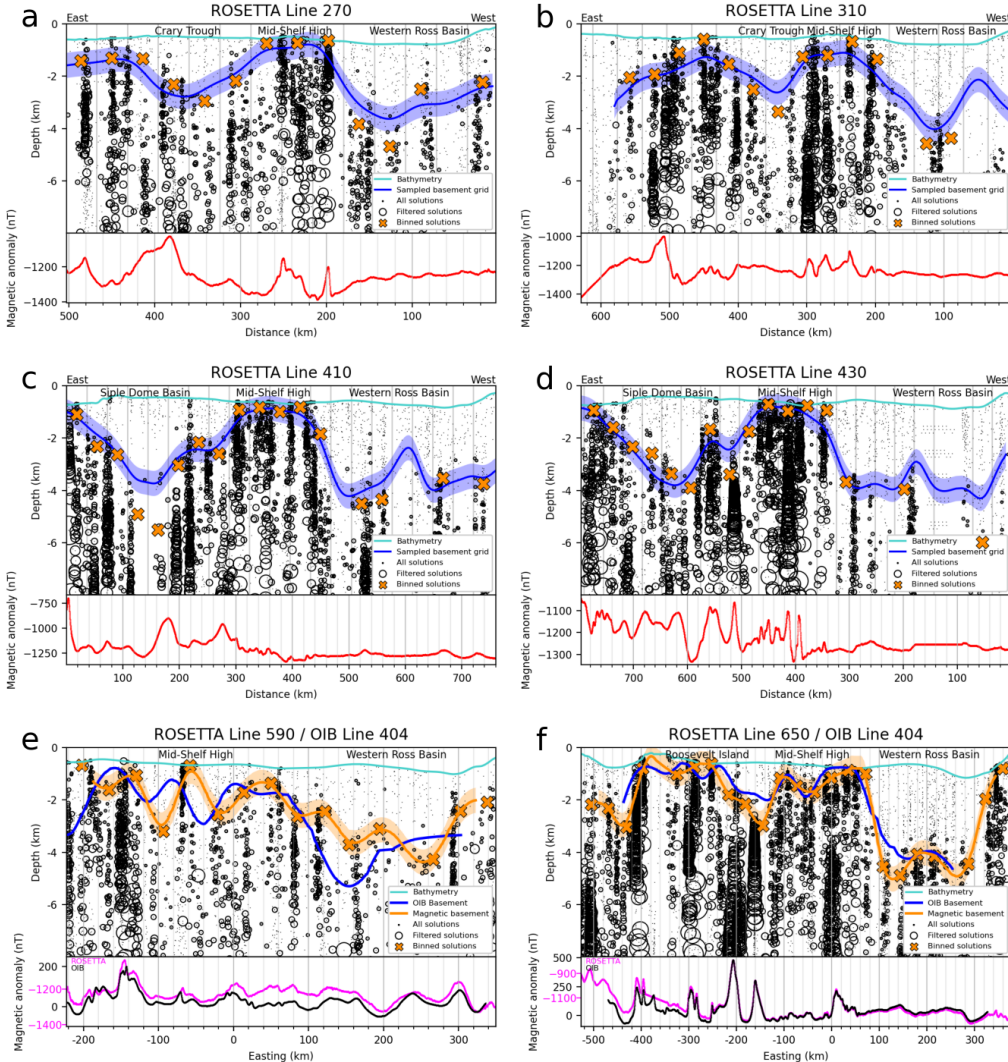


Figure A.3: Werner deconvolution solutions for a selection of ROSETTA-Ice lines, locations highlighted in Figure A.4. Bathymetry from Bedmap2 (Fretwell et al., 2013). Dots, circles, and vertical grey lines same as Figure A.2. **a-d)** Comparison between magnetic basement before and after filtering and gridding. Orange crosses are magnetic basement solutions, shown as black dots in Figure A.4, and highlighted for these lines. Blue lines are magnetic basement sampled from the grid of Figure 1a, after gridding and filtering. Red lines show 258 ROSETTA-Ice magnetics data. **e-f)** Comparison between magnetic basement resulting from Werner deconvolution of coincident OIB and ROSETTA-Ice flight lines. Location is shown in Figures 2.1b and A.4. These two lines were used to tie the ROSETTA-Ice survey to the OIB survey (Section A.5). Blue lines are OIB magnetic basement results, orange crosses and fitted orange lines with uncertainty bands are ROSETTA-Ice magnetic basement. ROSETTA-Ice (pink) and OIB (black) magnetics data are shown in lower panels.

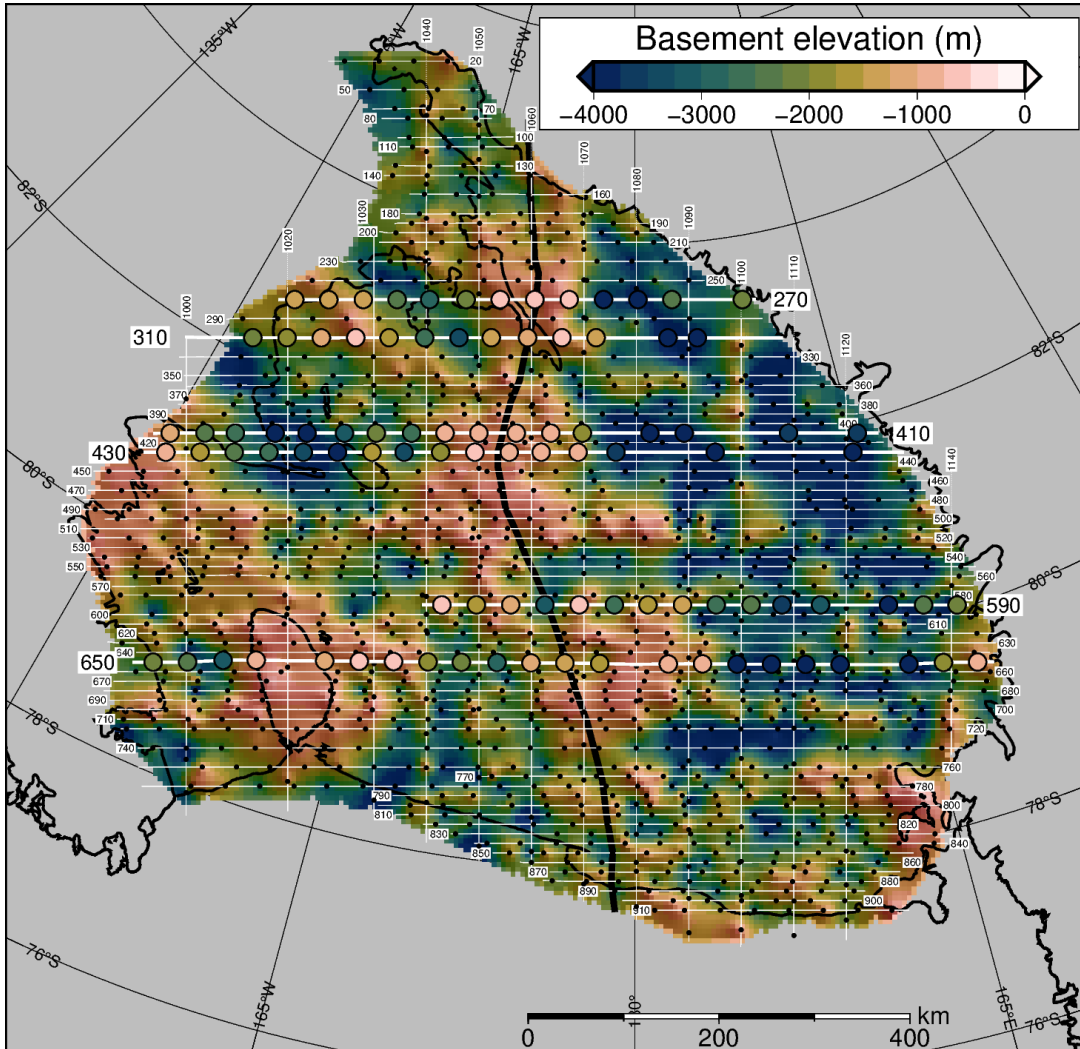


Figure A.4: Unfiltered magnetic basement. Point solutions (black dots here, orange crosses in Figure A.3) along ROSETTA-Ice flight lines (labelled) were gridded with a 5 km cell size and a minimum curvature spline with a tension factor of 0.35. Figure A.3 flight lines (bold white) and point solutions (coloured circles) are shown. Black line through the Mid-Shelf High shows the East-West Antarctic divide used in colorbar histograms of Figures 2.3 and 2.4a. Grounding line and coastlines in black (Rignot et al., 2013).

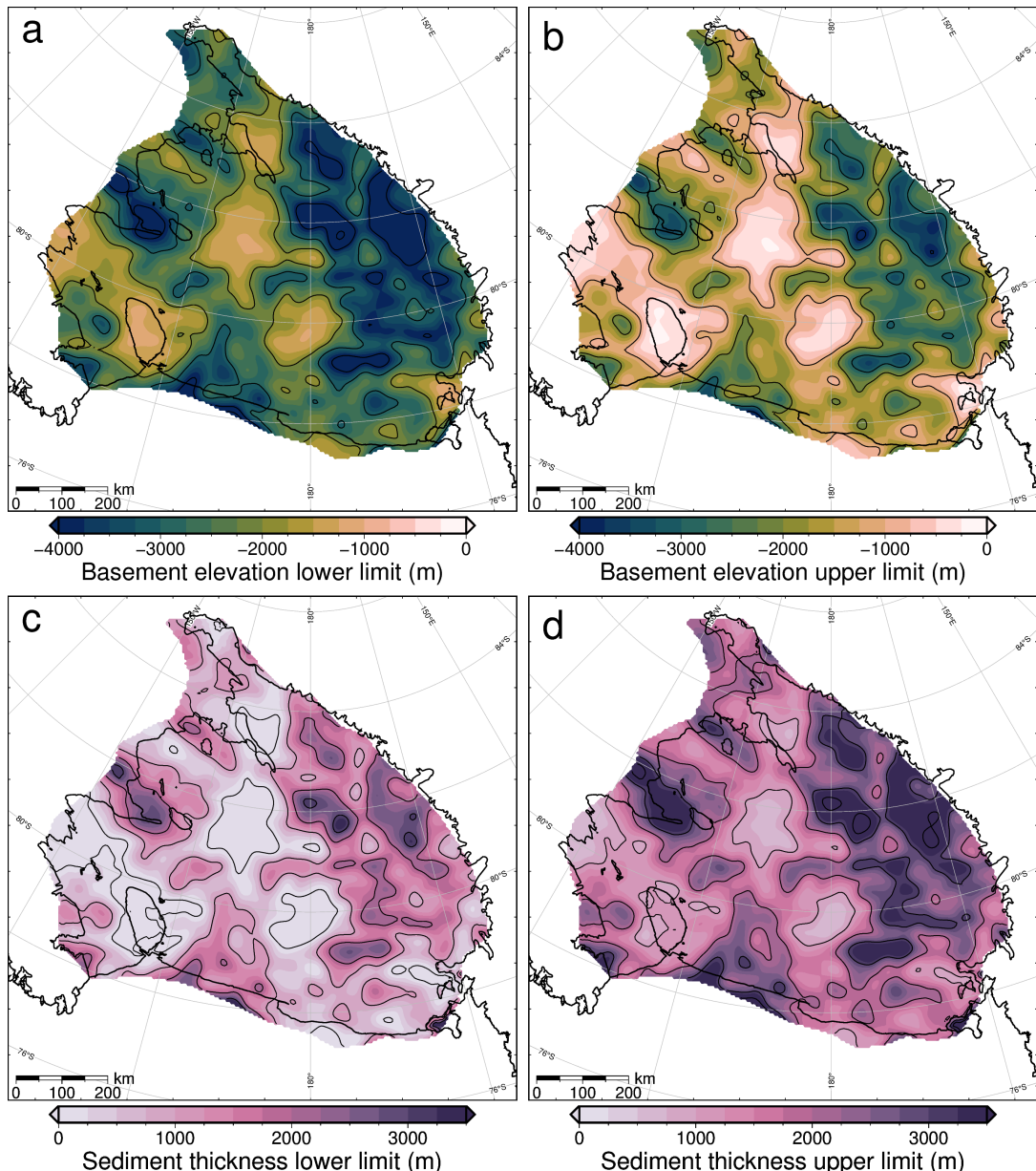


Figure A.5: Upper and lower limits of uncertainty applied to a-b) magnetic basement and c-d) sediment thickness. See Section A.8 for how these uncertainties were determined.

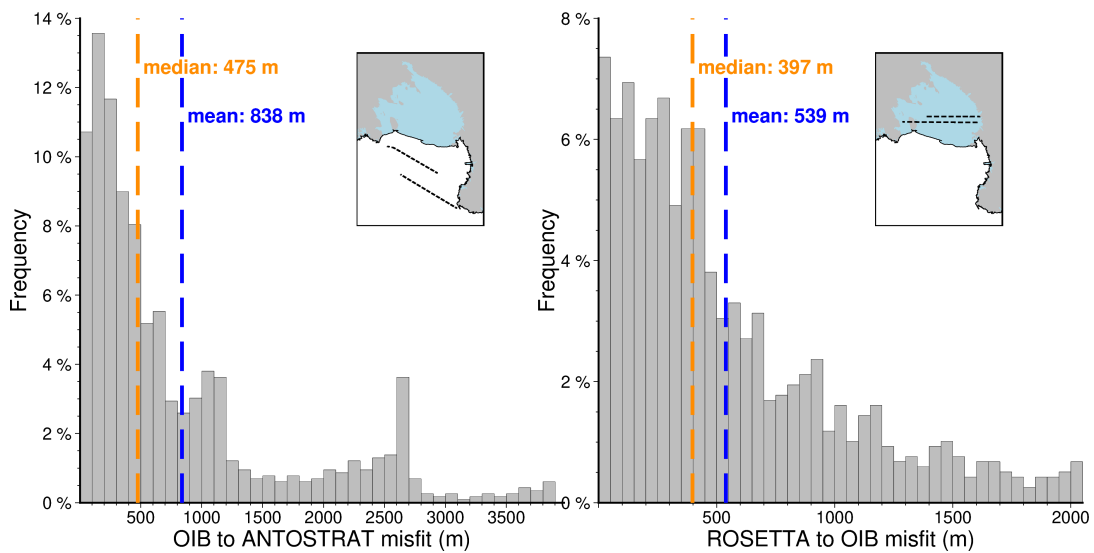


Figure A.6: Misfit distributions for comparisons between **a)** OIB magnetic basement and ANTOSTRAT seismic basement and between **b)** ROSETTA magnetic basement and OIB magnetic basement. Inset maps show the locations of flight lines. Basement models were sampled at 1 km intervals for the comparison.

4553 Appendix B

4554 This appendix section provides supplementary information to Chapter 3.

4555 B.1 Synthetic inversion with a regional field

4556 Regional separation techniques

4557 Figure B.1 shows profiles comparing the various regional separation techniques
4558 shown in Figure 3.19 of Chapter 3.

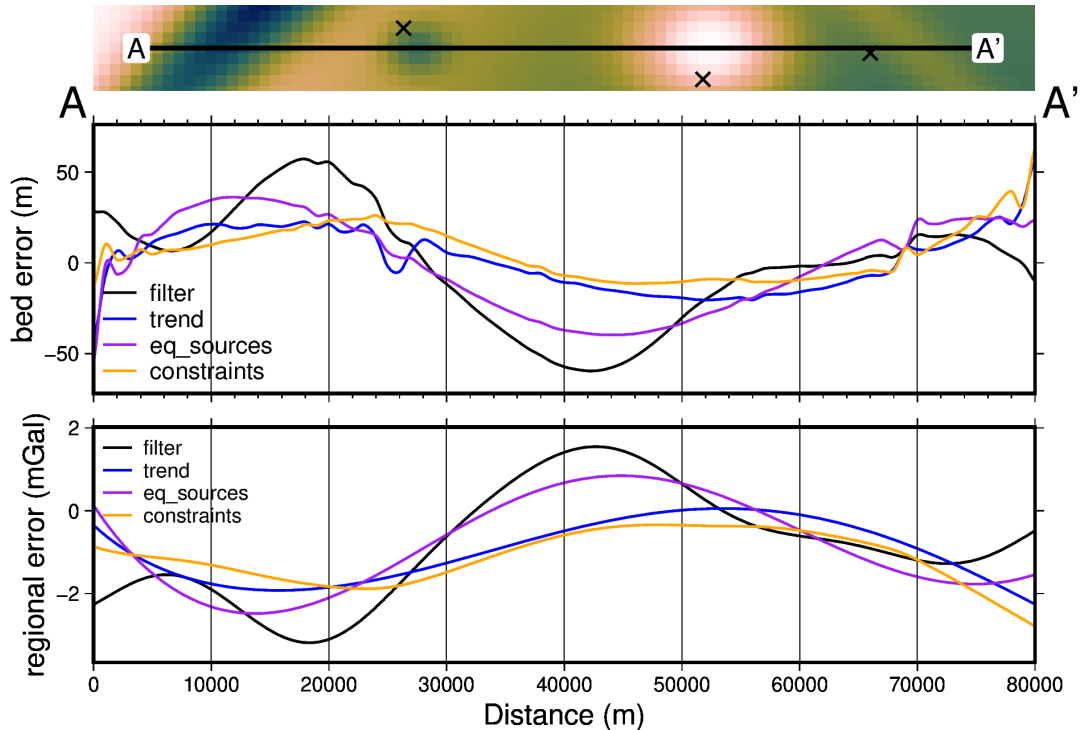


Figure B.1: Comparison of four methods of regional separation. **Upper panel** shows the error in the inverted bathymetry models for each method. **Lower panel** shows the errors in the regional field estimation of each method. Profile location shown at the top.

4559 Constraint point minimization grinding techniques

4560 Figure B.1 shows profiles comparing the various gridding techniques for the con-
4561 straint point minimization regional separation method. These various gridding tech-
4562 niques are shown in map view in Figure 3.20 of Chapter 3.

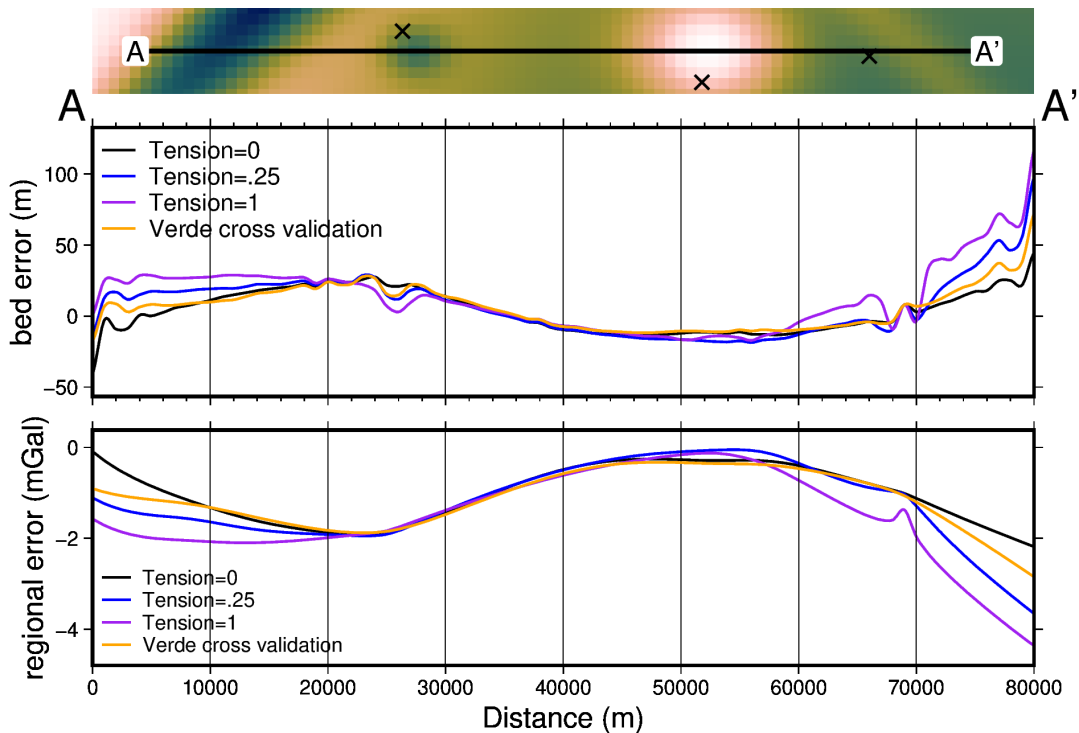


Figure B.2: Comparison of gridding techniques for the constraint point minimization method of regional separation. **Upper panel** shows the error in the inverted bathymetry models for each method. **Lower panel** shows the errors in the regional field estimation of the each method. Profile location shown at the top.

4563 Added noise

4564 Here, we repeat the inversion from Section 3.4 with noise added to the observed
 4565 gravity data. Noise was from a Gaussian distribution with a mean of 0 and a stan-
 4566 dard deviation of 2% of the max absolute values of the data, equating to 0.24 mGal.
 4567 The cross validation curve and a profile across the inverted bathymetry as shown in
 4568 Figure B.3. The inverted bathymetry and difference with the true bathymetry as
 4569 shown in Figure B.4. The error in the inverted bathymetry is compared to the error
 4570 in the regional field estimation in Figure B.5.

4571 Lower-resolution gravity survey

4572 This same inversion is now repeated with a lower-resolution gravity survey. Instead
 4573 of the original 1 km survey grid, a 4 km grid is used.

4574 B.2 Ross Sea synthetic model

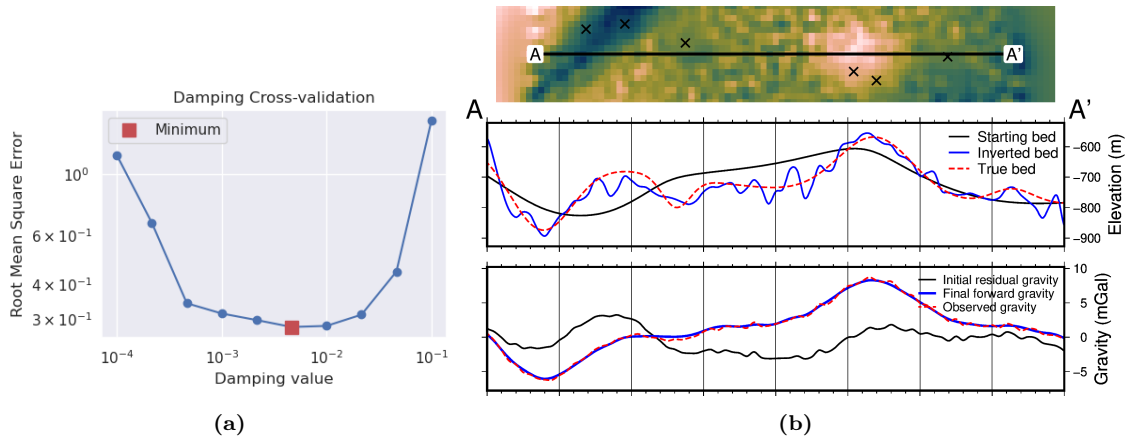


Figure B.3: Cross-validation and profiles for the simple synthetic inversion with a regional component removed and 2% noise added to the observed gravity data. a) Cross-validation curve showing the optimal damping parameter (red square). b) 2D profile of the inversion results. The top panel shows profile location and constraint points (black crosses). The middle panel contains topographic profiles of the starting, inverted, and true bathymetries. The bottom panel contains gravity anomaly profiles.

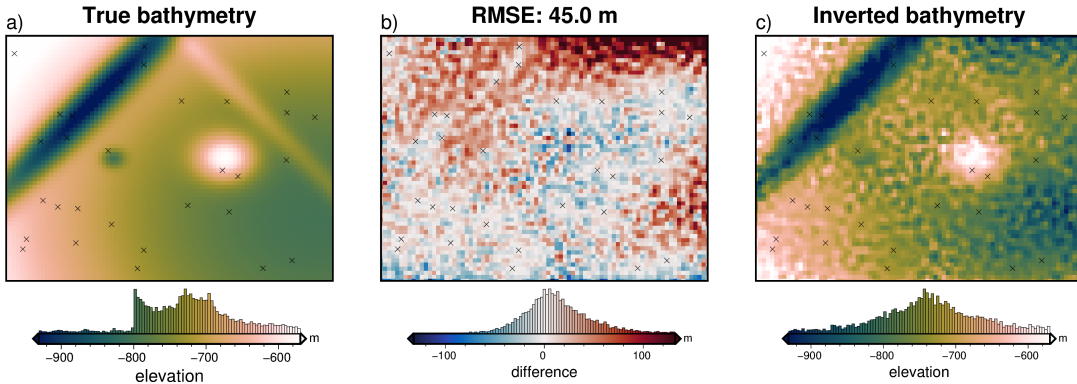


Figure B.4: Simple synthetic model inversion with a removed regional component and noise contamination. a) True bathymetry, b) difference between a) and c), c) final inverted bathymetry. Black crosses are constraint points. The RMS difference with the true bathymetry at these constraints is 2 m.

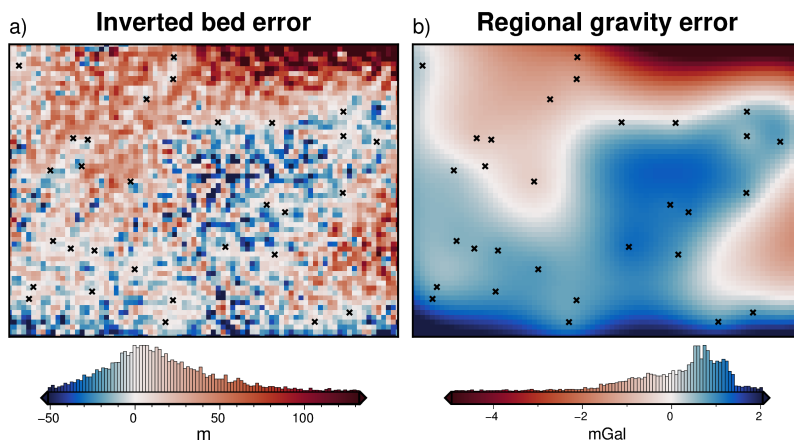


Figure B.5: Source of inverted bathymetry error for model with regional field and noise. a) Inverted bathymetry error from Figure 3.22b. b) Error in the estimation of the regional component of gravity from comparison with the true regional component (Figure 3.18b). Black cross show constraint points. Colormaps are opposed to highlight the similarities and the mean has been removed from the regional error.

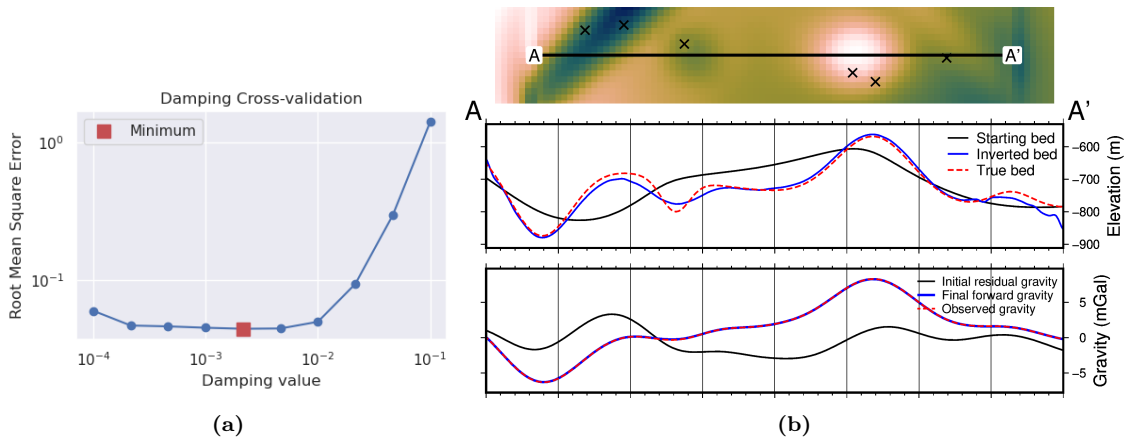


Figure B.6: Cross-validation and profiles for the simple synthetic inversion with a regional component removed and low-resolution gravity data. a) Cross-validation curve showing the optimal damping parameter (red square). b) 2D profile of the inversion results. The top panel shows profile location and constraint points (black crosses). The middle panel contains topographic profiles of the starting, inverted, and true bathymetries. The bottom panel contains gravity anomaly profiles.

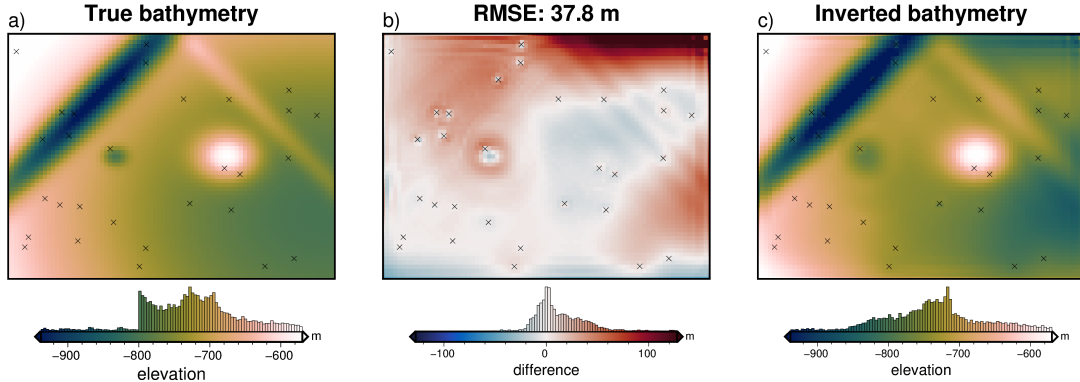


Figure B.7: Simple synthetic model inversion with a removed regional component and gravity resampling. a) True bathymetry, b) difference between a) and c), c) final inverted bathymetry. Black crosses are constraint points. The RMS difference with the true bathymetry at these constraints is 2 m.

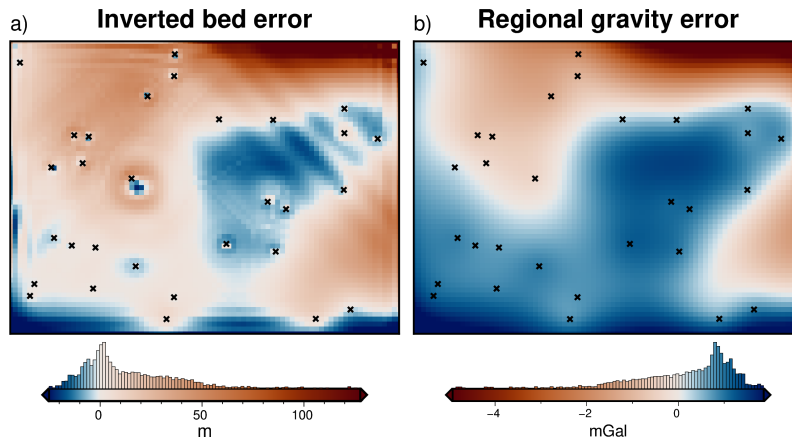


Figure B.8: Source of inverted bathymetry error for model with regional field and re-sampled gravity data. a) Inverted bathymetry error from Figure 3.22b. b) Error in the estimation of the regional component of gravity from comparison with the true regional component (Figure 3.18b). Black cross show constraint points. Colormaps are opposed to highlight the similarities and the mean has been removed from the regional error.

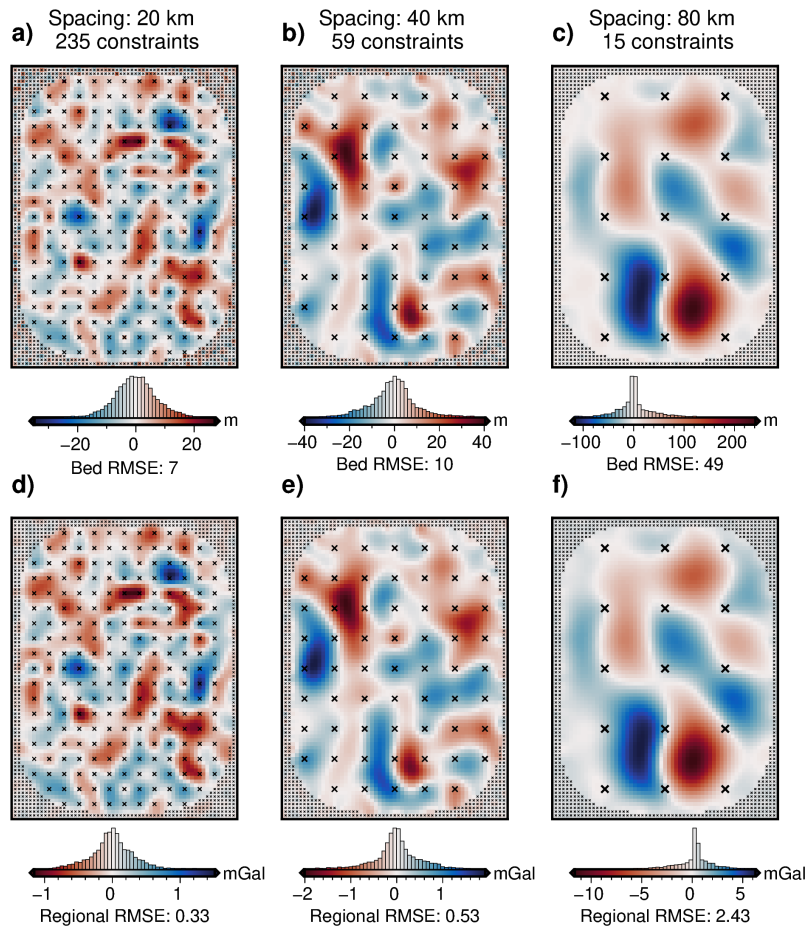


Figure B.9: Source of inverted bathymetry error for three inversion with varying constraint spacings. a) Inverted bathymetry error from three of the models in the constraint ensemble of Figure 3.31. b) Error in the estimation of the regional component of gravity from comparison with the true regional component for each model. Black cross show constraint points. Colormaps are opposed to highlight the similarities and the mean has been removed from the regional error.

4575

Appendix C

4576 This appendix provides supplemental information to Chapter 4.

4577

C.1 Gravity disturbance vs anomaly

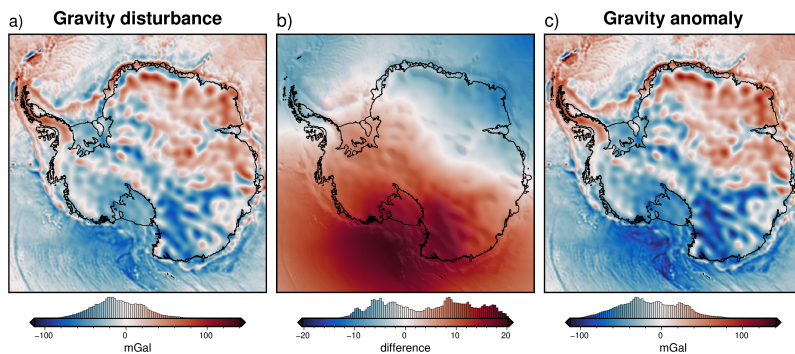


Figure C.1: Difference between the gravity disturbance and anomaly for Antarctica. Observed gravity is from Förste et al. (2014) and the normal gravity for each was calculated with the python package Boule (Fatiando a Terra Project et al., 2022). See Section 4.2.1 for further details.

4578 Appendix D

4579 Antarctic-Plots

4580 This appendix briefly describes the Python package Antarctic-Plots (Tankersley,
4581 2023) which I developed during this thesis and is used in all of the chapters. The
4582 documentation of the package is hosted at the following link; <https://antarctic-plots.readthedocs.io/en/latest/index.html> and the code is stored and developed in the fol-
4583 lowing GitHub repository; https://github.com/mdtanker/antarctic_plots.
4584

4585
4586 The Antarctic-Plots Python package aims to help automate common tasks as-
4587 sociated with researching Antarctica. There are four main modules of the package;
4588 **Fetch**, **Map**, **Profile**, and **Regions**.

4589 D.1 Fetch

4590 The Fetch module contains functions to download data related to Antarctica. These
4591 downloads are accomplished with the Python package Pooch Uieda et al. (2020).
4592 Calls to these functions will download the respective data and store it in a com-
4593 mon folder in your system. Subsequent calls to the same function will retrieve the
4594 already downloaded file. There is no need for remembering file paths or having
4595 multiple copies of the same data throughout your projects. Additionally, some of
4596 this data is pre-processed. This pre-processing includes re-projecting all data (grid-
4597 ded or tabular) to a common projection, South Polar Stereographic (EPSG:3031),
4598 and converting pre-gridded tabular data into more useful formats, such as Xarray
4599 dataarrays. (Hoyer & Hamman, 2017).

4600 This module currently contains over 40 datasets, which include; topography
4601 products, imagery, grounding line, coastline, and basin shapefiles, gravity, magnetics,
4602 geothermal heat flow, ice velocity, sediment thickness, moho depths, basal melt, ice
4603 mass change, and geologic units and faults. Below is an example that downloads,
4604 or retrieves if already download, BedMachine v3 surface elevation data, converted
4605 to be referenced to the WGS-84 ellipsoid (as opposed to the original data which is
4606 referenced to the geoid), and resampled at a 5 km spacing.

```
4607  
4608 from antarctic_plots import fetch  
4609  
4610 surface_data = fetch.bedmachine(  
4611     layer="surface",  
4612     reference="ellipsoid",  
4613     spacing=5000,  
4614 )
```

4616 D.2 Map

4617 The Map module provides convenient methods for plotting geospatial data. Most of
4618 these plotting functions use the Python package PyGMT (Uieda et al., 2021). All
4619 of the maps in Chapters 3, 4, & 5 were created with the help of these functions. In
4620 addition to static figures, there are several functions for creating interactive figures,
4621 which help with data visualization.

4622 D.3 Profile

4623 The Profile module is used to sample gridded data along specified profiles, and plot
4624 cross-sections and profiles of the data. The cross-section plots of Chapters 3 & 4 were
4625 created using these functions. Profiles can be defined by clicking on an interactive
4626 map to help with quickly exploring and visualizing datasets.

4627 D.4 Regions

4628 The Regions module provides pre-defined variables of region boundaries in EPSG:3031
4629 for commonly studied Antarctic areas. These region variables are used by the
4630 other modules to subset the desired region. For example, if you only want to fetch
4631 BedMap2 surface topography only for the Ross Ice Shelf, instead of the whole continent,
4632 you can pass the parameter "region = regions.ross_ice_shelf".

4633 Additionally, there are geospatial tools provided for re-projecting, masking, and
4634 gridding data. This package is still early in it's development and many more datasets
4635 and functions will still be added.

4636 Bibliography

- 4637 Adusumilli, S., Fricker, H. A., Medley, B., Padman, L., & Siegfried, M. R. (2020). Interannual
4638 variations in meltwater input to the Southern Ocean from Antarctic ice shelves. *Nature
4639 Geoscience*, *13*(9), 616–620. <https://doi.org/10.1038/s41561-020-0616-z> (cit. on pp. 16,
4640 38, 88, 128–130, 137)
- 4641 Aitken, A., Li, L., Kulessa, B., Schroeder, D., Jordan, T., Whittaker, J., Anandakrishnan, S.,
4642 Dawson, E., Wiens, D., Eisen, O., & Siegert, M. (2023a). *Antarctic sedimentary basin
4643 distribution and classification* (Version v1.04). Zenodo. <https://doi.org/10.5281/zenodo.7984586>. (Cit. on p. 135)
- 4644 Aitken, A. R., Li, L., Kulessa, B., Schroeder, D. M., Jordan, T. A., Whittaker, J. M., Anandakr-
4645 ishnan, S., Dawson, E. J., Wiens, D. A., Eisen, O., & Siegert, M. J. (2023b). *Antarctica's
4646 sedimentary basins and their influence on ice sheet dynamics* (Preprint). Preprints. <https://doi.org/10.11002/essoar.10510905.2>. (Cit. on pp. 17, 20, 134)
- 4647 Akiba, T., Sano, S., Yanase, T., Ohta, T., & Koyama, M. (2019). Optuna: A Next-generation
4648 Hyperparameter Optimization Framework. *Proceedings of the 25th ACM SIGKDD Interna-
4649 tional Conference on Knowledge Discovery & Data Mining*, 2623–2631. <https://doi.org/10.1145/3292500.3330701> (cit. on p. 50)
- 4650 Aleshkova, N. D., Golynsky, A. V., Kurinin, R. G., & Mandrikov, V. S. (2000). Gravity Mapping in
4651 the Southern Weddell Sea Region. (Explanatory note for free-air and Bouguer anomalies
4652 maps). *Polarforschung*, 15 pages. <https://doi.org/10.2312/POLARFORSCHUNG.67.3.163>
4653 (cit. on p. 145)
- 4654 Alley, R. B., Blankenship, D. D., Bentley, C. R., & Rooney, S. T. (1986). Deformation of till
4655 beneath ice stream B, West Antarctica. *Nature*, *322*(6074), 57–59. <https://doi.org/10.1038/322057a0> (cit. on pp. 19, 140)
- 4656 An, L., Rignot, E., Elieff, S., Morlighem, M., Millan, R., Mouginot, J., Holland, D. M., Holland,
4657 D., & Paden, J. (2017). Bed elevation of Jakobshavn Isbrae, West Greenland, from high-
4658 resolution airborne gravity and other data. *Geophysical Research Letters*, *44*(8), 3728–
4659 3736. <https://doi.org/10.1002/2017GL073245> (cit. on pp. 103, 104, 117)
- 4660 An, L., Rignot, E., Chauche, N., Holland, D. M., Holland, D., Jakobsson, M., Kane, E., Wood,
4661 M., Klaucke, I., Morlighem, M., Velicogna, I., Weinrebe, W., & Willis, J. K. (2019a).
4662 Bathymetry of Southeast Greenland From Oceans Melting Greenland (OMG) Data. *Geo-
4663 physical Research Letters*, *46*(20), 11197–11205. <https://doi.org/10.1029/2019GL083953>
4664 (cit. on pp. 46, 62, 103–105, 117, 120)
- 4665 An, L., Rignot, E., Millan, R., Tinto, K., & Willis, J. (2019b). Bathymetry of Northwest Greenland
4666 Using “Ocean Melting Greenland” (OMG) High-Resolution Airborne Gravity and Other
4667 Data. *Remote Sensing*, *11*(2), 131. <https://doi.org/10.3390/rs11020131> (cit. on pp. 103–
4668 105)
- 4669 An, M., Wiens, D. A., Zhao, Y., Feng, M., Nyblade, A. A., Kanao, M., Li, Y., Maggi, A., & Lévéque,
4670 J.-J. (2015). S-velocity model and inferred Moho topography beneath the Antarctic Plate
4671 from Rayleigh waves: Antarctic S-velocities and Moho. *Journal of Geophysical Research:
4672 Solid Earth*, *120*(1), 359–383. <https://doi.org/10.1002/2014JB011332> (cit. on pp. 29, 151)
- 4673 Anandakrishnan, S., Blankenship, D. D., Alley, R. B., & Stoffa, P. L. (1998). Influence of subglacial
4674 geology on the position of a West Antarctic ice stream from seismic observations. *Nature*,
4675 *394*(6688), 62–65. <https://doi.org/10.1038/27889> (cit. on p. 20)
- 4676 Anderson, J. B., Conway, H., Bart, P. J., Witus, A. E., Greenwood, S. L., McKay, R., Hall, B. H.,
4677 Ackert, R. P., Licht, K., Jakobsson, M., & Stone, J. O. (2014). Ross Sea paleo-ice drainage
4678 and deglacial history during and since the LGM. *Quaternary Science Reviews*, *100*, 31–54.
4679 <https://doi.org/10.1016/j.quascirev.2013.08.020> (cit. on p. 16)

- 4684 Anderson, J. B., Simkins, L. M., Bart, P. J., De Santis, L., Halberstadt, A. R. W., Olivo, E., &
 4685 Greenwood, S. L. (2019). Seismic and geomorphic records of Antarctic Ice Sheet evolution
 4686 in the Ross Sea and controlling factors in its behaviour. *Geological Society, London, Special*
 4687 *Publications*, 475(1), 223–240. <https://doi.org/10.1144/SP475.5> (cit. on pp. 16, 20, 141–
 4688 143)
- 4689 Andrews, J. T., & LeMasurier, W. (2021). Resolving the argument about volcanic bedrock under
 4690 the West Antarctic Ice Sheet and implications for ice sheet stability and sea level change.
Earth and Planetary Science Letters, 568, 117035. [https://doi.org/10.1016/j.epsl.2021.](https://doi.org/10.1016/j.epsl.2021.117035)
 4692 117035 (cit. on p. 148)
- 4693 Aster, R. C., Borchers, B., & Thurber, C. H. (2018). *Parameter estimation and inverse problems*.
 4694 Elsevier. (Cit. on pp. 42, 48, 100, 104).
- 4695 Austermann, J., Pollard, D., Mitrovica, J. X., Moucha, R., Forte, A. M., DeConto, R. M., Rowley,
 4696 D. B., & Raymo, M. E. (2015). The impact of dynamic topography change on Antarctic
 4697 ice sheet stability during the mid-Pliocene warm period. *Geology*, 43(10), 927–930. <https://doi.org/10.1130/G36988.1> (cit. on p. 26)
- 4699 Bamber, J. L., Oppenheimer, M., Kopp, R. E., Aspinall, W. P., & Cooke, R. M. (2022). Ice
 4700 Sheet and Climate Processes Driving the Uncertainty in Projections of Future Sea Level
 4701 Rise: Findings From a Structured Expert Judgement Approach. *Earth's Future*, 10(10).
 4702 <https://doi.org/10.1029/2022EF002772> (cit. on pp. 15, 16)
- 4703 Bamber, J., & Bentley, C. R. (1994). A comparison of satellite-altimetry and ice-thickness mea-
 4704 surements of the Ross Ice Shelf, Antarctica. *Annals of Glaciology*, 20, 357–364. <https://doi.org/10.3189/1994AoG20-1-357-364> (cit. on p. 39)
- 4706 Barbosa, V. C., Menezes, P. T., & Silva, J. B. (2007). Gravity data as a tool for detecting faults:
 4707 In-depth enhancement of subtle Almada's basement faults, Brazil. *GEOPHYSICS*, 72(3),
 4708 B59–B68. <https://doi.org/10.1190/1.2713226> (cit. on p. 42)
- 4709 Barletta, V. R., Bevis, M., Smith, B. E., Wilson, T., Brown, A., Bordoni, A., Willis, M., Khan,
 4710 S. A., Rovira-Navarro, M., Dalziel, I., Smalley, R., Kendrick, E., Konfal, S., Caccamise,
 4711 D. J., Aster, R. C., Nyblade, A., & Wiens, D. A. (2018). Observed rapid bedrock uplift in
 4712 Amundsen Sea Embayment promotes ice-sheet stability. *Science*, 360(6395), 1335–1339.
 4713 <https://doi.org/10.1126/science.aa01447> (cit. on pp. 18, 139, 140)
- 4714 Bart, P., & De Santis, L. (2012). Glacial intensification during the Neogene: A review of seismic
 4715 stratigraphic evidence from the Ross Sea, Antarctica, continental shelf. *Oceanography*,
 4716 25(3), 166–183. <https://doi.org/10.5670/oceanog.2012.92> (cit. on p. 34)
- 4717 Bart, P. J., Krogmeier, B. J., Bart, M. P., & Tulaczyk, S. (2017). The paradox of a long grounding
 4718 during West Antarctic Ice Sheet retreat in Ross Sea. *Scientific Reports*, 7(1), 1262. <https://doi.org/10.1038/s41598-017-01329-8> (cit. on p. 142)
- 4720 Beaudoin, B. C., ten Brink, U. S., & Stern, T. A. (1992). Characteristics and processing of seismic
 4721 data collected on thick, floating ice: Results from the Ross Ice Shelf, Antarctica. *Geo-
 4722 physics*, 57(10), 1359–1372. <https://doi.org/10.1190/1.1443205> (cit. on p. 31)
- 4723 Begeman, C. B., Tulaczyk, S. M., & Fisher, A. T. (2017). Spatially Variable Geothermal Heat
 4724 Flux in West Antarctica: Evidence and Implications. *Geophysical Research Letters*, 44(19),
 4725 9823–9832. <https://doi.org/10.1002/2017GL075579> (cit. on pp. 28, 140)
- 4726 Bell, R. E., Blankenship, D. D., Finn, C. A., Morse, D. L., Scambos, T. A., Brozena, J. M., &
 4727 Hodge, S. M. (1998). Influence of subglacial geology on the onset of a West Antarctic ice
 4728 stream from aerogeophysical observations. *Nature*, 394(6688), 58–62. <https://doi.org/10.1038/27883> (cit. on p. 19)
- 4730 Bell, R. E., Studinger, M., Karner, G., Finn, C. A., & Blankenship, D. D. (2006). Identifying
 4731 major sedimentary basins beneath the West Antarctic Ice Sheet from aeromagnetic data
 4732 analysis. In D. K. Fütterer, D. Damaske, G. Kleinschmidt, H. Miller, & F. Tessensohn
 4733 (Eds.), *Antarctica* (pp. 117–121). Springer-Verlag. https://doi.org/10.1007/3-540-32934-X_13. (Cit. on pp. 28, 30–32, 149)
- 4735 Bell, R. E., Ferraccioli, F., Creyts, T. T., Braaten, D., Corr, H., Das, I., Damaske, D., Frearson,
 4736 N., Jordan, T., Rose, K., Studinger, M., & Wolovick, M. (2011). Widespread Persistent
 4737 Thickening of the East Antarctic Ice Sheet by Freezing from the Base. *Science*, 331(6024),
 4738 1592–1595. <https://doi.org/10.1126/science.1200109> (cit. on p. 26)
- 4739 Bennett, H. F. (1964). *A gravity and magnetic survey of the Ross Ice Shelf area, Antarctica* (tech.
 4740 rep. No. 64-3). The University of Wisconsin. Madison. (Cit. on p. 105).
- 4741 Bentley, C. R., Crary, A. P., Ostenso, N. A., & Thiel, E. C. (1960). Structure of West Antarctica.
 4742 *Science*, 131(3394), 131–136. <https://doi.org/10.1126/science.131.3394.131> (cit. on p. 21)

- 4743 Bentley, C. R. (1984). The Ross Ice Shelf: Glaciology and Geophysics Paper 1: Introduction and
 4744 summary of measurements performed. In C. R. Bentley & D. E. Hayes (Eds.), *Antarctic*
 4745 *Research Series* (pp. 1–20). American Geophysical Union. <https://doi.org/10.1029/AR042p0001>. (Cit. on pp. 18, 21, 89, 105, 108)
- 4746 Block, A. E., Bell, R. E., & Studinger, M. (2009). Antarctic crustal thickness from satellite gravity:
 4747 Implications for the Transantarctic and Gamburtsev Subglacial Mountains. *Earth and*
 4748 *Planetary Science Letters*, 288(1-2), 194–203. <https://doi.org/10.1016/j.epsl.2009.09.022>
 4749 (cit. on p. 131)
- 4750 Boghosian, A., Tinto, K., Cochran, J. R., Porter, D., Elieff, S., Burton, B. L., & Bell, R. E. (2015).
 4751 Resolving bathymetry from airborne gravity along Greenland fjords. *Journal of Geophysical*
 4752 *Research: Solid Earth*, 120(12), 8516–8533. <https://doi.org/10.1002/2015JB012129>
 4753 (cit. on pp. 78, 102–105, 117)
- 4754 Borg, S. G., Depaolo, D. J., & Smith, B. M. (1990). Isotopic structure and tectonics of the central
 4755 Transantarctic mountains. *Journal of Geophysical Research*, 95(B5), 6647. <https://doi.org/10.1029/JB095iB05p06647> (cit. on pp. 32, 34)
- 4756 Borghi, A. (2022). Moho depths for Antarctica Region by the inversion of ground-based gravity
 4757 data. *Geophysical Journal International*, 231(2), 1404–1420. <https://doi.org/10.1093/gji/ggac249> (cit. on p. 42)
- 4758 Bougamont, M., Christoffersen, P., Price, S. F., Fricker, H. A., Tulaczyk, S., & Carter, S. P. (2015).
 4759 Reactivation of Kamb Ice Stream tributaries triggers century-scale reorganization of Siple
 4760 Coast ice flow in West Antarctica: Restructuring of Siple Coast Ice Flow. *Geophysical*
 4761 *Research Letters*, 42(20), 8471–8480. <https://doi.org/10.1002/2015GL065782> (cit. on
 4762 p. 141)
- 4763 Bourgeois, B. S., Elmore, P. A., Avera, W. E., & Zambo, S. J. (2016). Achieving comparable uncer-
 4764 tainty estimates with Kalman filters or linear smoothers for bathymetry data. *Geochemistry,*
 4765 *Geophysics, Geosystems*, 17(7), 2576–2590. <https://doi.org/10.1002/2015GC006239>
 4766 (cit. on pp. 83, 85)
- 4767 Brancolini, G., Busetti, M., Marchetti, A., Santis, L. D., Zanolla, C., Cooper, A. K., Cochrane,
 4768 G. R., Zayatz, I., Belyaev, V., Knyazev, M., Vinnikovskaya, O., Davey, F. J., & Hinze, K.
 4769 (1995). Descriptive text for the seismic stratigraphic atlas of the Ross Sea, Antarctica. In
 4770 A. K. Cooper, P. F. Barker, & G. Brancolini (Eds.), *Geology and Seismic Stratigraphy of*
 4771 *the Antarctic Margin* (A271–A286). American Geophysical Union. <https://doi.org/10.1002/9781118669013.app1>. (Cit. on pp. 26–28, 67, 68, 143, 147, 149, 152)
- 4772 Brisbourne, A. M., Kulessa, B., Hudson, T., Harrison, L., Holland, P., Luckman, A., Bevan, S.,
 4773 Ashmore, D., Hubbard, B., Pearce, E., White, J., Booth, A., Nicholls, K., & Smith, A.
 4774 (2020). An updated seabed bathymetry beneath Larsen C Ice Shelf, Antarctic Peninsula.
 4775 *Earth System Science Data*, 12(2), 887–896. <https://doi.org/10.5194/essd-12-887-2020>
 4776 (cit. on pp. 69, 122, 145)
- 4777 Brisbourne, A. M., Smith, A. M., King, E. C., Nicholls, K. W., Holland, P. R., & Makinson,
 4778 K. (2014). Seabed topography beneath Larsen C Ice Shelf from seismic soundings. *The*
 4779 *Cryosphere*, 8(1), 1–13. <https://doi.org/10.5194/tc-8-1-2014> (cit. on pp. 45, 80, 96, 117)
- 4780 Burton-Johnson, A., Dziadek, R., & Martin, C. (2020). Geothermal heat flow in Antarctica: Current
 4781 and future directions. *The Cryosphere Discussions*, 1–45. <https://doi.org/10.5194/tc-2020-59> (cit. on pp. 32, 135, 140, 141)
- 4782 Calder, B., & Elmore, P. (2017). Development of an Uncertainty Propagation Equation for Scalar
 4783 Fields. *Marine Geodesy*, 40(5), 341–360. <https://doi.org/10.1080/01490419.2017.1345811>
 4784 (cit. on p. 85)
- 4785 Catania, G., Hulbe, C., Conway, H., Scambos, T., & Raymond, C. (2012). Variability in the
 4786 mass flux of the Ross ice streams, West Antarctica, over the last millennium. *Journal of*
 4787 *Glaciology*, 58(210), 741–752. <https://doi.org/10.3189/2012JoG11J219> (cit. on p. 141)
- 4788 Chen, B., Haeger, C., Kaban, M. K., & Petrunin, A. G. (2018). Variations of the effective elastic
 4789 thickness reveal tectonic fragmentation of the Antarctic lithosphere. *Tectonophysics*, 746,
 4790 412–424. <https://doi.org/10.1016/j.tecto.2017.06.012> (cit. on p. 139)
- 4791 Cheng, W., Hu, X. G., & Liu, L. T. (2021). Anisotropy Gradients in the Middle of the Ross Sea
 4792 Embayment, West Antarctica: Evidence From QL Scattered Surface Waves. *Geophysical*
 4793 *Research Letters*, 48(6). <https://doi.org/10.1029/2020GL091232> (cit. on p. 33)
- 4794 Chiappini, M., Ferraccioli, F., Bozzo, E., & Damaske, D. (2002). Regional compilation and analysis
 4795 of aeromagnetic anomalies for the Transantarctic Mountains–Ross Sea sector of the Antarc-

- tic. *Tectonophysics*, 347(1-3), 121–137. [https://doi.org/10.1016/S0040-1951\(01\)00241-4](https://doi.org/10.1016/S0040-1951(01)00241-4) (cit. on p. 30)
- Christoffersen, P., Bougamont, M., Carter, S. P., Fricker, H. A., & Tulaczyk, S. (2014). Significant groundwater contribution to Antarctic ice streams hydrologic budget. *Geophysical Research Letters*, 41(6), 2003–2010. <https://doi.org/10.1002/2014GL059250> (cit. on pp. 19, 26, 140, 141)
- Clough, J. W., & Hansen, B. L. (1979). The Ross Ice Shelf Project. *Science*, 203(4379), 433–434. <https://doi.org/10.1126/science.203.4379.433> (cit. on pp. 18, 89)
- Cochran, J. R., Burton, B., Frearson, N., & Tinto, K. (2014a). IceBridge Scintrex CS-3 Cesium magnetometer L1B geolocated magnetic anomalies, version 2. [Line 403, 404]. *Boulder, Colorado USA. NASA National Snow and Ice Data Center Distributed Active Archive Center*. <https://doi.org/10.5067/OY7C2Y61YSYW> (cit. on pp. 28, 147, 149)
- Cochran, J. R., Jacobs, S. S., Tinto, K. J., & Bell, R. E. (2014b). Bathymetric and oceanic controls on Abbot Ice Shelf thickness and stability. *The Cryosphere*, 8(3), 877–889. <https://doi.org/10.5194/tc-8-877-2014> (cit. on pp. 103, 104)
- Cochran, J. R., & Bell, R. E. (2012). Inversion of IceBridge gravity data for continental shelf bathymetry beneath the Larsen Ice Shelf, Antarctica. *Journal of Glaciology*, 58(209), 540–552. <https://doi.org/10.3189/2012JoG11J033> (cit. on pp. 102–104, 145)
- Cochran, J. R., Tinto, K. J., & Bell, R. E. (2020). Detailed Bathymetry of the Continental Shelf Beneath the Getz Ice Shelf, West Antarctica. *Journal of Geophysical Research: Earth Surface*, 125(10). <https://doi.org/10.1029/2019JF005493> (cit. on pp. 46, 102–104, 144)
- Coenen, J. J., Scherer, R. P., Baudoin, P., Warny, S., Castañeda, I. S., & Askin, R. (2019). Paleogene marine and terrestrial development of the West Antarctic Rift System. *Geophysical Research Letters*, 47(3). <https://doi.org/10.1029/2019GL085281> (cit. on pp. 26, 33, 143)
- Colleoni, F., De Santis, L., Montoli, E., Olivo, E., Sorlien, C. C., Bart, P. J., Gasson, E. G. W., Bergamasco, A., Sauli, C., Wardell, N., & Prato, S. (2018). Past continental shelf evolution increased Antarctic ice sheet sensitivity to climatic conditions. *Scientific Reports*, 8(1), 11323. <https://doi.org/10.1038/s41598-018-29718-7> (cit. on p. 26)
- Constantino, R. R., & Tinto, K. J. (2023). Cook Ice Shelf and Ninnis Glacier Tongue Bathymetry From Inversion of Operation Ice Bridge Airborne Gravity Data. *Geophysical Research Letters*, 50(11), e2023GL103815. <https://doi.org/10.1029/2023GL103815> (cit. on pp. 104, 117)
- Constantino, R. R., Tinto, K. J., Bell, R. E., Porter, D. F., & Jordan, T. A. (2020). Seafloor Depth of George VI Sound, Antarctic Peninsula, From Inversion of Aerogravity Data. *Geophysical Research Letters*, 47(21). <https://doi.org/10.1029/2020GL088654> (cit. on pp. 102, 103, 105, 117, 119)
- Cooper, A. K., Barker, P. F., & Brancolini, G. (Eds.). (1995). *Geology and seismic stratigraphy of the Antarctic margin*. AGU. <https://doi.org/10.1029/AR068>. (Cit. on p. 31)
- Coulon, V., Bulthuis, K., Whitehouse, P. L., Sun, S., Haubner, K., Zipf, L., & Pattyn, F. (2021). Contrasting response of West and East Antarctic Ice Sheets to glacial isostatic adjustment. *Journal of Geophysical Research: Earth Surface*, 126(7). <https://doi.org/10.1029/2020JF006003> (cit. on pp. 18, 33, 140)
- Cox, S. C., Smith Lyttle, B., Elkind, S., Smith Siddoway, C., Morin, P., Capponi, G., Abu-Alam, T., Ballinger, M., Bamber, L., Kitchener, B., Lelli, L., Mawson, J., Millikin, A., Dal Seno, N., Whitburn, L., White, T., Burton-Johnson, A., Crispini, L., Elliot, D., ... Wilson, G. (2023). A continent-wide detailed geological map dataset of Antarctica. *Scientific Data*, 10(1), 250. <https://doi.org/10.1038/s41597-023-02152-9> (cit. on pp. 135, 148)
- Crary, A. P. (1961). Marine-sediment thickness in the eastern Ross Sea area, Antarctica. *Geological Society of America Bulletin*, 72(5), 787. [https://doi.org/10.1130/0016-7606\(1961\)72\[787:MTITER\]2.0.CO;2](https://doi.org/10.1130/0016-7606(1961)72[787:MTITER]2.0.CO;2) (cit. on p. 152)
- Crary, A. P., Robinson, E. S., Bennett, H. F., & Boyd, W. (1962). *Glaciological studies on the Ross Ice Shelf, Antarctica; 1957-1960* (tech. rep. No. 6). American Geographical Society. New York, NY, USA. (Cit. on pp. 89, 105).
- Crary, A. (1959). Oversnow Traverses from IGY Little American Station. *Transactions, American Geophysical Union*, 40(3), 311–315. <https://doi.org/10.1029/TR040i003p00269> (cit. on pp. 21, 89, 105)
- Crary, A., & Robinson, E. (1962). Oversnow Traverse from McMurdo to the South Pole. *Science*, 135(3500), 291–295. <https://doi.org/10.1126/science.135.3500.291> (cit. on pp. 89, 105)

- 4859 Dampney, C. N. G. (1969). The equivalent source technique, 15. <https://doi.org/10.1190/1.1439996>
 4860 (cit. on pp. 56, 109)
- 4861 Das, I., Padman, L., Bell, R. E., Fricker, H. A., Tinto, K. J., Hulbe, C. L., Siddoway, C. S.,
 4862 Dhakal, T., Frearson, N. P., Mosbeux, C., Cordero, S. I., & Siegfried, M. R. (2020). Multi-
 4863 decadal basal melt rates and structure of the Ross Ice Shelf, Antarctica using airborne ice
 4864 penetrating radar. *Journal of Geophysical Research: Earth Surface*, 1–20. <https://doi.org/10.1029/2019JF005241> (cit. on pp. 21, 39, 129, 130, 137)
- 4865 De Rydt, J., Holland, P. R., Dutrieux, P., & Jenkins, A. (2014). Geometric and oceanographic
 4866 controls on melting beneath Pine Island Glacier. *Journal of Geophysical Research: Oceans*,
 4867 119(4), 2420–2438. <https://doi.org/10.1002/2013JC009513> (cit. on pp. 16, 89)
- 4868 De Santis, L. (1999). The Eastern Ross Sea continental shelf during the Cenozoic: Implications for
 4869 the West Antarctic ice sheet development. *Global and Planetary Change*, 23(1-4), 173–196.
 4870 [https://doi.org/10.1016/S0921-8181\(99\)00056-9](https://doi.org/10.1016/S0921-8181(99)00056-9) (cit. on p. 143)
- 4871 De Santis, L., Anderson, J. B., Brancolini, G., & Zayatz, I. (1995). Seismic record of late Oligocene
 4872 through Miocene glaciation on the central and eastern continental shelf of the Ross Sea. In
 4873 A. K. Cooper, P. F. Barker, & G. Brancolini (Eds.), *Antarctic Research Series* (pp. 235–
 4874 260). American Geophysical Union. <https://doi.org/10.1029/AR068p0235>. (Cit. on pp. 34,
 4875 143)
- 4876 DeConto, R. M., & Pollard, D. (2003). A coupled climate–ice sheet modeling approach to the
 4877 Early Cenozoic history of the Antarctic ice sheet. *Palaeogeography, Palaeoclimatology,*
 4878 *Palaeoecology*, 198(1-2), 39–52. [https://doi.org/10.1016/S0031-0182\(03\)00393-6](https://doi.org/10.1016/S0031-0182(03)00393-6) (cit. on
 4879 p. 26)
- 4880 Deng, X., & Tang, Z.-a. (2011). Moving Surface Spline Interpolation Based on Green's Function.
 4881 *Mathematical Geosciences*, 43(6), 663–680. <https://doi.org/10.1007/s11004-011-9346-5>
 4882 (cit. on p. 63)
- 4883 Dinniman, M. S., Klinck, J. M., & Smith, W. O. (2011). A model study of Circumpolar Deep Water
 4884 on the West Antarctic Peninsula and Ross Sea continental shelves. *Deep Sea Research Part*
 4885 *II: Topical Studies in Oceanography*, 58(13–16), 1508–1523. <https://doi.org/10.1016/j.dsr2.2010.11.013> (cit. on pp. 88, 129)
- 4886 Dorschel, B., Hehemann, L., Viquerat, S., Warnke, F., Dreutter, S., Tenberge, Y. S., Accettella, D.,
 4887 An, L., Barrios, F., Bazhenova, E., Black, J., Bohoyo, F., Davey, C., De Santis, L., Dotti,
 4888 C. E., Fremand, A. C., Fretwell, P. T., Gales, J. A., Gao, J., ... Arndt, J. E. (2022). The
 4889 International Bathymetric Chart of the Southern Ocean Version 2. *Scientific Data*, 9(1),
 4890 275. <https://doi.org/10.1038/s41597-022-01366-7> (cit. on pp. 67, 68, 70)
 4891 IBCSO
- 4892 Dowdeswell, J., Evans, J., Mugford, R., Griffiths, G., McPhail, S., Millard, N., Stevenson, P., Brandon,
 4893 M., Banks, C., Heywood, K., Price, M., Dodd, P., Jenkins, A., Nicholls, K., Hayes, D.,
 4894 Abrahamsen, E., Tyler, P., Bett, B., Jones, D., ... Ackley, S. (2008). Autonomous
 4895 underwater vehicles (AUVs) and investigations of the ice–ocean interface in Antarctic
 4896 and Arctic waters. *Journal of Glaciology*, 54(187), 661–672. <https://doi.org/10.3189/002214308786570773> (cit. on p. 18)
- 4897 Drenth, B. J., Grauch, V., Turner, K. J., Rodriguez, B. D., Thompson, R. A., & Bauer, P. W.
 4898 (2019). A shallow rift basin segmented in space and time: The southern San Luis Basin,
 4899 Rio Grande rift, northern New Mexico, U.S.A. *Rocky Mountain Geology*, 54(2), 97–131.
 4900 <https://doi.org/10.24872/rmgjournal.54.2.97> (cit. on p. 28)
- 4901 Dupont, T. K., & Alley, R. B. (2005). Assessment of the importance of ice-shelf buttressing to
 4902 ice-sheet flow. *Geophysical Research Letters*, 32, 1–4. <https://doi.org/10.1029/2004GL022024> (cit. on pp. 16, 38, 88)
- 4903 Durand, G., van den Broeke, M. R., Le Cozannet, G., Edwards, T. L., Holland, P. R., Jourdain,
 4904 N. C., Marzeion, B., Mottram, R., Nicholls, R. J., Pattyn, F., Paul, F., Slangen, A. B. A.,
 4905 Winkelmann, R., Burgard, C., van Calcar, C. J., Barré, J.-B., Bataille, A., & Chapuis, A.
 4906 (2022). Sea-Level Rise: From Global Perspectives to Local Services. *Frontiers in Marine*
 4907 *Science*, 8, 709595. <https://doi.org/10.3389/fmars.2021.709595> (cit. on pp. 15, 133)
- 4908 Dutrieux, P., De Rydt, J., Jenkins, A., Holland, P. R., Ha, H. K., Lee, S. H., Steig, E. J., Ding,
 4909 Q., Abrahamsen, E. P., & Schröder, M. (2014). Strong Sensitivity of Pine Island Ice-Shelf
 4910 Melting to Climatic Variability. *Science*, 343(6167), 174–178. <https://doi.org/10.1126/science.1244341> (cit. on p. 89)
- 4911 Edwards, T. L., Nowicki, S., Marzeion, B., Hock, R., Goelzer, H., Seroussi, H., Jourdain, N. C.,
 4912 Slater, D. A., Turner, F. E., Smith, C. J., McKenna, C. M., Simon, E., Abe-Ouchi, A.,
 4913

- 4918 Gregory, J. M., Larour, E., Lipscomb, W. H., Payne, A. J., Shepherd, A., Agosta, C., ...
 4919 Zwinger, T. (2021). Projected land ice contributions to twenty-first-century sea level rise.
 4920 *Nature*, 593(7857), 74–82. <https://doi.org/10.1038/s41586-021-03302-y> (cit. on p. 15)
- 4921 Eisermann, H., Eagles, G., Ruppel, A., Smith, E. C., & Jokat, W. (2020). Bathymetry Beneath Ice
 4922 Shelves of Western Dronning Maud Land, East Antarctica, and Implications on Ice Shelf
 4923 Stability. *Geophysical Research Letters*, 47(12). <https://doi.org/10.1029/2019GL086724>
 4924 (cit. on pp. 45, 102–104, 117)
- 4925 Eisermann, H., Eagles, G., Ruppel, A. S., Läufer, A., & Jokat, W. (2021). Bathymetric Control
 4926 on Borchgrevink and Roi Baudouin Ice Shelves in East Antarctica. *Journal of Geophysical*
 4927 *Research: Earth Surface*, 126(10). <https://doi.org/10.1029/2021JF006342> (cit. on pp. 103,
 4928 104, 117)
- 4929 Fahnestock, M. A., Scambos, T. A., Bindschadler, R. A., & Kvaran, G. (2000). A millennium of
 4930 variable ice flow recorded by the Ross Ice Shelf, Antarctica. *Journal of Glaciology*, 13.
 4931 <https://doi.org/10.3189/172756500781832693> (cit. on p. 139)
- 4932 Fatiando a Terra Project, Dinneen, C., Gomez, M., Li, L., Pesce, A., Soler, S. R., & Uieda, L.
 4933 (2022). Boule v0.4.1: Reference ellipsoids for geodesy and geophysics. <https://doi.org/10.5281/zenodo.7258175>. (Cit. on p. 165)
- 4934 Fatiando a Terra Project, Esteban, F. D., Li, L., Oliveira, V. C., Pesce, A., Shea, N., Soler, S. R.,
 4935 Tankersley, M., & Uieda, L. (2023). Harmonica v0.6.0: Forward modeling, inversion, and
 4936 processing gravity and magnetic data. <https://doi.org/10.5281/zenodo.7690145>. (Cit. on
 4937 pp. 42, 47, 50, 92)
- 4938 Ferraccioli, F., Bozzo, E., & Damaske, D. (2002). Aeromagnetic signatures over western Marie Byrd
 4939 Land provide insight into magmatic arc basement, mafic magmatism and structure of the
 4940 Eastern Ross Sea Rift flank. *Tectonophysics*, 347, 139–165. [https://doi.org/10.1016/S0040-1951\(01\)00242-6](https://doi.org/10.1016/S0040-1951(01)00242-6) (cit. on p. 30)
- 4941 Filina, I. Y., Blankenship, D. D., Thoma, M., Lukin, V. V., Masolov, V. N., & Sen, M. K. (2008).
 4942 New 3D bathymetry and sediment distribution in Lake Vostok: Implication for pre-glacial
 4943 origin and numerical modeling of the internal processes within the lake. *Earth and Planetary*
 4944 *Science Letters*, 276(1-2), 106–114. <https://doi.org/10.1016/j.epsl.2008.09.012>
 4945 (cit. on pp. 104, 117)
- 4946 Finn, C. (2002). *Examples of the utility of magnetic anomaly data for geologic mapping* (Open-File
 4947 Report No. 02-400). USGS. Denver, Colorado. (Cit. on p. 28).
- 4948 Fisher, A. T., Mankoff, K. D., Tulaczyk, S. M., Tyler, S. W., Foley, N., & and the WISSARD
 4949 Science Team. (2015). High geothermal heat flux measured below the West Antarctic Ice
 4950 Sheet. *Science Advances*, 1, 1–9. <https://doi.org/10.1126/sciadv.1500093> (cit. on pp. 33,
 4951 141)
- 4952 Ford, A., & Barrett, P. J. (1975). *Basement rocks of the south-central Ross Sea, site 270, DSDP*
 4953 *leg 28* (tech. rep.). Texas A & M University, Ocean Drilling Program. College Station, TX,
 4954 United States. <https://doi.org/10.2973/dsdp.proc.28.130.1975>. (Cit. on p. 26)
- 4955 Forsberg, R. (2020). Preliminary compilation of Antarctica gravity and gravity gradient data (cit.
 4956 on p. 135).
- 4957 Förste, C., Bruinsma, S., Abrikosov, O., Lemoine, J.-M., Marty, J. C., Flechtner, F., Balmino, G.,
 4958 Barthelmes, F., & Biancale, R. (2014). EIGEN-6C4 The latest combined global gravity
 4959 field model including GOCE data up to degree and order 2190 of GFZ Potsdam and GRGS
 4960 Toulouse. <https://doi.org/10.5880/ICGEM.2015.1>. (Cit. on pp. 93, 165)
- 4961 Fox Maule, C., Purucker, M. E., Olsen, N., & Mosegaard, K. (2005). Heat Flux Anomalies in
 4962 Antarctica Revealed by Satellite Magnetic Data. *Science*, 309(5733), 464–467. <https://doi.org/10.1126/science.1106888> (cit. on p. 140)
- 4963 Frederick, B. C., Young, D. A., Blankenship, D. D., Richter, T. G., Kempf, S. D., Ferraccioli, F.,
 4964 & Siegert, M. J. (2016). Distribution of subglacial sediments across the Wilkes Subglacial
 4965 Basin, East Antarctica. *Journal of Geophysical Research: Earth Surface*, 121(4), 790–813.
 4966 <https://doi.org/10.1002/2015JF003760> (cit. on pp. 28, 149)
- 4967 Frémard, A. C., Fretwell, P., Bodart, J., Pritchard, H. D., Aitken, A., Bamber, J. L., Bell, R.,
 4968 Bianchi, C., Bingham, R. G., Blankenship, D. D., Casassa, G., Catania, G., Christianson,
 4969 K., Conway, H., Corr, H. F. J., Cui, X., Damaske, D., Damm, V., Drews, R., ... Zirizzotti,
 4970 A. (2022). Antarctic Bedmap data: FAIR sharing of 60 years of ice bed, surface and
 4971 thickness data. *Earth System Science Data Discussions*, 1–25. <https://doi.org/10.5194/essd-2022-355> (cit. on p. 17)

- 4976 Fretwell, P., Pritchard, H. D., Vaughan, D. G., Bamber, J. L., Barrand, N. E., Bell, R. E., Bianchi,
 4977 C., Bingham, R. G., Blankenship, D. D., Casassa, G., Catania, G., Callens, D., Conway,
 4978 H., Cook, A. J., Corr, H. F. J., Damaske, D., Damm, V., Ferraccioli, F., Forsberg, R.,
 4979 ... Zirizzotti, A. (2013). Bedmap2: Improved ice bed, surface and thickness datasets for
 4980 Antarctica. *The Cryosphere*, 7(1), 375–393. <https://doi.org/10.5194/tc-7-375-2013> (cit.
 4981 on pp. 15, 18, 20, 76, 88, 89, 95, 96, 105, 121, 133, 145, 155)
- 4982 Fricker, H. A., Popov, S., Allison, I., & Young, N. (2001). Distribution of marine ice beneath the
 4983 Amery Ice Shelf. *Geophysical Research Letters*, 28(11), 2241–2244. <https://doi.org/10.1029/2000GL012461> (cit. on p. 119)
- 4985 Fürst, J. J., Durand, G., Gillet-Chaulet, F., Tavard, L., Rankl, M., Braun, M., & Gagliardini, O.
 4986 (2016). The safety band of Antarctic ice shelves. *Nature Climate Change*, 6(5), 479–482.
 4987 <https://doi.org/10.1038/nclimate2912> (cit. on p. 87)
- 4988 Gladish, C. V., Holland, D. M., Rosing-Asvid, A., Behrens, J. W., & Boje, J. (2015). Oceanic
 4989 Boundary Conditions for Jakobshavn Glacier. Part I: Variability and Renewal of Ilulissat
 4990 Icefjord Waters, 2001–14. *Journal of Physical Oceanography*, 45(1), 3–32. <https://doi.org/10.1175/JPO-D-14-0044.1> (cit. on p. 89)
- 4992 Goldberg, D. N., Gourmelen, N., Kimura, S., Millan, R., & Snow, K. (2019). How Accurately
 4993 Should We Model Ice Shelf Melt Rates? *Geophysical Research Letters*, 46(1), 189–199.
 4994 <https://doi.org/10.1029/2018GL080383> (cit. on p. 89)
- 4995 Goldberg, D. N., Smith, T. A., Narayanan, S. H. K., Heimbach, P., & Morlighem, M. (2020).
 4996 Bathymetric Influences on Antarctic Ice-Shelf Melt Rates. *Journal of Geophysical Research: Oceans*, 125(11). <https://doi.org/10.1029/2020JC016370> (cit. on pp. 16, 89)
- 4998 Golledge, N. R., Marsh, O. J., Rack, W., Braaten, D., & Jones, R. S. (2014). Basal conditions of two
 4999 Transantarctic Mountains outlet glaciers from observation-constrained diagnostic mod-
 5000 ellng. *Journal of Glaciology*, 60(223), 855–866. <https://doi.org/10.3189/2014JoG13J131>
 5001 (cit. on p. 140)
- 5002 Golynsky, A. V., Ferraccioli, F., Hong, J. K., Golynsky, D. A., von Frese, R. R. B., Young, D. A.,
 5003 Blankenship, D. D., Holt, J. W., Ivanov, S. V., Kiselev, A. V., Masolov, V. N., Eagles, G.,
 5004 Gohl, K., Jokat, W., Damaske, D., Finn, C., Aitken, A., Bell, R. E., Armadillo, E., ...
 5005 Roberts, J. L. (2018). New Magnetic Anomaly Map of the Antarctic: ADMAP2. *Geophys-
 5006 ical Research Letters*, 45(13), 6437–6449. <https://doi.org/10.1029/2018GL078153> (cit. on
 5007 p. 135)
- 5008 Gooch, B. T., Young, D. A., & Blankenship, D. D. (2016). Potential groundwater and heteroge-
 5009 neous heat source contributions to ice sheet dynamics in critical submarine basins of East
 5010 Antarctica. *Geochemistry, Geophysics, Geosystems*, 17(2), 395–409. <https://doi.org/10.1002/2015GC006117> (cit. on pp. 19, 26, 33, 140, 141)
- 5012 Goodge, J. W. (2020). Geological and tectonic evolution of the Transantarctic Mountains, from
 5013 ancient craton to recent enigma. *Gondwana Research*, 80, 50–122. <https://doi.org/10.1016/j.gr.2019.11.001> (cit. on pp. 26, 30, 130)
- 5015 Granot, R., & Dyment, J. (2018). Late Cenozoic unification of East and West Antarctica. *Nature
 5016 Communications*, 9(1), 3189. <https://doi.org/10.1038/s41467-018-05270-w> (cit. on pp. 26,
 5017 31)
- 5018 Greenbaum, J. S., Blankenship, D. D., Young, D. A., Richter, T. G., Roberts, J. L., Aitken, A. R. A.,
 5019 Legresy, B., Schroeder, D. M., Warner, R. C., van Ommen, T. D., & Siegert, M. J. (2015).
 5020 Ocean access to a cavity beneath Totten Glacier in East Antarctica. *Nature Geoscience*,
 5021 8(4), 294–298. <https://doi.org/10.1038/ngeo2388> (cit. on pp. 102–104, 117)
- 5022 Greischar, L. L., Bentley, C. R., & Whiting, L. R. (1992). An analysis of gravity measurements on
 5023 the Ross Ice Shelf, Antarctica. In *Contributions to Antarctic Research III* (pp. 105–155).
 5024 American Geophysical Union (AGU). <https://doi.org/10.1029/AR057p0105>. (Cit. on
 5025 pp. 21, 32, 152)
- 5026 Griggs, J. A., & Bamber, J. L. (2011). Antarctic ice-shelf thickness from satellite radar altimetry.
 5027 *Journal of Glaciology*, 57(203), 485–498. <https://doi.org/10.3189/002214311796905659>
 5028 (cit. on pp. 39, 110)
- 5029 Gustafson, C. D., Key, K., Siegfried, M. R., Winberry, J. P., Fricker, H. A., Venturelli, R. A.,
 5030 & Michaud, A. B. (2022). A dynamic saline groundwater system mapped beneath an
 5031 Antarctic ice stream. *Science*, 376(6593), 640–644. <https://doi.org/10.1126/science.abm3301> (cit. on pp. 19, 26, 32, 33, 140, 141, 152)
- 5033 Halberstadt, A. R. W., Simkins, L. M., Greenwood, S. L., & Anderson, J. B. (2016). Past ice-
 5034 sheet behaviour: Retreat scenarios and changing controls in the Ross Sea, Antarctica. *The*

- 5035 *Cryosphere*, 10(3), 1003–1020. <https://doi.org/10.5194/tc-10-1003-2016> (cit. on pp. 16,
 5036 20, 34, 131, 133, 141, 143)
- 5037 Hammer, S. (1939). Terrain corrections for gravimeter stations. *GEOPHYSICS*, 4(3), 184–194.
 5038 <https://doi.org/10.1190/1.1440495> (cit. on p. 47)
- 5039 Harlan, R. B. (1968). Eotvos corrections for airborne gravimetry. *Journal of Geophysical Research*,
 5040 73(14), 4675–4679. <https://doi.org/10.1029/JB073i014p04675> (cit. on p. 109)
- 5041 Helton, J., Johnson, J., Sallaberry, C., & Storlie, C. (2006). Survey of sampling-based methods for
 5042 uncertainty and sensitivity analysis. *Reliability Engineering & System Safety*, 91(10-11),
 5043 1175–1209. <https://doi.org/10.1016/j.ress.2005.11.017> (cit. on pp. 72, 98, 99, 113)
- 5044 Hinze, W. J., Aiken, C., Brozena, J., Coakley, B., Dater, D., Flanagan, G., Forsberg, R., Hilden-
 5045 brand, T., Keller, G. R., Kellogg, J., Kucks, R., Li, X., Mainville, A., Morin, R., Pilk-
 5046 ington, M., Plouff, D., Ravat, D., Roman, D., Urrutia-Fucugauchi, J., ... Winchester, D.
 5047 (2005). New standards for reducing gravity data: The North American gravity database.
 5048 *GEOPHYSICS*, 70(4), J25–J32. <https://doi.org/10.1190/1.1988183> (cit. on p. 91)
- 5049 Hinze, W. J., Von Frese, R., & Saad, A. H. (2013). *Gravity and magnetic exploration: Principles,
 5050 practices, and applications*. Cambridge University Press. (Cit. on p. 91).
- 5051 Hodgson, D. A., Jordan, T. A., De Rydt, J., Fretwell, P. T., Seddon, S. A., Becker, D., Hogan,
 5052 K. A., Smith, A. M., & Vaughan, D. G. (2019). Past and future dynamics of the Brunt Ice
 5053 Shelf from seabed bathymetry and ice shelf geometry. *The Cryosphere*, 13(2), 545–556.
 5054 <https://doi.org/10.5194/tc-13-545-2019> (cit. on pp. 46, 103, 104, 117)
- 5055 Hofmann-Wellenhof, B., & Moritz, H. (2006). *Physical geodesy* (2nd, corrected ed). SpringerWien-
 5056 NewYork. (Cit. on pp. 90, 92).
- 5057 Hofstede, C., Beyer, S., Corr, H., Eisen, O., Hattermann, T., Helm, V., Neckel, N., Smith, E. C.,
 5058 Steinhage, D., Zeising, O., & Humbert, A. (2020). *Subglacial sediment transport upstream
 5059 of a basal channel in the ice shelf of Support Force Glacier (West Antarctica), identified by
 5060 reflection seismics* (Preprint). Ice sheets/Ice Shelf. <https://doi.org/10.5194/tc-2020-54>.
 5061 (Cit. on p. 118)
- 5062 Holland, P. R. (2008). A model of tidally dominated ocean processes near ice shelf grounding
 5063 lines. *Journal of Geophysical Research*, 113(C11), C11002. <https://doi.org/10.1029/2007JC004576> (cit. on pp. 16, 130, 137)
- 5064 Horgan, H. J., Hulbe, C., Alley, R. B., Anandakrishnan, S., Goodsell, B., Taylor-Offord, S., &
 5065 Vaughan, M. J. (2017). Poststagnation Retreat of Kamb Ice Stream's Grounding Zone.
 5066 *Geophysical Research Letters*, 44(19), 9815–9822. <https://doi.org/10.1002/2017GL074986>
 5067 (cit. on pp. 21, 126)
- 5068 Horgan, H. J., Walker, R. T., Anandakrishnan, S., & Alley, R. B. (2011). Surface elevation changes
 5069 at the front of the Ross Ice Shelf: Implications for basal melting. *Journal of Geophysical
 5070 Research*, 116(C2), C02005. <https://doi.org/10.1029/2010JC006192> (cit. on p. 129)
- 5071 Horgan, H. J., Christianson, K., Jacobel, R. W., Anandakrishnan, S., & Alley, R. B. (2013). Sediment
 5072 deposition at the modern grounding zone of Whillans Ice Stream, West Antarctica.
 5073 *Geophysical Research Letters*, 40(15), 3934–3939. <https://doi.org/10.1002/grl.50712> (cit.
 5074 on p. 118)
- 5075 Hoyer, S., & Hamman, J. (2017). Xarray: N-D labeled Arrays and Datasets in Python. *Journal of
 5076 Open Research Software*, 5(1), 10. <https://doi.org/10.5334/jors.148> (cit. on p. 167)
- 5077 IceBridge Sander AIRGrav L1B Geolocated Free Air Gravity Anomalies, Version 1. (2020). (Cit.
 5078 on p. 145).
- 5079 Intergovernmental Panel on Climate Change (IPCC). (2022). *The Ocean and Cryosphere in a
 5080 Changing Climate: Special Report of the Intergovernmental Panel on Climate Change*
 5081 (First). Cambridge University Press. <https://doi.org/10.1017/9781009157964>. (Cit. on
 5082 pp. 15, 133)
- 5083 Jacobs, S., Helmer, H., Doake, C. S. M., Jenkins, A., & Frolich, R. M. (1992). Melting of ice
 5084 shelves and the mass balance of Antarctica. *Journal of Glaciology*, 38(130), 375–387. <https://doi.org/10.3189/S0022143000002252> (cit. on pp. 87, 89)
- 5085 Jacoby, W., & Smilde, P. L. (2009). *Gravity interpretation: Fundamentals and application of gravity
 5086 inversion and geological interpretation ; with CD-ROM*. Springer. (Cit. on pp. 41, 42, 91)
 5087 OCLC: 845389531.
- 5088 Jansen, M. J. W., Rossing, W. A. H., & Daamen, R. A. (1994). Monte Carlo Estimation of Un-
 5089 certainty Contributions from Several Independent Multivariate Sources. In J. Grasman
 5090 & G. van Straten (Eds.), *Predictability and Nonlinear Modelling in Natural Sciences and*
 5091 5092

- 5093 *Economics* (pp. 334–343). Springer Netherlands. https://doi.org/10.1007/978-94-011-0962-8_28. (Cit. on pp. 72, 74, 98, 99)
- 5094 Jenkins, A., Dutrieux, P., Jacobs, S. S., McPhail, S. D., Perrett, J. R., Webb, A. T., & White, D.
- 5095 (2010). Observations beneath Pine Island Glacier in West Antarctica and implications for
- 5096 its retreat. *Nature Geoscience*, 3(7), 468–472. <https://doi.org/10.1038/ngeo890> (cit. on
- 5097 p. 38)
- 5098 Jolie, E., Scott, S., Faulds, J., Chambefort, I., Axelsson, G., Gutiérrez-Negrín, L. C., Regenspurg,
- 5099 S., Ziegler, M., Ayling, B., Richter, A., & Zemedkun, M. T. (2021). Geological controls on
- 5100 geothermal resources for power generation. *Nature Reviews Earth & Environment*, 2(5),
- 5101 324–339. <https://doi.org/10.1038/s43017-021-00154-y> (cit. on pp. 19, 26, 141)
- 5102 Jordan, T. A., Ferraccioli, F., Vaughan, D. G., Holt, J. W., Corr, H., Blankenship, D. D., &
- 5103 Diehl, T. M. (2010). Aerogravity evidence for major crustal thinning under the Pine Island
- 5104 Glacier region (West Antarctica). *Geological Society of America Bulletin*, 122(5-6), 714–
- 5105 726. <https://doi.org/10.1130/B26417.1> (cit. on pp. 78, 85)
- 5106 Jordan, T. A., Riley, T. R., & Siddoway, C. S. (2020a). The geological history and evolution of
- 5107 West Antarctica. *Nature Reviews Earth & Environment*, 1, 117–133. <https://doi.org/10.1038/s43017-019-0013-6> (cit. on pp. 31, 145)
- 5108 Jordan, T. A., Porter, D., Tinto, K., Millan, R., Muto, A., Hogan, K., Larter, R. D., Graham,
- 5109 A. G. C., & Paden, J. D. (2020b). New gravity-derived bathymetry for the Thwaites,
- 5110 Crosson, and Dotson ice shelves revealing two ice shelf populations. *The Cryosphere*, 14(9),
- 5111 2869–2882. <https://doi.org/10.5194/tc-14-2869-2020> (cit. on pp. 102–104, 117)
- 5112 Kachuck, S. B., Martin, D. F., Bassis, J. N., & Price, S. F. (2020). Rapid Viscoelastic Deformation
- 5113 Slows Marine Ice Sheet Instability at Pine Island Glacier. *Geophysical Research Letters*,
- 5114 47(10). <https://doi.org/10.1029/2019GL086446> (cit. on pp. 18, 140)
- 5115 Karner, G. D., Studinger, M., & Bell, R. E. (2005). Gravity anomalies of sedimentary basins and
- 5116 their mechanical implications: Application to the Ross Sea basins, West Antarctica. *Earth*
- 5117 and *Planetary Science Letters*, 235, 577–596. <https://doi.org/10.1016/j.epsl.2005.04.016>
- 5118 (cit. on pp. 26, 28, 143, 149)
- 5119 Kingslake, J., Scherer, R. P., Albrecht, T., Coenen, J., Powell, R. D., Reese, R., Stansell, N. D.,
- 5120 Tulaczyk, S., Wearing, M. G., & Whitehouse, P. L. (2018). Extensive retreat and re-
- 5121 advance of the West Antarctic Ice Sheet during the Holocene. *Nature*, 558(7710), 430–
- 5122 434. <https://doi.org/10.1038/s41586-018-0208-x> (cit. on pp. 33, 129, 141)
- 5123 Kirkpatrick, S., Gelatt, C. D., & Vecchi, M. P. (1983). Optimization by Simulated Annealing.
- 5124 *Science*, 220(4598), 671–680. <https://doi.org/10.1126/science.220.4598.671> (cit. on
- 5125 p. 104)
- 5126 Koch, P., Wujek, B., Golovidov, O., & Gardner, S. (2017). Automated Hyperparameter Tuning for
- 5127 Effective Machine Learning. *SAS Institute Inc.* (cit. on p. 101).
- 5128 Kulhanek, D. K., Levy, R. H., Clowes, C. D., Prebble, J. G., Rodelli, D., Jovane, L., Morgans,
- 5129 H. E., Kraus, C., Zwingmann, H., Griffith, E. M., Scher, H. D., McKay, R. M., & Naish,
- 5130 T. R. (2019). Revised chronostratigraphy of DSDP Site 270 and late Oligocene to early
- 5131 Miocene paleoecology of the Ross Sea sector of Antarctica. *Global and Planetary Change*,
- 5132 178, 46–64. <https://doi.org/10.1016/j.gloplacha.2019.04.002> (cit. on pp. 34, 143)
- 5133 Larour, E., Morlighem, M., Seroussi, H., Schiermeier, J., & Rignot, E. (2012). Ice flow sensitivity to
- 5134 geothermal heat flux of Pine Island Glacier, Antarctica. *Journal of Geophysical Research: Earth Surface*, 117(F04023), 1–12. <https://doi.org/10.1029/2012JF002371> (cit. on p. 140)
- 5135 Le Brocq, A. M., Payne, A. J., & Vieli, A. (2010). An improved Antarctic dataset for high resolution
- 5136 numerical ice sheet models (ALBMAP v1). *Earth System Science Data*, 2(2), 247–260.
- 5137 <https://doi.org/10.5194/essd-2-247-2010> (cit. on pp. 89, 121, 122)
- 5138 Leckie, F. M. (1983). Late Oligocene-early Miocene glacial record of the Ross Sea, Antarctica:
- 5139 Evidence from DSDP Site 270. *Geology*, 11, 578–582. [https://doi.org/10.1130/0091-7613\(1983\)11<578:LOMGRO>2.0.CO;2](https://doi.org/10.1130/0091-7613(1983)11<578:LOMGRO>2.0.CO;2) (cit. on pp. 34, 143)
- 5140 Li, L., Aitken, A., Lindsay, M., & Kulessa, B. (2021). *Subglacial sedimentary basins focus key*
- 5141 *vulnerabilities of the Antarctic ice-sheet* (Preprint). In Review. <https://doi.org/10.21203/rs.3.rs-1117673/v1>. (Cit. on p. 31)
- 5142 Li, L., Aitken, A. R. A., Lindsay, M. D., & Kulessa, B. (2022). Sedimentary basins reduce stability
- 5143 of Antarctic ice streams through groundwater feedbacks. *Nature Geoscience*. <https://doi.org/10.1038/s41561-022-00992-5> (cit. on pp. 19, 141, 152)

- 5150 Li, X., Zattin, M., & Olivetti, V. (2020). Apatite fission track signatures of the Ross Sea ice flows
 5151 during the Last Glacial Maximum. *Geochemistry, Geophysics, Geosystems*, 21(10), 1–21.
 5152 <https://doi.org/10.1029/2019GC008749> (cit. on pp. 33, 144)
- 5153 Li, X., & Götze, H.-J. (2001). Ellipsoid, geoid, gravity, geodesy, and geophysics. *Geophysics*, 66(6),
 5154 1660–1668. <https://doi.org/10.1190/1.1487109> (cit. on pp. 91, 93)
- 5155 Licht, K. J., Hennessy, A. J., & Welke, B. M. (2014). The U-Pb detrital zircon signature of
 5156 West Antarctic ice stream tills in the Ross embayment, with implications for Last Glacial
 5157 Maximum ice flow reconstructions. *Antarctic Science*, 26(6), 687–697. <https://doi.org/10.1017/S0954102014000315> (cit. on pp. 33, 144)
- 5158 Licht, K. J., Lederer, J. R., & Jeffrey Swope, R. (2005). Provenance of LGM glacial till (sand
 5159 fraction) across the Ross embayment, Antarctica. *Quaternary Science Reviews*, 24(12-13),
 5160 1499–1520. <https://doi.org/10.1016/j.quascirev.2004.10.017> (cit. on p. 144)
- 5161 Lindeque, A., Gohl, K., Wobbe, F., & Uenzelmann-Neben, G. (2016). Preglacial to glacial sediment
 5162 thickness grids for the Southern Pacific Margin of West Antarctica: Preglacial, transitional
 5163 and full glacial isopach maps, West Antarctica. *Geochemistry, Geophysics, Geosystems*,
 5164 17(10), 4276–4285. <https://doi.org/10.1002/2016GC006401> (cit. on pp. 151, 153)
- 5165 Lloyd, A. J., Wiens, D. A., Nyblade, A. A., Anandakrishnan, S., Aster, R. C., Huerta, A. D.,
 5166 Wilson, T. J., Dalziel, I. W. D., Shore, P. J., & Zhao, D. (2015). A seismic transect across
 5167 West Antarctica: Evidence for mantle thermal anomalies beneath the Bentley Subglacial
 5168 Trench and the Marie Byrd Land Dome. *Journal of Geophysical Research: Solid Earth*,
 5169 120(12), 8439–8460. <https://doi.org/10.1002/2015JB012455> (cit. on p. 32)
- 5170 Llubes, M., Lanseau, C., & Rémy, F. (2006). Relations between basal condition, subglacial hydro-
 5171 logical networks and geothermal flux in Antarctica. *Earth and Planetary Science Letters*,
 5172 241(3-4), 655–662. <https://doi.org/10.1016/j.epsl.2005.10.040> (cit. on p. 18)
- 5173 Lowry, D. P., Golledge, N. R., Bertler, N. A. N., Jones, R. S., & McKay, R. (2019). Deglacial
 5174 grounding-line retreat in the Ross Embayment, Antarctica, controlled by ocean and atmo-
 5175 sphere forcing. *Science Advances*, 5, 1–12. <https://doi.org/10.1126/sciadv.aav8754> (cit. on
 5176 pp. 20, 33, 88, 129, 133)
- 5177 Lowry, D. P., Golledge, N. R., Bertler, N. A., Jones, R. S., McKay, R., & Stutz, J. (2020). Geo-
 5178 logic controls on ice sheet sensitivity to deglacial climate forcing in the Ross Embayment,
 5179 Antarctica. *Quaternary Science Advances*, 1, 1–17. <https://doi.org/10.1016/j.qsa.2020.100002> (cit. on pp. 33, 141)
- 5180 Luyendyk, B., Sorlien, C. C., Wilson, D. S., Bartek, L. R., & Siddoway, C. S. (2001). Structural
 5181 and tectonic evolution of the Ross Sea rift in the Cape Colbeck region, Eastern Ross Sea,
 5182 Antarctica. *Tectonics*, 20(6), 933–958. <https://doi.org/10.1029/2000TC001260> (cit. on
 5183 p. 30)
- 5184 Luyendyk, B., Wilson, D. S., & Siddoway, C. S. (2003). Eastern margin of the Ross Sea Rift in
 5185 western Marie Byrd Land, Antarctica: Crustal structure and tectonic development. *Geo-
 5186 chemistry, Geophysics, Geosystems*, 4(10), 1–25. <https://doi.org/10.1029/2002GC000462>
 5187 (cit. on p. 26)
- 5188 Martins, C. M., Barbosa, V. C., & Silva, J. B. (2010). Simultaneous 3D depth-to-basement and
 5189 density-contrast estimates using gravity data and depth control at few points. *GEO-
 5190 PHYSICS*, 75(3), I21–I28. <https://doi.org/10.1190/1.3380225> (cit. on p. 103)
- 5191 Matsuoka, K., Hindmarsh, R. C., Moholdt, G., Bentley, M. J., Pritchard, H. D., Brown, J., Con-
 5192 way, H., Drews, R., Durand, G., Goldberg, D., Hattermann, T., Kingslake, J., Lenaerts,
 5193 J. T., Martín, C., Mulvaney, R., Nicholls, K. W., Pattyn, F., Ross, N., Scambos, T., &
 5194 Whitehouse, P. L. (2015). Antarctic ice rises and ripples: Their properties and signifi-
 5195 cance for ice-sheet dynamics and evolution. *Earth-Science Reviews*, 150, 724–745. <https://doi.org/10.1016/j.earscirev.2015.09.004> (cit. on pp. 16, 88)
- 5196 McCubbine, J. (2016). *Airborne Gravity Across New Zealand - For An Improved Vertical Datum*
 5197 (Doctoral dissertation). Victoria University of Wellington. (Cit. on pp. 46, 47).
- 5198 McKay, R., Golledge, N., Maas, S., Naish, T., Levy, R., Dunbar, G., & Kuhn, G. (2016). Antarctic
 5199 marine ice-sheet retreat in the Ross Sea during the early Holocene. *Geology*, 44(1), 7–10.
 5200 <https://doi.org/10.1130/G37315.1> (cit. on p. 141)
- 5201 Menke, W. (2012). *Geophysical data analysis: Discrete inverse theory* (Matlab ed., 3rd ed). Academic Press. (Cit. on p. 39).
- 5202 Millan, R., Rignot, E., Mouginot, J., Wood, M., Bjørk, A. A., & Morlighem, M. (2018). Vulner-
 5203 ability of Southeast Greenland Glaciers to Warm Atlantic Water From Operation Ice-

- 5208 Bridge and Ocean Melting Greenland Data. *Geophysical Research Letters*, 45(6), 2688–
 5209 2696. <https://doi.org/10.1002/2017GL076561> (cit. on pp. 103, 104, 117)
- 5210 Millan, R., Rignot, E., Bernier, V., Morlighem, M., & Dutrieux, P. (2017). Bathymetry of the
 5211 Amundsen Sea Embayment sector of West Antarctica from Operation IceBridge gravity
 5212 and other data. *Geophysical Research Letters*, 44(3), 1360–1368. <https://doi.org/10.1002/2016GL072071> (cit. on pp. 102–104, 117, 145)
- 5214 Millan, R., St-Laurent, P., Rignot, E., Morlighem, M., Mouginot, J., & Scheuchl, B. (2020). Con-
 5215 straining an Ocean Model Under Getz Ice Shelf, Antarctica, Using A Gravity-Derived
 5216 Bathymetry. *Geophysical Research Letters*, 47(13). <https://doi.org/10.1029/2019GL086522>
 5217 (cit. on pp. 46, 62, 63, 102–104, 117, 120, 145)
- 5218 Moholdt, G., Padman, L., & Fricker, H. A. (2014). Basal mass budget of Ross and Filchner-Ronne
 5219 ice shelves, Antarctica, derived from Lagrangian analysis of ICESat altimetry: Ice shelf
 5220 basal melting from altimetry. *Journal of Geophysical Research: Earth Surface*, 119(11),
 5221 2361–2380. <https://doi.org/10.1002/2014JF003171> (cit. on pp. 20, 88, 129, 133)
- 5222 Mooney, W. D., Laske, G., & Masters, T. G. (1998). CRUST 5.1: A global crustal model at 5° ×
 5223 5°. *Journal of Geophysical Research: Solid Earth*, 103(B1), 727–747. <https://doi.org/10.1029/97JB02122> (cit. on p. 151)
- 5225 Morlighem, M. (2022). MEaSUREs BedMachine Antarctica, Version 3. (Cit. on pp. 38, 89, 105–
 5226 107, 110–112, 115, 116, 121, 123, 125, 128, 142)
 5227 <https://doi.org/10.5067/FPSU0V1MWUB6>.
- 5228 Morlighem, M., Rignot, E., Binder, T., Blankenship, D., Drews, R., Eagles, G., Eisen, O., Ferraci-
 5229 cioli, F., Forsberg, R., Fretwell, P., Goel, V., Greenbaum, J. S., Gudmundsson, H., Guo,
 5230 J., Helm, V., Hofstede, C., Howat, I., Humbert, A., Jokat, W., ... Young, D. A. (2020). Deep
 5231 glacial troughs and stabilizing ridges unveiled beneath the margins of the Antarctic
 5232 ice sheet. *Nature Geoscience*, 13(2), 132–137. <https://doi.org/10.1038/s41561-019-0510-8>
 5233 (cit. on pp. 18, 27, 28, 32, 38, 68, 89, 105–107, 110–112, 115, 121, 142, 151, 153)
 5234 BedMachine
- 5235 Mouginot, J., Rignot, E., & Scheuchl, B. (2019). Continent-wide, interferometric SAR phase, map-
 5236 ping of Antarctic ice velocity. *Geophysical Research Letters*, 46(16), 9710–9718. <https://doi.org/10.1029/2019GL083826> (cit. on p. 32)
- 5238 Mouginot, J., Scheuchl, B., & Rignot, E. (2017). MEaSUREs Antarctic Boundaries for IPY 2007–
 5239 2009 from Satellite Radar, Version 2. (Cit. on pp. 88, 106–108, 125, 129, 135)
 5240 <https://doi.org/10.5067/AXE4121732AD>.
- 5241 Müller, R. D., Gohl, K., Cande, S. C., Goncharov, A., & Golynsky, A. V. (2007). Eocene to Miocene
 5242 geometry of the West Antarctic Rift System. *Australian Journal of Earth Sciences*, 54(8),
 5243 1033–1045. <https://doi.org/10.1080/08120090701615691> (cit. on pp. 29, 151)
- 5244 Muto, A., Anandakrishnan, S., & Alley, R. B. (2013a). Subglacial bathymetry and sediment layer
 5245 distribution beneath the Pine Island Glacier ice shelf, West Antarctica, modeled using
 5246 aerogravity and autonomous underwater vehicle data. *Annals of Glaciology*, 54(64), 27–
 5247 32. <https://doi.org/10.3189/2013AoG64A110> (cit. on pp. 102, 104, 145)
- 5248 Muto, A., Christianson, K., Horgan, H. J., Anandakrishnan, S., & Alley, R. B. (2013b). Bathymetry
 5249 and geological structures beneath the Ross Ice Shelf at the mouth of Whillans Ice Stream,
 5250 West Antarctica, modeled from ground-based gravity measurements. *Journal of Geophys-
 5251 ical Research: Solid Earth*, 118(8), 4535–4546. <https://doi.org/10.1002/jgrb.50315> (cit. on
 5252 pp. 21, 32, 103, 127, 130, 131)
- 5253 Muto, A., Peters, L. E., Gohl, K., Sasgen, I., Alley, R. B., Anandakrishnan, S., & Riverman, K. L.
 5254 (2016). Subglacial bathymetry and sediment distribution beneath Pine Island Glacier ice
 5255 shelf modeled using aerogravity and in situ geophysical data: New results. *Earth and
 5256 Planetary Science Letters*, 433, 63–75. <https://doi.org/10.1016/j.epsl.2015.10.037> (cit. on
 5257 pp. 46, 103, 104, 145)
- 5258 Nagy, D., Papp, G., & Benedek, J. (2000). The gravitational potential and its derivatives for the
 5259 prism. *Journal of Geodesy*, 74(7–8), 552–560. <https://doi.org/10.1007/s001900000116>
 5260 (cit. on pp. 42, 46, 48, 94)
- 5261 Naish, T., Powell, R., Levy, R., Wilson, G., Scherer, R., Talarico, F., Krissek, L., Niessen, F.,
 5262 Pompilio, M., Wilson, T., Carter, L., DeConto, R., Huybers, P., McKay, R., Pollard,
 5263 D., Ross, J., Winter, D., Barrett, P., Browne, G., ... Williams, T. (2009). Obliquity-
 5264 paced Pliocene West Antarctic ice sheet oscillations. *Nature*, 458(7236), 322–328. <https://doi.org/10.1038/nature07867> (cit. on pp. 20, 88, 133)

- 5266 Nerem, R. S., Beckley, B. D., Fasullo, J. T., Hamilton, B. D., Masters, D., & Mitchum, G. T. (2018).
 5267 Climate-change-driven accelerated sea-level rise detected in the altimeter era. *Proceedings*
 5268 *of the National Academy of Sciences*, 115(9), 2022–2025. <https://doi.org/10.1073/pnas.1717312115> (cit. on p. 15)
- 5269 Neuhaus, S. U., Tulaczyk, S. M., Stansell, N. D., Coenen, J. J., Scherer, R. P., Mikucki, J. A., &
 5270 Powell, R. D. (2021). Did Holocene climate changes drive West Antarctic grounding line
 5271 retreat and readvance? *The Cryosphere*, 15(10), 4655–4673. <https://doi.org/10.5194/tc-15-4655-2021> (cit. on p. 33)
- 5271 Nicholls, K. W., Abrahamsen, E. P., Buck, J. J. H., Dodd, P. A., Goldblatt, C., Griffiths, G.,
 5272 Heywood, K. J., Hughes, N. E., Kaletzky, A., Lane-Serff, G. F., McPhail, S. D., Millard,
 5273 N. W., Oliver, K. I. C., Perrett, J., Price, M. R., Pudsey, C. J., Saw, K., Stansfield, K.,
 5274 Stott, M. J., ... Wilkinson, J. P. (2006). Measurements beneath an Antarctic ice shelf
 5275 using an autonomous underwater vehicle. *Geophysical Research Letters*, 33(8), L08612.
 5276 <https://doi.org/10.1029/2006GL025998> (cit. on p. 18)
- 5277 Oldenburg, D. W. (1974). The inversion and interpretation of gravity anomalies. *Geophysics*, 39(4),
 5278 526–536 (cit. on p. 104).
- 5279 Oldenburg, D. W., & Li, Y. (2005). Inversion for applied geophysics: A tutorial. In D. K. Butler
 5280 (Ed.), *Near-Surface Geophysics*. Society of Exploration Geophysicists. <https://doi.org/10.1190/1.9781560801719>. (Cit. on pp. 39, 100)
- 5281 Oldenburg, D. W., & Pratt, D. (2007). Geophysical inversion for mineral exploration: A decade
 5282 of progress in theory and practice. In B. Milkereit (Ed.), *Proceedings of Exploration 07*
 5283 (pp. 61–95). (Cit. on p. 42).
- 5284 Oliveira, V. C., & Uieda, L. (2014). Tópicos de inversão em geofísica. *figshare*. <https://doi.org/http://dx.doi.org/10.6084/m9.figshare.1192984> (cit. on p. 40)
- 5285 Oliveira, V. C., Uieda, L., & Hallam, K. A. T. (2018). Should geophysicists use the gravity distur-
 5286 bance or the anomaly?, 11. <https://doi.org/10.5281/zenodo.1255305> (cit. on p. 92)
- 5287 Olivetti, V., Balestrieri, M. L., Chew, D., Zurli, L., Zattin, M., Pace, D., Drakou, F., Cornamusini,
 5288 G., & Perotti, M. (2023). Ice volume variations and provenance trends in the Oligocene-
 5289 early Miocene glaciomarine sediments of the Central Ross Sea, Antarctica (DSDP Site 270).
 5290 *Global and Planetary Change*, 104042. <https://doi.org/10.1016/j.gloplacha.2023.104042>
 5291 (cit. on pp. 143, 144)
- 5292 Otosaka, I. N., Shepherd, A., Ivins, E. R., Schlegel, N.-J., Amory, C., van den Broeke, M. R.,
 5293 Horwath, M., Joughin, I., King, M. D., Krinner, G., Nowicki, S., Payne, A. J., Rignot, E.,
 5294 Scambos, T., Simon, K. M., Smith, B. E., Sørensen, L. S., Velicogna, I., Whitehouse, P. L.,
 5295 ... Wouters, B. (2023). Mass balance of the Greenland and Antarctic ice sheets from 1992
 5296 to 2020. *Earth System Science Data*, 15(4), 1597–1616. <https://doi.org/10.5194/essd-15-1597-2023> (cit. on pp. 15, 16)
- 5297 Paige, C. C., & Saunders, M. A. (1982). LSQR: An Algorithm for Sparse Linear Equations and
 5298 Sparse Least Squares. *ACM Transactions on Mathematical Software*, 8(1), 43–71. <https://doi.org/10.1145/355984.355989> (cit. on p. 48)
- 5299 Pappa, F., Ebbing, J., & Ferraccioli, F. (2019). Moho Depths of Antarctica: Comparison of Seismic,
 5300 Gravity, and Isostatic Results. *Geochemistry, Geophysics, Geosystems*, 20(3), 1629–1645.
 5301 <https://doi.org/10.1029/2018GC008111> (cit. on pp. 103, 139)
- 5302 Parker, R. L. (1972). The Rapid Calculation of Potential Anomalies. *Geophysical Journal International*, 31(4), 447–455. <https://doi.org/10.1111/j.1365-246X.1973.tb06513.x> (cit. on
 5303 p. 104)
- 5304 Patterson, M. O., Levy, R. H., Kulhanek, D. K., van de Flierdt, T., Horgan, H., Dunbar, G. B.,
 5305 Naish, T. R., Ash, J., Pyne, A., Mandeno, D., Winberry, P., Harwood, D. M., Florindo,
 5306 F., Jimenez-Espejo, F. J., Läufer, A., Yoo, K.-C., Seki, O., Stocchi, P., Klages, J. P., ...
 5307 the SWAIS 2C Science Team. (2022). Sensitivity of the West Antarctic Ice Sheet to +2
 5308 °C (SWAIS 2C). *Scientific Drilling*, 30, 101–112. <https://doi.org/10.5194/sd-30-101-2022>
 5309 (cit. on pp. 18, 21)
- 5310 Paulsen, T., Encarnación, J., & Grunow, A. (2004). Structure and timing of transpressional defor-
 5311 mation in the Shackleton Glacier area, Ross orogen, Antarctica. *Journal of the Geological
 5312 Society*, 161(6), 1027–1038. <https://doi.org/10.1144/0016-764903-040> (cit. on p. 34)
- 5313 Paxman, G. J. G., Jamieson, S. S., Hochmuth, K., Gohl, K., Bentley, M. J., Leitchenkov, G., &
 5314 Ferraccioli, F. (2019). Reconstructions of Antarctic topography since the Eocene–Oligocene
 5315 boundary. *Palaeogeography, Palaeoclimatology, Palaeoecology*, 535, 109346. <https://doi.org/10.1016/j.palaeo.2019.109346> (cit. on pp. 26, 34, 143, 151)

- 5325 Pekar, S. F., DeConto, R. M., & Harwood, D. M. (2006). Resolving a late Oligocene conundrum:
 5326 Deep-sea warming and Antarctic glaciation. *Palaeogeography, Palaeoclimatology, Palaeoecology*, 231, 29–40. <https://doi.org/10.1016/j.palaeo.2005.07.024> (cit. on p. 34)
- 5328 Peltier, W. R., Wu, P. P.-C., Argus, D. F., Li, T., & Velay-Vitow, J. (2022). Glacial isostatic
 5329 adjustment: Physical models and observational constraints. *Reports on Progress in Physics*,
 5330 85(9), 096801. <https://doi.org/10.1088/1361-6633/ac805b> (cit. on pp. 19, 139)
- 5331 Pérez, F., & Granger, B. E. (2007). IPython: A system for interactive scientific computing. *Com-
 5332 puting in Science and Engineering*, 9(3), 21–29. <https://doi.org/10.1109/MCSE.2007.53>
 5333 (cit. on p. 51)
- 5334 Pérez, L. F., De Santis, L., McKay, R. M., Larter, R. D., Ash, J., Bart, P. J., Böhm, G., Brancatelli,
 5335 G., Browne, I., Colleoni, F., Dodd, J. P., Geletti, R., Harwood, D. M., Kuhn, G., Sverre
 5336 Laberg, J., Leckie, R. M., Levy, R. H., Marschalek, J., Mateo, Z., ... 374 Scientists,
 5337 I. O. D. P. E. (2021). Early and middle Miocene ice sheet dynamics in the Ross Sea: Results
 5338 from integrated core-log-seismic interpretation. *GSA Bulletin*. <https://doi.org/10.1130/B35814.1> (cit. on p. 26)
- 5340 Perozzi, L., Guglielmetti, L., & Moscariello, A. (2021). Quantitative uncertainty analysis of gravity
 5341 disturbance. The case of the Geneva Basin (Switzerland). *Journal of Applied Geophysics*,
 5342 193, 104431. <https://doi.org/10.1016/j.jappgeo.2021.104431> (cit. on p. 85)
- 5343 Phillips, G., & Läufer, A. (2009). Brittle deformation relating to the Carboniferous–Cretaceous
 5344 evolution of the Lambert Graben, East Antarctica: A precursor for Cenozoic relief develop-
 5345 ment in an intraplate and glaciated region. *Tectonophysics*, 471(3-4), 216–224. <https://doi.org/10.1016/j.tecto.2009.02.012> (cit. on p. 33)
- 5347 Pollard, D., DeConto, R. M., & Nyblade, A. A. (2005). Sensitivity of Cenozoic Antarctic ice sheet
 5348 variations to geothermal heat flux. *Global and Planetary Change*, 49(1-2), 63–74. <https://doi.org/10.1016/j.gloplacha.2005.05.003> (cit. on pp. 18, 140)
- 5350 Pritchard, H. D., Ligtenberg, S. R. M., Fricker, H. A., Vaughan, D. G., van den Broeke, M. R., &
 5351 Padman, L. (2012). Antarctic ice-sheet loss driven by basal melting of ice shelves. *Nature*,
 5352 484(7395), 502–505. <https://doi.org/10.1038/nature10968> (cit. on pp. 38, 88)
- 5353 Rashidifard, M., Giraud, J., Lindsay, M., Jessell, M., & Ogarko, V. (2021). Constraining 3D geo-
 5354 metric gravity inversion with a 2D reflection seismic profile using a generalized level
 5355 set approach: Application to the eastern Yilgarn Craton. *Solid Earth*, 12(10), 2387–2406.
 5356 <https://doi.org/10.5194/se-12-2387-2021> (cit. on p. 54)
- 5357 Ravier, E., & Buoncristiani, J.-F. (2018). Glaciohydrogeology. In *Past Glacial Environments* (pp. 431–
 5358 466). Elsevier. <https://doi.org/10.1016/B978-0-08-100524-8.00013-0>. (Cit. on pp. 19, 33)
- 5359 Rignot, E., Jacobs, S., Mouginot, J., & Scheuchl, B. (2013). Ice-Shelf Melting Around Antarctica.
 5360 *Science*, 341(6143), 266–270. <https://doi.org/10.1126/science.1235798> (cit. on pp. 16, 20,
 5361 27, 87, 88, 106, 133, 153, 156)
- 5362 Rignot, E., Mouginot, J., & Scheuchl, B. (2011). Antarctic grounding line mapping from differential
 5363 satellite radar interferometry. *Geophysical Research Letters*, 38, 1–6. <https://doi.org/10.1029/2011GL047109> (cit. on pp. 20, 133)
- 5365 Rignot, E., Mouginot, J., Scheuchl, B., van den Broeke, M., van Wessem, M. J., & Morlighem, M.
 5366 (2019). Four decades of Antarctic Ice Sheet mass balance from 1979–2017. *Proceedings of
 5367 the National Academy of Sciences*, 116(4), 1095–1103. <https://doi.org/10.1073/pnas.1812883116> (cit. on p. 38)
- 5369 Robertson, J. D., & Bentley, C. R. (1989). The Ross Ice Shelf: Glaciology and geophysics paper
 5370 3: Seismic studies on the grid western half of the Ross Ice Shelf: RIGGS I and RIGGS II.
 5371 In C. R. Bentley & D. E. Hayes (Eds.), *Antarctic Research Series* (pp. 55–86). American
 5372 Geophysical Union. <https://doi.org/10.1029/AR042p0055>. (Cit. on p. 152)
- 5373 Rooney, S. T., Blankenship, D. D., & Bentley, C. R. (1987). Seismic refraction measurements of
 5374 crustal structure in West Antarctica. In G. D. McKenzie (Ed.), *Geophysical Monograph Series*
 5375 (pp. 1–7). American Geophysical Union. <https://doi.org/10.1029/GM040p0001>.
 5376 (Cit. on p. 152)
- 5377 Rosier, S. H. R., Hofstede, C., Brisbourne, A. M., Hattermann, T., Nicholls, K. W., Davis, P. E. D.,
 5378 Anker, P. G. D., Hillenbrand, C.-D., Smith, A. M., & Corr, H. F. J. (2018). A New
 5379 Bathymetry for the Southeastern Filchner-Ronne Ice Shelf: Implications for Modern Oceanographic
 5380 Processes and Glacial History. *Journal of Geophysical Research: Oceans*, 123(7),
 5381 4610–4623. <https://doi.org/10.1029/2018JC013982> (cit. on p. 145)
- 5382 Roy, L., Sen, M. K., Blankenship, D. D., Stoffa, P. L., & Richter, T. G. (2005). Inversion and
 5383 uncertainty estimation of gravity data using simulated annealing: An application over Lake

- 5384 Vostok, East Antarctica. *Geophysics*, 70(1), J1–J12. <https://doi.org/10.1190/1.1852777>
 5385 (cit. on p. 104)
- 5386 Salvini, F., Brancolini, G., Busetti, M., Storti, F., Mazzarini, F., & Coren, F. (1997). Cenozoic
 5387 geodynamics of the Ross Sea region, Antarctica: Crustal extension, intraplate strike-slip
 5388 faulting, and tectonic inheritance. *Journal of Geophysical Research: Solid Earth*, 102(B11),
 5389 24669–24696. <https://doi.org/10.1029/97JB01643> (cit. on pp. 30, 31)
- 5390 Sandwell, D. T. (1987). Biharmonic spline interpolation of GEOS-3 and SEASAT altimeter data.
 5391 *Geophysical Research Letters*, 14(2), 139–142. <https://doi.org/10.1029/GL014i002p00139>
 5392 (cit. on pp. 62, 63, 98, 106)
- 5393 Santos, D. F., Silva, J. B. C., Martins, C. M., dos Santos, R. D. C. S., Ramos, L. C., & de
 5394 Araújo, A. C. M. (2015). Efficient gravity inversion of discontinuous basement relief. *GEO-
 5395 PHYSICS*, 80(4), G95–G106. <https://doi.org/10.1190/geo2014-0513.1> (cit. on pp. 42,
 5396 103)
- 5397 Sauli, C., Sorlien, C., Busetti, M., De Santis, L., Geletti, R., Wardell, N., & Luyendyk, B. P. (2021).
 5398 Neogene development of the Terror Rift, western Ross Sea, Antarctica. *Geochemistry,
 5399 Geophysics, Geosystems*, 22(3). <https://doi.org/10.1029/2020GC009076> (cit. on pp. 30,
 5400 31)
- 5401 Scambos, T. A., Bohlander, J., Shuman, C., & Skvarca, P. (2004). Glacier acceleration and thin-
 5402 ning after ice shelf collapse in the Larsen B embayment, Antarctica. *Geophysical Research
 5403 Letters*, 31(18), L18402. <https://doi.org/10.1029/2004GL020670> (cit. on p. 88)
- 5404 Scambos, T., Haran, T., Fahnestock, M., Painter, T., & Bohlander, J. (2007). MODIS-based Mosaic
 5405 of Antarctica (MOA) data sets: Continent-wide surface morphology and snow grain size.
 5406 *Remote Sensing of Environment*, 111(2-3), 242–257. <https://doi.org/10.1016/j.rse.2006.12.020>
 5407 (cit. on pp. 27, 88, 111, 115, 116, 123, 128, 129, 135)
- 5408 Scheinert, M., Ferraccioli, F., Schwabe, J., Bell, R., Studinger, M., Damaske, D., Jokat, W.,
 5409 Aleshkova, N., Jordan, T., Leitchenkov, G., Blankenship, D. D., Damiani, T. M., Young,
 5410 D., Cochran, J. R., & Richter, T. D. (2016). New Antarctic gravity anomaly grid for
 5411 enhanced geodetic and geophysical studies in Antarctica. *Geophysical Research Letters*,
 5412 43(2), 600–610. <https://doi.org/10.1002/2015GL067439> (cit. on p. 145)
- 5413 Schlegel, N.-J., Seroussi, H., Schodlok, M. P., Larour, E. Y., Boening, C., Limonadi, D., Watkins,
 5414 M. M., Morlighem, M., & van den Broeke, M. R. (2018). Exploration of Antarctic Ice Sheet
 5415 100-year contribution to sea level rise and associated model uncertainties using the ISSM
 5416 framework. *The Cryosphere*, 12(11), 3511–3534. <https://doi.org/10.5194/tc-12-3511-2018>
 5417 (cit. on p. 15)
- 5418 Schnaidt, S., & Heinson, G. (2015). Bootstrap resampling as a tool for uncertainty analysis in 2-D
 5419 magnetotelluric inversion modelling. *Geophysical Journal International*, 203(1), 92–106.
 5420 <https://doi.org/10.1093/gji/ggv264> (cit. on pp. 73, 99)
- 5421 Schön, J. H. (2015). Density. In *Developments in Petroleum Science* (pp. 109–118). Elsevier. <https://doi.org/10.1016/B978-0-08-100404-3.00004-4>. (Cit. on pp. 110, 113, 126)
- 5422 Seroussi, H., Ivins, E. R., Wiens, D. A., & Bondzio, J. (2017). Influence of a West Antarctic mantle
 5423 plume on ice sheet basal conditions. *Journal of Geophysical Research: Solid Earth*, 122(9),
 5424 7127–7155. <https://doi.org/10.1002/2017JB014423> (cit. on p. 140)
- 5425 Shen, W., Wiens, D. A., Anandakrishnan, S., Aster, R. C., Gerstoft, P., Bromirski, P. D., Hansen,
 5426 S. E., Dalziel, I. W. D., Heeszel, D. S., Huerta, A. D., Nyblade, A. A., Stephen, R., Wilson,
 5427 T. J., & Winberry, J. P. (2018a). The crust and upper mantle structure of Central and
 5428 West Antarctica from bayesian inversion of Rayleigh wave and receiver functions. *Journal
 5429 of Geophysical Research: Solid Earth*, 123(9), 7824–7849. <https://doi.org/10.1029/2017JB015346>
 5430 (cit. on pp. 32, 35)
- 5431 Shen, W., Wiens, D. A., Lloyd, A. J., & Nyblade, A. A. (2020). A geothermal heat flux map
 5432 of Antarctica empirically constrained by seismic structure. *Geophysical Research Letters*,
 5433 47(14). <https://doi.org/10.1029/2020GL086955> (cit. on pp. 135, 141)
- 5434 Shen, W., Wiens, D. A., Stern, T., Anandakrishnan, S., Aster, R. C., Dalziel, I., Hansen, S., Heeszel,
 5435 D. S., Huerta, A., Nyblade, A., Wilson, T. J., & Winberry, J. P. (2018b). Seismic evidence
 5436 for lithospheric foundering beneath the southern Transantarctic Mountains, Antarctica.
 5437 *Geology*, 46(1), 71–74. <https://doi.org/10.1130/G39555.1> (cit. on p. 32)
- 5438 Shipp, S., Anderson, J., & Domack, E. (1999). Late Pleistocene-Holocene retreat of the West
 5439 Antarctic Ice-Sheet system in the Ross Sea: Part 1 - Geophysical results. *Geological Society
 5440 of America Bulletin*, 111(10), 32. <https://doi.org/10.1130/0016-7606%281999%29111%3C1486%3ALPHROT%3E2.3.CO%3B2> (cit. on p. 16)

- 5443 Siddoway, C. S. (2008). Tectonics of the West Antarctic Rift System: New light on the history
 5444 and dynamics of distributed intracontinental extension. In A. K. Cooper, P. J. Barrett, H.
 5445 Stagg, B. C. Storey, W. Stump, W. Wise, & 10th ISAES editorial team (Eds.), *Antarctica:
 5446 A Keystone in a Changing World*. The National Academies Press. <https://doi.org/10.3133/ofr20071047KP09>. (Cit. on p. 30)
- 5448 Siegert, M. J., Kulessa, B., Bougamont, M., Christoffersen, P., Key, K., Andersen, K. R., Booth,
 5449 A. D., & Smith, A. M. (2018). Antarctic subglacial groundwater: A concept paper on
 5450 its measurement and potential influence on ice flow. *Geological Society, London, Special
 5451 Publications*, 461(1), 197–213. <https://doi.org/10.1144/SP461.8> (cit. on p. 26)
- 5452 Siegert, M. J., Taylor, J., Payne, A. J., & Hubbard, B. (2004). Macro-scale bed roughness of the
 5453 simple coast ice streams in West Antarctica. *Earth Surface Processes and Landforms*, 29(13),
 5454 1591–1596. <https://doi.org/10.1002/esp.1100> (cit. on p. 20)
- 5455 Slater, T., & Shepherd, A. (2018). Antarctic ice losses tracking high. *Nature Climate Change*,
 5456 8(12), 1025–1026. <https://doi.org/10.1038/s41558-018-0284-9> (cit. on p. 15)
- 5457 Smith, B., Fricker, H. A., Gardner, A. S., Medley, B., Nilsson, J., Paolo, F. S., Holschuh, N.,
 5458 Adusumilli, S., Brunt, K., Csatho, B., Harbeck, K., Markus, T., Neumann, T., Siegfried,
 5459 M. R., & Zwally, H. J. (2020a). Pervasive ice sheet mass loss reflects competing ocean and
 5460 atmosphere processes. *Science*, eaaz5845. <https://doi.org/10.1126/science.aaz5845> (cit. on
 5461 p. 38)
- 5462 Smith, E. C., Hattermann, T., Kuhn, G., Gaedicke, C., Berger, S., Drews, R., Ehlers, T. A.,
 5463 Franke, D., Gromig, R., Hofstede, C., Lambrecht, A., Läufer, A., Mayer, C., Tiedemann,
 5464 R., Wilhelms, F., & Eisen, O. (2020b). Detailed Seismic Bathymetry Beneath Ekström Ice
 5465 Shelf, Antarctica: Implications for Glacial History and Ice-Ocean Interaction. *Geophysical
 5466 Research Letters*, 47(10). <https://doi.org/10.1029/2019GL086187> (cit. on p. 118)
- 5467 Smith, W. H. F., & Wessel, P. (1990). Gridding with continuous curvature splines in tension.
 5468 *GEOPHYSICS*, 55(3), 293–305. <https://doi.org/10.1190/1.1442837> (cit. on pp. 61, 62,
 5469 96, 98, 106, 119, 151)
- 5470 Soler, S. R., & Uieda, L. (2021). Gradient-boosted equivalent sources. *Geophysical Journal International*,
 5471 227(3), 1768–1783. <https://doi.org/10.1093/gji/ggab297> (cit. on pp. 50, 56, 61,
 5472 109)
- 5473 Sorlien, C. C., Luyendyk, B., Wilson, D. S., Decesari, R. C., Bartek, L. R., & Diebold, J. B.
 5474 (2007). Oligocene development of the West Antarctic Ice Sheet recorded in eastern Ross
 5475 Sea strata. *Geology*, 35(5), 467. <https://doi.org/10.1130/G23387A.1> (cit. on p. 26)
- 5476 Spector, P., Stone, J., Cowdery, S. G., Hall, B., Conway, H., & Bromley, G. (2017). Rapid early-
 5477 Holocene deglaciation in the Ross Sea, Antarctica. *Geophysical Research Letters*, 44(15),
 5478 7817–7825. <https://doi.org/10.1002/2017GL074216> (cit. on p. 88)
- 5479 Steffen, H., Olesen, O., & Sutinen, R. (2021). Glacially Triggered Faulting: A Historical Overview
 5480 and Recent Developments. In H. Steffen, O. Olesen, & R. Sutinen (Eds.), *Glacially-
 5481 Triggered Faulting* (First, pp. 3–19). Cambridge University Press. <https://doi.org/10.1017/9781108779906.003>. (Cit. on pp. 19, 139)
- 5483 Stern, T. A., Davey, F. J., & Delisle, G. (1991). Lithospheric flexure induced by the load of the
 5484 Ross Archipelago, southern Victoria land, Antarctica. In M. Thomson, A. Crame, & J.
 5485 Thomson (Eds.), *Geological Evolution of Antarctica* (pp. 323–328). Cambridge University
 5486 Press. (Cit. on p. 31).
- 5487 Stern, T. A., Ten Brink, U. S., Beaudoin, B. C., & Bannister, S. (1994). Seismic Reflection Experiments
 5488 on the Ross Ice Shelf: 1985–1991. *Terra Antarctica*, 1(3), 513–516 (cit. on p. 21).
- 5489 Stern, T. A., & ten Brink, U. S. (1989). Flexural uplift of the Transantarctic Mountains. *Journal
 5490 of Geophysical Research: Solid Earth*, 94(B8), 10315–10330. <https://doi.org/10.1029/JB094iB08p10315> (cit. on p. 130)
- 5492 Stevens, C., Hulbe, C., Brewer, M., Stewart, C., Robinson, N., Ohneiser, C., & Jendersie, S. (2020).
 5493 Ocean mixing and heat transport processes observed under the Ross Ice Shelf control its
 5494 basal melting. *Proceedings of the National Academy of Sciences*, 117(29), 16799–16804.
 5495 <https://doi.org/10.1073/pnas.1910760117> (cit. on p. 89)
- 5496 Still, H., Campbell, A., & Hulbe, C. (2019). Mechanical analysis of pinning points in the Ross Ice
 5497 Shelf, Antarctica. *Annals of Glaciology*, 60(78), 32–41. <https://doi.org/10.1017/aog.2018.31> (cit. on pp. 20, 26, 33, 89, 128, 138, 139)
- 5499 Still, H., & Hulbe, C. (2021). Mechanics and dynamics of pinning points on the Shirase Coast,
 5500 West Antarctica. *The Cryosphere*, 15(6), 19. <https://doi.org/10.5194/tc-15-2647-2021>
 5501 (cit. on p. 138)

- 5502 St-Laurent, P., Klinck, J. M., & Dinniman, M. S. (2013). On the Role of Coastal Troughs in the
 5503 Circulation of Warm Circumpolar Deep Water on Antarctic Shelves. *Journal of Physical*
 5504 *Oceanography*, 43(1), 51–64. <https://doi.org/10.1175/JPO-D-11-0237.1> (cit. on p. 38)
- 5505 Studinger, M., Bell, R., Fitzgerald, P., & Buck, W. (2006). Crustal architecture of the Transantarctic
 5506 Mountains between the Scott and Reedy Glacier region and South Pole from aerogeophysical data.
 5507 *Earth and Planetary Science Letters*, 250(1-2), 182–199. <https://doi.org/10.1016/j.epsl.2006.07.035> (cit. on p. 34)
- 5509 Studinger, M., Bell, R. E., Buck, W., Karner, G. D., & Blankenship, D. D. (2004a). Sub-ice geology
 5510 inland of the Transantarctic Mountains in light of new aerogeophysical data. *Earth and*
 5511 *Planetary Science Letters*, 220(3-4), 391–408. [https://doi.org/10.1016/S0012-821X\(04\)00066-4](https://doi.org/10.1016/S0012-821X(04)00066-4) (cit. on pp. 28, 149)
- 5513 Studinger, M., Bell, R. E., & Tikku, A. A. (2004b). Estimating the depth and shape of subglacial
 5514 Lake Vostok's water cavity from aerogravity data: ESTIMATING LAKE VOSTOK'S WA-
 5515 TER DEPTH. *Geophysical Research Letters*, 31(12), n/a–n/a. <https://doi.org/10.1029/2004GL019801> (cit. on pp. 104, 117)
- 5517 Studinger, M., & Miller, H. (1999). Crustal structure of the Filchner-Ronne Shelf and Coats Land,
 5518 Antarctica, from gravity and magnetic data: Implications for the breakup of Gondwana.
 5519 *Journal of Geophysical Research: Solid Earth*, 104(B9), 20379–20394. <https://doi.org/10.1029/1999JB900117> (cit. on p. 145)
- 5521 Talwani, M., Worzel, J. L., & Landisman, M. (1959). Rapid gravity computations for two-dimensional
 5522 bodies with application to the Mendocino submarine fracture zone. *Journal of Geophysical*
 5523 *Research*, 64(1), 49–59. <https://doi.org/10.1029/JZ064i001p00049> (cit. on p. 104)
- 5524 Tankersley, M., Horgan, H. J., Siddoway, C. S., Caratori Tontini, F., & Tinto, K. J. (2022). Base-
 5525 ment Topography and Sediment Thickness Beneath Antarctica's Ross Ice Shelf. *Geophys-*
 5526 *ical Research Letters*, 49(10). <https://doi.org/10.1029/2021GL097371> (cit. on pp. 22, 113,
 5527 126, 131, 147)
- 5528 Tankersley, M. D. (2023). Antarctic_plots: V0.0.6. <https://doi.org/10.5281/zenodo.7750998>.
 5529 (Cit. on pp. 23, 50, 167)
- 5530 Tankersley, M. (2022). Mdtanker/RIS_basement_sediment: V2.0. <https://doi.org/10.5281/zenodo.6499863>. (Cit. on p. 23)
- 5532 Tankersley, M., Horgan, H., & Caratori-Tontini, F. (2023). Mdtanker/RIS_gravity_inversion:
 5533 First release associated with PhD thesis. <https://doi.org/10.5281/zenodo.8084469>.
 5534 (Cit. on p. 23)
- 5535 Tarantola, A. (2005). *Inverse Problem Theory and Methods for Model Parameter Estimation*. So-
 5536 ciety for Industrial and Applied Mathematics. <https://doi.org/10.1137/1.9780898717921>.
 5537 (Cit. on p. 39)
- 5538 ten Brink, U. S., Bannister, S., Beaudoin, B. C., & Stern, T. A. (1993). Geophysical investigations
 5539 of the tectonic boundary between East and West Antarctica. *Science*, 261(5117), 45–50.
 5540 <https://doi.org/10.1126/science.261.5117.45> (cit. on pp. 21, 31, 130)
- 5541 Thomas, R. H. (1979). Ice Shelves: A Review. *Journal of Glaciology*, 24(90), 273–286. <https://doi.org/10.3189/S0022143000014799> (cit. on p. 16)
- 5543 Timmermann, R., Brocq, A. L., Deen, T., Domack, E., Dutrieux, P., Galton-Fenzi, B., Hellmer,
 5544 H., Humbert, A., Jansen, D., Jenkins, A., Lambrecht, A., Makinson, K., Niederjasper, F.,
 5545 Nitsche, F., Nøst, O. A., Smetsrud, L. H., & Smith, W. H. F. (2010). A consistent data set
 5546 of Antarctic ice sheet topography, cavity geometry, and global bathymetry. *Earth System*
 5547 *Science Data*, 2(2), 13. <https://doi.org/10.5194/essd-2-261-2010> (cit. on pp. 89, 121)
- 5548 Tinto, K. J., & Bell, R. E. (2011). Progressive unpinning of Thwaites Glacier from newly identified
 5549 offshore ridge: Constraints from aerogravity. *Geophysical Research Letters*, 38, 1–6. <https://doi.org/10.1029/2011GL049026> (cit. on pp. 46, 103, 104, 117, 145)
- 5551 Tinto, K. J., Padman, L., Siddoway, C. S., Springer, S. R., Fricker, H. A., Das, I., Caratori Tontini,
 5552 F., Porter, D. F., Frearson, N. P., Howard, S. L., Siegfried, M. R., Mosbeux, C., Becker,
 5553 M. K., Bertinato, C., Boghosian, A., Brady, N., Burton, B. L., Chu, W., Cordero, S. I.,
 5554 ... Bell, R. E. (2019). Ross Ice Shelf response to climate driven by the tectonic imprint on
 5555 seafloor bathymetry. *Nature Geoscience*, 12(6), 441–449. <https://doi.org/10.1038/s41561-019-0370-2> (cit. on pp. 20, 21, 26–29, 32, 33, 38, 46, 67, 88, 89, 102, 103, 105, 108, 117,
 5557 119, 121, 124, 126, 129–137, 144, 148, 152, 153)
- 5558 Tinto, K. J., Bell, R. E., Cochran, J. R., & Münchow, A. (2015). Bathymetry in Petermann fjord
 5559 from Operation IceBridge aerogravity. *Earth and Planetary Science Letters*, 422, 58–66.
 5560 <https://doi.org/10.1016/j.epsl.2015.04.009> (cit. on pp. 16, 45, 46, 103, 104, 117)

- 5561 Tulaczyk, S., Kamb, W. B., & Engelhardt, H. F. (2000). Basal mechanics of Ice Stream B, west
 5562 Antarctica: 2. Undrained plastic bed model. *Journal of Geophysical Research: Solid Earth*,
 5563 105(B1), 483–494. <https://doi.org/10.1029/1999JB900328> (cit. on pp. 18, 140)
- 5564 Uieda, L. (2018). Verde: Processing and gridding spatial data using Green's functions. *Journal of
 5565 Open Source Software*, 3(29), 957. <https://doi.org/10.21105/joss.00957> (cit. on pp. 50, 51,
 5566 61, 63, 69, 96)
- 5567 Uieda, L., & Barbosa, V. C. (2017). Fast nonlinear gravity inversion in spherical coordinates with
 5568 application to the South American Moho. *Geophysical Journal International*, 208(1), 162–
 5569 176. <https://doi.org/10.1093/gji/ggw390> (cit. on pp. 42, 48, 49, 52, 54, 84, 97, 103, 145)
- 5570 Uieda, L., Soler, S., Rampin, R., van Kemenade, H., Turk, M., Shapero, D., Banihirwe, A., & Lee-
 5571 man, J. (2020). Pooch: A friend to fetch your data files. *Journal of Open Source Software*,
 5572 5(45), 1943. <https://doi.org/10.21105/joss.01943> (cit. on p. 167)
- 5573 Uieda, L., Tian, D., Leong, W. J., Jones, M., Schlitzer, W., Toney, L., Grund, M., Yao, J., Magen,
 5574 Y., Materna, K., Newton, T., Anant, A., Ziebarth, M., Wessel, P., & Quinn, J. (2021).
 5575 PyGMT: A Python interface for the Generic Mapping Tools. <https://doi.org/10.5281/zenodo.5607255>. (Cit. on pp. 35, 50, 168)
- 5577 *Understanding the Bouguer Anomaly*. (2017). Elsevier. <https://doi.org/10.1016/B978-0-12-812913-5.00008-7>. (Cit. on p. 91)
- 5579 Vajda, P., Ellmann, A., Meurers, B., Vaníček, P., Novák, P., & Tenzer, R. (2008a). Global ellipsoid-
 5580 referenced topographic, bathymetric and stripping corrections to gravity disturbance. *Stu-
 5581 dia Geophysica et Geodaetica*, 52(1), 19–34. <https://doi.org/10.1007/s11200-008-0003-5>
 5582 (cit. on p. 102)
- 5583 Vajda, P., Ellmann, A., Meurers, B., Vaníček, P., Novák, P., & Tenzer, R. (2008b). Gravity dis-
 5584 turbances in regions of negative heights: A reference quasi-ellipsoid approach. *Stu-
 5585 dia Geophysica et Geodaetica*, 52(1), 35–52. <https://doi.org/10.1007/s11200-008-0004-4> (cit. on
 5586 p. 91)
- 5587 Vajda, P., Vaníček, P., & Meurers, B. (2006). A new physical foundation for anomalous gravity.
*Stu-
 5588 dia Geophysica et Geodaetica*, 50(2), 189–216. <https://doi.org/10.1007/s11200-006-0012-1> (cit. on p. 94)
- 5589 Vajda, P., Vaníček, P., Novák, P., Tenzer, R., & Ellmann, A. (2007). Secondary indirect effects
 5590 in gravity anomaly data inversion or interpretation. *Journal of Geophysical Research*,
 5591 112(B6), B06411. <https://doi.org/10.1029/2006JB004470> (cit. on pp. 92, 101)
- 5593 Vajda, P., Vaníček, P., & Meurers, B. (2004). On the removal of the effect of topography on gravity
 5594 disturbance in gravity data inversion or interpretation. *Contributions to Geophysics and
 5595 Geodesy*, 34 (cit. on p. 92).
- 5596 Vaňková, I., Winberry, J. P., Cook, S., Nicholls, K. W., Greene, C. A., & Galton-Fenzi, B. K. (2023).
 5597 High Spatial Melt Rate Variability Near the Totten Glacier Grounding Zone Explained by
 5598 New Bathymetry Inversion. *Geophysical Research Letters*, 50(10), e2023GL102960. <https://doi.org/10.1029/2023GL102960> (cit. on pp. 103, 104)
- 5600 Venturelli, R. A., Siegfried, M. R., Roush, K. A., Li, W., Burnett, J., Zook, R., Fricker, H. A., Priscu,
 5601 J. C., Leventer, A., & Rosenheim, B. E. (2020). Mid-Holocene grounding line retreat and
 5602 readvance at Whillans Ice Stream, West Antarctica. *Geophysical Research Letters*, 47(15).
 5603 <https://doi.org/10.1029/2020GL088476> (cit. on pp. 20, 32, 33, 35, 88, 129, 133)
- 5604 Virtanen, P., Gommers, R., Oliphant, T. E., Haberland, M., Reddy, T., Cournapeau, D., Burovski,
 5605 E., Peterson, P., Weckesser, W., Bright, J., van der Walt, S. J., Brett, M., Wilson, J.,
 5606 Millman, K. J., Mayorov, N., Nelson, A. R. J., Jones, E., Kern, R., Larson, E., ... SciPy
 5607 1.0 Contributors. (2020). SciPy 1.0: Fundamental algorithms for scientific computing in
 5608 python. *Nature Methods*, 17, 261–272. <https://doi.org/10.1038/s41592-019-0686-2> (cit. on
 5609 p. 50)
- 5610 Wannamaker, P., Hill, G., Stodt, J., Maris, V., Ogawa, Y., Selway, K., Boren, G., Bertrand,
 5611 E., Uhlmann, D., Ayling, B., Green, A. M., & Feucht, D. (2017). Uplift of the central
 5612 transantarctic mountains. *Nature Communications*, 8(1), 1588. <https://doi.org/10.1038/s41467-017-01577-2> (cit. on pp. 21, 130, 131)
- 5614 Wei, W., Blankenship, D. D., Greenbaum, J. S., Gourmelen, N., Dow, C. F., Richter, T. G., Greene,
 5615 C. A., Young, D. A., Lee, S., Kim, T.-W., Lee, W. S., & Assmann, K. M. (2020). Getz Ice
 5616 Shelf melt enhanced by freshwater discharge from beneath the West Antarctic Ice Sheet.
 5617 *The Cryosphere*, 14(4), 1399–1408. <https://doi.org/10.5194/tc-14-1399-2020> (cit. on
 5618 pp. 103, 104, 117, 144)

- 5619 Werner, S. (1953). Interpretation of magnetic anomalies at sheet-like bodies. In *Sveriges Geologiska
5620 Undersök* (pp. 413–449). Stockholm Norstedt. (Cit. on pp. 28, 148).
- 5621 Wessel, P., Luis, J. F., Uieda, L., Scharroo, R., Wobbe, F., Smith, W. H. F., & Tian, D. (2019).
5622 The Generic Mapping Tools version 6. *Geochemistry, Geophysics, Geosystems*, 20(11),
5623 5556–5564. <https://doi.org/10.1029/2019GC008515> (cit. on pp. 35, 62)
- 5624 Wessel, P., & Bercovici, D. (1998). Interpolation with splines in tension: A Green's function ap-
5625 proach. *Mathematical Geology*, 30(1), 77–93. <https://doi.org/10.1023/A:1021713421882>
5626 (cit. on p. 62)
- 5627 White-Gaynor, A. L., Nyblade, A. A., Aster, R. C., Wiens, D. A., Bromirski, P. D., Gerstoft, P.,
5628 Stephen, R. A., Hansen, S. E., Wilson, T., Dalziel, I. W., Huerta, A. D., Paul Winberry,
5629 J., & Anandakrishnan, S. (2019). Heterogeneous upper mantle structure beneath the Ross
5630 Sea Embayment and Marie Byrd Land, West Antarctica, revealed by P-wave tomography.
5631 *Earth and Planetary Science Letters*, 513, 40–50. <https://doi.org/10.1016/j.epsl.2019.02.013> (cit. on p. 33)
- 5632 Whitehouse, P. L., Gomez, N., King, M. A., & Wiens, D. A. (2019). Solid Earth change and the
5633 evolution of the Antarctic Ice Sheet. *Nature Communications*, 10(1), 503. <https://doi.org/10.1038/s41467-018-08068-y> (cit. on pp. 19, 33)
- 5634 Wilkinson, M. D., Dumontier, M., Aalbersberg, I. J., Appleton, G., Axton, M., Baak, A., Blomberg,
5635 N., Boiten, J.-W., da Silva Santos, L. B., Bourne, P. E., Bouwman, J., Brookes, A. J., Clark,
5636 T., Crosas, M., Dillo, I., Dumon, O., Edmunds, S., Evelo, C. T., Finkers, R., ... Mons,
5637 B. (2016). The FAIR Guiding Principles for scientific data management and stewardship.
5638 *Scientific Data*, 3(1), 160018. <https://doi.org/10.1038/sdata.2016.18> (cit. on p. 23)
- 5639 Wilson, D. S., Jamieson, S. S., Barrett, P. J., Leitchenkov, G., Gohl, K., & Larter, R. D. (2012).
5640 Antarctic topography at the Eocene–Oligocene boundary. *Palaeogeography, Palaeoclima-
5641 tology, Palaeoecology*, 335–336, 24–34. <https://doi.org/10.1016/j.palaeo.2011.05.028>
5642 (cit. on pp. 34, 143, 151)
- 5643 Wilson, D. S., & Luyendyk, B. (2009). West Antarctic paleotopography estimated at the Eocene-
5644 Oligocene climate transition. *Geophysical Research Letters*, 36(16), L16302. <https://doi.org/10.1029/2009GL039297> (cit. on pp. 26, 34, 143, 151, 153)
- 5645 Wilson, D. S., Pollard, D., DeConto, R. M., Jamieson, S. S., & Luyendyk, B. (2013). Initiation of
5646 the West Antarctic Ice Sheet and estimates of total Antarctic ice volume in the earliest
5647 Oligocene. *Geophysical Research Letters*, 40(16), 4305–4309. <https://doi.org/10.1002/grl.50797> (cit. on pp. 26, 34)
- 5648 Yamasaki, T., Miura, H., & Nogi, Y. (2008). Numerical modelling study on the flexural uplift of
5649 the Transantarctic Mountains. *Geophysical Journal International*, 174(1), 377–390. <https://doi.org/10.1111/j.1365-246X.2008.03815.x> (cit. on p. 130)
- 5650 Yang, J., Guo, J., Greenbaum, J. S., Cui, X., Tu, L., Li, L., Jong, L. M., Tang, X., Li, B., Blanken-
5651 ship, D. D., Roberts, J. L., Ommen, T., & Sun, B. (2021). Bathymetry Beneath the Amery
5652 Ice Shelf, East Antarctica, Revealed by Airborne Gravity. *Geophysical Research Letters*,
5653 48(24). <https://doi.org/10.1029/2021GL096215> (cit. on pp. 38, 46, 62, 102–104, 117, 120)
- 5654 Yang, J., Jekeli, C., & Liu, L. (2018). Seafloor Topography Estimation From Gravity Gradients
5655 Using Simulated Annealing. *Journal of Geophysical Research: Solid Earth*. <https://doi.org/10.1029/2018JB015883> (cit. on p. 104)
- 5656 Yang, J., Luo, Z., & Tu, L. (2020a). Ocean Access to Zachariæ Isstrøm Glacier, Northeast Green-
5657 land, Revealed by OMG Airborne Gravity. *Journal of Geophysical Research: Solid Earth*,
5658 125(11). <https://doi.org/10.1029/2020JB020281> (cit. on pp. 78, 103, 104)
- 5659 Yang, J., Luo, Z., Tu, L., Li, S., Guo, J., & Fan, D. (2020b). On the Feasibility of Seafloor To-
5660 polography Estimation from Airborne Gravity Gradients: Performance Analysis Using Real
5661 Data. *Remote Sensing*, 12(24), 4092. <https://doi.org/10.3390/rs12244092> (cit. on p. 102)
- 5662 Yokoyama, Y., Anderson, J. B., Yamane, M., Simkins, L. M., Miyairi, Y., Yamazaki, T., Koizumi,
5663 M., Suga, H., Kusahara, K., Prothro, L., Hasumi, H., Southon, J. R., & Ohkouchi, N.
5664 (2016). Widespread collapse of the Ross Ice Shelf during the late Holocene. *Proceedings
5665 of the National Academy of Sciences*, 113(9), 2354–2359. <https://doi.org/10.1073/pnas.1516908113> (cit. on p. 88)
- 5666 Zhao, C., Gladstone, R. M., Warner, R. C., King, M. A., Zwinger, T., & Morlighem, M. (2018).
5667 Basal friction of Fleming Glacier, Antarctica – Part 1: Sensitivity of inversion to temper-
5668 ature and bedrock uncertainty. *The Cryosphere*, 12(8), 2637–2652. <https://doi.org/10.5194/tc-12-2637-2018> (cit. on p. 15)

- 5677 Zhao, K. X., Stewart, A. L., & McWilliams, J. C. (2019). Sill-Influenced Exchange Flows in Ice Shelf
5678 Cavities. *Journal of Physical Oceanography*, 49(1), 163–191. [https://doi.org/10.1175/JPO-](https://doi.org/10.1175/JPO-D-18-0076.1)
5679 D-18-0076.1 (cit. on pp. 16, 89)
- 5680 Zhou, Z., Wiens, D. A., Shen, W., Aster, R. C., Nyblade, A., & Wilson, T. J. (2022). Radial
5681 Anisotropy and Sediment Thickness of West and Central Antarctica Estimated From
5682 Rayleigh and Love Wave Velocities. *Journal of Geophysical Research: Solid Earth*, 127(3).
5683 <https://doi.org/10.1029/2021JB022857> (cit. on pp. 31, 152)